



HAL
open science

Time and Frequency Multiplexing for Continuous-Variable Quantum Networks

Francesca Sansavini

► **To cite this version:**

Francesca Sansavini. Time and Frequency Multiplexing for Continuous-Variable Quantum Networks. Quantum Physics [quant-ph]. Sorbonne Université; Helsingin yliopisto (Finland), 2023. English. NNT : 2023SORUS642 . tel-04521754

HAL Id: tel-04521754

<https://theses.hal.science/tel-04521754>

Submitted on 26 Mar 2024

HAL is a multi-disciplinary open access archive for the deposit and dissemination of scientific research documents, whether they are published or not. The documents may come from teaching and research institutions in France or abroad, or from public or private research centers.

L'archive ouverte pluridisciplinaire **HAL**, est destinée au dépôt et à la diffusion de documents scientifiques de niveau recherche, publiés ou non, émanant des établissements d'enseignement et de recherche français ou étrangers, des laboratoires publics ou privés.



COLLÈGE
DE FRANCE
1530



**Thèse de doctorat de
Sorbonne Université
et University of Helsinki**

présentée par

Francesca Sansavini

sur le sujet:

**Time and Frequency Multiplexing
for Continuous-Variable Quantum Networks**



Membres du jury :

Dr. Giulia FERRINI	Rapporteur
Dr. Marco BELLINI	Rapporteur
Pr. Eleni DIAMANTI	Examineur
Dr. Paolo MURATORE-GINANNESCHI	Examineur
Pr. Virginia D'AURIA	Membre invité
Pr. Nicolas TREPS	Membre invité
Pr. Valentina PARIGI	Directrice de thèse
Pr. Sabrina MANISCALCO	Directrice de thèse

ISBN 978-951-51-9564-7 (print)
ISBN 978-951-51-9565-4 (online)
ISSN 2954-2898 (print)
ISSN 2954-2952 (online)
PunaMusta, Joensuu 2023

A mio babbo Antonio

Abstract

Multimode quantum light fields have emerged as a promising tool for the generation of multipartite entangled states, known as cluster states, and the advancement of continuous-variable (CV)-based quantum information technologies. In our approach, the nodes of the entangled network represent individual temporal/frequency modes of the electromagnetic field, while the links are tailored entanglement correlations. In this thesis we demonstrate the generation of multimode squeezed states that are multiplexed both in the temporal and in the spectral domain. Our setup is based on a train of ultrashort pulses that drive a spontaneous parametric down conversion process in a non-linear periodically poled KTP waveguide. Here, we produced the largest number of spectral modes of squeezed vacuum measured via homodyne detection in a single-pass configuration. Moreover, we performed pulse-resolved (pulse-by-pulse) squeezing measurements, confirming the existence of the multimode spectral structure at a single pulse level; this paves the way for generating entangled structures at the repetition rate of the laser. While temporal multiplexing has already enabled the generation of the largest CV cluster states, multimode squeezing in the spectral modes of a femtosecond source provides complete reconfigurability of the entanglement network. In addition to the generation of multiplexed entangled networks, this thesis explores other types of quantum information processing applications for multimode squeezed light. The high number of pulsed modes allows us to implement quantum walks on a graph for search purposes, analogously to the Grover algorithm. Multimode squeezed light has also been exploited in this work to investigate the field of quantum simulations, and in particular to observe the emergence of quantum synchronization effects.

Acknowledgements

This thesis is the conclusion of something that started long ago when I wrote to Nicolas an email asking to be considered for a (theoretical!) internship at LKB. Since that time in 2018, I have feared the moment of my PhD defence because, while this PhD has not always been an easy journey, the lab has always been home. And it will not be easy, going forward, to find another home that can match what LKB and the people of LKB were to me. I hope that with these acknowledgements, I can manage to transmit at least a small part of the gratitude that I feel towards all of you.

I will start by thanking the jury for reviewing my work and for being present at my PhD defence. Thanks in particular to Giulia Ferrini and Marco Bellini, who had the difficult task of reviewing my (very) long manuscript. Thanks a lot for the interesting questions you asked during the defence; it was a real pleasure to discuss with you the work we did in these last years and to show the various aspects of my research in detail.

Thanks to all the people at LKB that contribute to make the lab the wonderful place it is. Merci à David, Laetitia, Céline et Stéphanie. Merci pour l'organisation des événements, des commandes, des contrats, de la cafétéria (et surtout de l'énorme patience que vous avez pour gérer le café!). Franchement, vous êtes incroyables et j'espère que vous savez que si le labo tourne comme il faut c'est principalement grâce à vous. Merci à l'atelier électronique, Loïc, David et Eli, et un grand merci à Bérangère pour l'aide apportée sur les manips ces dernières années. Merci à Carou et à toute l'équipe de l'atelier mécanique pour être toujours disponibles pour réaliser n'importe quelle pièce, même les plus chiantes.

And of course, thanks a lot to all the colleagues who came and went and who shared a part of my PhD at LKB. Thanks to Alex, I learnt so much from you and you really are an amazing scientist. Thank you for taking the time to answer all my questions and for doing that weird thing with your teacup when you are thinking, thank you for the moments spent in the lab listening to your wonderful playlist and talking. Thanks to Niels, because you're the sun that shines into the darkness of our cave and you're a 10/10. Thanks to Iris, for your empathy and for making sure that I'm alright when you sense something is off. I would have liked to spend more time with you in the lab, but I am glad that I am leaving my dear experiment in very good hands. Thanks to Ganaël, with whom I shared all of my PhD. Our relationship has been rocky from the very start and our two very different and stubborn personalities did not help. But in four years I transitioned from wanting to push

you off a cliff to actually enjoying the time spent together. I especially want to thank you for your sensitivity and advice during these last difficult months, where I try to come to terms with life after the PhD. Thanks a lot to Paul and Matthieu, without your help it would have taken forever just to learn how to properly put a mirror on a table. I came to LKB as a poor theoretician who didn't know how to use an oscilloscope and you transformed me into an ok-experimentalist. Paul, thank you for your friendship and our fights (notably over stuff like Tenet and French ham) and for sitting on the grass sometimes even though you hate it. Matthieu, thanks for your patience and your teaching skills, and for all those late afternoons spent in the lab taking measurements. Thank you for being optimistic when I was pessimistic, and for lifting up my spirits when I thought we would never find squeezing. Thanks to Beate and Clémentine, my girl squad. Thanks for our lunches, coffee (or tea) breaks and for all the moments spent together, thanks for being spies all together and saving Professor Lock and for buying potions from a Troll with me. Having you at my side in the lab has been more precious than I can tell. Last but not least, thanks a lot to Nicolas. I always joke about you ghosting me, but you have always been there whenever I needed help and I know that I can always count on you. So thank you for the patience with my 100 questions about sidebands, thank you for the beers at La Bulle à Bière, for sharing with me and Ganaël the best Corsican weekend and for being a witness at my “marriage”. And I will never thank you enough for forwarding my email to Valentina six years ago, despite the very high risk of having ANOTHER Italian in your team.

While not as long as my time at LKB, I had the opportunity to spend quite some time in Helsinki during my PhD. The cotutelle has been quite challenging, especially from an administrative point of view, but I couldn't be more glad I did it. Apart from discovering the joy of the sauna, I got to meet wonderful people, both in the office and outside. Thank you Sabrina, for the opportunity to come to Helsinki, for your explosive energy, your crazy stories and your 1000 different projects. Thank you for thinking of me and always including me in whichever bookclub, Quantum Jam, or whatever else pops up in your mind. The part of my life spent in Helsinki has been wonderful, and it was possible because of you. Thanks to my colleagues, Nicola, Marco and Otto, sharing the office with you has been great. Thank you for the daily comments on the Unicafe menu AND thank you so much for knighting me and giving me the means for FINALLY stabbing properly people who annoy me, with a magnificent PhD longsword that is bigger than I am. Marco and Nicola, a special thank you for making me feel at home from the very first day. Thanks to Marco for being the bad guy and to Nicola for being the good guy, so that it makes it easy for me to decide who I should save in a trolley problem.

I want to thank two people in particular who make it extremely hard to leave the lab behind: my supervisor Valentina and my sottoposto Johan. Valentina, you already know everything and more that I could possibly write here but I want to put it in black and white so that the poor souls that have the misfortune of going through my thesis will know what kind of supervisor you are. You are an incredible scientist, an exceptional human and a

great friend. You have always been there for whichever professional or personal problems I encountered during these years, constantly encouraging me and supporting me throughout this whole journey. Thank you, because I can share with you my stupid birds stickers on Telegram, but also my life in front of a beer. I could have never wished for a better supervisor. Merci Johan. Merci parce que t'es un super physicien et expérimentateur (surtout pour tout ce qui est mode-matching) et manipuler avec toi a été incroyable, merci parce que t'es multitâche (heureusement), merci parce que t'acceptes d'être menacé avec un mini-couteau et un râteau télescopique. Et merci parce que, ce qui est encore plus important que d'être un bon physicien, t'es une personne bien au-delà de l'exceptionnel... à part quelques défauts à corriger, qui vont d'un haussement compulsif des sourcils quand on est en désaccord à un manque de goût extrême que j'essaie de corriger. Il est impossible de faire une liste de tout ce qu'on a partagé et découvert ensemble (notamment sur des sombres subreddits) et surtout de tout ce que tu m'as appris pendant ces années et d'à quel point t'étais une source d'inspiration constante. C'est incroyable qu'avec tout cela j'ai quand même réussi à faire une thèse. Merci pour tout ce que t'es.

This achievement has been reached also thanks to the constant support of my friends and family. Thanks to all of my friends, because it could be easy to get lost, while living in different parts of the world. And this doesn't happen. Thanks to Quique, Leire and Paula. You are the reason why, during my time in Helsinki, I learnt more about Spanish culture than Finnish culture. Thank you for the Mus, the Parchis, *la primavera trompetera*, the very late dinners, the saunas (especially with you, Quique, all those hours talking at 90 degrees will stay in my heart forever), thank you for the Lofoten and Costa Rica and for your incredible support, thank you for the best and most heartfelt birthday cake. The time spent in Lato with you was one of the best moments of my PhD years and I'm so grateful I got room 210 in building 15 that January. Merci à Gabriel, pour avoir été le premier dans plein de choses: pour la première balade souterraine, le premier avec qui j'ai eu le courage de parler en français dans ton appart rue des Trois Frères, pour avoir été mon premier vrai ami de ma terre adoptive. Grazie Lucia perché siamo cresciute insieme ed hai vissuto con me i momenti più belli e quelli più brutti. Grazie per tutti quei pomeriggi passati alla Esse, per le serate infinite alla Collina, per aver ascoltato e cantato con me i Blastema, per tutte le frasi scarabocchiate sul muro della mia stanza. Grazie Pier, grazie per gli anni passati insieme e per essere rimasto, grazie perché a volte mi innervosisci da morire e io sono insopportabile ma tu ci sei sempre. Grazie Mef, perché mi fai alzare la mattina per fare colazione in centro, perché sei sempre in giro per il mondo ma sempre presente chissà come. Grazie Fra, per la prima discussione sulle balene, per tutte quelle ore in aula studio a rompersi la testa sulla meccanica analitica, sulla meccanica statistica, su qualsiasi cosa. Grazie perché per colpa mia ora odi le mele, per tutte le Spinali Nere, per i Buongiollo, per essere sempre al mio fianco. Grazie Ale, per Rue de l'Abreuvoir, per aver condiviso con me i miei crampi notturni e i topi in casa, per la tua carbonara, per gli episodi di Chuck. Grazie per quel primo anno a Parigi, per quelli che sono venuti dopo e per quelli che verranno. Grazie Dia. Per il tuo

ottimismo e il tuo farti in quattro, anzi in cento, per me, per i messaggi vocali di trenta minuti (quando va bene), per le tue castagnole e la tua pasta fresca. Grazie Linda. Per gli attacchi di nervi condivisi davanti alle macchinette del caffè, perché esci di casa con le scarpe spaiate, perché sei la mia anima gemella, perché sei un vulcano di idee e sentimenti e... cose, mille cose, sei un vulcano di tutte le cose che esistono al mondo. Grazie Terry. Per esserci in ogni momento, per avermi accompagnato nelle mie cadute e aver detto sempre la cosa giusta per farmi rialzare, per le Goccioline, le pizze e i crescioni divisi a metà.

Merci à ma famille française, Chrystel, Philippe, Marie et Nicolas. Merci pour votre bonheur constant, votre accueil, les ateliers et les mille idées différentes, merci de me faire sentir une Mottier-Magnabosco d'adoption. Nico, merci pour ces années passées ensemble, pour les moments heureux et les moments tristes, les disputes et les rires. Merci d'être le maître des tartines à la maison même si tu mets trop de beurre, merci de me pousser constamment à suivre tout ce qui me traverse l'esprit, que ce soit partir à l'étranger ou me lancer dans l'horlogerie, merci de toujours venir me chercher, même quand je te déteste et quand je suis au top du désagréable. Merci pour ton amour. Ed infine, grazie infinite a tutta la mia famiglia. Grazie a Romeo, per essere l'unico che a volte riesce a farmi uscire bene in una foto, per esserci sempre, per fare parte della nostra famiglia. Grazie ai nonni, per l'infanzia meravigliosa, per avermi fatto costruire castelli con sedie e tavoli e mangiare cappelletti al ragù e Gibi-Gibi, grazie agli zii e ai cugini. Grazie Paola, per le serate passate sul terrazzo del mare a fare le cornici concentriche e a leggere, e grazie per avermi raccontato tutte quelle favole da piccola, che mi frullano in testa ancora adesso trent'anni dopo. Grazie Simo, per le ore passate su Spyro con me, per aver giocato alla Luna Nera con la luce spenta prima di addormentarsi, per far parte delle fondamenta della mia vita. Grazie mamma, per il tuo supporto incondizionato, per avermi resa ciò che sono, per essere il porto sicuro che mi aspetta in ogni momento, per essere la mia migliore amica. Grazie babbo, per avermi insegnato ad arrivare dove volevo, per tutta la forza e la determinazione che mi hai trasmesso, per le notti trascorse sul terrazzo del mare a guardare le stelle. Sei sempre la mia roccia.

Contents

Introduction	1
I Theoretical Background	5
1 Quantum Light	7
1.1 The multimode classical electromagnetic field	8
1.1.1 The classical electromagnetic field	8
1.1.2 Multimode description	10
1.1.3 Gaussian Beam	11
1.1.4 Temporal and spectral modes	13
1.1.5 Quadratures of the field	14
1.2 Quantization of the field	15
1.2.1 From classical mechanics to quantum mechanics	16
1.2.2 Quadratures as quantum operators	17
1.3 Multimode quantum light	19
1.3.1 The multimode electric field operator	19
1.3.2 Basis change and two Hilbert spaces	20
1.3.3 Intrinsic single-mode states	21
1.4 Description of quantum states	22
1.4.1 Discrete variables and Continuous variables	22
1.4.2 Pure and Mixed states	24
1.4.3 Wigner function	25
1.5 Common states in Quantum optics	26
1.5.1 Fock states	26
1.5.2 Coherent states	29
1.5.3 Squeezed states	30
1.5.4 EPR state	32

2	Gaussian states and measurements	37
2.1	Gaussian states and operations	38
2.1.1	Gaussian states	38
2.1.2	Generalities on Gaussian operations	39
2.1.3	Linear optics transformations	41
2.1.4	Decompositions of states and unitaries	42
2.2	Sidebands in optics	43
2.2.1	Classical modulations of the field	43
2.2.2	Sidebands quantum operators	46
2.2.3	Sidebands as quantum states	47
2.3	Measurement of quantum states	49
2.3.1	Intensity measure	50
2.3.2	Noise spectrum and quantum noise	51
2.3.3	Homodyne detection in the temporal domain	52
2.3.4	Homodyne detection in the spectral domain	54
3	Nonlinear optics	59
3.1	Introduction to nonlinear optics	60
3.1.1	The forced wave equation	60
3.1.2	Nonlinear polarization	62
3.1.3	Contracted notation	64
3.1.4	Nonlinear processes in KTP	64
3.2	Second-Harmonic Generation	66
3.2.1	SHG with a broadband field	66
3.2.2	Phase matching	67
3.2.3	Quasi-phase-matching	69
3.3	Parametric Down-Conversion	71
3.3.1	PDC with a broadband field	71
3.3.2	Eigenmodes of the PDC	73
3.3.3	Quantum treatment (SPDC)	74
3.3.4	Hamiltonian derivation	77
II	Experimental Tools	81
4	Experimental setup for squeezing generation	83
4.1	Scheme of the setup	84
4.2	The ultrafast light source	86
4.2.1	Mode-locked lasers	86
4.2.2	The Synergy laser	90
4.2.3	Frequency combs	91

4.2.4	Gaussian pulses	92
4.3	Nonlinear ppKTP Waveguides	94
4.3.1	Generalities on waveguides	94
4.3.2	Guided modes in diffused waveguides	95
4.3.3	Spectral modes for type-0	98
4.3.4	Waveguides injection and characterization	101
4.4	Second-Harmonic generation via ppKTP	105
4.4.1	The history of SHG in this setup	105
4.4.2	Simulation of the second-harmonic spectrum	106
4.4.3	Experimental second-harmonic generation	109
4.5	The pulse shaper	111
4.5.1	General introduction	111
4.5.2	Spectral phase and amplitude shaping	112
4.5.3	Characteristics of our pulse shaper	115
5	Measuring multimode squeezing multiplexed in time and frequency	119
5.1	Alignment procedure	119
5.1.1	Parametric amplification	120
5.1.2	Visibility between seed and LO	122
5.2	Measuring squeezing	125
5.2.1	Sidebands measurement	125
5.2.2	Temporal measurement: alignment and mode definition	126
5.2.3	Temporal measurement: measurement and results	128
5.3	Covariance matrix reconstruction	130
5.3.1	Covariance matrix measurement	131
5.3.2	Supermodes reconstruction	134
5.3.3	Bipartite entanglement in the frexel basis	136
6	Towards a time-frequency multiplexed CV network	141
6.1	Time-frequency multiplexed cluster state	141
6.1.1	Building a multiplexed network	141
6.1.2	Second waveguide	143
6.1.3	Implementation of an EPR state	145
6.2	Locking system	146
6.2.1	The PID controller	147
6.2.2	DC lock and AC lock	148
6.2.3	Experimental implementation of phase locks	150
6.2.4	Measurement-hold phase	154

III	Quantum Information Processing with Squeezed Light	157
7	Continuous-Time Quantum Walks in a photonics setup	159
7.1	Quantum Walks	160
7.1.1	Random walks on graphs	160
7.1.2	Continuous-time Quantum Walks for spatial search	161
7.1.3	Quantum Walk search in a complete graph	164
7.2	Mapping from theory to experiment	168
7.2.1	Encoding qudits in photon-subtracted squeezed states	168
7.2.2	Encoding of the states and operations for the walk	169
7.3	Photonic implementation of Quantum Walks	171
7.3.1	Building an interferometer	171
7.3.2	A simple instructive attempt	173
7.3.3	Interferometer for quantum search	175
7.3.4	Fidelity with the target state of the walk	178
7.3.5	Generalities on a realistic experimental implementation	180
8	Quantum Synchronization of two coupled oscillators	183
8.1	Quantum synchronization	184
8.1.1	Introduction to quantum synchronization	184
8.1.2	Generalities on open quantum systems	185
8.1.3	Coupled dissipative harmonic oscillators	185
8.2	Mapping with experiment	187
8.2.1	Environment as a network of oscillators	188
8.2.2	Interaction between system and environment	189
8.2.3	Simulating the evolution with squeezing and linear optics	190
8.2.4	Local oscillator shaping for basis change	193
8.3	Synchronization in an optical setup	194
8.3.1	Simulation of the dynamics	195
8.3.2	LO shaping for simulation of the dynamics	196
8.3.3	Experimental limitations	199
	Conclusion & outlooks	201
	Appendices	203
A	Pictures in quantum mechanics	205
B	More details on ultrafast light	209
C	Signal processing and derivative	215

D Details on calculations	219
References	224

Introduction

Since the dawn of history, people worldwide have celebrated light as the source of life on Earth, associating it to prosperity, creation, knowledge. The Sun has been one of the major deities in many of the *pantheons* of ancient religions: the Greek god Helios, that rode his chariot through the sky to bring the day, whose figure was sculpted into one of the seven wonders of the ancient world; the Egyptian Ra, the earliest god to have emerged from the primordial waters and creator of all forms of life; and the god Tonatiuh, that ruled the world and all living beings, and in the name of whom the Aztecs made sacrifices in order to ensure his daily voyage from the east to the west, securing the continuation of daylight. In the Jewish and Christian Bible, “Let there be light” is one of the first acts of creation, to illuminate the darkness of a “formless and empty earth”. Over time, the association of light with goodness and darkness, the absence of light, with evil has endured: in popular culture, we are all aware that the “dark side of the Force” is the bad side.

While the symbolic and spiritual exploration of light has persisted since prehistory, the scientific investigation of light began around 2500 years ago in ancient Greece, in strict connection with the study of visual perception. Euclid’s *Optics*, in which he delineates the geometry of “visual rays”, emitted from the eyes and traveling in straight lines, is the ancestor of the modern ray optics model. Throughout the centuries, countless philosophers and scientists have tried to unravel the mysteries of the properties of light through various theories and experiments. More than a millennium after Euclid’s *Optics*, Ibn al-Haytham *Optics*, where we discover that vision is the result of light interacting with objects and being directed into the eye, marked another monumental milestone. During the Middle Ages, advancements in lens-making and optics allowed to deepen the study of the properties of light and laid the foundation for the development of eyeglasses and, some centuries later, of telescopes. This allowed the field of astronomy to flourish, permitting astronomical observations that challenged the geocentric view of the cosmos in the 16th century.

In the 17th century, Sir Isaac Newton conducted groundbreaking experiments on light and color, demonstrating that white light is composed of a spectrum of colors, that can be separated when passed through a prism. Newton was a supporter of the corpuscular theory of light, believing that light was made of “corpuscles” that travelled in a straight line at finite speed [Newton 04]. Even if he was his contemporary, Christiaan Huygens proposed an entirely different theory, suggesting that light propagates as a wave [Huygens 90]. The

wave theory of light gained significant traction, and was predominant until the beginning of the 20th century [Fresnel 19, Foucault 53, Fizeau 49]. After countless brilliant intuitions and missteps, with the help of cornerstones experiments like Young’s interference experiment, at the end of the 19th century the classical electromagnetic theory is finally fully described: light is an electromagnetic radiation obeying Maxwell equations [Maxwell 96].

However, this was just the beginning. In less than a century, a new theory of the nature of light takes over, the *quantum theory of light*. This theory reveals light as a quantum field, whose excitations, the *photons*, can be identified as the elementary particles of light. The discovery of unsettling properties, such as entanglement [Einstein 35] and non-locality [Bell 64], and their experimental verification [Aspect 82], challenged long-established classical concepts, leading to a revolutionary paradigm shift in our understanding of the natural worlds: this is the first Quantum Revolution.

The focus of this first revolution is on fundamental research. During this period, scientists spent decades applying the principles of Quantum Mechanics to the world around us; suddenly, many phenomena unexplainable with classical physics started to make sense. Understanding the natural world was the goal of this generation of scientists. However, throughout human history, knowledge has consistently served as a wellspring of inspiration for creativity and innovation. Mere understanding isn’t enough. Humans don’t stop at knowing that striking a piece of obsidian with a hammerstone results in the removal of stone flakes; they want to use this knowledge to shape the obsidian into a tool with a specific purpose. Since time immemorial, fundamental science has been the driving force behind technological advancement. The fundamental knowledge acquired during the first Quantum Revolution is no different. By learning how nature works, we aim to use this knowledge to shape the physical world at will, to serve a specific purpose. This marks the advent of the Second Quantum Revolution, where our understanding of the physical world has paved the way for numerous applications, collectively referred to as *Quantum Technologies* [Dowling 03, Bruss 19].

The seed for the flourishing of Quantum Technologies was planted 40 years ago, when during the “Physics of Computation Conference” Richard Feynman proposed a Quantum computer to simulate nature: “Nature isn’t classical, dammit, and if you want to make a simulation of nature, you’d better make it quantum mechanical, and by golly it’s a wonderful problem because it doesn’t look so easy” [Feynman 82]. Since his talk, the idea gained widespread attention. The scientific community started to investigate the notion of Quantum Computers and their advantages [Deutsch 85, Bernstein 93], and the first Quantum Algorithms, with a consistent speedup with respect to classical ones, were proposed [Shor 94, Grover 96]. More than 40 years later, while still remaining “not so easy”, the field of Quantum Information is thriving [Nielsen 10]. Attempts to build quantum computers are taking place across a diverse range of platforms, and although fault-tolerant quantum computing remains on the horizon, recent developments [Arute 19, Zhong 20] hold the promise of near-term *noisy-intermediate-scale-quantum* (NISQ)

technology [Preskill 18].

In this context, Quantum Networks, a collection of quantum systems linked by quantum channels, emerge as an essential resource for Quantum Information Processing. They serve as the foundational framework for allowing long-distance quantum communication between parties [Cirac 97] and for implementing multiparty distributed quantum computing [Preskill 99, Gottesman 99, Daiss 21] or a quantum internet [Kimble 08, Pirandola 16]. Quantum Networks can also be used as a support for Measurement-Based-Quantum-Computing (MBQC), that employs specific entangled states, known as *cluster states*, to propagate quantum information through the network via successive measurements and feedforward operations [Raussendorf 01].

Quantum technologies are in principle supported by a wide variety of physical systems, each one with its unique challenges. Among them, photonic quantum technologies emerge nowadays as one of the leading technologies [O'Brien 07, O'Brien 09]. In this work, we focus on multimode light fields for the development of Continuous-variable (CV) quantum technologies [Braunstein 05b, Weedbrook 12, Adesso 14]. In particular, squeezed states and CV-entangled states are an essential resource for many applications, such as MBQC [Menicucci 06, Gu 09, Bourassa 21], quantum sensing [Zhang 21, Pinel 12, Gessner 18], quantum communication [Cai 17, Arzani 19b] and simulations [Nokkala 18], and quantum-enhanced machine learning [Nokkala 21].

Squeezed states and cluster states can be deterministically generated via nonlinear optics interactions, followed by linear optics operations, in the frequency domain [Roslund 14, Cai 17]. Here, we generate multimode squeezing both in the temporal and in the spectral degree of freedom [Kouadou 23], with the final aim (still in-progress) to implement cluster states multiplexed both in the spectral and the temporal domain, that offer both good scalability (due to a high number of modes) and reconfigurability of our resource. Indeed, temporal multiplexing already permitted the generation of the largest entangled networks [Yokoyama 13, Asavanant 19, Larsen 19], while spectral multiplexing enables full reconfigurability of the entanglement links [Cai 17, Chen 14] and mode-selective non-gaussian operations via ultrafast-pulse shaping [Ra 20].

In addition to providing scalable multiplexed resources for MBQC, we can leverage the benefits of having numerous modes and reconfigurable quantum correlations for various quantum information processing techniques. In this work we concentrate on quantum walks [Childs 04a, Matthews 12] and simulation of open quantum systems [Nokkala 18, Renault 23].

Outline of this thesis

The first part of this thesis has the aim of providing the reader with the fundamental concepts that are needed for the understanding of this work. In the first chapter, we introduce the concept of classical and quantum electromagnetic field and we give the notations used throughout this work. We begin by providing a classical definition of the multimode electromagnetic field, with a particular focus on time-frequency modes, which are of primary interest in this work. Successively, we switch to a quantum description, and we provide the basics of the description of quantum light, focusing on a continuous-variable (CV) framework. In the second chapter, we present Gaussian states and measurements. Here, we describe squeezing and linear-optics operations and their effect on Gaussian states, as well as the measurement technique of balanced homodyne detection. In the third chapter, we introduce nonlinear optics. We start by giving general notions of nonlinear optical processes and we later focus on second-order nonlinearities, concentrating in particular on second-harmonic generation (SHG) and parametric-down conversion, the two nonlinear processes present in the experimental setup. Spontaneous parametric down-conversion (SPDC), that enables squeezing generation, will be treated in the last part of this chapter.

The second part of this thesis gives a detailed description of the experimental setup for multimode squeezing generation and presents the measurement results. The fourth chapter presents the experiment in all its components: the ultrafast light source, nonlinear waveguides for SPDC, the SHG process and pulse-shaping are described in detail. The fifth chapter presents the measurement results, recently published in [Kouadou 23]. Here, we describe the multimode squeezing measurement in the spectral domain and in the temporal domain, demonstrating the time-frequency multiplexing of our resource, and we present the measurement of the covariance matrix. In the sixth chapter we present the ongoing efforts for the implementation of a cluster state multiplexed both in time and in frequency. The experimental setup, which includes a second waveguide, and the locking system are presented.

In the third part, we investigate quantum information processing applications of the squeezed resource generated in the experiment. In the seventh chapter, we discuss continuous-time quantum walks (CTQW) for the task of quantum search on a network. A description of the quantum walk framework is provided, and we present an experimental mapping for the implementation of CTQW on a photonics setup, using squeezed light and photon subtraction operations. In the eighth chapter, we investigate the use of our experimental setup for quantum simulation, in the context of open quantum systems, aiming to observe the emergence of quantum synchronization. We present the experimental mapping and the numerical simulations of the experimental parameters needed for the success of the experiment.

Part I

Theoretical Background

Chapter 1

Quantum Light

Contents

1.1	The multimode classical electromagnetic field	8
1.1.1	The classical electromagnetic field	8
1.1.2	Multimode description	10
1.1.3	Gaussian Beam	11
1.1.4	Temporal and spectral modes	13
1.1.5	Quadratures of the field	14
1.2	Quantization of the field	15
1.2.1	From classical mechanics to quantum mechanics	16
1.2.2	Quadratures as quantum operators	17
1.3	Multimode quantum light	19
1.3.1	The multimode electric field operator	19
1.3.2	Basis change and two Hilbert spaces	20
1.3.3	Intrinsic single-mode states	21
1.4	Description of quantum states	22
1.4.1	Discrete variables and Continuous variables	22
1.4.2	Pure and Mixed states	24
1.4.3	Wigner function	25
1.5	Common states in Quantum optics	26
1.5.1	Fock states	26
1.5.2	Coherent states	29
1.5.3	Squeezed states	30
1.5.4	EPR state	32

The goal of this chapter is to establish the definitions and conventions that we will use throughout this work and to outline the multimode framework within which we are operating. We will start with a classical description of a multimode electromagnetic field and we will later transition from the classical realm to the quantum domain. In the quantum

domain, our focus will be on Continuous-Variable states and the encoding of quantum information into fluctuations of light's quadratures. Additionally, we will introduce useful tools for describing CV quantum states and we will explore the most common quantum states in quantum optics.

1.1 The multimode classical electromagnetic field

In this section, we present a classical description of a multimode light field, focusing on both the temporal and spectral domains, connected by the Fourier transform. Moreover, we will establish a rigorous definition of what constitutes "multimode" light.

1.1.1 The classical electromagnetic field

From a classical point of view, light is an electromagnetic wave, whose propagation through linear and nonlinear media is described by the well-known Maxwell equations [Maxwell 96, Griffiths 14, Jackson 12]. The wave equation for the propagation in a medium with refractive index n reads:

$$\nabla^2 \mathbf{E}(\mathbf{r}, t) - \frac{1}{v} \frac{\partial^2}{\partial t^2} \mathbf{E}(\mathbf{r}, t) = 0 \quad (1.1)$$

where $v = c/n$ is the propagation velocity of the field in said medium. The most common solution to this equation is the monochromatic plane wave:

$$\mathbf{E}(\mathbf{r}, t) = \mathbf{E}_0 \cos(\mathbf{k}\mathbf{r} - \omega t + \phi_0) \quad (1.2)$$

where \mathbf{k} is the propagation vector and ω is the angular frequency. The same equation can be expressed as:

$$\mathbf{E}(\mathbf{r}, t) = \mathbf{E}_0 e^{i(\mathbf{k}\mathbf{r} - \omega t + \phi_0)} + \text{c.c} \quad (1.3)$$

While these two expressions are equivalent¹, using complex exponentials permits us to carry out calculations more conveniently. As the wave equation is linear, a variety of solutions can stem from a solution basis. Indeed, a superposition of two solutions is still a solution of the Maxwell equations. Linearity also precludes light-by-light interaction, implying that non-linearity is a necessary condition for the interaction of EM fields. This thesis will concentrate on how to exploit non-linearity to drive an interacting Hamiltonian term between the EM fields.

It is useful to treat the $\mathbf{E}(\mathbf{r}, t)$ fields in the frequency domain, as we work with broadband fields, i.e. fields with many frequency components. Going to the Fourier space, we can write

¹A factor of 1/2 is usually omitted but it can be found in some of the literature.

the electric field along with its Fourier transform:

$$\mathbf{E}(\mathbf{r}, t) = \int_{\mathbb{R}} \frac{d\omega}{\sqrt{2\pi}} \mathbf{E}(\mathbf{r}, \omega) e^{-i\omega t} \quad (1.4)$$

$$\mathbf{E}(\mathbf{r}, \omega) = \int_{\mathbb{R}} \frac{dt}{\sqrt{2\pi}} \mathbf{E}(\mathbf{r}, t) e^{i\omega t} \quad (1.5)$$

As the electric field is a real quantity, we have:

$$[\mathbf{E}(\mathbf{r}, \omega)]^* = \mathbf{E}(\mathbf{r}, -\omega) \quad (1.6)$$

This symmetry highlights the presence of redundant information in Eq. 1.4. Therefore, to get rid of redundancy, we define the so-called *analytic signal* $\mathbf{E}^{(+)}(\mathbf{r}, t)$ as:

$$\mathbf{E}^{(+)}(\mathbf{r}, t) = \int_{\mathbb{R}^+} \frac{d\omega}{\sqrt{2\pi}} \mathbf{E}(\mathbf{r}, \omega) e^{-i\omega t} \quad (1.7)$$

where we integrate only on positive frequencies. We note that, differently from $\mathbf{E}(\mathbf{r}, t)$, $\mathbf{E}^{(+)}(\mathbf{r}, t)$ is complex. We define the complex conjugate of the analytic signal as:

$$\left[\mathbf{E}^{(+)}(\mathbf{r}, t) \right]^* = \mathbf{E}^{(-)}(\mathbf{r}, t) \quad (1.8)$$

that represents the integration over the negative frequencies. In terms of the analytic signals, the real electric field can be written as:

$$\mathbf{E}(\mathbf{r}, t) = \mathbf{E}^{(+)}(\mathbf{r}, t) + \mathbf{E}^{(-)}(\mathbf{r}, t) \quad (1.9)$$

We define the Fourier transform of the analytic signal as:

$$\mathbf{E}^{(+)}(\mathbf{r}, \omega) = \int_{\mathbb{R}} \frac{dt}{\sqrt{2\pi}} \mathbf{E}^{(+)}(\mathbf{r}, t) e^{i\omega t} \quad (1.10)$$

so that:

$$\left[\mathbf{E}^{(+)}(\mathbf{r}, \omega) \right]^* = \mathbf{E}^{(-)}(\mathbf{r}, -\omega) \quad (1.11)$$

The real electric field in the frequency domain can be written as:

$$\mathbf{E}(\mathbf{r}, \omega) = \mathbf{E}^{(+)}(\mathbf{r}, \omega) + \mathbf{E}^{(-)}(\mathbf{r}, \omega) \quad (1.12)$$

1.1.2 Multimode description

Due to the linearity of the Maxwell equations, we can expand the EM field into an infinite sum of monochromatic plane-waves with different complex amplitudes. The derivation can be found in [Loudon 00, Grynberg 10, Gerry 05]. Its analytic signal takes the form of:

$$\mathbf{E}^{(+)}(\mathbf{r}, t) = i \sum_l \boldsymbol{\varepsilon}_l \mathcal{E}_l \alpha_l e^{i(\mathbf{k}_l \mathbf{r} - \omega_l t)} \quad (1.13)$$

where $\boldsymbol{\varepsilon}_l$ is the polarization vector and \mathcal{E}_l is a constant given by:

$$\mathcal{E}_l = \sqrt{\frac{\hbar \omega_l}{2 \epsilon_0 V}} \quad (1.14)$$

The purpose of this constant is to ensure that the α_l coefficients are dimensionless and satisfy the usual commutation relations when we later promote them to creation and annihilation operators, as we will show in section 1.2. In this equation we used mono-chromatic plane waves as the orthonormal basis of the Hilbert space of the EM field. More generally, the EM field can be expressed as¹:

$$\boxed{\mathbf{E}^{(+)}(\mathbf{r}, t) = \sum_l \mathcal{E}_l \alpha_l \mathbf{f}_l(\mathbf{r}, t)} \quad (1.15)$$

where $\{\mathbf{f}_l(\mathbf{r}, t)\}$ is a suitable orthonormal basis. The vector field $\mathbf{f}_l(\mathbf{r}, t)$ is what we call a *mode*. A mode is a normalized solution to the Maxwell equations that satisfies at any time t the normalization condition:

$$\frac{1}{V} \int_V d^3 r |\mathbf{f}_l(\mathbf{r}, t)|^2 = 1 \quad (1.16)$$

where V is a large volume that contains the EM field of interest.

Starting with a specific mode $\mathbf{f}_l(\mathbf{r}, t)$, we can build an orthonormal basis of modes, denoted as $\mathbf{f}_l(\mathbf{r}, t)$, such that any solution to the Maxwell equations can be represented as a linear combination of these basis modes. In other words, $\mathbf{f}_l(\mathbf{r}, t)$ forms an orthonormal basis in the Hilbert space to which the operator $\mathbf{E}^{(+)}(\mathbf{r}, t)$ belongs. This orthonormality requirement entails that for any time t :

$$\frac{1}{V} \int_V d^3 \mathbf{r} \mathbf{f}_l^*(\mathbf{r}, t) \mathbf{f}_{l'}(\mathbf{r}, t) = \delta_{ll'} \quad (1.17)$$

It is worth noting that the field can be equivalently described in a different basis. We will not cover the basis change details in the classical case; however, we will address this topic in section 1.3.2 within the context of multimode quantum light. More details on the multimode nature of light can be found in [Fabre 20].

¹We dropped the i factor as it is a global phase and can be included in the $\mathbf{f}_l(\mathbf{r}, t)$ term.

We will now introduce two important approximations used extensively in this thesis: the paraxial approximation and the narrowband approximation. The paraxial approximation is based on the assumption that the different wave-vectors \mathbf{k}_l of the plane-waves composing the EM field have very small angular deviation among each other and can be approximated by a mean value \mathbf{k} . We will assume here that the propagation direction is along z . The narrowband approximation is applicable if the spectral bandwidth is narrow and centered around the optical frequency ω_0 , i.e. $\Delta\omega \ll \omega_0$. It is also known as the slowly-varying envelope approximation (SVEA), as in the temporal domain this implies that the pulse envelope changes slowly with time compared to the optical period¹. Under these assumption, we can approximate $\mathcal{E}_l \sim \mathcal{E}_0$. The field can finally be rewritten as:

$$E^{(+)}(\mathbf{r}, t) = \mathcal{E}_0 e^{i(kz - \omega_0 t)} \sum_l \alpha_l f_l(\mathbf{r}, t) \quad (1.18)$$

where we adopt a linear polarization and consider the fields as scalars for simplicity. In this context, the term $e^{i(kz - \omega_0 t)}$ is referred to as the carrier plane wave, where ω_0 is the carrier frequency.

In this thesis, we restrict to modes that can be factorized in a transverse and longitudinal component as:

$$f_l(\mathbf{r}, t) = f_m^T(\mathbf{r}) u_n(z, t) \quad (1.19)$$

where the subscript l is used as a shorthand notation for the subscripts (m, n) . In this decomposition, the term $f_m^T(\mathbf{r})$ correspond to a transverse (or spatial) mode, that accounts for the spatial shape of the light beam in the plane perpendicular to the propagation, while $u_n(z, t)$ is a longitudinal (or temporal) mode, responsible for the EM wave pattern along the temporal (or z) axis. Some examples of spatial mode bases include the spatial Hermite-Gauss basis, the spatial Laguerre-Gauss basis and the spatial pixel mode basis². Some examples of temporal-frequency mode bases include the frequency Hermite-Gauss basis, the frequency pixel mode basis, the sideband mode basis and the time-bin mode basis; we will deal with all of them, more or less extensively, within this manuscript.

1.1.3 Gaussian Beam

The spatial modes of a laser beam can often be approximated by the family of Hermite-Gauss modes (or TEM modes), when the paraxial approximation is satisfied [Siegman 86, Yariv 89]. In particular, the beam in our experiment is spatially single-mode, and its intensity distribution can be approximated by the TEM00 mode. This mode exhibits a Gaussian

¹When we deal with femtosecond pulses of near-infrared and visible light, we are at the limit of this approximation, as the period of an optical cycle is around $T = \frac{2\pi}{\omega_0} \sim 2.7$ fs. This is particularly true in our case, as our laser delivers 22-fs pulses, which contain only a few optical cycles.

²The spatial pixel mode basis is useful to describe the detection process of an array of photodiodes. Pixel modes are constant over a specific pixel area and zero outside. This basis is not complete.

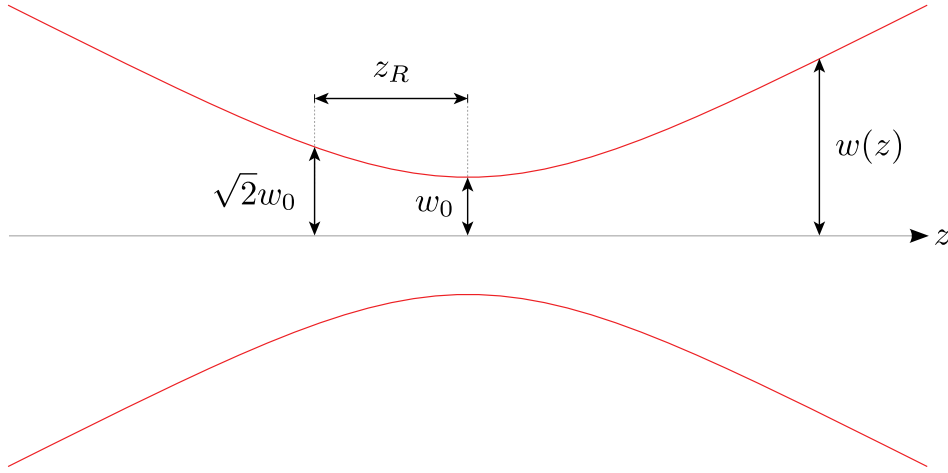


Figure 1.1: Gaussian beam radius $w(z)$ as a function of z . w_0 is the beam waist and z_R is the Rayleigh length.

spatial profile and it is often called, for this reason, *Gaussian beam*. From Eq. 1.18, a spatially single-mode field can be written as:

$$E^{(+)}(\mathbf{r}, t) = \mathcal{E}_0 e^{i(kz - \omega_0 t)} f_0^T(\mathbf{r}) \sum_l \alpha_l u_l(z, t) \quad (1.20)$$

where $f_0^T(\mathbf{r})$ represents the TEM00 mode. The Gaussian beam is expressed as:

$$f_0^T(\mathbf{r} = (\boldsymbol{\rho}, z)) = \frac{w_0}{w(z)} e^{-\rho^2/w^2(z)} e^{-ik_0 \rho^2/2R(z)} e^{i\phi(z)} \quad (1.21)$$

where $R(z)$ is the radius of curvature of the beam's wavefronts and $\phi(z)$ is the Gouy phase. The term $w(z)$ is the radius of the beam, that represents the radial coordinate at which the field amplitude decreases to $1/e$ of its axial values and whose behaviour is shown in Fig. 1.1. The radius at the focal point, denoted as w_0 , is called *waist* of the beam, and it corresponds to the smallest beam size. In the above equations, we defined the Gaussian beam as centered at $z = 0$, so that $w_0 = w(0)$. These terms $R(z)$, $\phi(z)$ and $w(z)$ are defined as:

$$w^2(z) = w_0^2 \left(1 + \frac{z^2}{z_R^2} \right) \quad (1.22)$$

$$\frac{1}{R(z)} = \frac{z}{z^2 + z_R^2} \quad (1.23)$$

$$\phi(z) = \arctan \left(\frac{z}{z_R} \right) \quad (1.24)$$

where

$$z_R = \frac{\pi w_0^2 n}{\lambda} \quad (1.25)$$

is called *Rayleigh length* and it represents the distance at which the beam section doubles compared to its waist, i.e. $w(z_R) = \sqrt{2}w_0$.

To avoid confusion, we point out that, according to the definitions given, the beam radius is measured at $1/e$ of the field amplitude. The radius corresponds then to twice the standard deviation of the intensity distribution of the Gaussian beam. In terms of the Full-Width-Half-Maximum (FWHM) of the intensity, it holds:

$$w(z) = \frac{FWHM(z)}{\sqrt{2\ln 2}} \quad (1.26)$$

1.1.4 Temporal and spectral modes

We now investigate time-frequency modes, represented by the longitudinal component $u_l(z, t)$ of the field modes. These modes represent the main focus of our work as they are the natural basis for describing light pulses. In particular, throughout this thesis we will often omit the single-mode spatial component, to focus our attention on the longitudinal field. In terms of temporal modes, the field can be expressed as:

$$E^{(+)}(z, t) = \mathcal{E}_0 \alpha(z, t) e^{i(kz - \omega_0 t)} \quad (1.27)$$

where $\alpha(z, t) = \sum_l \alpha_l u_l(z, t)$ is the pulse envelope and $\{u_l(z, t)\}$ is a basis of orthonormal temporal modes. For a non-distorted pulse propagating at the speed of light, the explicit dependence on (z, t) reads $u_l(z, t) = u_l(t - z/c)$. However, our primary interest lies in the temporal dependence; for simplicity, we can evaluate the field at $z = 0$, which we can, for example, consider as the position of the detector. This will lead us to:

$$\boxed{E^{(+)}(t) = \mathcal{E}_0 \alpha(t) e^{-i\omega_0 t}} \quad (1.28)$$

where $\alpha(t) = \sum_l \alpha_l u_l(t)$. We stress that the envelope $\alpha(t)$ is complex. The Fourier transform of this field reads:

$$\boxed{E^{(+)}(\omega) = \mathcal{E}_0 \alpha(\Omega)} \quad (1.29)$$

where $\Omega = \omega - \omega_0$ is the frequency with respect to the carrier¹. In this work, ω typically refers to optical frequencies in the THz range, while Ω represents electronic frequencies ranging from kHz to MHz. Note that $\alpha(\Omega)$ is the Fourier transform of $\alpha(t)$ with respect to the Ω frequency, differently from $\alpha(\omega)$; $\alpha(\Omega)$ (and, by consequence, $E^{(+)}(\omega)$) is centered around ω_0 ², while $\alpha(\omega)$ is centered around 0.

¹In some texts $E^{(+)}(\omega)$ is referred to as $E^{(+)}(\Omega)$. If we want to be strict, $E^{(+)}(\Omega)$ is supposed to represent $E^{(+)}(\Omega) \propto \int dt e^{i\Omega t} E^{(+)}(t)$ but in most cases it indicates $E^{(+)}(\omega) = \mathcal{E}_0 \alpha(\Omega)$.

²The Fourier transform of the real field $E(t)$ has two contributions, one centered around ω_0 and the other around $-\omega_0$.

1.1.5 Quadratures of the field

The classical electric field of Eq. 1.28 features the slowly-varying complex envelope function $\alpha(t)$. It is often useful to break down this envelope into its real and imaginary parts, that we call *quadratures* of the field¹[Bachor 19]. These are defined as follows:

$$q(t) = \alpha(t)^* + \alpha(t) \quad (1.30)$$

$$p(t) = i(\alpha(t)^* - \alpha(t)) \quad (1.31)$$

where $\alpha(t)$ is the envelope of the field. Note that, by definition, the q and p quadratures are real variables. The inverse relations are given by:

$$\alpha(t) = \frac{q(t) + ip(t)}{2} \quad (1.32)$$

$$\alpha^*(t) = \frac{q(t) - ip(t)}{2} \quad (1.33)$$

The real electric field can then be rewritten in terms of quadratures as:

$$E(t) = \mathcal{E}_0 [q(t) \cos(\omega_0 t) + p(t) \sin(\omega_0 t)] \quad (1.34)$$

The complex amplitude at one specific point in time can be depicted by using the phasor diagram, a two-dimensional chart of q and p , shown in Figure 1.2a. In the phasor diagram, the complex amplitude $\alpha(t) = |\alpha(t)|e^{i\phi(t)}$ corresponds to a point with coordinates (q, p) . These coordinates are identified by a vector that is proportional to the magnitude $|\alpha(t)|$, with an angle ϕ measured with respect to the q -axis, given by the phase $\phi = \arctan(p/q)$. Note that here the phasor diagram represents only the complex amplitude $\alpha(t)$, and the carrier oscillations of Eq. 1.34 are not taken into account. In practical terms, when dealing with phasors, we place ourselves in a rotating reference frame at the carrier frequency ω_0 . It is customary to set the global phase at $\phi = 0$; this way, if the light exhibits no fluctuations, $\alpha(t) = \alpha$ and the vector lies on the q axis of the phasor diagram [Bachor 19]. In some references, the phasor diagram is used to describe the electric field instead of the complex amplitude [Grynberg 10]. In this case, the vector magnitude is rescaled by \mathcal{E}_0 and it rotates at frequency ω_0 in the diagram.

The description of the light field in terms of quadratures and the corresponding phasor diagram are useful when we work with fluctuations of the electric field. In general, light fluctuates both in phase and in amplitude. This can be expressed as:

$$\alpha(t) = \alpha + \delta\alpha(t) = \alpha + \frac{\delta q(t)}{2} + i\frac{\delta p(t)}{2} \quad (1.35)$$

¹In this section we focused on a field in the SVEA approximation. Quadratures can also be analogously defined for a field $\mathbf{E}^{(+)}(\mathbf{r}, t) = \sum_l \mathcal{E}_l \alpha_l e^{i(\mathbf{k}_l \cdot \mathbf{r} - \omega_l t)}$. In this case we often rewrite the real field as $E(\mathbf{r}, t) = \sum_l \mathcal{E}_l [q \cos(\mathbf{k} \cdot \mathbf{r} - \omega t) + p \sin(\mathbf{k} \cdot \mathbf{r} - \omega t)]$, where we define $q = \alpha_l^* + \alpha_l$ and $p = i(\alpha_l^* - \alpha_l)$.

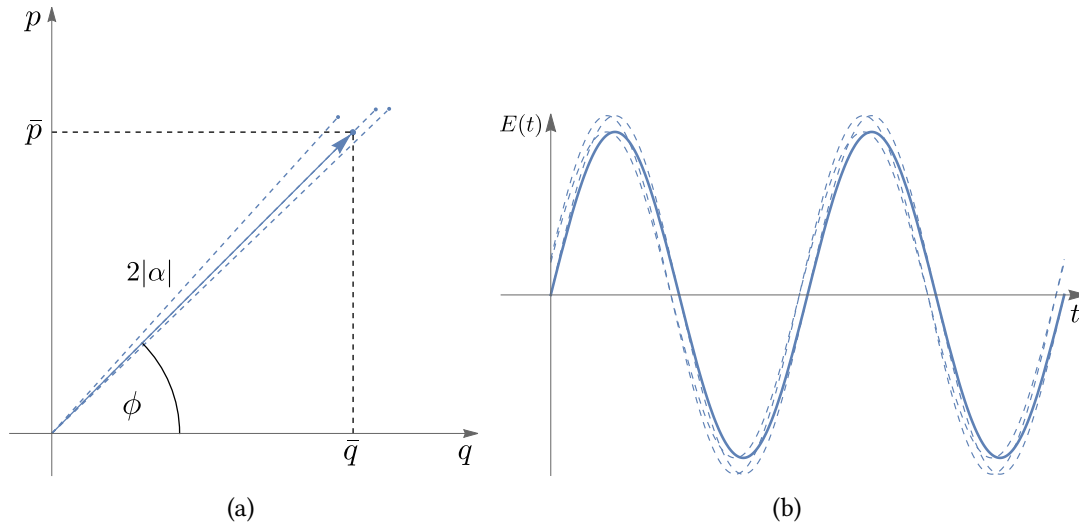


Figure 1.2: Monochromatic electric field represented with a phasor diagram (a) and plotted as a function of time (b). In these two figures the mean value of the field is represented with a solid line. Small fluctuations $\delta\alpha(t)$ of amplitude and phase of the electric field are mapped into fluctuations around the mean value in the phasor diagram, represented with dashed lines.

where α is the mean value of the field amplitude and the δ indicates small fluctuations. Fluctuations of the field amplitude and phase are translated into fluctuations of the field quadratures. These fluctuations (modulations) are represented on the phasor diagram as a series of random points around the mean value, within an area defined by the magnitude of the fluctuations, as shown in Figure 1.2. Fluctuations may be due to random noise or may also be imprinted intentionally on the light field to carry information, like in the case of classical amplitude and phase modulations, that we will describe later in section 2.2.1.

1.2 Quantization of the field

Now that we have introduced the most important classical quantities, we can investigate their quantum counterpart. While a semi-classical theory can account for many processes, including the photoelectric effect [Scully 72, Loudon 00], quantizing the radiation is a necessary step when dealing with other physical phenomena, for instance spontaneous emission. In this section, we will present the main features of quantized radiation, emphasizing distinctive quantum characteristics that are absent in classical light, such as the existence of non-commuting observables and the emergence of the concept of photons. Details on the quantization of the EM field can be found in [Loudon 00, Grynberg 10].

1.2.1 From classical mechanics to quantum mechanics

A common method for transitioning from the classical treatment of light to its quantum counterpart involves promoting the complex amplitudes to creation and annihilation operators: $\alpha \rightarrow \hat{a}$ and $\alpha^* \rightarrow \hat{a}^\dagger$. However, formally, the standard approach for quantizing a classical theory is based on the canonical quantization method that stems from Hamiltonian mechanics. The Hamilton (or canonical) equations of motion govern the evolution, prescribed by a Hamiltonian H , of a set of conjugate canonical variables (\mathbf{q}, \mathbf{p}) in the phase space.

Therefore, our point of departure is the Hamiltonian of the free-field, and the identification of the conjugate canonical variables that obey Hamilton's equations. The energy of the free-radiation¹ reads $H = \sum_l H_l$, where

$$H_l = \frac{\omega_l}{2} (Q_l^2 + P_l^2) \quad (1.37)$$

is the energy carried by a mode of radiation. The variables Q_l and P_l are defined as:

$$Q_l = \sqrt{\frac{4\epsilon_0 V}{\omega_l}} \mathcal{E}_l \text{Re}(\alpha_l) \quad (1.38)$$

$$P_l = \sqrt{\frac{4\epsilon_0 V}{\omega_l}} \mathcal{E}_l \text{Im}(\alpha_l) \quad (1.39)$$

where we recall that α_l is the complex amplitude of the electric field as it is defined in Eq. 1.13. The variables Q and P satisfy the Hamilton equations of motion:

$$\frac{dQ_l}{dt} = \frac{dH_l}{dp} \quad (1.40)$$

$$\frac{dP_l}{dt} = -\frac{dH_l}{dq} \quad (1.41)$$

and therefore they represent the canonical variables of our system. Following the prescriptions of canonical quantization, we proceed by promoting Q_l and P_l to quantum operators \hat{Q}_l and \hat{P}_l that obey the following canonical commutation relations:

$$[\hat{Q}_i, \hat{P}_j] = i\hbar\delta_{ij}\mathbb{1} \quad (1.42)$$

$$[\hat{Q}_i, \hat{Q}_j] = [\hat{P}_i, \hat{P}_j] = 0 \quad (1.43)$$

¹The energy of free radiation is defined as [Grynberg 10]

$$H = \frac{\epsilon_0}{2} \int_V d^3r [\mathbf{E}^2(\mathbf{r}, t) + c^2 \mathbf{B}^2(\mathbf{r}, t)] = 2\epsilon_0 V \sum_l \mathcal{E}_l^2 |\alpha_l|^2 \quad (1.36)$$

so that we can express the total energy of the field as $H = \sum_l H_l$, where H_l is the energy of a single mode l of the field.

and that follow the evolution prescribed by the quantum counterpart of the Hamiltonian 1.37. We stress that \hat{Q} and \hat{P} are not the quantum version of the classical quadratures q and p that we encountered in section 1.1.5, as they have dimensions $[\hbar]$: they will need to be rescaled accordingly, as we will see later. By setting $\hat{Q}_l + i\hat{P}_l = \sqrt{2\hbar}\hat{a}_l$ we can check that the creation and annihilation operators¹ \hat{a}_i^\dagger and \hat{a}_j satisfy the commutation relations:

$$[\hat{a}_i, \hat{a}_j^\dagger] = \mathbb{1}\delta_{ij} \quad (1.44)$$

$$[\hat{a}_i, \hat{a}_j] = [\hat{a}_i^\dagger, \hat{a}_j^\dagger] = 0 \quad (1.45)$$

The Hamiltonian of the free-field can be expressed as follows:

$$\hat{H} = \sum_l \hbar\omega_l \left(\hat{a}_l^\dagger \hat{a}_l + \frac{1}{2} \right) \quad (1.46)$$

This equation describes a system consisting of a collection of uncoupled quantum harmonic oscillators, where each mode l acts as an independent oscillator. In this framework, the concept of a *photon* emerges as an excitation of mode l with energy $\hbar\omega_l$.

The Hamiltonian 1.46 is an operator acting on a Hilbert space that describes a many-particle system, the *Fock space*. The Fock space is commonly used in the second quantization framework to model systems with a variable number of either bosons or fermions. In the bosonic case it is defined as:

$$\mathcal{F}_S(\mathcal{H}) = \bigoplus_{n=0}^{\infty} \mathcal{H}_S^n \quad (1.47)$$

where the subscript S indicates that the subspaces of the Fock space are symmetric (as opposed to antisymmetric for the case of fermions) and where \mathcal{H}_S^n represents the Hilbert space of a system of n particles. In the occupation number representation, an orthonormal basis of the Fock space can be written as:

$$\{|n_1, n_2, \dots, n_k, \dots\rangle\}_{(n_1, n_2, \dots, n_k)} \quad (1.48)$$

where n_k denotes the number of particles in mode k and it can range from zero to infinity. Fock states are among the most common states encountered in quantum optics, and they will be given a more detailed description later in section 1.5.1.

1.2.2 Quadratures as quantum operators

The photon-number (Fock) representation of a quantum state of light is widely used in the field of Quantum Information. However, in this work, the quantum features of our interest

¹We remind that the creation and annihilation operators are non-Hermitian and, therefore, do not represent observables.

are encoded into fluctuations of the light field. Therefore, we concentrate on the quantum analogue of the classical quadratures of the field, introduced in section 1.1.5.

Analogously to the classical case, we can define quadrature operators as¹:

$$\hat{q}_l = \hat{a}_l^\dagger + \hat{a}_l \quad (1.49)$$

$$\hat{p}_l = i \left(\hat{a}_l^\dagger - \hat{a}_l \right) \quad (1.50)$$

These operators obey the following commutation relations:

$$[\hat{q}_i, \hat{p}_j] = 2i\delta_{ij}\mathbb{1} \quad (1.51)$$

$$[\hat{q}_i, \hat{q}_j] = [\hat{p}_i, \hat{p}_j] = 0 \quad (1.52)$$

The creation and annihilation operators are expressed in term of quadrature operators as:

$$\hat{a}_l = \frac{\hat{q}_l^\dagger + i\hat{p}_l}{2} \quad (1.53)$$

$$\hat{a}_l^\dagger = \frac{\hat{q}_l^\dagger - i\hat{p}_l}{2} \quad (1.54)$$

Using these equations, the Hamiltonian of the free-field in Eq. 1.46 can be rewritten as:

$$H = \sum_l \frac{\hbar\omega_l}{4} (\hat{q}_l^2 + \hat{p}_l^2) \quad (1.55)$$

Since \hat{q} and \hat{p} are non-commuting observables, they must satisfy a form of generalized Heisenberg uncertainty relations, known as Robertson–Schrödinger uncertainty relations [Robertson 29]. These relations are expressed as:

$$\Delta^2 q_i \Delta^2 p_j - \text{cov}(\hat{q}_i, \hat{p}_j) \geq \left| \frac{1}{2i} \langle [\hat{q}_i, \hat{p}_j] \rangle \right|^2 = \delta_{ij} \quad (1.56)$$

where $\Delta^2 q_i$ and $\Delta^2 p_j$ are the variances of the two operators² and $\text{cov}(\hat{q}_i, \hat{p}_j)$ is the covariance term. The states that minimize this relation are known as *minimum uncertainty states*.

We note that the quadrature operators \hat{q} and \hat{p} defined here do not depend on time: they can be considered operators in the Schrödinger picture, or, equivalently, in the Heisenberg picture at $t = 0$ (see Appendix A). It is worth emphasizing that equivalent definitions can also be provided for the time-dependent case, i.e., for quadrature operators in the Heisenberg

¹The quantized canonical variables are connected to quadrature operators as follows: $\hat{Q} = \hat{q}\sqrt{\hbar/2}$ and $\hat{P} = \hat{p}\sqrt{\hbar/2}$.

²We recall that the variance of an operator \hat{O} is given by $\hat{O} = \langle \hat{O}^2 \rangle - \langle \hat{O} \rangle^2 = \langle \psi | \hat{O}^2 | \psi \rangle - \langle \psi | \hat{O} | \psi \rangle^2$.

picture, denoted as $\hat{q}(t)$ and $\hat{p}(t)$. They are defined as linear combinations of $\hat{a}(t)$ and $\hat{a}^\dagger(t)$, with equations that are equivalent to the ones presented in this section.

Similar to our approach with classical fluctuations, when dealing with fluctuations of the field, we can decompose the operator into two contributing terms:

$$\hat{a}(t) = \langle \hat{a} \rangle \mathbb{1} + \delta \hat{a}(t) \quad (1.57)$$

where we neglect higher order terms assuming small fluctuations. The identity operator that multiplies the expectation value $\langle \hat{a} \rangle$ is omitted most of the times. The fluctuating term $\delta \hat{a}(t)$ and its Fourier transform will be analyzed extensively in the next chapter.

1.3 Multimode quantum light

In section 1.1.2, we presented the multimode description of a classical light field. Here, we aim to do the same but in the context of quantized radiation. Details are given in [Fabre 20].

1.3.1 The multimode electric field operator

In analogy to Eq. 1.15, the quantized EM field can be expressed as:

$$\hat{\mathbf{E}}^{(+)}(\mathbf{r}, t) = \sum_l \mathcal{E}_l \hat{a}_l \mathbf{f}_l(\mathbf{r}, t) \quad (1.58)$$

where \hat{a}_l is the annihilation operator associated with a specific optical mode $\mathbf{f}_l(\mathbf{r}, t)$. From this equation, we observe the emergence of an important concept within the framework of multimode quantum light. The operator $\hat{\mathbf{E}}^{(+)}(\mathbf{r}, t)$ accounts for the existence of two distinct Hilbert spaces: the Hilbert space of optical modes, spanned by the orthonormal basis $\mathbf{f}_l(\mathbf{r}, t)$ and the Hilbert space of quantum states, identified by the annihilation operators \hat{a}_l . It follows that the operators \hat{a}_l are annihilation operators associated with an excitation of the optical mode $\mathbf{f}_l(\mathbf{r}, t)$. Therefore, in a multimode framework, it is crucial to consistently specify the modes associated with specific creation and annihilation operators of the field.

As for the classical field, it is common to encounter the expansion of the quantum electric field into a basis of monochromatic plane waves:

$$\hat{E}(\mathbf{r}, t) = \sum_l \mathcal{E}_l \left(\hat{a}_l e^{i(\mathbf{k}_l \mathbf{r} - \omega_l t)} + \hat{a}_l^\dagger e^{-i(\mathbf{k}_l \mathbf{r} - \omega_l t)} \right) = \quad (1.59)$$

$$= \sum_l \mathcal{E}_l \left(\hat{q}_l \cos(\mathbf{k}_l \mathbf{r} - \omega_l t) + \hat{p}_l \sin(\mathbf{k}_l \mathbf{r} - \omega_l t) \right) \quad (1.60)$$

We note that the operator $\hat{E}(\mathbf{r}, t)$ does evolve with time and it is therefore described here in the Heisenberg picture. A Schrödinger picture description is equivalent and can be found in some of the literature [Grynberg 10].

1.3.2 Basis change and two Hilbert spaces

In general, there is not a preferred basis for the description of the electromagnetic field and the expansion in any basis is equally valid to describe the physical system. However, one basis might be more suitable for a certain task with respect to another, emerging as more natural for the description of a particular quantum system or for the detection process. A basis change is performed by applying a unitary transformation:

$$\hat{b}_i^\dagger = \sum_j U_{ij} \hat{a}_j^\dagger \quad (1.61)$$

This corresponds to a transformation in the modal Hilbert space:

$$\mathbf{g}_i(\mathbf{r}, t) = \sum_j U_{ij} \mathbf{f}_j(\mathbf{r}, t) \quad (1.62)$$

Note that optical modes and the associated creation operators of the field transform in the same way. The electric field can be written equivalently in the $\{\mathbf{f}_l(\mathbf{r}, t)\}$ and in the $\{\mathbf{g}_l(\mathbf{r}, t)\}$ basis:

$$\hat{\mathbf{E}}^{(+)}(\mathbf{r}, t) = \sum_l \mathcal{E}_l \hat{a}_l \mathbf{f}_l(\mathbf{r}, t) = \sum_l \mathcal{E}_l \hat{b}_l \mathbf{g}_l(\mathbf{r}, t) \quad (1.63)$$

The same quantum state has a different expression if we consider its expansion in a different mode basis. As already mentioned in the previous section, when we consider a specific quantum state of light, e.g. a squeezed state, it is important to always specify the mode basis it is associated with. As a title of example, two single photon states occupying the first modes of the basis $\{\mathbf{f}_i(\mathbf{r}, t)\}$ can be written as:

$$|\psi\rangle = |1 : \mathbf{f}_1\rangle \otimes |1 : \mathbf{f}_2\rangle \quad (1.64)$$

Through a balanced beam-splitter transformation, we apply the basis change $\mathbf{f}_\pm = (\mathbf{f}_1 \pm \mathbf{f}_2)/\sqrt{2}$ and in the new basis the quantum state can be rewritten as:

$$|\psi\rangle = |2 : \mathbf{f}_+\rangle \otimes |0 : \mathbf{f}_-\rangle - |0 : \mathbf{f}_+\rangle \otimes |2 : \mathbf{f}_-\rangle \quad (1.65)$$

A basis change allowed us to transition from a separable state to an entangled state; this is because applying a global basis change corresponds to repartitioning the system. It's important to emphasize that the quantum state remains the same; however, changing the basis might unveil quantum correlations. In other words, the presence (or absence) of entanglement correlations is dependent on the basis. Something analogous happens with squeezed states and EPR states (investigated in the next sections), which represent the same quantum state, up to a basis change. Indeed, via the same beam-splitter transformation we obtain:

$$|\psi\rangle = |\text{squeezed} : \mathbf{f}_+\rangle \otimes |\text{squeezed} : \mathbf{f}_-\rangle \rightarrow |\psi\rangle = |\text{EPR state} : \mathbf{f}_+, \mathbf{f}_-\rangle \quad (1.66)$$

While the emergence of quantum correlations depends on the choice of basis, certain quantities are basis-independent. For instance, the total number of photons is an intrinsic quantity:

$$\hat{N}_{tot} = \sum_l \hat{a}^\dagger \hat{a} = \sum_l \hat{b}^\dagger \hat{b} \quad (1.67)$$

as well as the negativity of the Wigner function, a tool that we will explore in the next chapter.

1.3.3 Intrinsic single-mode states

We have just mentioned the possibility of describing the multimode quantum state of light in any chosen basis. A question naturally arises: is there a basis where a multimode quantum state can be reduced to a single-mode one? A state can be referred to as *single-mode state*, when it can be rewritten in the form:

$$|\psi\rangle = |\phi_1\rangle |0, 0, \dots\rangle \quad (1.68)$$

for a specific basis $\{\mathbf{f}_l(\mathbf{r}, t)\}$ where $|0, 0, \dots\rangle$ is the multimode vacuum. When such basis exists, the state is said to be *intrinsically single-mode*. Conversely, if no such basis exists, it is *intrinsically multimode*. A necessary and sufficient condition for a state $|\psi\rangle$ to be intrinsically single-mode, is that the action of the annihilation operators \hat{a}_l in any basis on the state $|\psi\rangle$ must yield collinear vectors, i.e. all the vectors $|\psi_l\rangle = \hat{a}_l |\psi\rangle$ must be proportional [Trep05].

An example is the multimode coherent state which, despite the name, is intrinsically single mode. It can be written as:

$$|\psi\rangle = |\alpha_1 : \mathbf{f}_1\rangle \otimes \dots \otimes |\alpha_l : \mathbf{f}_l\rangle \otimes \dots \quad (1.69)$$

We define the mode:

$$\mathbf{g}_1 = \frac{1}{\beta} \sum_l \alpha_l \mathbf{f}_l \quad (1.70)$$

where $|\beta|^2 = \sum_l |\alpha_l|^2$. Starting from \mathbf{g}_1 we build an orthonormal basis $\{\mathbf{g}_l\}$ and it can be demonstrated that in this new basis the state $|\psi\rangle$ can be rewritten as:

$$|\psi\rangle = |\beta : \mathbf{g}_1\rangle \otimes |0, 0, \dots\rangle \quad (1.71)$$

It follows that any multimode coherent state is intrinsically single-mode.

We point out that for an intrinsic single-mode state, the quantum properties of interest can be entirely described within a single mode description. In such cases, the equivalent multimode description does not reveal properties that cannot be assessed using the single-mode approach. However, in the context of this work, a multi-mode description is necessary. This is because a multimode squeezed state, which is the primary focus of this thesis, cannot be rewritten as a single-mode state. The multi-mode squeezed vacuum state is inherently multi-mode, and, as a result, the quantum properties associated with it cannot be fully described using only a single mode of the field.

1.4 Description of quantum states

In this section, we outline different ways of describing quantum states of light. We mostly restrict to the single mode description, which offers the advantage of keeping our notation simple without sacrificing any crucial concepts, as the multimode generalization is often straightforward.

1.4.1 Discrete variables and Continuous variables

The same quantum state $|\psi\rangle$ can be represented in different ways, according to the choice of the orthonormal basis of the Hilbert space he belongs to. We already mentioned in section 1.2.1 the Fock basis, a possible orthonormal basis for the Hilbert space of the free-radiation. In the Fock basis, a pure single-mode quantum state is expressed as:

$$|\psi\rangle = \sum_n c_n |n\rangle \quad (1.72)$$

and the completeness relation reads:

$$\sum |n\rangle\langle n| = \mathbb{1} \quad (1.73)$$

Generalizing to many modes, we can express the quantum state as:

$$|\psi\rangle = \sum_n c_{n_1, n_2, \dots} |n_1, n_2, \dots, n_k, \dots\rangle \quad (1.74)$$

The Fock basis description is particularly useful when working in the photon counting regime, where discrete quantities n correspond to the photon number. In this context, we refer to such work as being conducted within a *discrete variables* (DV) regime [Nielsen 10], as we encode the relevant information in discrete variables of our physical system, implementing *qubits* (two-level system) or *qudits* (n -dimensional system). For instance, in an optical framework, to encode a qubit we can exploit the polarization or the presence-absence of a single-photon, while to encode a qudit we can use the photon number n of a state. Conversely, we can work in the *continuous variables regime* (CV) [Braunstein 05b], where the orthonormal basis of the Hilbert space is indexed with continuous values instead of discrete values. This is the case for one of the main representations in quantum mechanics, the *position representation*, used extensively in the context of the first quantization for the description of the wavefunction.

In the position representation, a quantum state can be expanded in the orthonormal basis indexed by the position variable, denoted as $\{|q\rangle\}_{q \in \mathbb{R}}$. The orthonormal and completeness relations read:

$$\langle q|q'\rangle = \delta(q - q') \quad (1.75)$$

$$\int_{\mathbb{R}} dq |q\rangle\langle q| = \mathbb{1} \quad (1.76)$$

and the $\{|q\rangle\}_{q \in \mathbb{R}}$ vectors are eigenvectors of the position operator

$$\langle q | \hat{q} = \langle q | q \quad (1.77)$$

A generic pure quantum state can then be expressed in this basis as

$$|\psi\rangle = \int_{\mathbb{R}} dq \psi(q) |q\rangle \quad (1.78)$$

where $\psi(q) = \langle q | \psi \rangle$. In the multimode generalization, the quantum state is written as

$$|\psi\rangle = \int dq_1 \int dq_2 \cdots \int dq_k \cdots \psi(q_1, q_2, \dots, q_k, \dots) |q_1, q_2, \dots, q_k, \dots\rangle \quad (1.79)$$

and the orthonormality and completeness relations are generalized accordingly.

We can equivalently work in the *momentum* representation, where the orthonormal basis is denoted by $\{|p\rangle\}_{p \in \mathbb{R}}$. In this case, we write the quantum state as

$$|\psi\rangle = \int_{\mathbb{R}} dp \tilde{\psi}(p) |p\rangle \quad (1.80)$$

where $\tilde{\psi}(p) = \langle p | \psi \rangle$ is the conjugate wavefunction of $\psi(q)$. The other relations are analogous to the ones of the position representation. The position and momentum representations are linked through the relation

$$\langle q | p \rangle = \frac{e^{\frac{i}{\hbar} q p}}{(2\pi\hbar)^{1/2}} \quad (1.81)$$

It is worth to make one last remark before concluding this section. A quantum state can be equivalently described both in the photon-number basis and in the position basis. A good exemplary case is the vacuum state, that does not contain any photon and is well identified by the relation $\hat{a} |0\rangle = 0$. The vacuum state is generally described in the photon-number basis, as $|\psi\rangle = |0\rangle$. However, we can also represent the vacuum state in the position basis as:

$$|\psi\rangle = \int_{\mathbb{R}} dq \frac{1}{\sqrt[4]{\pi}} e^{-\frac{q^2}{2}} |q\rangle \quad (1.82)$$

CV is the most natural regime when working with the quadratures \hat{q}, \hat{p} of the field. As just seen, the description of the quantum field of light can be equivalently carried out both in DV and in CV; what ultimately discriminates between the two regimes is the detection process: homodyne detection is the detection process of choice in the CV regime, while photon counting detectors, or more realistically on/off detectors, are used in the DV regime.

1.4.2 Pure and Mixed states

In the previous section, we represented the state $|\psi\rangle$ by expressing it in terms of an orthonormal basis of our choosing, denoted as $|\psi_n\rangle$. This representation takes the form $|\psi\rangle = \sum_n c_n |\psi_n\rangle$ for discrete variables, while for continuous variables we replace the sum with an integral. This mathematical formulation helps us understand that $|\psi\rangle$ is a vector within a Hilbert space, specifically referred to as *pure state*. Not all the quantum states can be described by pure states. In the most general case, a quantum state is not described by a vector but rather by an operator, known as *density operator*. The density operator characterizes a statistical ensemble of state vectors $|\psi_i\rangle$, giving rise to what is termed as *mixed state*, defined as:

$$\hat{\rho} = \sum_i p_i |\psi_i\rangle \langle\psi_i| \quad (1.83)$$

where $\sum_i p_i = 1$ and where p_i is the probability that the system is in state $|\psi_i\rangle$. In the specific case of a pure state, all the weights are null except for one, and the density operator can be written as:

$$\hat{\rho} = |\psi\rangle \langle\psi| \quad (1.84)$$

By evaluating $\text{Tr}(\hat{\rho}^2)$, we can determine whether a given state is pure or mixed: we will obtain $\text{Tr}(\hat{\rho}^2) = 1$ for pure states and $\text{Tr}(\hat{\rho}^2) < 1$ for mixed states.

The density operator, like any other operator, can be expressed in terms of a chosen orthonormal basis of the Hilbert space:

$$\hat{\rho} = \sum_{ij} \rho_{ij} |i\rangle \langle j| \quad (1.85)$$

The off-diagonal terms represent interference or coherence terms, and they contain the crucial information about the relative phases between different basis states. We use the term “coherent superposition” when these off-diagonal terms are present, which indicates a well-defined relative phase relationship between the states. In this case, the effect of quantum interference may appear. In contrast, an “incoherent mixture” of states lacks information about these off-diagonal terms.

Mixed states are often referred to as classical mixtures because their probabilistic measurement outcomes result from classical uncertainty or lack of knowledge about the quantum system of interest. Statistical mixtures typically arise due to various factors, including the preparation of the quantum state, losses incurred during the system’s interaction with an uncontrollable environment where the information leaks to, or when we focus on a specific subsystem within an entangled quantum system and “trace out” the degrees of freedom from the other subsystem. In contrast, the probabilistic nature of a coherent superposition does not stem from lack of knowledge, but rather from the fundamental principles of quantum mechanics and it can be exploited to carry quantum information.

1.4.3 Wigner function

In section 1.4.1, we discussed how to describe a quantum state of light using continuous variables q and p , and we saw that we have the option to expand it in either the position or momentum basis. Here we introduce the Wigner function [Wigner 32, Leonhardt 97], a phase-space distribution that employs the statistics of both the q and the p quadratures to represent a quantum state. While in the DV regime it is customary to represent quantum states through their expansion in the occupation-number basis, in the CV regime we often make use of the Wigner function to describe a given quantum state. More specifically, the Wigner function is a *quasiprobability distribution*: it differs from classical probability distributions, exhibiting counterintuitive behaviors, such as the presence of negative regions, a necessary feature for achieving speedup in quantum computation [Tan 20, Chabaud 21, Mari 12], but it allows the calculation of expectation values and it exhibits other types of classical-like features.

The Wigner function for a single-mode quantum state described by the density matrix $\hat{\rho}$ is defined as:

$$W(q, p) = \frac{1}{4\pi} \int_{\mathbb{R}} dy e^{\frac{ipy}{2}} \left\langle q - \frac{y}{2} \left| \hat{\rho} \right| q + \frac{y}{2} \right\rangle \quad (1.86)$$

Analogously to classical probability distributions, the Wigner function yields the probability distributions for q and p :

$$\int_{\mathbb{R}} dp W(q, p) = \langle q | \hat{\rho} | q \rangle = p(q) \quad (1.87)$$

$$\int_{\mathbb{R}} dq W(q, p) = \langle p | \hat{\rho} | p \rangle = p(p) \quad (1.88)$$

We recall that for a pure state $p(q) = |\psi(q)|^2$ and $p(p) = |\tilde{\psi}(p)|^2$, which represent the probability to measure the value q or p following a position or momentum measurement. The marginal distributions can be generalized to a rotated quadrature $p(q_\theta)$ for every θ , a feature that has a crucial role in the process of quantum state tomography for the reconstruction of a quantum state.

From the hermiticity of the density matrix and the condition $\text{Tr}(\hat{\rho}) = 1$ we can demonstrate that the Wigner function is real and normalized:

$$W(q, p) = W^*(q, p) \quad (1.89)$$

$$\int_{\mathbb{R}} dq dp W(q, p) = 1 \quad (1.90)$$

Up to now, we have defined the Wigner function of a density operator $\hat{\rho}$. However, we can analogously define the Wigner function $W_{\hat{O}}(q, p)$ of a generic operator \hat{O} , by replacing $\hat{\rho}$ in Eq. 1.86 with \hat{O} , such that:

$$W_{\hat{O}}(q, p) = \frac{1}{4\pi} \int_{\mathbb{R}} dy e^{\frac{ipy}{2}} \left\langle q - \frac{y}{2} \left| \hat{O} \right| q + \frac{y}{2} \right\rangle \quad (1.91)$$

Additionally, we introduce the overlap formula

$$\text{Tr}(\hat{O}_1\hat{O}_2) = 4\pi \int_{\mathbb{R}} dqdp W_{\hat{O}_1}(q,p)W_{\hat{O}_2}(q,p) \quad (1.92)$$

that proves useful in many situation of interest. For instance, we can calculate the expectation value of an observable if we set $\hat{O}_1 = \hat{\rho}$, or we can assess the purity of a quantum state if we set $\hat{O}_1 = \hat{O}_2 = \hat{\rho}$; this leads us to:

$$\langle \hat{O}_2 \rangle = \text{Tr}(\hat{\rho}\hat{O}_2) = 4\pi \int_{\mathbb{R}} dqdp W(q,p)W_{\hat{O}_2}(q,p) \quad (1.93)$$

$$\text{Purity} = \text{Tr}(\hat{\rho}^2) = 4\pi \int_{\mathbb{R}} dqdp W(q,p)^2 \quad (1.94)$$

Here, the first equation reflects the classical rule for calculating expectation values in statistical mechanics: the Wigner function of the state corresponds to a classical probability density, while the Wigner function of the operator $W_{\hat{O}_2}(q,p)$ represents the physical quantity of interest.

In contrast to classical probability densities, which are always positive, the Wigner function of a state can have negative regions. This is the case for photon-number states with $n > 0$, shown in Fig. 1.4b.

The generalization to many modes is straightforward. The Wigner function of a N -mode quantum state is:

$$W(\mathbf{q}, \mathbf{p}) = \left(\frac{1}{4\pi}\right)^N \int_{\mathbb{R}^N} d^N \mathbf{y} e^{\frac{i\mathbf{p}\cdot\mathbf{y}}{2}} \left\langle \mathbf{q} - \frac{\mathbf{y}}{2} \left| \hat{\rho} \right| \mathbf{q} + \frac{\mathbf{y}}{2} \right\rangle \quad (1.95)$$

The other formulas explored in this section can be adjusted accordingly.

1.5 Common states in Quantum optics

In this section, we will discuss the most common states encountered in the field of Quantum Optics. This includes Fock states, coherent states, and the main focus of this thesis: squeezed states of light and EPR states. Similar to the previous section, we will present a simplified single-mode description of these states whenever possible, although a multimode generalization is often straightforward.

1.5.1 Fock states

Fock states have already been introduced in section 1.2, where we encountered the quantized Hamiltonian of the electric field in the form of Eq. 1.46 and we introduced the Fock space and

its orthonormal occupation-number basis. Here, we aim to give a more complete description of the Fock states and their properties.

Fock states are eigenstates of the number operator $\hat{n} = \hat{a}^\dagger \hat{a}$. As a consequence, measuring the number of photons of a Fock state with an ideal photon-resolving detector yields a precise outcome:

$$\hat{n} |n\rangle = n |n\rangle \quad (1.96)$$

and it is straightforward to calculate the first and second moments as $\langle n \rangle = n$ and $\Delta^2 n = 0$.

We now aim at calculating the expectation value of the electric field operator $\hat{E}(\mathbf{r}, t)$, defined in section 1.3.1¹. The first and second moment are:

$$\langle \hat{E} \rangle = 0 \quad (1.97)$$

$$\Delta^2 E = \mathcal{E}_0^2 (2n + 1) \quad (1.98)$$

The mean electric field vanishes, regardless of the number of photons of the Fock state. Moreover, a measurement performed at any time t could result in any outcome within the range defined by $\Delta^2 E$. Indeed, the phase of a Fock state takes a random value at any time t and it can vary from 0 to $\pi/2$ ². For this reason, the behaviour of the electric field of the Fock state differs significantly from the oscillatory pattern we are familiar with.

The mean value and variance of the quadratures read:

$$\langle q \rangle = \langle p \rangle = 0 \quad (1.99)$$

$$\Delta^2 q = \Delta^2 p = 2n + 1 \quad (1.100)$$

From these relations we see that, among all the Fock states, only the vacuum field is a minimum uncertainty state, i.e. it minimizes the Heisenberg uncertainty relations 1.56.

The Wigner function of a Fock state with photon number n is expressed as:

$$W_{|n\rangle}(q, p) = \frac{(-1)^n}{2\pi} e^{-\frac{q^2+p^2}{2}} L_n(q^2 + p^2) \quad (1.101)$$

where L_n are Laguerre polynomials. Only the Wigner function of the vacuum state $|0\rangle$ is Gaussian, while the Wigner function of a Fock state with $n > 0$ exhibits non-classical behavior, due to the presence of negative regions. An example of Wigner function of the vacuum state and of a Fock state with $n = 10$ can be seen in Fig. 1.4.

¹We work here in the Heisenberg picture, where the electric field operator depends on time $\hat{E}(\mathbf{r}, t)$, but we recall the results are independent on the picture used to carry out the calculations.

²We should expect it from the number-phase uncertainty relation that stems from the non-commuting observables $[\hat{n}, \hat{\phi}] = 1$, where $\hat{\phi}$ is a phase operator whose definition has some subtle problems that we will not mention here. For Fock states, as the number is perfectly defined, the uncertainty of the phase tends to infinity [Grynberg 10].

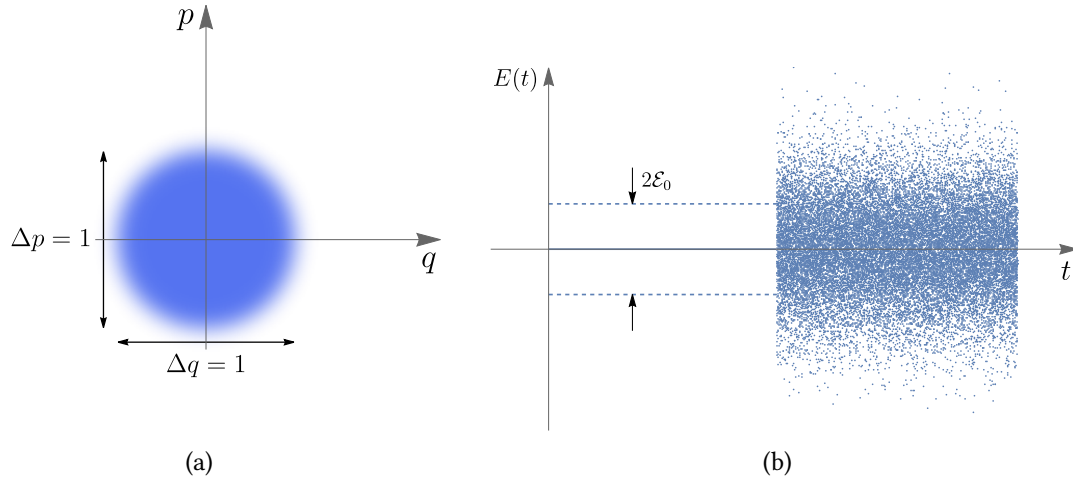


Figure 1.3: Phase diagram (a) and electric field (b) of the vacuum state $|0\rangle$. The field fluctuates around a vanishing mean value.

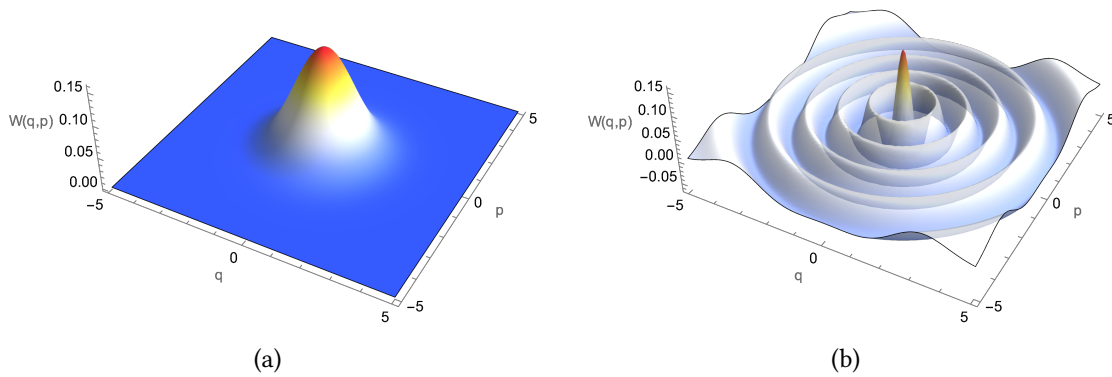


Figure 1.4: Wigner function of the vacuum state $|0\rangle$ (a) and of the Fock state $|10\rangle$ (b).

1.5.2 Coherent states

In order to obtain a classical oscillatory behavior, we introduce coherent states, also considered the “most classical states of light” among pure states. They are defined as eigenstates of the annihilation operator:

$$\hat{a} |\alpha\rangle = \alpha |\alpha\rangle \quad (1.102)$$

It can be shown that these eigenstates exist if the eigenvalues α are complex numbers, represented as $\alpha = |\alpha|e^{i\phi}$, as \hat{a} is not hermitian. The first and second moments of the electric field, evaluated at $\mathbf{r} = 0$, are:

$$\langle \hat{E}(\mathbf{r} = 0, t) \rangle = \mathcal{E}_0 \alpha e^{-i\omega t} + \text{c.c.} \quad (1.103)$$

$$\Delta^2 E(\mathbf{r} = 0, t) = \mathcal{E}_0^2 \quad (1.104)$$

From the expression of $\langle \hat{E} \rangle$ it is evident that we have retrieved the oscillatory nature characteristic of a monochromatic wave. Additionally, $\Delta^2 E$ is independent of both position and time.

The quadratures of the field are given by:

$$\langle q \rangle = 2\text{Re}(\alpha) \quad \text{and} \quad \langle p \rangle = 2\text{Im}(\alpha) \quad (1.105)$$

$$\Delta^2 q = \Delta^2 p = 1 \quad (1.106)$$

therefore we can conclude that coherent states are minimum uncertainty states. In Fig. 1.5 the behavior of a coherent state is shown.

Coherent states can be expanded in the basis of Fock states as $|\alpha\rangle = \sum_n |n\rangle \langle n|\alpha\rangle$. After calculating the terms $\langle n|\alpha\rangle$, it can be shown that:

$$|\alpha\rangle = e^{-\frac{|\alpha|^2}{2}} \sum_{n=0}^{\infty} \frac{\alpha^n}{\sqrt{n!}} |n\rangle \quad (1.107)$$

where we see that coherent states are linear superpositions of Fock states, and therefore they do not have a definite number of photons. More specifically, the probability distribution $p(n) = |\langle n|\alpha\rangle|^2$ follows a Poisson distribution with parameter $|\alpha|^2$, resulting in $\langle \hat{n} \rangle = \Delta^2 n = |\alpha|^2$, as it can also be directly calculated. It is to note that two coherent states are not orthogonal, as $\langle \alpha|\beta\rangle = e^{|\beta-\alpha|^2}$, so that we cannot build an orthonormal basis from coherent states.

The Wigner function of a coherent state is given by:

$$W_{|\alpha\rangle} = \frac{1}{2\pi} e^{-\frac{(q-q_0)^2}{2} - \frac{(p-p_0)^2}{2}} \quad (1.108)$$

where $(q_0 + ip_0)/2 = \alpha$, which represents a Gaussian distribution, as expected for semi-classical states. We note that the Wigner function of a coherent state is obtained by displacing the Wigner function of the vacuum state in the phase-space by the values (q_0, p_0) .

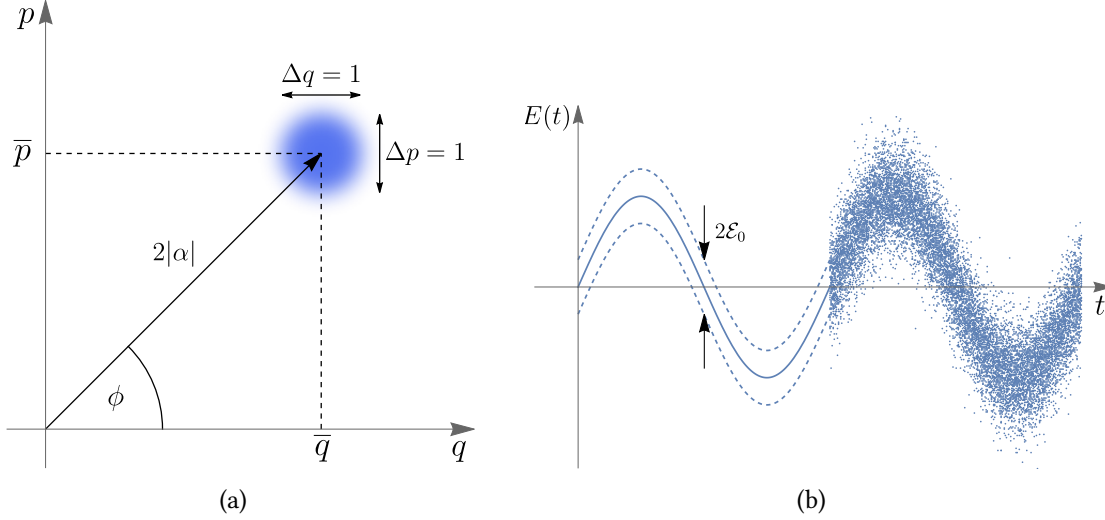


Figure 1.5: Typical phasor diagram (a) and electric field (b) of a coherent state. We note here that, regardless of the magnitude of the vector, the uncertainty area remains constant. For $|\alpha| \gg 1$ we can recover a classical field, where quantum fluctuations are negligible.

1.5.3 Squeezed states

We finally describe the class of states that is of most interest in this dissertation: squeezed states of light. Squeezed states are minimum uncertainty states characterized by reduced variance in one quadrature, at the expense of the other quadrature, where variance is increased. Indeed, the two variances do not need to be equal to minimize the uncertainty relations, and we can have quadrature variances of the type $\Delta^2 q = a$ and $\Delta^2 p = 1/a$ that still fulfill the Heisenberg uncertainty principle. We will see in this section how to implement such states and what are their main properties. It is to note that here we will investigate *single-mode* squeezed states, as opposed to *two-mode squeezed states* or twin beams that we will review in the next section. Single-mode squeezing occurs from a degenerate SPDC process, when the emitted pairs of photons are indistinguishable. In Chapter 3, we will see how this specific nonlinear process generates squeezed states. A comprehensive review on squeezed states can be found in [Lvovsky 16].

Squeezed vacuum states are defined by:

$$|\zeta\rangle = \hat{S}(\zeta) |0\rangle \quad (1.109)$$

where $\hat{S}(\zeta)$ is the unitary squeezing operator¹:

$$\hat{S}(\zeta) = e^{\frac{1}{2}(\zeta \hat{a}^{\dagger 2} - \zeta^* \hat{a}^2)} \quad (1.110)$$

¹A different convention defines $\hat{S}(\zeta) = e^{\frac{1}{2}(\zeta \hat{a}^2 - \zeta^* \hat{a}^{\dagger 2})}$. In this convention the state is initially q -squeezed and p -antisqueezed.

Here, $\zeta = re^{i\phi}$ is the squeezing parameter and r and ϕ are real numbers, where ϕ determines the angle of the squeezed quadrature. In most cases, for simplicity we set $\phi = 0$ and we refer to the operator $\hat{S}(r)$. The squeezing operator $\hat{S}(r)$ acts on the creation and annihilation operators as:

$$\hat{S}^\dagger(r)\hat{a}\hat{S}(r) = \hat{a} \cosh r + \hat{a}^\dagger \sinh r \quad (1.111)$$

$$\hat{S}^\dagger(r)\hat{a}^\dagger\hat{S}(r) = \hat{a}^\dagger \cosh r + \hat{a} \sinh r \quad (1.112)$$

From these relations we can straightforwardly derive the electric field first and second moments:

$$\langle E \rangle = 0 \quad (1.113)$$

$$\Delta^2 E = \mathcal{E}_0^2 [\cosh^2 r + \sinh^2 r + \cosh r \sinh r (e^{-i2\omega t} + e^{i2\omega t})] \quad (1.114)$$

The transformation of \hat{q} and \hat{p} under a squeezing operation reads:

$$\hat{S}^\dagger(r)\hat{q}\hat{S}(r) = e^r \hat{q} \quad (1.115)$$

$$\hat{S}^\dagger(r)\hat{p}\hat{S}(r) = e^{-r} \hat{p} \quad (1.116)$$

in which case we define q as the anti-squeezed quadrature and p as the squeezed quadrature¹. From these relations we can calculate the first and second moments of the position and momentum operator:

$$\langle q \rangle = \langle p \rangle = 0 \quad (1.117)$$

$$\Delta^2 q = e^{2r}, \Delta^2 p = e^{-2r} \quad (1.118)$$

where we see that squeezed states are minimum uncertainty states. We define $s = e^{2r}$ as the *squeezing factor*² that we often quantify in decibels:

$$s_{dB} = 10 \log_{10}(s) \quad (1.119)$$

Fig. 1.6 illustrates the behavior of a squeezed vacuum state along with its distinctive quadrature distribution and electric field.

Despite being called squeezed vacuum state, $|r\rangle$ is not void of photons. To assess this, we can represent this state in the photon-number basis and describe its photon number statistics, obtaining:

$$|r\rangle = \frac{1}{\sqrt{\cosh r}} \sum_{n=0}^{\infty} (-\tanh r)^n \frac{\sqrt{(2n)!}}{2^n n!} |2n\rangle \quad (1.120)$$

¹In the general case where the squeezing phase is non-zero, we identify an anti-squeezed rotated quadrature \hat{q}^ϕ and a squeezed rotated quadrature \hat{p}^ϕ as the quadratures of the rotated operator $\hat{a}^\phi = \hat{a}e^{-i\phi}$.

²The squeezing factor is always rescaled by the variance of the vacuum noise: $s = \Delta^2 q / \Delta^2 q_0$. In our convention, $\Delta^2 q_0 = 1$ and we obtain simply $s = \Delta^2 q$.

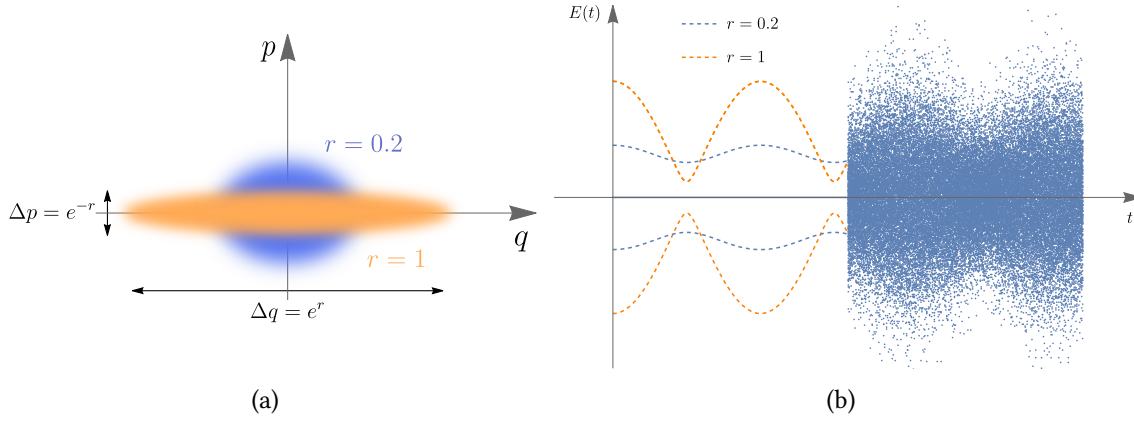


Figure 1.6: Typical phasor diagram (a) and electric field (b) of squeezed vacuum states with two different squeezing parameters. The fluctuations in the second half of (b) correspond to the $r = 0.2$ squeezing parameter.

We note that squeezed states are coherent superpositions of even number Fock states, where the probability amplitude weights decrease as we increase the number of photons. This is expected from the definition of the squeezing operator in Eq. 1.110, that contains the square of the creation operator. The physical meaning behind the sole presence of even number states is intrinsic from the SPDC process, which is a three-wave-mixing nonlinear process where a pump photon is converted into two twin photons. From Eq. 1.120 we can also calculate the mean photon number of a squeezed vacuum state, that is given by:

$$\langle n \rangle = \sinh^2 r \quad (1.121)$$

Another common way of describing squeezed states is via the position or momentum representation. The wavefunction in the position basis reads:

$$\psi_r(q) = \frac{1}{(s\pi)^{1/4}} e^{-\frac{q^2}{2s}} \quad (1.122)$$

and the Wigner function is:

$$W_{|r\rangle} = \frac{1}{2\pi} e^{-\frac{q^2}{2s} - \frac{sp^2}{2}} \quad (1.123)$$

An example of the Wigner function of a squeezed state is depicted in Fig. 1.7b.

1.5.4 EPR state

EPR states have been a milestone in the development of Quantum theory and technologies, since their theoretical introduction in 1935, by Einstein, Podolsky and Rosen. In their

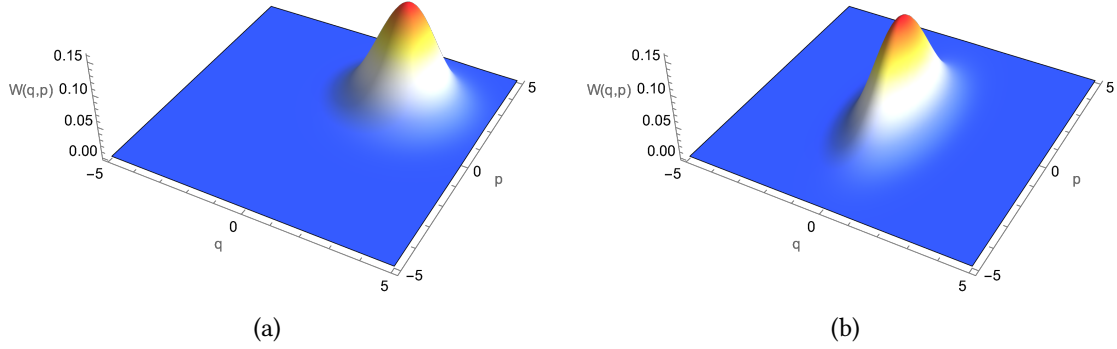


Figure 1.7: Wigner function of (a) a coherent state centered at $(q_0, p_0) = (2, 2)$ and (b) of a 3 dB q -squeezed state (b).

original formulation, they represent a system of two distant particles characterized by the following unnormalized wavefunction:

$$\psi(q_1, q_2) = \delta(q_1 - q_2) \quad (1.124)$$

$$\psi(p_1, p_2) = \delta(p_1 + p_2) \quad (1.125)$$

where the positions (resp. momenta) of the two particles are perfectly correlated (resp. anticorrelated). In particular, the EPR state is a non-separable state, meaning that the correlations among the two particles of the EPR pair cannot be regarded as classical correlations: the EPR state exhibits entanglement correlations and the two systems are entangled.

Here, we cannot give a single-mode description, as we did in the rest of this section, as we obviously need at least two modes to define an entangled state. We define the two-mode squeezed vacuum state (TMSV), of which the EPR state constitutes a limiting case. The TMSV is generated by acting on the vacuum with the two-mode squeezing operator:

$$\hat{S}_2(\zeta) = \exp \left[\zeta^* \hat{a}_1^\dagger \hat{a}_2^\dagger - \zeta \hat{a}_1 \hat{a}_2 \right] \quad (1.126)$$

where $\zeta = r e^{2i\theta}$. Assuming $\theta = 0$ for simplicity, we find that the corresponding transformation $\hat{S}_2(r)$ on the annihilation operators in the Heisenberg picture gives the outcome:

$$\hat{a}_1(r) = \hat{a}_1 \cosh r + \hat{a}_2^\dagger \sinh r \quad (1.127)$$

$$\hat{a}_2(r) = \hat{a}_2 \cosh r + \hat{a}_1^\dagger \sinh r \quad (1.128)$$

The two-mode vacuum state generated by the action of the operator $\hat{S}_2(r)$ on the vacuum can be physically implemented by a non-degenerate parametric down conversion process.

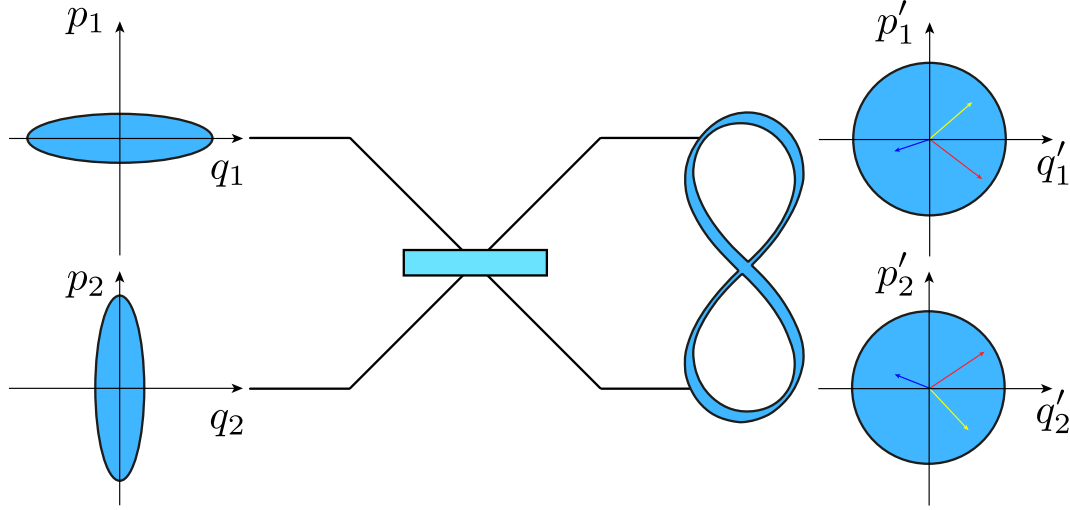


Figure 1.8: A two-mode squeezed vacuum state can be implemented by mixing two squeezed states on a 50:50 beam-splitter (BS). Each quadrature of the TMSV exhibits excess of noise. However, the q quadratures are partially correlated, while the p quadratures are partially anticorrelated.

Equivalently, it can be realized by combining two single-mode squeezed states with linear optics, as shown in Fig. 1.8.

While the individual quadratures of the EPR state show fluctuations above the vacuum noise:

$$\Delta^2 q_1 = \Delta^2 q_2 = \Delta^2 p_1 = \Delta^2 p_2 = \frac{e^{2r} + e^{-2r}}{2} \quad (1.129)$$

we can find specific linear combinations of the quadratures that exhibit noise below the vacuum level:

$$\Delta^2(\hat{q}_1 - \hat{q}_2) = 2e^{-2r} \quad (1.130)$$

$$\Delta^2(\hat{p}_1 + \hat{p}_2) = 2e^{-2r} \quad (1.131)$$

For $r \rightarrow \infty$, the noise of the relative position and of the sum of the momenta decreases and we retrieve the behavior of an ideal EPR state.

The TMSV state exhibits correlations not only in position and momentum, but also in photon number. Indeed, in the Fock basis, the TMSV is written as:

$$\hat{S}_2(r) |00\rangle = \frac{1}{\cosh r} \sum_{n=0}^{\infty} (\tanh r)^n |n\rangle |n\rangle \quad (1.132)$$

which shows that the TMSV state can be written as a superposition of states with the same photon number.

Finally, the Wigner function for the two-mode squeezed vacuum reads:

$$W_{EPR}(q, p) = \frac{1}{4\pi^2} \exp \left\{ -\frac{[(q_1 + q_2)^2 + (p_1 - p_2)^2]}{4e^{2r}} - \frac{[(q_1 - q_2)^2 + (p_1 + p_2)^2]}{4e^{-2r}} \right\} \quad (1.133)$$

This Wigner state is gaussian: the two-mode squeezed state is then a gaussian state and it can be completely characterized by its covariance matrix, as we will see in the next chapter.

Chapter 2

Gaussian states and measurements

Contents

2.1 Gaussian states and operations	38
2.1.1 Gaussian states	38
2.1.2 Generalities on Gaussian operations	39
2.1.3 Linear optics transformations	41
2.1.4 Decompositions of states and unitaries	42
2.2 Sidebands in optics	43
2.2.1 Classical modulations of the field	43
2.2.2 Sidebands quantum operators	46
2.2.3 Sidebands as quantum states	47
2.3 Measurement of quantum states	49
2.3.1 Intensity measure	50
2.3.2 Noise spectrum and quantum noise	51
2.3.3 Homodyne detection in the temporal domain	52
2.3.4 Homodyne detection in the spectral domain	54

A central role in quantum optics is assumed by the category of Gaussian states, which includes some of the states encountered in section 1.4.3, such as coherent states, squeezed states and EPR states. Despite their inherent limitations [Mari 12], together with Gaussian operations they constitute a foundational resource for CV Quantum Information Processing [Ferraro 05, Weedbrook 12, Braunstein 98, Braunstein 00]. In this chapter, we will review Gaussian states and operations, with a focus on linear optics and squeezing transformations. Moreover, we will investigate homodyne detection, a Gaussian measurement technique widely used in CV quantum optics, both in the spectral and in the temporal domains.

2.1 Gaussian states and operations

In this section, we review the main definitions and tools for Gaussian states and operations of interest for our work. More extensive details on the subject can be found in [Ferraro 05, Weedbrook 12, Adesso 14, Braunstein 05b].

2.1.1 Gaussian states

A Gaussian state is, by definition, a state whose Wigner quasi-probability distribution is a multi-variate Gaussian function in phase space. The Wigner function of an n -mode Gaussian state can be expressed as follows:

$$W(\mathbf{x}) = \frac{1}{(2\pi)^n \sqrt{\det \mathbf{V}}} \exp \left[-\frac{1}{2} (\mathbf{x} - \bar{\mathbf{x}})^T \mathbf{V}^{-1} (\mathbf{x} - \bar{\mathbf{x}}) \right] \quad (2.1)$$

where $\mathbf{x} = (\mathbf{q}, \mathbf{p})$, and where $\bar{\mathbf{x}}$ is the mean value (or first moment) and \mathbf{V} is the covariance matrix (or second moment) of the state. These are defined as:

$$\bar{\mathbf{x}} = \langle \hat{\mathbf{x}} \rangle = \text{Tr}(\hat{\mathbf{x}} \hat{\rho}) \quad (2.2)$$

$$V_{ij} = \frac{1}{2} \langle \hat{x}_i \hat{x}_j + \hat{x}_j \hat{x}_i \rangle - \langle \hat{x}_i \rangle \langle \hat{x}_j \rangle \quad (2.3)$$

From Eq. 2.1, it can be concluded that the mean value and the covariance matrix are sufficient to fully characterize a Gaussian state. In this thesis, we often assume, without loss of generality, that $\bar{\mathbf{x}} = 0$. This is because the mean value can be centered at the origin of the phase space through a displacement operation, which preserves correlations among the quadratures [Adesso 14]. Specifically, in the quantum states of interest for our work, quantum information is encoded in quadrature variances and correlations, and it remains preserved under such displacements. Therefore, we concentrate on the essential properties of the covariance matrix of the state¹.

The covariance matrix of a quantum state must adhere to certain constraints. Similar to the covariance matrix used in statistics to describe covariances between random variables, the quantum state's covariance matrix must also be real, symmetric and positive-definite. However, unlike a "classical" covariance matrix, the covariance matrix of a quantum state must satisfy an additional constraint imposed by the Heisenberg uncertainty relations, namely:

$$\mathbf{V} - i\mathbf{J} \geq 0 \quad (2.4)$$

¹We point out that we are using the notation $\mathbf{x} = (x_1, x_2, \dots, x_N, p_1, p_2, \dots, p_N)$. A different notation according to which the vector is described as $\mathbf{x} = (x_1, p_1, \dots, x_N, p_N)$ exists. The two approaches are equivalent and the most important equations in both notations can be found in [Ferraro 05].

where \mathbf{J} is the $2n \times 2n$ symplectic matrix:

$$\mathbf{J} = \begin{pmatrix} 0 & -\mathbb{1} \\ \mathbb{1} & 0 \end{pmatrix} \quad (2.5)$$

This relation is necessary and sufficient to ensure that the covariance matrix represents a physical quantum state.

The purity of an n -mode quantum state can be determined from its covariance matrix as follows:

$$\mu_\rho = \frac{1}{\det \mathbf{V}} \quad (2.6)$$

It follows that a quantum state is pure if and only if $\det \mathbf{V} = 1$.

In this thesis, we will encounter the covariance matrices of several common states. The covariance matrix for the single-mode vacuum state, coherent state and squeezed state, read:

$$V_{|0\rangle} = \mathbb{1} \quad (2.7)$$

$$V_{|\alpha\rangle} = \mathbb{1} \quad (2.8)$$

$$V_{|r\rangle} = \begin{pmatrix} e^{2r} & 0 \\ 0 & e^{-2r} \end{pmatrix} \quad (2.9)$$

The covariance matrix for the two-mode EPR state reads:

$$V_{|EPR\rangle} = \begin{pmatrix} \cosh 2r & \sinh 2r & 0 & 0 \\ \sinh 2r & \cosh 2r & 0 & 0 \\ 0 & 0 & \cosh 2r & -\sinh 2r \\ 0 & 0 & -\sinh 2r & \cosh 2r \end{pmatrix} \quad (2.10)$$

2.1.2 Generalities on Gaussian operations

The transformation that a quantum system undergoes is described by a quantum operation that acts on the quantum state of the system. When addressing an open system, one that interacts with an environment, the quantum operation is a completely positive linear map that operates on the initial state [Nielsen 10, Breuer 02]. In general, this operation is non trace-preserving, as it is the case with measurements on a state. A trace preserving map is called a *quantum channel* and it is reversible if and only if it is unitary. Therefore, the action of a quantum channel is expressed as:

$$\hat{\rho} \rightarrow \hat{U} \hat{\rho} \hat{U}^\dagger \quad (2.11)$$

A Gaussian operation is defined as a transformation that maps Gaussian states into Gaussian states. In this thesis we focus on Gaussian operations, that include Gaussian unitaries (Gaussian quantum channels) and Gaussian measurements, notably homodyne detection.

Gaussian unitaries are operators of the form $\hat{U} = e^{-\frac{i}{\hbar}\hat{H}}$, where \hat{H} is at most quadratic in the creation and annihilation operators:

$$\hat{H} = i\hbar \sum_{ij} A_{ij} \hat{a}_i^\dagger \hat{a}_j + B_{ij} \hat{a}_i^\dagger \hat{a}_j^\dagger + \gamma_i \hat{a}_i^\dagger + \text{h.c.} \quad (2.12)$$

In the Heisenberg picture this translates to a linear unitary Bogoliubov transformation of the creation and annihilation operators:

$$\hat{a}_k \rightarrow \hat{U}^\dagger \hat{a}_k \hat{U} = \sum_j \alpha_{jk} \hat{a}_j + \beta_{jk} \hat{a}_j^\dagger + \gamma_k \quad (2.13)$$

$$\hat{a}_k^\dagger \rightarrow \hat{U}^\dagger \hat{a}_k^\dagger \hat{U} = \sum_j \alpha_{jk}^* \hat{a}_j^\dagger + \beta_{jk}^* \hat{a}_j + \gamma_k^* \quad (2.14)$$

or in matrix form:

$$\hat{U}^\dagger \begin{pmatrix} \hat{\mathbf{a}} \\ \hat{\mathbf{a}}^\dagger \end{pmatrix} \hat{U} = \begin{pmatrix} \boldsymbol{\alpha} & \boldsymbol{\beta} \\ \boldsymbol{\beta}^* & \boldsymbol{\alpha}^* \end{pmatrix} \begin{pmatrix} \hat{\mathbf{a}} \\ \hat{\mathbf{a}}^\dagger \end{pmatrix} + \begin{pmatrix} \boldsymbol{\gamma} \\ \boldsymbol{\gamma}^* \end{pmatrix} \quad (2.15)$$

where $\boldsymbol{\alpha}$ and $\boldsymbol{\beta}$ are $n \times n$ matrices. Due to the unitarity of the transformation, the commutation relations must be preserved. This imposes the following constraint on the $\boldsymbol{\alpha}$ and $\boldsymbol{\beta}$ matrices:

$$\boldsymbol{\alpha} \boldsymbol{\alpha}^\dagger = \boldsymbol{\beta} \boldsymbol{\beta}^\dagger + \mathbb{1} \quad (2.16)$$

$$\boldsymbol{\alpha} \boldsymbol{\beta}^T = \boldsymbol{\beta} \boldsymbol{\alpha}^T \quad (2.17)$$

These equations are the defining relations of the complex form of the real symplectic group $\text{Sp}(2n, \mathbb{R})$ ¹. We can write more compactly Eq. 2.15 as follows:

$$\hat{U}^\dagger \hat{\boldsymbol{\xi}}^{(c)} \hat{U} = \mathbf{S}^{(c)} \hat{\boldsymbol{\xi}}^{(c)} + \mathbf{d}^{(c)} \quad (2.18)$$

where $\hat{\boldsymbol{\xi}}^{(c)} = (\hat{\mathbf{a}}, \hat{\mathbf{a}}^\dagger)^T$. On the quadrature operators this transformation translates to:

$$\hat{U}^\dagger \hat{\mathbf{x}} \hat{U} = \mathbf{S} \hat{\mathbf{x}} + \mathbf{d} \quad (2.19)$$

where $\hat{\mathbf{x}} = (\hat{q}_1, \dots, \hat{q}_n, \hat{p}_1, \dots, \hat{p}_n)^T$, $\mathbf{d} \in \mathbb{R}^{2n}$ and it can be shown that $\mathbf{S} \in \text{Sp}(2n, \mathbb{R})$. The two forms are related by the relations:

$$\hat{\mathbf{x}} = \boldsymbol{\Omega}^{-1} \hat{\boldsymbol{\xi}}^{(c)} \quad (2.20)$$

$$\mathbf{d} = \boldsymbol{\Omega}^{-1} \mathbf{d}^{(c)} \quad (2.21)$$

$$\mathbf{S} = \boldsymbol{\Omega}^{-1} \mathbf{S}^{(c)} \boldsymbol{\Omega} \quad (2.22)$$

¹We recall that the real symplectic group is defined by matrices that, if we write \mathbf{S} in block-form as $\mathbf{S} = \begin{pmatrix} \mathbf{A} & \mathbf{B} \\ \mathbf{C} & \mathbf{D} \end{pmatrix}$, satisfy the following constraints: 1) $\mathbf{A}\mathbf{B}^T$ and $\mathbf{C}\mathbf{D}^T$ must be symmetric, 2) $\mathbf{A}\mathbf{D}^T - \mathbf{B}\mathbf{C}^T = \mathbb{1}$ where $\mathbf{A}, \mathbf{B}, \mathbf{C}, \mathbf{D}$ are $n \times n$ matrices.

where:

$$\Omega = \begin{pmatrix} \mathbb{1}_n & i\mathbb{1}_n \\ \mathbb{1}_n & -i\mathbb{1}_n \end{pmatrix} \quad (2.23)$$

A useful approach involves translating the effects of this unitary transformation from the Hilbert space to a transformation operating on statistical moments within the quantum phase space. For a Gaussian unitary the following transformation holds:

$$\boxed{\bar{\mathbf{x}}' = \mathbf{S}\bar{\mathbf{x}} + \mathbf{d}} \quad (2.24)$$

$$\boxed{\mathbf{V}' = \mathbf{S}\mathbf{V}\mathbf{S}^T} \quad (2.25)$$

We conclude that the effect of Gaussian unitary on a Gaussian state is completely characterized by the transformations operated on the first and second moment of the state.

Finally, we note that under a symplectic transformation the Wigner function transforms as:

$$W(\mathbf{x}) \rightarrow W'(\mathbf{x}) = W(\mathbf{S}^{-1}(\mathbf{x} - \mathbf{d})) \quad (2.26)$$

2.1.3 Linear optics transformations

We introduce here a subgroup of $\text{Sp}(2n, \mathbb{R})$ that plays a central role in quantum optics and that will frequently appear in the next chapters: the *unitary subgroup*, denoted by $K(n)$ and of dimension n^2 . This subgroup contains the transformations that do not mix the creation and annihilation operators, and whose action is expressed as:

$$\hat{a}_k \rightarrow \sum_j U_{jk} \hat{a}_j \quad (2.27)$$

$$\hat{a}_k^\dagger \rightarrow \sum_j U_{jk}^* \hat{a}_j^\dagger \quad (2.28)$$

where \mathbf{U} is a unitary matrix that we can decompose into its real and imaginary parts as $\mathbf{U} = \mathbf{X} + i\mathbf{Y}$. The corresponding $\mathbf{S}^{(c)}$ matrix, which acts on the creation and annihilation operators, reads:

$$\mathbf{S}^{(c)} = \begin{pmatrix} \mathbf{U} & 0 \\ 0 & \mathbf{U}^* \end{pmatrix} \quad (2.29)$$

Using Eq. 2.22, we can retrieve the \mathbf{S} matrix that operates on quadrature operators:

$$\mathbf{S} = \begin{pmatrix} \mathbf{X} & -\mathbf{Y} \\ \mathbf{Y} & \mathbf{X} \end{pmatrix} \quad (2.30)$$

We can check that \mathbf{S} represents a real symplectic transformation. Indeed, the condition for unitarity $UU^\dagger = U^\dagger U = \mathbb{1}$ translates to the matrices \mathbf{X} and \mathbf{Y} as $\mathbf{X}\mathbf{X}^T + \mathbf{Y}\mathbf{Y}^T = \mathbb{1}$ and $\mathbf{X}\mathbf{Y}^T =$

YX^T . These conditions align with the criteria defining a symplectic matrix and, moreover, they imply orthogonality. Therefore, we conclude that a symplectic transformation that belongs to the subgroup $K(N)$ is also orthogonal.

Orthogonal symplectic transformations preserve the trace of the covariance matrix \mathbf{V} , i.e. the mean energy of the system¹. As a result, these transformations are often referred to as *passive* transformations, in contrast to *active* transformations, such as squeezing operations, which do not preserve the energy of the system. Passive transformations correspond to linear optical devices, such as beam splitters and phase shifters.

2.1.4 Decompositions of states and unitaries

Any element \mathbf{S} that belongs to the symplectic group can be decomposed in several ways. In this section we will describe the *Bloch-Messiah decomposition* (also known as *Euler decomposition*). A symplectic transformation can be decomposed via Bloch-Messiah decomposition into the product of three operations, namely:

$$\mathbf{S} = \mathbf{O}_1 \mathbf{K} \mathbf{O}_2 \quad (2.31)$$

where $\mathbf{O}_1 = \mathbf{S}(\mathbf{X}_1, \mathbf{Y}_1)$ and $\mathbf{O}_2 = \mathbf{S}(\mathbf{X}_2, \mathbf{Y}_2)$ are symplectic orthogonal matrices defined as in 2.30 and $\mathbf{K} = \mathbf{K}(\mathbf{d})$ is a diagonal positive-definite matrix such that $\mathbf{K}(\mathbf{k}) = \text{diag}(d_1, \dots, d_n, d_1^{-1} \dots d_N^{-1})$. We can reinterpret this mathematical tool in an optics framework: the \mathbf{O}_1 and \mathbf{O}_2 matrices represent linear optics operations, defined in section 2.1.3, while the \mathbf{K} matrix can be identified as a squeezing transformation where $d_i = e^{r_i}$. We can draw the following remarkable conclusion: any Gaussian unitary can be decomposed into a multiport linear inteferometer, followed by a set of n single-mode squeezers and by another multiport linear interferometer [Braunstein 05a].

Bloch-Messiah decomposition shows us how to decompose a Gaussian unitary. The *Williamson decomposition*, instead, involves the decomposition of Gaussian states. The Williamson theorem states that every positive-definite real matrix \mathbf{V} of dimension $2n$ can be diagonalized by a symplectic transformation as:

$$\mathbf{V} = \mathbf{S} \mathbf{W} \mathbf{S}^T \quad (2.32)$$

where $\mathbf{W} = \text{diag}(k_1, \dots, k_N, k_1, \dots, k_n)$ and its elements are called symplectic eigenvalues [Williamson 36]. If \mathbf{V} represents the covariance matrix of a state, the k_i symplectic eigenvalues satisfy $k_i \geq 1$, as a consequence of Eq. 2.4. We draw the following conclusion: any Gaussian state, pure or mixed, described by a covariance matrix \mathbf{V} , can be obtained from a thermal state, described by a diagonal matrix \mathbf{D} and subjected to a given Gaussian unitary \mathbf{S} [Weedbrook 12, Ferraro 05].

¹The mean energy of the system is proportional to the mean number of photons $\langle n \rangle = \frac{1}{m} \sum_k \langle \hat{a}_k^\dagger \hat{a}_k \rangle = \text{Tr} \sigma / m - 1$, with m number of modes.

Combining the Williamson decomposition and the Bloch-Messiah reduction, the covariance matrix of a Gaussian state can be expressed as:

$$\mathbf{V} = \mathbf{O}_1 \mathbf{K} \mathbf{O}_2 \mathbf{W} \mathbf{O}_2^T \mathbf{K} \mathbf{O}_1^T \quad (2.33)$$

For a pure Gaussian state, $\mathbf{W} = \mathbb{1}$, and the covariance matrix reads:

$$\mathbf{V} = \mathbf{O}_1 \mathbf{K}^2 \mathbf{O}_1^T \quad (2.34)$$

This indicates that any pure Gaussian state can be obtained by acting on vacuum with a squeezing transformation, followed by a basis change on the independently squeezed modes, which creates quantum correlations. When the state is mixed, Eq. 2.33 cannot be further simplified. The matrix \mathbf{W} indicates the basis where each mode is in a thermal state, characterized by excess noise in both quadratures. This thermal noise includes losses and classical noise from the laser. The basis change \mathbf{O}_2 is responsible for creating classical correlations between the modes. Subsequently, we apply a squeezing operation and another basis change \mathbf{O}_1 . This decomposition explicitly identifies the two bases in which the classical noise (thermal noise) and the quantum noise (squeezing) are decoupled [Fabre 20].

2.2 Sidebands in optics

In the context of waveforms and signals, the term *sidebands* refers to the spectral components that are located on either side of a carrier frequency in the frequency domain. In this section, we use the terminology that has been introduced in the field of radio communication, well before the study of quantum information encoded in an optical field. Indeed, both disciplines deal with an electromagnetic field and with the encoding and decoding of information (classical or quantum). In optics, the main field is in the THz region, while the information we are interested in is often encoded in radio-frequencies (RF) relative to an optical carrier.

2.2.1 Classical modulations of the field

The modulation of an optical field is analogous to the well-known FM (frequency modulation) or AM (amplitude modulation) radio broadcasting, where the signal to be transmitted is encoded in modulations of the carrier wave. In radio communication, the receiver is responsible for demodulating the received radio wave to recover the original signal. Here, we will be mostly interested in amplitude modulation (AM) and phase modulation (PM) of the optical field. We can indeed decompose every noise or signal present in our light source into amplitude or phase modulations (or fluctuations). We stress here that the terms fluctuations and modulations will be used interchangeably. We are interested in the sidebands of the optical field, that contain the information on the amplitude and phase modulations imprinted on the field.

To summarize, the essential aspect to grasp in this section is the following: light can serve as a medium for transmitting classical information, in the form of combinations of AM and PM of the carrier wave. These modulations manifest themselves as sidebands in the frequency domain. Therefore, classical information is encoded into sidebands of the light field. This concept extends to the quantum domain as well, but with significant differences, as we will explore in the next section. The goal of this section is to investigate the basics of classical modulation, in particular how to exploit AM or PM of the carrier to send a signal via the appearance of sidebands in the frequency domain [Bachor 19].

Here, we assume that we deal with an electric field in the slowly-varying envelope approximation, defined in Eq. 1.28. We modulate¹ the amplitude of the electric field with a sinusoidal signal of the type $m(t) = M \cos(\Omega_{mod}t)$, where $M < 1$ and where Ω_{mod} falls in the RF range. The modulated field reads:

$$E_{AM}^{(+)}(t) = \mathcal{E}_0 \alpha(t) (1 + m(t)) e^{-i\omega_0 t} \quad (2.35)$$

Consequently, following Eq. 1.29, its Fourier transform becomes:

$$E_{AM}^{(+)}(\omega) = \mathcal{E}_0 \left(\alpha(\Omega) + \frac{M}{2} \alpha(\Omega + \Omega_{mod}) + \frac{M}{2} \alpha(\Omega - \Omega_{mod}) \right) \quad (2.36)$$

where $\Omega = \omega - \omega_0$. The effect of amplitude modulation is to generate sidebands at $+\Omega_{mod}$ (upper sideband) and at $-\Omega_{mod}$ (lower sideband) relative to Ω . For the case in which $\alpha(t)$ is a constant, this results in $\delta(\Omega_{mod})$ and $\delta(-\Omega_{mod})$ in the frequency domain, as depicted in Fig. 2.1a. The sidebands are equal and perfectly correlated, having the same amplitude and phase.

Phase modulation is analogous, but this time we use the signal $p(t) = M \sin(\Omega_{mod}t)$ to modulate the phase of the field:

$$E_{PM}^{(+)}(t) = \mathcal{E}_0 \alpha(t) e^{ip(t)} e^{-i\omega_0 t} \quad (2.37)$$

If the modulation factor M is small, we can expand this expression to first order:

$$E_{PM}^{(+)}(t) \approx \mathcal{E}_0 \alpha(t) (1 + ip(t)) e^{-i\omega_0 t} \quad (2.38)$$

In the Fourier domain, this becomes:

$$E_{PM}^{(+)}(\omega) = \mathcal{E}_0 \left(\alpha(\Omega) + \frac{M}{2} \alpha(\Omega + \Omega_{mod}) - \frac{M}{2} \alpha(\Omega - \Omega_{mod}) \right) \quad (2.39)$$

The sidebands for phase modulation are equal in magnitude but perfectly anti-correlated, differently from the AM case. The effect of this difference between AM and PM can be seen in the phasor diagrams of Fig. 2.1b and 2.1c.

¹We point out, to avoid confusion, that the electric field in general can be already optically modulated, for example in the case of pulsed light, via the complex envelope $\alpha(t)$ that modulates the amplitude of the carrier wave.

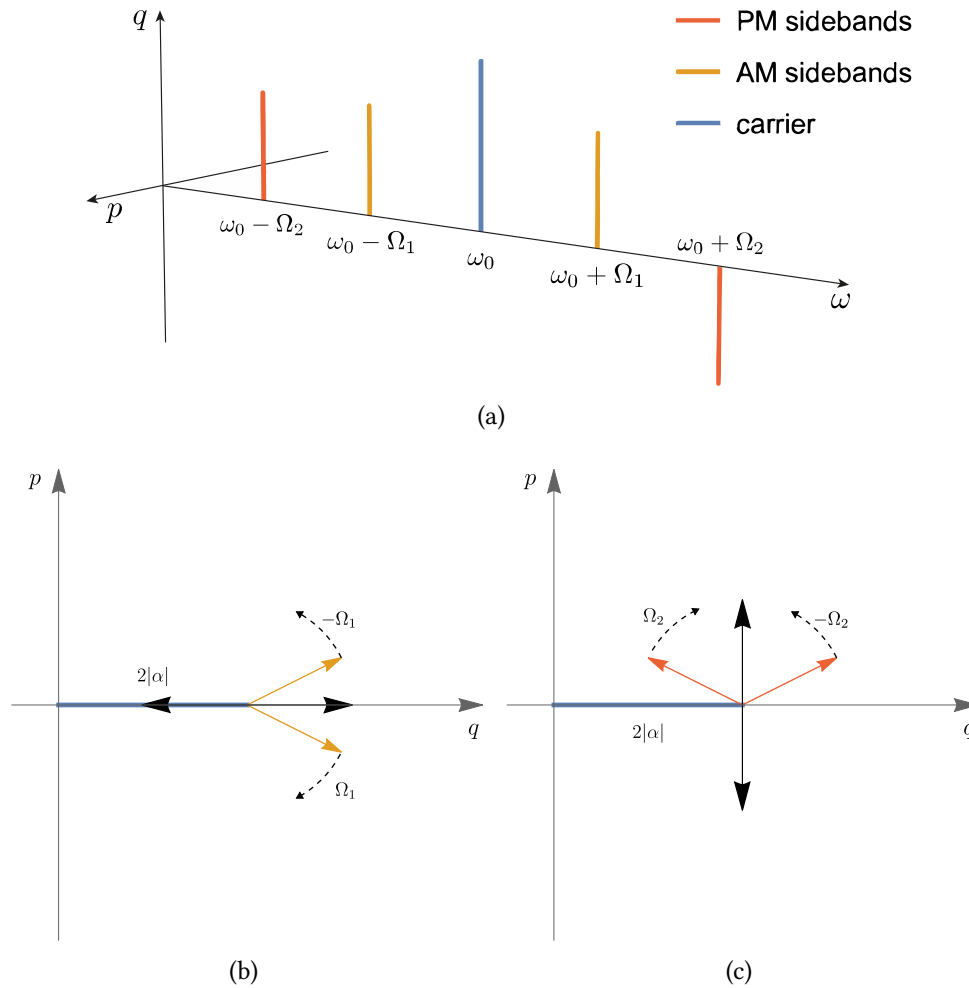


Figure 2.1: AM and PM modulations of a continuous-wave carrier ω_0 , resulting from Eq. 2.36 and Eq. 2.39. In a) we see the emergence of modulation sidebands at optical frequencies $\omega_0 \pm \Omega_1$ for AM and $\omega_0 \pm \Omega_2$ for PM. Note that the PM sidebands are π out-of-phase. In b) and c) the phasor diagrams in the rotating frame at carrier frequency ω_0 are shown. When modulation is not present, the vector lays on the q axis. In the case of AM (b) the sidebands rotate at frequency $\pm\Omega_1$ in the diagram: the vector still lays on the q axis but as a net result its magnitude oscillates. In the case of PM (c) the sidebands rotate at frequency $\pm\Omega_2$ in the diagram, and as a net result the vector p -axis component is not vanishing but it oscillates. Note that the upper sidebands of AM and PM have a phase difference of π .

In our experiment, we work with a train of femtosecond pulses, collectively forming a *frequency comb* when represented in the frequency domain. The comb consists of evenly spaced Dirac delta peaks, often referred to as the “teeth” of the comb. While a detailed description of the frequency comb will be provided in section 4.2, here we aim to understand the impact of applying amplitude and phase modulation to such a train of light pulses. In this context, $\alpha(\Omega)$ represents the multitude of frequency teeth, essentially Dirac deltas, with specific spacing. Referring to Eqs. 2.36 and 2.39, the modulation introduces the following effect on the frequency comb: it generates sidebands reflecting the structure of $\alpha(\Omega)$ at $\pm\Omega_{mod}$, while attenuating them by a factor of $\frac{M}{2}$, and eventually adding a phase shift in upper sidebands, if dealing with PM. As a result, the amplitude modulation (AM) and phase modulation (PM) sidebands are generated around each individual tooth of the comb.

2.2.2 Sidebands quantum operators

In the previous section, we saw that classical modulations or fluctuations of the field are translated into the emergence of sidebands distributed around a carrier frequency ω_0 . The carrier itself conveys no information. Therefore, the goal of light detection is to extract the information embedded within the continuum of sideband modes surrounding the carrier. In this section, we will define the sideband operators, which are responsible for creating or annihilating sideband states, along with the associated quadrature operators.

In this context, we will adopt the notation ω to indicate optical frequencies (in the THz range) and Ω to indicate frequencies relative to the optical carrier ω_0 , in the electronic range (from kHz to GHz). The Fourier transforms will be evaluated around Ω , as most photodetectors and spectrum analyzer will resolve fluctuations of this order. We will also use the term upper sideband (resp. lower sideband) to denote the optical frequencies $\omega_0 + \Omega$ (resp. $\omega_0 - \Omega$).

As already seen in Eq. 1.35, in the Heisenberg picture the fluctuations of the field can be expressed as¹:

$$\hat{a}(t) = \bar{\alpha} + \delta\hat{a}(t) \quad (2.40)$$

where we recall that $\bar{\alpha} = |\bar{\alpha}|e^{i\phi}$ is the average value over time of $\hat{a}(t)$, while $\delta\hat{a}(t)$ represents the fluctuations of the field [Huntington 05, Bachor 19]. We neglect higher order terms assuming small fluctuations. Moreover, in many practical cases of interest, the mean value is zero, so that $\hat{a}(t)$ and $\delta\hat{a}(t)$ are often used interchangeably.

The Fourier transform of the operator $\hat{a}(t)$ defined in Eq 2.40 reads:

$$\hat{a}(\Omega) = \int_{\mathbb{R}} \frac{dt}{\sqrt{2\pi}} e^{i\Omega t} \hat{a}(t) \quad (2.41)$$

¹We point out that this operator is defined in the rotating frame at frequency ω_0 . In practice, this means that the vector in the phasor diagram representing the amplitude $\hat{a}(t)$ fluctuates around a fixed average value, represented by a vector of magnitude $\bar{\alpha}$ and with a certain angle ϕ .

The mean field $\bar{\alpha}$ yields simply a Dirac delta in the correspondence of the carrier frequency $\Omega = 0$. As this is of little interest, this part is usually discarded, and we frequently indicate $\hat{a}(\Omega)$ as the Fourier transform, with respect to Ω , only of the fluctuating term $\delta\hat{a}(t)$. We define the sideband operators as [Huntington 05]:

$$\hat{a}(\Omega) = \int_{\mathbb{R}} \frac{dt}{\sqrt{2\pi}} e^{i\Omega t} \delta\hat{a}(t) \quad (2.42)$$

$$\hat{a}(-\Omega) = \int_{\mathbb{R}} \frac{dt}{\sqrt{2\pi}} e^{-i\Omega t} \delta\hat{a}(t) \quad (2.43)$$

$$\hat{a}^\dagger(\Omega) = \int_{\mathbb{R}} \frac{dt}{\sqrt{2\pi}} e^{-i\Omega t} \delta\hat{a}^\dagger(t) \quad (2.44)$$

$$\hat{a}^\dagger(-\Omega) = \int_{\mathbb{R}} \frac{dt}{\sqrt{2\pi}} e^{i\Omega t} \delta\hat{a}^\dagger(t) \quad (2.45)$$

where the δ indicating the fluctuation is explicitly dropped in the frequency domain. These operators create or annihilate a photon at sideband frequency $\pm\Omega$ with respect to the carrier, i.e. at the optical frequency $\omega = \omega_0 \pm \Omega$ [Martinelli 23, Zhang 03, Barbosa 20].

To define quadratures $\hat{x}(\Omega)$ in the Fourier space we might be tempted to implement the Fourier transform of the quadratures $\hat{x}(t)$. However, this would not be the correct definition, because quadratures are defined as linear combinations of creation and annihilation operators of a specific mode. For example, for a monochromatic mode, we have $\hat{q}(\omega) = \hat{a}^\dagger(\omega) + \hat{a}(\omega)$, and for sideband modes analogously:

$$\hat{q}(\Omega) = \hat{a}^\dagger(\Omega) + \hat{a}(\Omega) \quad (2.46)$$

$$\hat{p}(\Omega) = i(\hat{a}^\dagger(\Omega) - \hat{a}(\Omega)) \quad (2.47)$$

However, the Fourier transform of the quadratures fluctuations $\delta\hat{x}(t)$ reads:

$$\hat{q}_{FT}(\Omega) = \int_{\mathbb{R}} \frac{dt}{\sqrt{2\pi}} e^{i\Omega t} \delta\hat{q}(t) = \hat{a}^\dagger(-\Omega) + \hat{a}(\Omega) \quad (2.48)$$

$$\hat{p}_{FT}(\Omega) = \int_{\mathbb{R}} \frac{dt}{\sqrt{2\pi}} e^{i\Omega t} \delta\hat{p}(t) = i(\hat{a}^\dagger(-\Omega) - \hat{a}(\Omega)) \quad (2.49)$$

We can see that $\hat{x}_{FT}(\Omega)$, the spectrum of the quadrature fluctuations $\delta\hat{x}(t)$, is different from the canonical quadrature $\hat{x}(\Omega)$. Indeed, this spectrum involves the operators of both the lower and upper sidebands. This is not surprising: we already saw in section 2.2.1 that a sinusoidal modulation in time at frequency Ω_{mod} results in the appearance of both the Ω_{mod} and the $-\Omega_{mod}$ sidebands in the frequency domain.

2.2.3 Sidebands as quantum states

In the previous section we introduced all the tools necessary to describe the electric field in the sideband mode basis, which is the natural basis of spectral homodyne detection, that

we will investigate in the next sections. We rewrite the expression of the electric field from Eq. 1.34:

$$\hat{E}(t) = \mathcal{E}_0 [\hat{q}(t) \cos(\omega_0 t) + \hat{p}(t) \sin(\omega_0 t)] \quad (2.50)$$

This expression can be reformulated, in terms of sidebands operators, as:

$$\begin{aligned} \hat{E}(t) = \mathcal{E}_0 \left[\cos(\omega_0 t) \int_{\mathbb{R}} \frac{dt}{\sqrt{2\pi}} e^{-i\Omega t} \hat{q}_{FT}(t) + \sin(\omega_0 t) \int_{\mathbb{R}} \frac{dt}{\sqrt{2\pi}} e^{-i\Omega t} \hat{p}_{FT}(t) \right] = \\ \mathcal{E}_0 \cos(\omega_0 t) \int_{\mathbb{R}} \frac{dt}{\sqrt{2\pi}} e^{-i\Omega t} \left(\hat{a}^\dagger(-\Omega) + \hat{a}(\Omega) \right) + \\ \mathcal{E}_0 \sin(\omega_0 t) \int_{\mathbb{R}} \frac{dt}{\sqrt{2\pi}} e^{-i\Omega t} i \left(\hat{a}^\dagger(-\Omega) - \hat{a}(\Omega) \right) \end{aligned} \quad (2.51)$$

This expansion reveals that the electric field can be expressed as a combination of creation and annihilation operators of the upper and lower sidebands, effectively representing it in a sideband mode basis.

Just like any other mode basis, the sideband modes can be populated by different quantum states, that can exhibit quantum correlations among themselves. For instance, a beam modulated at frequency Ω_{mod} can be written as:

$$|\psi\rangle = |\alpha : \Omega_{mod}\rangle |\alpha : -\Omega_{mod}\rangle |0 : \Omega \neq \pm\Omega_{mod}\rangle \quad (2.52)$$

In this state, the upper and lower sidebands $\pm\Omega_{mod}$ are occupied by a pair of coherent states, featuring perfectly correlated or anticorrelated signals, depending on whether we deal with amplitude or phase modulation. In this case, the state is Gaussian and separable [Barbosa 20, Bachor 19]. The emergence of classical sidebands due to modulation is consistent with the classical description we provided in section 2.2.1. What changes in the quantum description is that we must also consider inherent *quantum noise*. The difference between the classical and quantum descriptions is akin to how a classical state can be represented by a point in a phasor diagram, while in a quantum state we can never simultaneously assign given values to q and p and the best we can do is to give a mean value (a point) surrounded by noise. The noise in the sideband modes will define the quantum properties of the state [Bachor 19].

In the case of a coherent state, which represents the most classical pure state of light, the noise is random and uncorrelated across all sidebands. It is important to distinguish between classical signals and noise: for a modulated coherent state, the *noise* is uncorrelated, while the *signals*, which are the coherent amplitudes in the sidebands, are perfectly correlated [Barbosa 20, Barbosa 13]. This is depicted in Fig. 2.2a.

It is interesting to investigate the case of a state that is more “quantum” than the coherent state, for instance the squeezed vacuum state. In such state, the sidebands exhibit correlated noise, as depicted in Fig. 2.2b. The quantum state of the $\pm\Omega$ sidebands in this case is an EPR-like entangled state

$$|\psi\rangle = |\text{EPR} : \Omega, -\Omega\rangle \quad (2.53)$$

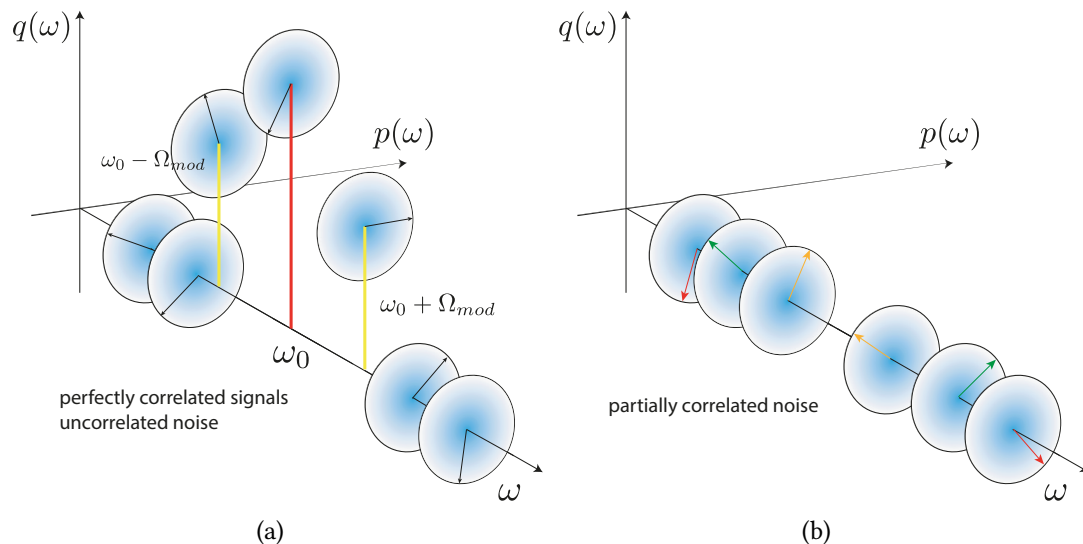


Figure 2.2: a) Sidebands description of an AM state, modulated at frequency Ω_{mod} . The emergence of correlated sidebands at $\pm\Omega_{mod}$ is expected also classically. In the quantum description, uncorrelated quantum noise is present at every frequency. b) Sidebands description of vacuum squeezed state. There is no coherent signal, but the noise in sidebands $\pm\Omega$ is partially correlated, depending on the squeezing level of the state. The correlations are EPR correlations (see Fig. 1.8, depicting correlations of the EPR state).

The closer this state is to an ideal EPR state, the bigger the squeezing value of the state [Zhang 03, Bachor 19].

2.3 Measurement of quantum states

In section 1.4.1, we emphasized that there is no inherently preferred basis for describing quantum states of light. Equivalently, we can employ photon-number states (a discrete-variable (DV) formalism), or opt for a continuous-variable (CV) description using quadratures of the field as our chosen observables. It is a common misconception to exclusively associate single photon states with DV and squeezed states with CV. However, a single photon state can be effectively described within a CV framework and, conversely, a squeezed state can be expanded in the Fock basis, as shown in Eq. 1.120. The underlying physics remains unchanged; it is merely a matter of selecting our preferred description. Nevertheless, when it comes to detection, a choice must be made. A DV description is favored when employing single-photon counters in the detection process, whereas a CV approach is more suitable when using a homodyne detector. In this work, our focus is on the latter, and in this section we will illustrate how to measure quadratures using homodyne

detection.

2.3.1 Intensity measure

The quantity of interest in the CV case is the photocurrent generated by photodetectors, that are hit by the beam of light we want to measure. The interaction of the photons with the semiconductor material of the photodetector liberates photoelectrons, depending on the quantum efficiency η_{det} , that is the ratio between liberated electrons per number of photons. Consequently, the photocurrent carries the information encoded in the incident light, which can then be analyzed using tools such as oscilloscopes or spectrum analyzers.

The intensity of the field is defined¹ as [Loudon 00]:

$$\hat{I}(\mathbf{r}, t) = 2\epsilon_0 n c \hat{E}^{(-)}(\mathbf{r}, t) \hat{E}^{(+)}(\mathbf{r}, t) \quad (2.54)$$

For a detector placed at $z = 0$, the generated photocurrent is given by:

$$\hat{i}(t) = R \int_S dS \int_{\mathbb{R}} d\tau r(\tau) I(x, y, t - \tau) \quad (2.55)$$

where the field intensity is integrated over the detector surface S and $r(\tau)$ is the impulse-response function of the detector. The responsivity of the detector R is defined as the ratio of the photocurrent to the power of the input beam and it is given by the formula:

$$R = \frac{qe\eta_{det}}{h\nu} \quad (2.56)$$

where q is the elementary charge and ν is the frequency of the incident photons. This expression can be simplified if we consider a single spatial mode contained in the detector surface and an instantaneous response function. Under these conditions, following the definition given in Eq. 2.54, we obtain:

$$\hat{i}(t) = q\eta_{det} \hat{a}^\dagger(t) \hat{a}(t) \quad (2.57)$$

This expression is consistent with what we expect: for perfect conversion efficiency $\eta_{det} = 1$, the photocurrent at time t is, trivially, the elementary charge multiplied by the number of photons detected at time t . Usually, we drop the elementary charge constant and we use, for simplicity, the dimensionless operator:

$$\hat{i}(t) = \hat{a}^\dagger(t) \hat{a}(t) \quad (2.58)$$

where here we assume $\eta_{det} = 1$.

In this framework, a light beam can be analyzed by measuring the photocurrent observable $\hat{i}(t)$ via direct detection, i.e. by using a single photodetector to measure the beam

¹For a polarized parallel light beam.

of interest. Referring to Eq. 2.58, and by splitting the creation and annihilation operators into their mean value and fluctuating terms as in Eq. 2.40, the photocurrent can be rewritten as:

$$\hat{i}(t) = \bar{\alpha}^2 + \bar{\alpha}\delta\hat{q}(t) \quad (2.59)$$

Fluctuations in the $\hat{q}(t)$ quadrature can then be directly measured by direct photodetection, as we have access to the term $\delta\hat{i}(t) = \bar{\alpha}\delta\hat{q}(t)$. In the literature $\hat{q}(t)$ is sometimes defined, for this reason, amplitude quadrature or in-phase quadrature, since intensity fluctuations are proportional to the mean field in the phasor representation. The $\hat{p}(t)$ quadrature, known as the phase quadrature, can be accessed by transforming phase information into amplitude information through interference with a reference beam, a concept we will explore in more detail later on.

We can discard the average term of the photocurrent, that yields a Dirac delta peak in $\Omega = 0$, and we define the quantity:

$$\hat{i}(\Omega) = \int \frac{dt}{\sqrt{2\pi}} e^{i\Omega t} \delta\hat{i}(t) = \bar{\alpha}\hat{q}_{FT}(\Omega) = \bar{\alpha} \left(\hat{a}^\dagger(-\Omega) + \hat{a}(\Omega) \right) \quad (2.60)$$

where, as usual, we omit the “ δ ” that indicates fluctuations in the Fourier space. This equation shows us that the spectral noise at a given frequency depends on the noise on the upper and lower sidebands, and it is proportional to the mean value of the detected light.

2.3.2 Noise spectrum and quantum noise

Fluctuations $\delta i(t)$ of the photocurrent can be measured in the temporal domain using an oscilloscope. Alternatively, we can also choose to investigate the properties and the quadrature statistics encoded in the photocurrent in the Fourier domain. The analysis of the photocurrent is carried out by analyzing the intensity noise spectrum, a plot of the noise as a function of Ω , the frequency relative to the carrier. More specifically, the quantity of interest is the power spectral density (or spectral noise power) of the photocurrent, which is defined as:

$$S(\Omega) = \lim_{T \rightarrow \infty} \frac{1}{T} \left| \int_{-T/2}^{T/2} \frac{dt}{\sqrt{2\pi}} i(t) e^{i\Omega t} \right|^2 \quad (2.61)$$

The Wiener-Khinchin theorem states that for a stationary process the power spectral density is equal to the Fourier transform of the autocorrelation function of the signal. The power spectral density $S(\Omega)$ can be rewritten as:

$$S(\Omega) = \int_{-\infty}^{\infty} \frac{d\tau}{\sqrt{2\pi}} \langle i(t)i(t+\tau) \rangle e^{i\Omega\tau} \quad (2.62)$$

where $\langle i(t)i(t+\tau) \rangle$ is the autocorrelation function of the photocurrent. The spectral noise power $S(\Omega)$ is the quantity obtained from the spectrum analyzer, and it measures the power

contained in a signal or noise at a specific frequency Ω relative to the carrier. Details on the useful relations and characteristics of the spectral noise power can be found in [Ansquer 22].

The spectral noise power captures not only the intensity fluctuations of the optical field (which include classical modulations, classical noise and quantum noise), but also the noise contribution of the electronics, such as amplifier noise, thermal noise, dark currents. To be able to detect fluctuations from the optical field, we require $\delta i_{el}(t) \ll \delta i_{opt}(t)$, where $\delta i_{el}(t)$ and $\delta i_{opt}(t)$ represent the photocurrent fluctuations arising from the electronics and from the optical field, respectively. The electronic noise can be easily evaluated by measuring the noise spectrum in the absence of input light.

According to classical physics, it could be in principle possible to transmit a signal using a modulated light beam without unwanted noise. However, we now understand that light intensity presents unavoidable fluctuations, *quantum noise*, prescribed by the laws of quantum physics [Gardiner 04]. Quantum noise emerges as an intrinsic feature in quadrature measurements due to the Heisenberg uncertainty principle governing non-commuting quadrature observables. This translates on a specific arrival time statistics of the photons, that is imprinted in the photocurrent. For a semi-classical coherent field, for example, the arrival times are random, resulting in a Poisson statistics. In such case, the quantum noise is called *shot noise*, and it is equivalent to the noise present in the vacuum. Shot noise power spectral density is independent of frequency, so that we can classify it as “white noise”. A more regular photon flux, such as the one of q -squeezed states of light, can result in photocurrent fluctuations below the shot noise. However, as already seen, going below the shot noise limit comes with a price, and the fluctuations in the conjugate quadrature are increased, so that we do not violate the Heisenberg uncertainty principle. We point out that quantum noise is not a consequence of the detection process, but it is an intrinsic feature of light itself.

Quantum noise is proportional to the intensity of the detected light, therefore it is useful to introduce a normalized version of the spectral noise power:

$$\tilde{S}(\Omega) = \frac{S(\Omega)}{S_{shot}(\Omega)} \quad (2.63)$$

where $S_{shot}(\Omega)$ is the “white noise” that corresponds to the power spectral density of the shot noise.

2.3.3 Homodyne detection in the temporal domain

Balanced homodyne detection [Yuen 83] is a measurement scheme widely used in quantum optics and quantum information experiments. This technique employs the interference on a 50:50 beam splitter between the signal beam (the light to be measured) and a local oscillator (LO) beam, which is usually a bright laser beam derived from the same source as the signal light; this ensures that the signal and the LO share the same classical noise characteristics.

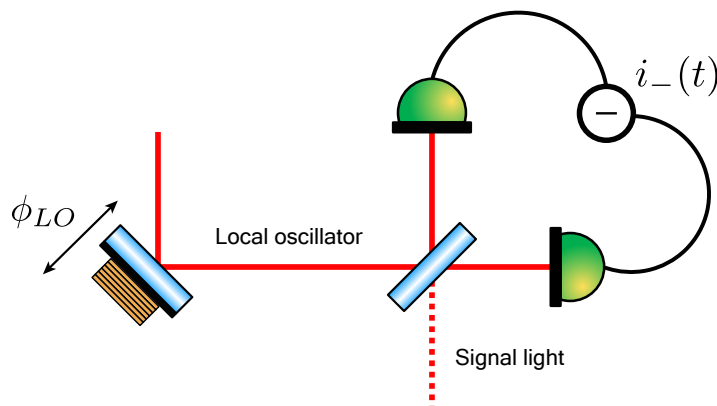


Figure 2.3: Homodyne detection scheme. The LO beam and the signal beam interfere on a 50:50 beam-splitter. The output beams are detected by two photodiodes and the resulting photocurrents are subtracted. The phase of the LO is typically adjusted using a piezoelectric actuator.

The result of this interference is two output beams, one from each output port of the beam splitter, that hit on two photodetectors, generating two photocurrents. These photocurrents are then subtracted from each other, producing the subtracted photocurrent, denoted as $i_-(t)$. A scheme of homodyne detection can be seen in Fig. 2.3.

Homodyne detection provides several practical advantages compared to direct detection. One of the primary advantages of this scheme is its ability to cancel out the classical noise of the LO, which is perfectly correlated in the two beams, as a consequence of the subtraction process. However, the quantum noise of the signal remains present in the subtracted current, as we will see shortly. Moreover, by changing the phase of the local oscillator we can also measure the phase quadrature of the signal light, which was not possible with direct detection, as shown in Eq. 2.59. Another interesting feature of balanced homodyne detection is that it constitutes a projective measurement of the signal light onto the LO mode. In practical terms, this allows us to selectively target the desired mode for measurement, even with highly multimode light sources, by sending it into the local oscillator beam.

We start by describing the transformation of the balanced beam-splitter on the annihilation operators of the two input beams, denoted as $\hat{a}(t)$ for the signal light and $\hat{a}_{LO}(t)$ for the LO light. The two output beams, directed towards photodetectors $D1$ and $D2$, can be expressed as:

$$\hat{a}_{D1}(t) = \frac{\hat{a}_{LO}(t) + \hat{a}(t)}{\sqrt{2}} \quad (2.64)$$

$$\hat{a}_{D2}(t) = \frac{\hat{a}_{LO}(t) - \hat{a}(t)}{\sqrt{2}} \quad (2.65)$$

From Eq. 2.58, we write the photocurrents generated by the two photodetectors as:

$$\hat{i}_{D1}(t) = \frac{1}{2} \left(\hat{a}_{LO}^\dagger \hat{a}_{LO} + \hat{a}^\dagger(t) \hat{a}(t) + \hat{a}_{LO}^\dagger(t) \hat{a}(t) + \hat{a}^\dagger(t) \hat{a}_{LO}(t) \right) \quad (2.66)$$

$$\hat{i}_{D2}(t) = \frac{1}{2} \left(\hat{a}_{LO}^\dagger \hat{a}_{LO} + \hat{a}^\dagger(t) \hat{a}(t) - \hat{a}_{LO}^\dagger(t) \hat{a}(t) - \hat{a}^\dagger(t) \hat{a}_{LO}(t) \right) \quad (2.67)$$

and the subtracted photocurrent $i_-(t)$ is obtained by subtracting the photodiodes photocurrents:

$$\hat{i}_-(t) = \hat{i}_{D1}(t) - \hat{i}_{D2}(t) = \hat{a}_{LO}^\dagger(t) \hat{a}(t) + \hat{a}^\dagger(t) \hat{a}_{LO}(t) \quad (2.68)$$

We assume a bright local oscillator of the form $\hat{a}_{LO}(t) = \alpha_{LO} + \delta \hat{a}(t)$. Here, $\alpha_{LO} = |\alpha_{LO}| e^{-i\phi_{LO}}$ and it is significantly larger than the other terms involved. We can then neglect all the terms except the ones proportional to α_{LO} and write:

$$\hat{i}_-(t) = |\alpha_{LO}| \left(e^{i\phi_{LO}} \hat{a}^*(t) + e^{-i\phi_{LO}} \hat{a}(t) \right) = |\alpha_{LO}| \hat{x}^{\phi_{LO}} \quad (2.69)$$

where $\hat{x}^{\phi_{LO}}$ is defined as the *rotated quadrature*. We note that the photocurrent is proportional to the LO amplitude, but the classical noise of the LO is canceled and does not affect the measurement. The fluctuating term of the photocurrent reads:

$$\delta \hat{i}_-(t) = |\alpha_{LO}| \left(e^{i\phi_{LO}} \delta \hat{a}^*(t) + e^{-i\phi_{LO}} \delta \hat{a}(t) \right) \quad (2.70)$$

or, in terms of quadratures:

$$\delta \hat{i}_-(t) = |\alpha_{LO}| (\cos \phi_{LO} \delta \hat{q}(t) + \sin \phi_{LO} \delta \hat{p}(t)) = |\alpha_{LO}| \delta \hat{x}^{\phi_{LO}}(t) \quad (2.71)$$

Tuning the phase of the local oscillator allows us to access the fluctuations in the $p(t)$ quadrature, which is not achievable through direct photocurrent detection, as seen in Eq. 2.59. We also note that the fluctuations are amplified by $|\alpha_{LO}|$.

The subtracted photocurrent, and specifically the generalized quadrature fluctuations $\delta \hat{x}^{\phi_{LO}}(t)$, can be analyzed using a time-resolving device, like an oscilloscope. However, the detector's response time is often insufficient to adequately resolve the mode of interest. To effectively resolve individual pulses of light, we require a detector whose bandwidth is comparable or higher than the repetition rate of the laser. In this work, a custom detector has been built, enabling us to access the quadrature fluctuations $\delta \hat{x}^{\phi_{LO}}(t)$ of individual light pulses [Kouadou 21].

2.3.4 Homodyne detection in the spectral domain

It is common to analyze the electronic spectrum $\hat{i}(\Omega)$ of the photocurrent to extract information about the noise statistics of a quantum state. This is particularly true in squeezing measurements, where the squeezing value is probed using a spectrum analyzer

at a specific electronic frequency $\Omega = \Omega_0$, often within the MHz range. This technique is very practical for directly measuring the squeezing value of a specific mode of light and it permits to get rid of unwanted sources of technical noise, such as drifts of the mean value of the photocurrent over time. However, analyzing photocurrents in the spectral domain has a significant limitation: the inability to fully reconstruct the quantum state. Despite this, we can still employ this technique to measure a specific class of quantum states. Indeed, this limitation is not problematic if the only quantity of interest is the noise variance of the state, as is the case for vacuum squeezed states.

The fluctuating term $\delta\hat{i}_-(t)$ in Eq. 2.71 can be analyzed in the Fourier space according to Eq. 2.60, and it reads:

$$\hat{i}(\Omega) = |\alpha_{LO}| \left(e^{i\phi_{LO}} \hat{a}^\dagger(-\Omega) + e^{-i\phi_{LO}} \hat{a}(\Omega) \right) \quad (2.72)$$

where we drop the “-” subscript in the subtracted photocurrent for notational simplicity. We note that the operators of both the upper and lower sidebands concur in defining the photocurrent in the spectral domain. The operator $\hat{i}(\Omega)$ is not self-adjoint, therefore, unlike $\hat{i}(t)$, it is not an observable¹. However, note that $\hat{i}^\dagger(\Omega) = \hat{i}(-\Omega)$. We define:

$$\hat{i}_+(\Omega) = \sqrt{2}\text{Re} [\hat{I}(\Omega)] \quad (2.73)$$

$$\hat{i}_-(\Omega) = \sqrt{2}\text{Im} [\hat{I}(\Omega)] \quad (2.74)$$

and we rewrite Eq. 2.72 as:

$$\hat{i}(\Omega) = \frac{|\alpha_{LO}|}{\sqrt{2}} (\hat{i}_+(\Omega) + i \cdot \hat{i}_-(\Omega)) \quad (2.75)$$

where $\hat{i}_+(\Omega)$ and $\hat{i}_-(\Omega)$ are observables, as they are self-adjoint by construction, being defined as the real and imaginary part of a complex-valued operator. Moreover, they commute, therefore they can be measured simultaneously. They can be rewritten as:

$$\hat{i}_+(\Omega) = \cos \phi \hat{q}_+(\Omega) + \sin \phi \hat{p}_+(\Omega) \equiv \hat{x}_+^\phi(\Omega) \quad (2.76)$$

$$\hat{i}_-(\Omega) = \cos \phi \hat{p}_-(\Omega) - \sin \phi \hat{q}_-(\Omega) \equiv \hat{x}_-^{\phi+\frac{\pi}{2}}(\Omega) \quad (2.77)$$

Here, we have defined the modes:

$$\hat{q}_\pm(\Omega) = \frac{\hat{q}(\Omega) \pm \hat{q}(-\Omega)}{\sqrt{2}} \quad (2.78)$$

$$\hat{p}_\pm(\Omega) = \frac{\hat{p}(\Omega) \pm \hat{p}(-\Omega)}{\sqrt{2}} \quad (2.79)$$

¹This can be surprising. Differently from $\hat{i}(t)$, $\hat{i}(\Omega)$ in general has complex eigenvalues. In particular, $\langle \hat{i}(\Omega) \rangle$ is complex, as $\langle \hat{i}(\Omega) \rangle \propto \int dt \langle \hat{i}(t) \rangle e^{i\Omega t}$. Physically, we cannot measure a complex number, but we can measure its real and imaginary part.

that are symmetric and asymmetric combination of sideband modes. In this context, $\hat{x}_+^\phi(\Omega)$ and $\hat{x}_-^{\phi+\frac{\pi}{2}}(\Omega)$ correspond to generalized quadratures of the symmetric and asymmetric modes. We emphasise two important points: firstly, the two generalized quadratures $\hat{x}_+^\phi(\Omega)$ and $\hat{x}_-^{\phi+\frac{\pi}{2}}(\Omega)$ commute allowing us to measure the real and imaginary parts of the photocurrent independently; it is evident that these quadratures cannot be rotated independently from each other since they share the same local oscillator and maintain a fixed phase difference of $\pi/2$. This implies that we can measure correlations of the type $\langle \hat{x}_+^\phi \hat{x}_-^{\phi+\frac{\pi}{2}} \rangle$ but we lack information about correlations like $\langle \hat{x}_+^\phi \hat{x}_-^\phi \rangle$. This inability to measure correlations among quadratures that differ from orthogonal ones results in the impossibility of gaining complete information about the quantum state using spectral homodyne detection.

In quantum squeezing experiments, we typically measure the spectral noise power, introduced in section 2.3.2, using a spectrum analyzer. In this case, the spectral noise power reads [Barbosa 13, Bachor 19, Zippilli 15]:

$$\begin{aligned} S(\Omega) &= \langle |\delta i(\Omega)|^2 \rangle = \frac{|\alpha_{LO}|^2}{2} (\langle i_+^2(\Omega) \rangle + \langle i_-^2(\Omega) \rangle) \\ &= \frac{|\alpha_{LO}|^2}{2} \left(\Delta^2 x_+^\phi(\Omega) + \Delta^2 x_-^{\phi+\frac{\pi}{2}}(\Omega) \right) \end{aligned} \quad (2.80)$$

In order to obtain this result, we made the assumption that $\Delta x_\pm^\phi = \langle x_\pm^\phi(\Omega)^2 \rangle$, which implies that the mean field of the sidebands, that cannot be measured with the spectrum analyzer, is zero. This assumption holds true in the case of a squeezed state. It is more common to refer to the normalized version of $S(\Omega)$, namely:

$$\tilde{S}(\Omega) = \frac{1}{2} \left(\Delta^2 x_+^\phi(\Omega) + \Delta^2 x_-^{\phi+\frac{\pi}{2}}(\Omega) \right) \quad (2.81)$$

From this equation we can see that, if the \pm modes are in the vacuum state (and, by consequence, the two $\pm\Omega$ sidebands are each in vacuum state as well), we recover shot noise $\tilde{S}(\Omega) = 1$, as expected. When we measure fluctuations below the shot noise, namely $\tilde{S}(\Omega) < 1$, Eq. 2.81 satisfies the Duan et al. criterion for inseparability [Duan 00]. According to this criterion, \hat{x}_+^ϕ and $\hat{x}_-^{\phi+\frac{\pi}{2}}$ are EPR-operators, meaning their variance is reduced. If, without loss of generality, we set the squeezing condition with the LO phase $\phi = 0$, we have that $\hat{x}_+^0 = \hat{q}_+$ and $\hat{x}_-^{\frac{\pi}{2}} = \hat{p}_-$ are operators that exhibit reduced variance. This means that entanglement is shared between the upper and lower sideband modes.

We note that the spectral noise power $S(\Omega)$ does not represent the variance of a well-defined field mode quadrature. Indeed, Eq. 2.81 merely tells us that $S(\Omega)$ can be calculated by adding the variances of the two well-defined quadratures \hat{x}_+^ϕ and $\hat{x}_-^{\phi+\frac{\pi}{2}}$. For $S(\Omega)$ to be the variance of a field quadrature, we need to infer the stationarity of the

process¹ [Zippilli 15, Barbosa 13]. Indeed, assuming a stationary photocurrent, we have additionally that:

$$\begin{cases} \Delta^2 x_+^\phi = \Delta^2 x_-^{\phi+\frac{\pi}{2}} \\ \langle \hat{x}_+^\phi \hat{x}_-^{\phi+\frac{\pi}{2}} \rangle = 0 \end{cases} \quad (2.82)$$

In such a case, the condition of $\tilde{S}(\Omega) < 1$ represents indeed the squeezing of a well-defined quadrature of the field, namely $\hat{x}_S^\phi = \hat{x}_+^\phi + \hat{x}_-^{\phi+\frac{\pi}{2}}$. In this case, we can write:

$$\tilde{S}(\Omega) = \Delta^2 x_S^\phi(\Omega) \quad (2.83)$$

and the spectral noise power can directly assess the squeezing or antisqueezing of the field quadrature $\hat{x}_S(\Omega)$. We assume, without loss of generality, squeezing for $\phi = 0$ and antisqueezing for $\phi = \pi/2$. In this case Eq. 2.82 becomes:

$$\begin{cases} \Delta^2 q_+ = \Delta^2 p_- = e^{-2r} \\ \Delta^2 p_+ = \Delta^2 q_- = e^{2r} \\ \langle \hat{q}_+ \hat{p}_- \rangle = \langle \hat{p}_+ \hat{q}_- \rangle = 0 \end{cases} \quad (2.84)$$

and

$$\Delta^2 (\hat{q}(\Omega) + \hat{q}(-\Omega)) = \Delta^2 (\hat{p}(\Omega) - \hat{p}(-\Omega)) = e^{-2r} \quad (2.85)$$

$$\Delta^2 (\hat{p}(\Omega) + \hat{p}(-\Omega)) = \Delta^2 (\hat{q}(\Omega) - \hat{q}(-\Omega)) = e^{2r} \quad (2.86)$$

where we recover explicitly EPR-like correlations between sidebands. We discover, then, that single-mode squeezing of the field in the time domain reveals two-mode squeezing or EPR correlations of the sideband modes.

Homodyne detection does not allow us to assess asymmetries between the two sidebands [Barbosa 13]. Assuming perfect symmetry between the sidebands, as in the case of the SPDC process, we obtain:

$$\Delta^2 q(\Omega) = \Delta^2 q(-\Omega) = \Delta^2 p(\Omega) = \Delta^2 p(-\Omega) = \frac{e^{-2r} + e^{2r}}{2} \quad (2.87)$$

Each sideband presents an excess of noise, as we expect from an entangled pair if we trace out one of the two subsystems [Zhang 03].

When we measure squeezing in the electronic frequency domain by observing spectral noise density below the shot noise ($S(\Omega) < 1$) we are actually measuring the EPR entanglement between the upper and lower sidebands at frequency Ω .

¹In the limit of large filtering times, the correlations of stationary field operators do not depend on time. This is due to the fact that the correlation function only depends on the time difference and it is symmetric (for extensive details on this point, see Appendix B of ref. [Zippilli 15]).

Chapter 3

Nonlinear optics

Contents

3.1	Introduction to nonlinear optics	60
3.1.1	The forced wave equation	60
3.1.2	Nonlinear polarization	62
3.1.3	Contracted notation	64
3.1.4	Nonlinear processes in KTP	64
3.2	Second-Harmonic Generation	66
3.2.1	SHG with a broadband field	66
3.2.2	Phase matching	67
3.2.3	Quasi-phase-matching	69
3.3	Parametric Down-Conversion	71
3.3.1	PDC with a broadband field	71
3.3.2	Eigenmodes of the PDC	73
3.3.3	Quantum treatment (SPDC)	74
3.3.4	Hamiltonian derivation	77

According to classical electrodynamics, light waves do not generally interact with each other. This is due to the linearity of the Maxwell equations, that forbids light-light interaction in vacuum. Today, consistently with the predictions of quantum electrodynamics (QED), light-by-light scattering has been observed in vacuum [Aaboud 17]. However, even while staying in a classical framework, we can exploit the nonlinear response of specific materials to introduce nonlinear terms to the Maxwell equations. This enables us to observe light-by-light interaction, mediated by the material, when the interacting fields are sufficiently strong.

Non-linear processes play an important role in photonic quantum technologies, where tailored media are used to produce quantum states of light. In particular, this work investigates and exploits second-order non-linearity in KTP to produce squeezed states. In this chapter we will briefly review the theory of second-order non-linear optics,

and we will focus on the processes of interest for our case, namely Second-Harmonic Generation (SHG) and Parametric Down-Conversion (PDC). We will follow the classical treatment of non-linear optics up to the point where it fails us: for Spontaneous Parametric Down-Conversion (SPDC), a quantum treatment is required, since the process is forbidden according to classical physics.

The main references used for this chapter are “Nonlinear Optics” by Boyd [Boyd 08] and “Ultrafast Optics” by Weiner [Weiner 11]. While [Boyd 08] is among the best-known references for an extensive treatise of non-linear optics, it focuses mainly on the Continuous-Wave (CW) case. In [Weiner 11] we can find more details on ultrafast non-linear processes.

3.1 Introduction to nonlinear optics

This section introduces the topic of nonlinear optics, providing the reader with the fundamental concepts needed to understand the underlying physics of the processes discussed in this work, all while avoiding to delve into intricate technical details. We start from the Maxwell equations and we gradually work our way through generalities on second-order nonlinear processes of our interest. We conclude by giving details on the processes occurring in KTP, the medium used for quantum light generation in this thesis work.

3.1.1 The forced wave equation

A nonlinear media is a material that responds in a nonlinear way to the strength of the applied optical field. To investigate the properties of the nonlinear processes that take place in a nonlinear media, we need first to go back to the very basics of electromagnetism: the Maxwell equations. It can be shown that to investigate the propagation of light in an optical medium we need to solve the equation:

$$\nabla \times \nabla \times \mathbf{E} + \frac{1}{c^2} \frac{\partial^2}{\partial t^2} \mathbf{E} = -\frac{1}{\epsilon_0 c^2} \frac{\partial \mathbf{P}}{\partial t^2} \quad (3.1)$$

that stems from the Maxwell equations and which is the most general form of the wave equation. Here, the polarization vector \mathbf{P} is the dipole moment induced by the light in the material per unit volume. The polarization vector can be separated into a linear and a nonlinear part, as $\mathbf{P} = \mathbf{P}_L + \mathbf{P}_{NL}$, that account respectively for a linear and a nonlinear response to the applied electric field. More details on this point will be given in the next section. Considering the identity $\nabla \times \nabla \times \mathbf{E} = \nabla (\nabla \cdot \mathbf{E}) - \nabla^2 \mathbf{E}$, we can further simplify this expression by neglecting $\nabla \cdot \mathbf{E}$. While this term is generally non vanishing in nonlinear optics, even in an isotropic material, in most cases the nonlinear polarization is weak, and

we can make the assumption $\nabla \cdot \mathbf{E} \sim 0$ [Weiner 11, Boyd 08]. We obtain then the expression:

$$\nabla^2 \mathbf{E} - \frac{1}{c^2} \frac{\partial^2}{\partial t^2} \mathbf{E} = \frac{1}{\epsilon_0 c^2} \frac{\partial \mathbf{P}}{\partial t^2} \quad (3.2)$$

that can alternatively be rewritten as:

$$\nabla^2 \mathbf{E} - \frac{1}{\epsilon_0 c^2} \frac{\partial^2}{\partial t^2} \mathbf{D}^{(1)} = \frac{1}{\epsilon_0 c^2} \frac{\partial \mathbf{P}_{NL}}{\partial t^2} \quad (3.3)$$

where $\mathbf{D}^{(1)}$ is the linear part of the electric displacement tensor $\mathbf{D} = \epsilon_0 \mathbf{E} + \mathbf{P} = \mathbf{D}^{(1)} + \mathbf{P}_{NL}$. This wave equation is often solved in the literature considering the simpler propagation in an isotropic and homogeneous medium. The isotropic condition is not always satisfied in nonlinear optics applications. This is because the anisotropy of the medium is often employed to achieve the so-called phase-matching, a necessary condition to generate constructive build-up of the nonlinear field, that will be explored in section 3.2.2 and 3.2.3. For anisotropic media, the linear part of the electric displacement field $\mathbf{D}^{(1)}$ reads:

$$\mathbf{D}^{(1)} = \boldsymbol{\epsilon}^{(1)} \mathbf{E} \quad (3.4)$$

where $\boldsymbol{\epsilon}^{(1)}$ is the dielectric permittivity tensor. For isotropic media, $\boldsymbol{\epsilon}^{(1)}$ reduces to a scalar quantity. The basis in which $\boldsymbol{\epsilon}^{(1)}$ is diagonal identifies the principal dielectric axes of the crystals¹. If the electric field is polarized along one of these axes, the material can be treated, for practical purposes, as isotropic [Dubreuil]. We will see later that, given the nonlinear processes and medium that we use in this work, we will be in this condition. When this condition is not satisfied, a dependence on the so-called *walk-off* angle between the \mathbf{D} and \mathbf{E} fields appears in the nonlinear wave equation [Weiner 11, Dubreuil].

We assume that the field propagates in the z direction and that it satisfies the *slowly varying envelope approximation*, where we consider that the envelope of the field $\alpha(z, t)$ varies slowly with respect to the wavelength scale:

$$\left| \frac{\partial^2 \alpha}{\partial z^2} \right| \ll k \left| \frac{\partial \alpha}{\partial z} \right| \quad \text{and} \quad \left| \frac{\partial \alpha}{\partial z} \right| \ll k |\alpha| \quad (3.5)$$

Carrying out the calculations in the frequency domain, we reach a scalar equation that must be satisfied for every polarization of the field:

$$\boxed{\frac{\partial A(z, \omega)}{\partial z} = \frac{i\omega}{2\epsilon_0 n c} P_{NL}^{(+)}(z, \omega) e^{-ik(\omega)z}} \quad (3.6)$$

¹In general, there is a distinction between dielectric axes and crystallographic axes, as the latter identify geometric properties of the crystal. In many nonlinear crystals, like the KTP crystal that we use in this work, they coincide [Dmitriev 14].

where the field amplitude is rewritten as $A(z, \omega) = \mathcal{E}_\omega \alpha(z, \omega)$ to include the field constant \mathcal{E}_ω and where $\mathbf{P}_{NL}^{(+)}(z, \omega)$ is the Fourier transform of the analytic signal of the non linear polarization vector. Details on the derivation of the equation can be found in [Dubreuil, Medeiros de Araujo 12, Grynberg 10, Weiner 11]. This equation shows that a field at frequency ω can be driven by the nonlinear source term $\mathbf{P}_{NL}(z, \omega)$, under the appropriate conditions that we will investigate.

3.1.2 Nonlinear polarization

We can express the induced polarization as:

$$\mathbf{P}(\mathbf{r}, t) = \epsilon_0 \left[\chi^{(1)} \mathbf{E}(\mathbf{r}, t) + \chi^{(2)} \mathbf{E}^2(\mathbf{r}, t) + \chi^{(3)} \mathbf{E}^3(\mathbf{r}, t) + \dots \right] \quad (3.7)$$

where ϵ_0 is the permittivity of free space and $\chi^{(n)}$ is the n-th order nonlinear susceptibility. In the general case, $\chi^{(n)}$ is a $(n + 1)$ rank tensor and in general it is complex and it depends on the frequencies of the interacting fields. Only for a lossless and dispersionless medium, $\chi^{(n)}$ is real and does not depend on the frequencies of the fields; in the time domain, this translates into an instantaneous response of the material. While nonlinear crystals are in general dispersive media, in the case where the frequencies of the fields are way smaller than the electronic absorption resonance frequency of the material we can consider the nonlinear susceptibility as dispersionless. Moreover, if we are below the electronic absorption range (typically in the UV) and above the vibrational resonances of the lattice (typically in the infrared region), we can treat the material as transparent. This allows for full permutational symmetry of the indices of the $\chi^{(n)}$ tensor, a condition known as *Kleinman symmetry*.

It is convenient to treat the nonlinear polarization and the process in the Fourier space, as we deal with broadband fields. Analogously to the definitions in Eqs. 1.4 and 1.5 for the electric field $\mathbf{E}(\mathbf{r}, t)$, we define the Fourier transform of the polarization vector and its inverse:

$$\mathbf{P}(\mathbf{r}, t) = \int_{\mathbb{R}} \frac{d\omega}{\sqrt{2\pi}} \mathbf{P}(\mathbf{r}, \omega) e^{-i\omega t} \quad (3.8)$$

$$\mathbf{P}(\mathbf{r}, \omega) = \int_{\mathbb{R}} \frac{d\omega}{\sqrt{2\pi}} \mathbf{P}(\mathbf{r}, t) e^{i\omega t} \quad (3.9)$$

and we can also define the analytic signal $\mathbf{P}^{(+)}(\mathbf{r}, t)$, where all the definitions and properties are equivalent to those introduced for the electric field in section 1.1.1. In the following, we drop the spatial dependence \mathbf{r} for simplicity.

In our experiment we work only with second-order nonlinear processes, driven by the $\chi^{(2)}$ term. From Eq. 3.7, rewritten in compact notation, where the sum over the indices is implicit, we will then be interested in the generation of fields driven by the nonlinear term:

$$P_i(t) = \epsilon_0 \chi_{ijk}^{(2)} E_j(t) E_k(t) \quad (3.10)$$

where we dropped the NL subscript. Higher-order nonlinearities have a negligible effect and are out of the scope of this thesis. The indices ijk in Eq. 3.10 represent the principal or dielectric axes of the nonlinear crystal. Depending on the notational choice, they will be indicated equivalently as $i, j, k \in \{x, y, z\}$ or as $i, j, k \in \{1, 2, 3\}$. The linear susceptibility $\chi_{ij}^{(1)}$ is diagonal in the same frame of the dielectric tensor and the two are linked by the relation:

$$\boldsymbol{\epsilon}^{(1)} = \epsilon_0(\mathbb{1} + \boldsymbol{\chi}^{(1)}) \quad (3.11)$$

We rewrite Eq. 3.10 in the frequency domain by substituting the fields with their expansion as:

$$P_i(t) = \epsilon_0 \int_{\mathbb{R}} \chi_{ijk}^{(2)} E_j(\omega_1) E_k(\omega_2) e^{i(\omega_1 + \omega_2)t} \frac{d\omega_1}{\sqrt{2\pi}} \frac{d\omega_2}{\sqrt{2\pi}} \quad (3.12)$$

so that the Fourier transform of $P_i(t)$ reads:

$$P_i(\omega) = \epsilon_0 \int_{\mathbb{R}} \chi_{ijk}^{(2)} E_j(\omega_1) E_k(\omega_2) e^{-i(\omega_1 + \omega_2 - \omega)t} \frac{d\omega_1}{\sqrt{2\pi}} \frac{d\omega_2}{\sqrt{2\pi}} \frac{dt}{\sqrt{2\pi}} = \quad (3.13)$$

$$\epsilon_0 \int_{\mathbb{R}} \chi_{ijk}^{(2)} E_j(\omega_1) E_k(\omega_2) \delta(\omega_1 + \omega_2 - \omega) \frac{d\omega_1 d\omega_2}{\sqrt{2\pi}} \quad (3.14)$$

where the delta of Dirac accounts for the energy conservation that must hold between the frequencies of the interacting fields.

The processes that can be triggered are: second harmonic generation (SHG), sum-frequency generation (SFG), difference frequency generation (DFG, also known as *parametric amplification* [Boyd 08] or *parametric down-conversion* (PDC)) and optical rectification. In particular sum frequency generation (or SHG in the case of degenerate frequencies) can be described by the process:

$$P_i(\omega) = \epsilon_0 \chi_{ijk}^{(2)} \int_{\mathbb{R}} E_j(\omega') E_k(\omega - \omega') \frac{d\omega'}{\sqrt{2\pi}} \quad (3.15)$$

that has been derived from Eq. 3.14 by integrating over ω_2 and renaming ω_1 as ω' .

In a similar way we can find the driving nonlinear polarization for the DFG process. From Eq. 3.14, by performing the change of variable $\omega_2 \rightarrow -\omega_2$ and by integrating over ω_1 and renaming ω_2 as ω' , remembering that $E(-\omega) = E^*(\omega)$, we can calculate the nonlinear polarization Fourier transform for DFG:

$$P_i(\omega) = \epsilon_0 \chi_{ijk}^{(2)} \int_{\mathbb{R}} E_j(\omega + \omega') E_k^*(\omega') \frac{d\omega'}{\sqrt{2\pi}} \quad (3.16)$$

The nonlinear polarization $\mathbf{P}(\omega)$ will generate a field of frequency ω in the direction of the polarization vector, as prescribed by the Helmholtz equation.

3.1.3 Contracted notation

The second order nonlinear susceptibility $\chi^{(2)} = \chi_{ijk}^{(2)}$ is a tensor of 27 elements. We can, however, exploit some symmetries to reduce the number of elements. Indeed, as already mentioned, if the material is lossless (transparent) and the nonlinear susceptibility is dispersionless, we recover the Kleinman symmetry condition. We define the tensor:

$$d_{ijk} = \frac{1}{2}\chi_{ijk}^{(2)} \quad (3.17)$$

When the Kleinman symmetry is valid, d_{ijk} is symmetric in the last two indices. We can then introduce a mapping $jk \rightarrow l$ following the convention:

$$\begin{array}{l} jk : 11 \ 22 \ 33 \ 23, 32 \ 13, 31 \ 12, 21 \\ l : 1 \ 2 \ 3 \ 4 \ 5 \ 6 \end{array} \quad (3.18)$$

and, applying the remaining constraints of the Kleinman symmetry condition, we find that the nonlinear process can be described by the matrix:

$$d_{ij} = \begin{pmatrix} d_{11} & d_{12} & d_{13} & d_{14} & d_{15} & d_{16} \\ d_{16} & d_{22} & d_{23} & d_{24} & d_{14} & d_{12} \\ d_{15} & d_{24} & d_{33} & d_{23} & d_{13} & d_{14} \end{pmatrix} \quad (3.19)$$

reducing the nonlinear parameters from 27 to 10 [Boyd 08].

3.1.4 Nonlinear processes in KTP

In this work, we use a Potassium Tytanil Phosphate (KTiOPO₄, known as KTP) crystal. In this section we will investigate which parametric processes are permitted in KTP, according to its nonlinear susceptibility tensor. For KTP, the matrix of equation 3.19 reads:

$$d_{ij} = \begin{pmatrix} 0 & 0 & 0 & 0 & 2.02 & 0 \\ 0 & 0 & 0 & 3.75 & 0 & 0 \\ 2.02 & 3.75 & 15.4 & 0 & 0 & 0 \end{pmatrix} \quad (3.20)$$

as shown in [Pack 04]¹. From this matrix we gain all the relevant information on the type of nonlinear processes permitted in KTP. We write again Eq. 3.15 substituting $\chi_{ijk}^{(2)}$ with the notation d_{ijk} , that we will later contract, and rewriting explicitly the sum:

$$P_i(\omega) = \epsilon_0 \sum_{jk} 2d_{ijk} \int_{\mathbb{R}} E_j(\omega') E_k(\omega - \omega') \frac{d\omega'}{\sqrt{2\pi}} \quad (3.21)$$

¹In the article, they measured separately the coefficients $d_{31} = 2.12$ pm/V and $d_{15} = 2.02$ pm/V, without assuming a priori Kleinmann symmetry. Here, we reported the matrix with $d_{31} = d_{15}$.

This equation has been derived from SHG, but the considerations that follow can be equivalently applied for PDC. We rewrite the equation for $P_i(\omega)$, explicitly for the three cartesian indices, for the case of KTP:

$$P_x(\omega) = 2\epsilon_0 d_{15} \int_{\mathbb{R}} (E_x(\omega')E_z(\omega - \omega') + E_z(\omega')E_x(\omega - \omega')) \frac{d\omega'}{\sqrt{2\pi}} \quad (3.22)$$

$$P_y(\omega) = 2\epsilon_0 d_{24} \int_{\mathbb{R}} (E_y(\omega')E_z(\omega - \omega') + E_z(\omega')E_y(\omega - \omega')) \frac{d\omega'}{\sqrt{2\pi}} \quad (3.23)$$

$$P_z(\omega) = 2\epsilon_0 \int_{\mathbb{R}} (d_{15}E_x(\omega')E_x(\omega - \omega') + d_{24}E_y(\omega')E_y(\omega - \omega') + d_{33}E_z(\omega')E_z(\omega - \omega')) \frac{d\omega'}{\sqrt{2\pi}} \quad (3.24)$$

where we carried out the summation \sum_{jk} , contracting d_{ijk} following the rules of section 3.1.3 and considering the null entries of 3.20.

These equations contain all the information about the permitted processes in our KTP crystal and the corresponding nonlinearities. It is important to correctly identify the axes of the crystal, and to specify how they relate to the propagation direction of the electric field and its polarization. In our case we have a x -cut KTP crystal, where the term “ x -cut” means that the propagation of the beam is along the x -axis of the crystal. To avoid confusion, we point out that in this thesis, as in most books of optics, we chose the propagation axis as the z -axis in our cartesian lab frame, indicating the propagation term of the beam by the exponential e^{ikz} . This doesn't have to be confused with the jk dielectric axes of the crystal: in principle, the lab frame and the dielectric frame of the crystal have no connection. In our case, the beam propagates along the z -axis in the lab frame, which corresponds to the x -axis of the dielectric frame of the crystal, being the crystal x -cut. The subscript jk of the electric fields will tell us along which axis, in the dielectric frame, the field is polarized.

We start by reviewing Eq. 3.22. This process describes a nonlinear polarization field (and generated field) polarized along the crystal x -axis. However, in our case the crystal x -axis corresponds to the propagation axis of the field, as said above, so that we cannot exploit this process in our experiment. Eq. 3.23 describes the generation of a field polarized along the y -axis of the crystal. This field can be driven by an electric field that is polarized at 45° with respect to the y and z axis of the crystal and the process is mediated by the nonlinear coefficient d_{24} . This is known as *type-II* process, for both SHG and PDC, and it is characterized by the fact that the fundamental (lower frequency) fields in the equation have orthogonal polarizations. Finally, we can explore in detail Eq. 3.24, for the generation of a field polarized along the z -axis of the crystal. Such field can be driven in three different ways: by fields polarized along the crystal x -axis and mediated by d_{15} , by fields polarized along the crystal y -axis and mediated by d_{24} and by fields polarized along the crystal z -axis and mediated by d_{33} . The first option is not viable for us for the same reasons mentioned for Eq. 3.22, i.e. it involves a field polarized along the propagation axis. The second option

is known as *type-I* process: the fundamental fields share the same polarization, while the polarization of the harmonic field is orthogonal to the one of the fundamental fields. Finally, the third option is the most interesting for us, as it is driven by the d_{33} coefficient that turns out to be the most nonlinear, with $d_{33} = 15.4$ pm/V. The corresponding nonlinear process is known as *type-0* process: all the beams are polarized along the z -axis of the crystal. This is the process we decided to exploit for squeezing generation.

Some final comments are due regarding SPDC, whose details will be given in the next sections. Both in type-0 and in type-I processes the signal and idler beams share the same polarization. If the output beams are also collinear, this process is degenerate, and it drives a single-mode squeezing Hamiltonian. However, as type-I is less nonlinear than type-0, it is uninteresting for practical purposes in our experiment. The type-II process drives a two-mode squeezing Hamiltonian and, while less nonlinear than type-0, it has some interesting features and a positive trade-off to compensate the lower nonlinearity [Roman-Rodriguez 21].

3.2 Second-Harmonic Generation

While generalities on second-order processes have been given in the previous sections, here we aim to focus on Second-Harmonic generation (SHG), a degenerate case of Sum-Frequency Generation (SFG). SHG is commonly described as a process in which a lower frequency field at ω_1 drives the generation of a higher frequency field at $2\omega_1$. However, when we deal with broadband fields, we need to consider both the spectral characteristics of the driving field and the properties of the nonlinear crystal in order to determine the characteristics of the generated second-harmonic field. In this section, we examine the SHG process in the context of broadband fields and we give details on the constraints that the nonlinear crystal must satisfy in order to efficiently mediate the SHG process. Extensive details can be found in [Weiner 11].

3.2.1 SHG with a broadband field

Reintroducing the spatial dependence and recalling that $E^{(+)}(z, \omega) = A(z, \omega)e^{ik(\omega)z}$, where $A(z, \omega)$ includes the field constant \mathcal{E}_0 , we rewrite Eq. 3.15, in the analytic signal form, as

$$P_i^{(+)}(z, \omega) = \epsilon_0 \chi_{ijk}^{(2)} \int_{\mathbb{R}} A_j(z, \omega') A_k(z, \omega - \omega') e^{i(k(\omega') + k(\omega - \omega'))z} \frac{d\omega'}{\sqrt{2\pi}} \quad (3.25)$$

For notational simplicity, we can now set the polarization of the fields and focus on one specific allowed process. In our case it will be $P_z(2\omega)$ driven by $E_z(\omega)E_z(\omega)$ and the corresponding nonlinear coefficient, that we indicate as $\chi^{(2)} = 2d_{eff}$, where d_{eff} is the effective coefficient that mediates the process. In the case of a type-0 process in KTP, we

have $d_{eff} = d_{33}$ (see section 3.1.4). We can then drop the ijk subscript. The nonlinear polarization $P^{(+)}(z, \omega)$ acts as a driving term in Eq. 3.6, such that:

$$\frac{\partial A_{2\omega}(z, \omega)}{\partial z} = \frac{i\omega_0}{n_{2\omega}c} \chi^{(2)} \int_{\mathbb{R}} A_{\omega}(z, \omega') A_{\omega}(z, \omega - \omega') e^{i\Delta k(\omega, \omega')z} \frac{d\omega'}{\sqrt{2\pi}} \quad (3.26)$$

where we have set $\omega \sim 2\omega_0$ in the multiplicative factor and where:

$$\Delta k(\omega, \omega') = k_{\omega}(\omega') + k_{\omega}(\omega - \omega') - k_{2\omega}(\omega) \quad (3.27)$$

is the *phase mismatch*. The 2ω and ω subscripts are used to specify if we are dealing with the fundamental or the harmonic field, as “pump” and “signal” might be misleading, as they are interchanged depending on the type of process we are looking at (SHG or PDC).

In the undepleted pump regime, $A_{\omega}(z, \omega') = A_{\omega}(\omega')$, leaving the complex exponential as the only term that depends on z . Considering a propagation in a medium of length L ¹, the generated field at the output of the nonlinear medium reads:

$$A_{2\omega}(\omega) = \frac{i\omega_0 L}{n_{2\omega}c} \chi^{(2)} \int_{\mathbb{R}} A_{\omega}(\omega') A_{\omega}(\omega - \omega') \text{sinc}\left(\frac{\Delta k(\omega, \omega')L}{2}\right) \frac{d\omega'}{\sqrt{2\pi}} \quad (3.28)$$

This equations accounts for dispersion. We define:

$$\Phi(\omega', \omega) = \text{sinc}\left(\frac{\Delta k(\omega, \omega')L}{2}\right) \quad (3.29)$$

and we call it *phase-matching function*.

3.2.2 Phase matching

We have seen in the previous sections how the nonlinear polarization can, in principle, drive a field with different frequency components than the ones of the original pump field. Nevertheless, the efficiency of the nonlinear process is not guaranteed. Indeed, the nonlinear polarization field is driven by the fundamental field, and as a consequence they share the same phase velocity, determined by the refractive index at the fundamental frequency $n(\omega_0)$. However, the generated SHG wave travels at a phase velocity prescribed by the index $n(2\omega_0)$. In most cases, $n(2\omega_0)$ is greater than $n(\omega_0)$, due to chromatic dispersion; consequently, after a certain propagation length, known as *coherence length*, the two fields cumulate a phase difference of π . This causes destructive interference, and the power starts to flow back into the fundamental field. The generated SHG field fluctuates periodically and never builds up.

¹The integration is performed between $-L/2$ and $L/2$. Integrating between 0 and L can also be done, but in this case an overall phase factor $e^{\frac{i\Delta kL}{2}}$, that is sometimes found in some of the literature, appears.

For the process to be efficient, a proper phase condition between the pump field and the nonlinear polarization needs to be ensured, in order for the generated field to interact constructively and to build-up coherently throughout the crystal. This condition is known as *phase-matching* condition. In order to achieve perfect phase matching, we have to fulfil

$$\Delta k = 0 \quad (3.30)$$

where $\Delta k = k_1 + k_2 - k_3$ (eventually up to a sign, depending on the process) is the wavevector mismatch among three interacting waves, where $\omega_3 = \omega_1 + \omega_2$. We rewrite here the wavevector mismatch already given in Eq. 3.27:

$$\Delta k(\omega, \omega') = k_\omega(\omega') + k_\omega(\omega - \omega') - k_{2\omega}(\omega) \quad (3.31)$$

Dealing with broadband fields, is it clear that we cannot achieve $\Delta k(\omega, \omega') = 0$ for every frequency component present in our fields. We thus ask for the condition to be fulfilled for the central frequencies ω_0 and $2\omega_0$ and we expand the wavevector mismatch at first order, neglecting higher order terms, to investigate how the function behaves around these frequencies¹. The phase mismatch at first order reads:

$$\Delta k(\omega) = 2k_\omega(\omega_0) - k_{2\omega}(2\omega_0) + \left(\left. \frac{\partial k_\omega}{\partial \omega} \right|_{\omega_0} - \left. \frac{\partial k_{2\omega}}{\partial \omega} \right|_{2\omega_0} \right) (\omega - 2\omega_0) + \mathcal{O} \left(\frac{\partial^2 k}{\partial \omega^2} \right) \quad (3.32)$$

The condition $\Delta k_0 = 0$, where $\Delta k_0 = 2k_\omega(\omega_0) - k_{2\omega}(2\omega_0)$, guarantees perfect phase matching for the central frequencies $2\omega_0$ and ω_0 . As we have a broadband field, being in the pulsed regime, we need now to look at the first order. Assuming perfect phase matching for the central frequencies and neglecting higher-order dispersion terms, we obtain:

$$\Delta k(\omega) = \left(\left. \frac{\partial k_\omega}{\partial \omega} \right|_{\omega_0} - \left. \frac{\partial k_{2\omega}}{\partial \omega} \right|_{2\omega_0} \right) (\omega - 2\omega_0) = \left(\frac{1}{v_g(\omega_0)} - \frac{1}{v_g(2\omega_0)} \right) (\omega - 2\omega_0) \quad (3.33)$$

where v_g indicates the group velocity. If we consider only the first-order term we can see that the phase mismatch depends only on ω . Eq. 3.28 then becomes:

$$A_\omega(\omega) = \frac{i\omega_0 \chi^{(2)} L}{n_{2\omega} c} F(\omega) \cdot \Phi(\omega) \quad (3.34)$$

where $F(\omega)$ is the self-convolution of the fundamental field. We see from this equation that the effect of the phase-matching function is that of a spectral filter acting on the second-harmonic field driven by the nonlinear polarization, “cutting out” frequencies that potentially the nonlinear polarization could drive.

¹Recall that the term $k_\omega(\omega - \omega')$ in the Taylor expansion gives contributions $\left. \frac{\partial k_\omega(\omega - \omega')}{\partial \omega} \right|_{\omega_0} (\omega - 2\omega_0) + \left. \frac{\partial k_\omega(\omega - \omega')}{\partial \omega'} \right|_{\omega_0} (\omega' - \omega_0)$. We can define $\Omega = \omega - \omega'$ so that $\frac{\partial k_\omega(\Omega)}{\partial \omega} = \frac{\partial k_\omega(\Omega)}{\partial \Omega} \frac{\partial \Omega}{\partial \omega}$ and $\frac{\partial k_\omega(\Omega)}{\partial \omega'} = \frac{\partial k_\omega(\Omega)}{\partial \Omega} \frac{\partial \Omega}{\partial \omega'}$. As $\frac{\partial \Omega}{\partial \omega} = 1$ and $\frac{\partial \Omega}{\partial \omega'} = -1$ and as the derivative with respect to a point can be redefined with whichever variable, i.e. $\frac{\partial k(\Omega)}{\partial \Omega} = \frac{\partial k(\omega)}{\partial \omega}$, we can rewrite the first order as $\left. \frac{\partial k_\omega(\omega)}{\partial \omega} \right|_{\omega_0} (\omega - 2\omega_0) - \left. \frac{\partial k_\omega(\omega)}{\partial \omega} \right|_{2\omega_0} (\omega' - \omega_0)$, where the second term will be canceled out by the first order of $k_\omega(\omega')$.

3.2.3 Quasi-phase-matching

Achieving the phase-matching condition for central frequencies is not trivial. For instance, for SHG, perfect phase matching with collinear beams requires:

$$n(\omega_0) = n(2\omega_0) \quad (3.35)$$

as a consequence of Eq. 3.30. However, in materials with normal dispersion, $n(\omega)$ is a monotone function of ω . We then have to resort to particular techniques to achieve the phase-matching conditions,

One of the most commonly used techniques is called *birefringent phase matching*, where we exploit the birefringence property of a crystal. Birefringence is a material's ability to refract light differently based on its polarization. In birefringent crystals, two orthogonal polarization components (called "e" and "o" in the literature) propagate with different refractive indices. This condition is exploited so that the fundamental and the SHG field have the same refractive index. This leads to a linear buildup of the SHG field amplitude and a quadratic buildup of the intensity. Birefringent phase matching can be very effective, but it has some drawbacks. First of all, it doesn't permit type-0 processes, which could give access to a higher nonlinearity, as in the case of KTP. Indeed, having all fields polarized along the same direction does not permit us to exploit the birefringence property. Moreover, birefringency can give rise to spatial walk-off, as the two polarization component propagate at different angles due to their differing refractive indices, leading to spatial separation. Lastly, the material's birefringence may not be sufficient to attain phase matching. In the case of KTP, the phase-matching range for the fundamental field wavelength is 984nm ~ 3400nm. In our case, being the fundamental wavelength $\lambda_0 = 795$ nm, we cannot exploit birefringent phase matching in KTP. To achieve phase matching, we have to resort to another technique, known as *quasi-phase-matching*.

Quasi-phase matching is alternatively used to achieve phase matching [Fejer 92]. Instead of equating the refractive indices of the fields to satisfy Eq. 3.35, this technique involves flipping the sign of the nonlinear coefficient at multiples of the coherence length, with the effect of resetting the π phase that had been cumulating during the propagation. We define a nonlinear effective coefficient dependent on the spatial coordinate:

$$d(z) = d_{eff} \cdot g(z) \quad (3.36)$$

where $|g(z)| \leq 1$. In the case of a periodic modulation, called *periodic poling*, we can decompose $g(z)$ into its Fourier components:

$$g(z) = \sum_{m=-\infty}^{\infty} G_m e^{iK_m z} \quad (3.37)$$

where the m-th harmonics reads:

$$K_m = \frac{2\pi m}{\Lambda} \quad (3.38)$$

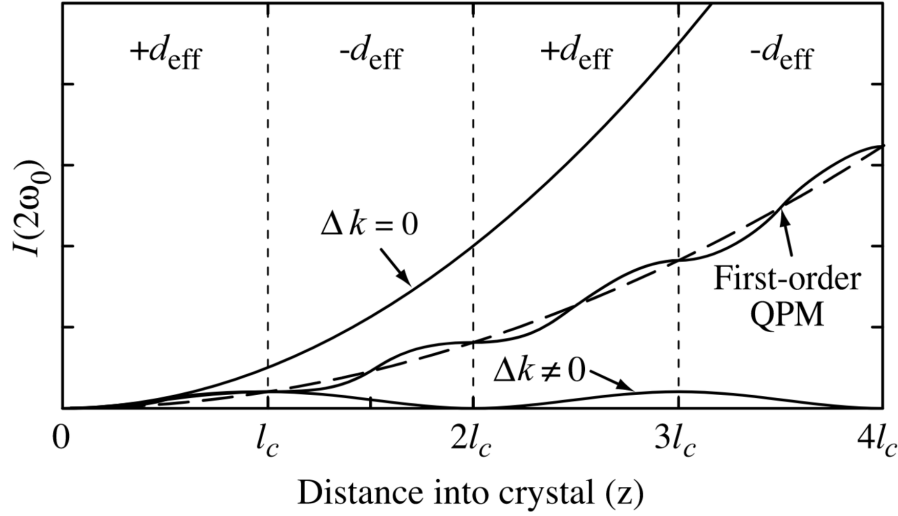


Figure 3.1: Intensity of the SHG as a function of z , the propagation distance into the crystal. The case of perfect birefringent phase matching, first-order quasi-phase-matching and a non-phase-matched crystal is shown. Note that the poling period is $\Lambda = 2l_c$, where l_c is the coherence length. Picture from [Weiner 11].

We redefine the phase-mismatch vector as:

$$\Delta k'(\omega, \omega') = \Delta k(\omega, \omega') + \frac{2\pi m}{\Lambda} \sim 0 \quad (3.39)$$

where $\Delta k(\omega, \omega')$ is the phase-mismatch defined in Eq. 3.31. In order to achieve quasi-phase matching for the central frequencies, one of the harmonics must satisfy:

$$\Delta k'_0 = \Delta k_0 + \frac{2\pi m}{\Lambda} \sim 0 \quad (3.40)$$

so that its contribution dominates the integral over the crystal length. We start from Eq. 3.26 and we replace $\chi^{(2)} = 2d_{eff}$ with $2d(z)$. Assuming $\Delta k'_0 = 0$ for the m -th harmonic and non depletion of the pump, and considering only the first-order contribution of the phase mismatch $\Delta k'(\omega', \omega)$, we can write:

$$A_{2\omega}(\omega) = \frac{i\omega_0 \chi^{(2)} L}{n_{2\omega} c} F(\omega) G_m \Phi'(\omega) \quad (3.41)$$

where $\Phi'(\omega)$ is the phase-matching function from Eq. 3.29, but redefined with $\Delta k'(\omega', \omega)$. In the case where the first harmonic ($m = \pm 1$) dominates, we talk about first-order quasi-phase-matching. When $g(z)$ equals 1 for one half of the crystal's length and -1

for the other half, the Fourier coefficients take the value $G_m = 2/m\pi$ for m odd and $G_m = 0$ for m even. Comparing this last equation with Eq. 3.34 obtained for perfect phase matching, we notice that quasi-phase-matching is less efficient, as it is attenuated by the factor G_m . Moreover, the highest the order of the phase matching, the lower the efficiency. The comparison between birefringent phase matching, quasi-phase-matching and non-phase-matched generation is shown in Fig. 3.1.

In the case of first-order quasi-phase-matching, Eq. 3.40 is written as:

$$\Delta k'_0 = \frac{2\omega_0}{c} (n_{2\omega}(2\omega_0) - n_\omega(\omega_0)) - \frac{2\pi}{\Lambda} \sim 0 \quad (3.42)$$

and to achieve phase-matching the poling period of the crystal must be engineered to be:

$$\Lambda = \frac{\pi c}{\omega_0} (n_{2\omega}(2\omega_0) - n_\omega(\omega_0)) \quad (3.43)$$

In section 4.4 we will investigate the characteristics of the SHG light using quasi-phase matched ppKTP.

3.3 Parametric Down-Conversion

Parametric down-conversion is a second-order nonlinear process that lies at the heart of many quantum applications, as it is exploited experimentally for the generation of squeezed states of light, entangled states and single-photons. It involves the interaction of a low-frequency field (the fundamental field) and a high-frequency field (the harmonic field) in a nonlinear crystal. When the fundamental field is absent, we talk about *spontaneous* parametric down-conversion (SPDC), a purely quantum effect, which is forbidden by classical electrodynamics. In SPDC, a photon of the second-harmonic field is down-converted into two photons of the fundamental field, that share entanglement correlations. When the two down-converted photons are indistinguishable, the process is termed *degenerate* SPDC and it results in the generation of squeezed vacuum states. Conversely, when the two down-converted photons are distinguishable, non-degenerate SPDC creates two-mode squeezed vacuum (TMSV) states [Loudon 00].

Here, we treat the case of degenerate SPDC of a broadband field. Details on the derivation can be found in the PhD thesis [Michel 21] and [Medeiros de Araujo 12].

3.3.1 PDC with a broadband field

We begin to investigate the degenerate PDC process from Eq. 3.16, that we rewrite here:

$$P_\omega(\omega) = \epsilon_0 \chi_{ijk}^{(2)} \int_{\mathbb{R}} E_{2\omega}(\omega + \omega') E_\omega^*(\omega') \frac{d\omega'}{\sqrt{2\pi}} \quad (3.44)$$

Here, we treat the case of the type-0 process, in which all the fields are polarized along the same axis, and we neglect the subscripts for notational simplicity. The analytic signal of the forcing term $P_\omega(\omega)$ is plugged in Eq. 3.6, and we obtain:

$$\frac{\partial \alpha_\omega(z, \omega)}{\partial z} = \frac{i\omega_0}{2n_{2\omega}c} \mathcal{E}_{0,2\omega} \chi^{(2)} \int_{\mathbb{R}} \alpha_{2\omega}(z, \omega + \omega') \alpha_\omega^*(z, \omega') e^{i\Delta k(\omega, \omega')z} \frac{d\omega'}{\sqrt{2\pi}} \quad (3.45)$$

At a first glance this equation may seem similar to the one obtained for SHG, for which finding an analytic solution was trivial after postulating an undepleted pump. However, as the process we are interested in is degenerate, the fundamental field is present both as a derivative and as an integral term. An analytic solution can be found straightforwardly, if we assume that the signal field is real, i.e. $\alpha_\omega^*(\omega') = \alpha_\omega(\omega')$. This is equivalent to assume that the spectral phase is at most linear, with no higher-order components. In this case, Eq. 3.45 can be rewritten as:

$$\frac{\partial \alpha_\omega(z, \omega)}{\partial z} = \mathcal{K}(z) \alpha_\omega(z, \omega) \quad (3.46)$$

where $\mathcal{K}(z)$ is an integral operator whose action is specified in Eq. 3.45. The solution to the above integro-differential equation reads¹:

$$\alpha_\omega(L, \omega) = e^{S_0} \alpha_\omega(0, \omega) \quad (3.47)$$

where

$$S_0 = \frac{i\omega_0 \mathcal{E}_{0,2\omega}}{2n_{2\omega}c} \chi^{(2)} \int_0^L \int_{\mathbb{R}} \alpha_{2\omega}(z, \omega + \omega') e^{i\Delta k(\omega, \omega')z} \frac{d\omega' dz}{\sqrt{2\pi}} \quad (3.48)$$

In the undepleted pump regime, this becomes:

$$S_0 = ig \int_{\mathbb{R}} L(\omega, \omega') \frac{d\omega'}{\sqrt{2\pi}} \quad (3.49)$$

where $g = \frac{\omega_0 L}{2n_{2\omega}c} \chi^{(2)} \mathcal{E}_{0,2\omega}$ and where we define the *joint spectral distribution* or *joint spectral amplitude* (JSA) as:

$$L(\omega, \omega') = \alpha_{2\omega}(\omega + \omega') \Phi(\omega', \omega) \quad (3.50)$$

The JSA contains all the information on the spectral characteristics of the parametric process. An example on how the pump amplitude and the phase-matching function contribute to the JSA can be found in Fig. 3.2.

¹The solution to the initial-value problem $y'(t) = A(t)y(t)$, $y(t_0) = y_0$ where $A(t)$ is a linear operator, reads: $y(t) = \exp(\int_{t_0}^t d\tau A(\tau))y_0$, provided that $A(t_1)A(t_2) = A(t_2)A(t_1)$, for every value of t_1, t_2 . When this condition is not satisfied, we have to use the so-called Magnus expansion [Magnus 54].

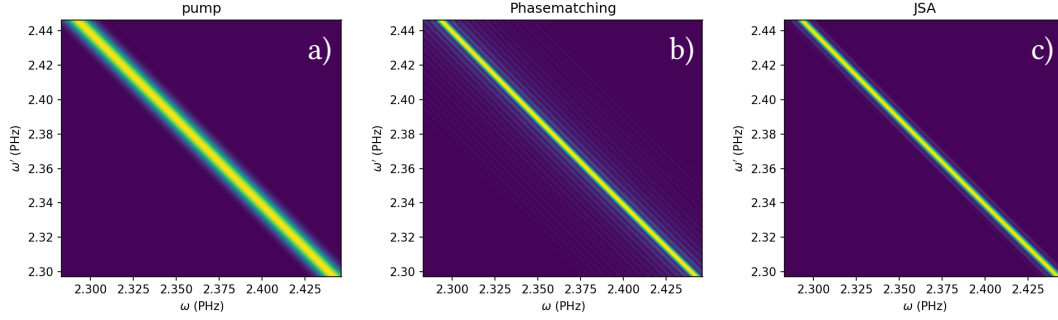


Figure 3.2: (a) Pump with 0.7 nm width (intensity FWHM) as a function of $\omega + \omega'$ and (b) phase-matching function for a type-0 process in KTP at pump wavelength of $\lambda_0 = 397.5$ nm, that result in the JSA displayed in (c).

3.3.2 Eigenmodes of the PDC

The operator e^{S_0} governs the evolution of the spectral input modes after the propagation into a crystal of length L . Under certain conditions, the operator can be diagonalized and we can recover the eigenmodes of the process, that we call *supermodes*. Supermodes can be described as the spectral modes whose shape is not altered by the parametric process, if they are used as input modes. As we assumed the condition of real field, this must hold also both at the input and the output of the crystal, i.e. $\alpha_\omega(0, \omega)$ and $\alpha_\omega(L, \omega)$ must be real. This puts a constraint on the operator e^{S_0} , as it must satisfy $S_0 = S_0^*$, which is satisfied only for a purely imaginary pump. We then require the pump to have the form $\alpha_{2\omega}(\omega + \omega') = \pm i|\alpha_{2\omega}(\omega + \omega')|$, so to be in quadrature with the signal. Under this condition we can check that $igL(\omega, \omega') = \pm g|\alpha_{2\omega}(\omega + \omega')|\Phi(\omega', \omega)$ is real; as it is also symmetric by definition, we can apply the spectral theorem and find an orthonormal basis of real eigenfunctions. We can rewrite the JSA in the diagonal basis as:

$$iL(\omega, \omega') = \sum_k \Lambda_k s_k(\omega) s_k(\omega') \quad (3.51)$$

where the functions $s_k(\omega)$ are the eigenmodes of the process and Λ_k are the eigenvalues. Acting with e^{S_0} on the eigenmodes leads us to:

$$s_k(L, \omega) = e^{S_0} s_k(0, \omega) = e^{\pm g \Lambda_k} s_k(0, \omega) \quad (3.52)$$

This equation shows us that at the output of the crystal the spectral eigenmodes are amplified or attenuated depending on the sign of the eigenvalues Λ_k and of the pump phase. For this reason, this process is known as *phase-sensitive amplification*, where phase-sensitivity is a consequence of degeneracy. In non-degenerate PDC (for example type-II PDC) the process is independent of the pump phase.

The eigenvalue problem can be solved analytically under the assumption of “Gaussian approximation”, as demonstrated in [Patera 08]. This consists of assuming a Gaussian pump

and a Gaussian phase-matching function; the latter can be approximated by a Gaussian if the tails of the sinc function bring negligible contribution to the JSA, for example in the case of a pump sensibly narrower than the phase-matching function. If this approximation is valid, the eigenfunctions are Hermite-Gauss modes, whose width depends on the crystal and on the pump characteristics. In particular, the eigenvalues Λ_k turn out to be a geometric sequence $\Lambda_k = \Lambda_0 \rho^k$, where $\rho = -1 + \epsilon$ and where ϵ is generally a small number that depends on the characteristic times of the process and the fields involved. We point out the fact that, as ρ is a negative number, the eigenvalues show an alternating sign. This means that, keeping the phase of the pump fixed, the process will alternate amplification and deamplification in consecutive spectral eigenmodes.

3.3.3 Quantum treatment (SPDC)

In the previous section, we restricted ourselves to the condition of real field $\alpha_s = \alpha_s^*$. Here, we treat the more general case of a complex field. This allows us to promote the field amplitudes to field creation and annihilation operators and to approach the solution from a quantum point of view. In this more general case, the JSA is still a symmetric function, by construction, but it is complex. We cannot apply the spectral theorem, which requires a Hermitian matrix. Instead, we must resort to the Autonne-Takagi factorization¹.

We rewrite the differential equation 3.45 as:

$$\frac{\partial \alpha_\omega(z, \omega)}{\partial z} = \mathcal{K}(z) \alpha_\omega(z, \omega) \quad (3.53)$$

where

$$\alpha_\omega(z, \omega) = \begin{pmatrix} \alpha_\omega(z, \omega) \\ \alpha_\omega^*(z, \omega) \end{pmatrix} \quad \mathcal{K}(z) = \begin{pmatrix} 0 & \mathcal{K}(z) \\ \mathcal{K}^*(z) & 0 \end{pmatrix} \quad (3.54)$$

The integral operator $\mathcal{K}(z)$ action on the field reads:

$$\mathcal{K}(z) \alpha_\omega^*(z, \omega) = ig \int_{\mathbb{R}} \alpha_{2\omega}(z, \omega + \omega') e^{i\Delta k(\omega, \omega')z} \alpha_\omega^*(z, \omega') \frac{d\omega'}{\sqrt{2\pi}} \quad (3.55)$$

As generally $\mathcal{K}(z_1)\mathcal{K}(z_2) \neq \mathcal{K}(z_2)\mathcal{K}(z_1)$, the solution cannot be written simply as the exponential of the integral of the $\mathcal{K}(z)$ operator, like we did in section 3.3.1 for the real field case. To solve this differential equation we must use the Magnus expansion [Magnus 54]. The solution takes the form:

$$\alpha_\omega(L, \omega) = e^{\sum_k \Omega_k(L, 0)} \alpha_\omega(0, \omega) \quad (3.56)$$

¹To be able to apply the spectral theorem we require the matrix A to be Hermitian, $A = A^\dagger$, and the diagonalization takes the form $A = VDV^\dagger$, with V unitary. In the case of the Takagi factorization we deal with a complex matrix $A = A^T$, and we can decompose in the form $A = VDV^T$ with V unitary.

where

$$\Omega_1(L, 0) = \int_0^L dz_1 \mathcal{K}(z_1) \quad (3.57)$$

$$\Omega_2(L, 0) = \frac{1}{2} \int_0^L dz_1 \int_0^{z_1} dz_2 [\mathcal{K}(z_1), \mathcal{K}(z_2)] \quad (3.58)$$

$$\Omega_3(L, 0) = \frac{1}{6} \int_0^L dz_1 \int_0^{z_1} dz_2 \int_0^{z_2} dz_3 ([\mathcal{K}(z_1), [\mathcal{K}(z_2), \mathcal{K}(z_3)]] + [\mathcal{K}(z_3), [\mathcal{K}(z_2), \mathcal{K}(z_1)]]) \quad (3.59)$$

$$\dots \quad (3.60)$$

Keeping only the first term of the expansion, under the assumption of small gain of the parametric process, leads us to:

$$\alpha_\omega(L, \omega) = e^{\mathcal{S}_0} \alpha_\omega(0, \omega) \quad (3.61)$$

where

$$\mathcal{S}_0 = \begin{pmatrix} 0 & \mathcal{S}_0 \\ \mathcal{S}_0^* & 0 \end{pmatrix} = \begin{pmatrix} 0 & \int_0^L dz \mathcal{K}(z) \\ \int_0^L dz \mathcal{K}^*(z) & 0 \end{pmatrix} = \quad (3.62)$$

$$\begin{pmatrix} 0 & ig \int_{\mathbb{R}} L(\omega, \omega') \frac{d\omega'}{\sqrt{2\pi}} \\ -ig \int_{\mathbb{R}} L^*(\omega, \omega') \frac{d\omega'}{\sqrt{2\pi}} & 0 \end{pmatrix} \quad (3.63)$$

Now that the field is allowed to be complex, we can promote it to an operator: $\alpha(\omega) \rightarrow \hat{a}(\omega)$. Moreover, we discretize the frequencies so that we can deal with matrices, which will simplify the calculations and the notation¹. We will then use the set of operators $\hat{a}_k = \hat{a}(\omega_k)$. We define the column vector:

$$\hat{\mathbf{a}} = (\hat{a}_1, \dots, \hat{a}_N, \hat{a}_1^\dagger, \dots, \hat{a}_N^\dagger) \quad (3.64)$$

and with such discretization the JSA can be re-expressed as a matrix and decomposed via the Autonne-Takagi factorization as:

$$i\mathbf{L} = \mathbf{V}\mathbf{\Lambda}\mathbf{V}^T \quad (3.65)$$

where \mathbf{V} is a unitary matrix and $\mathbf{\Lambda}$ is a diagonal matrix with non-negative entries. The discretized counterpart of $e^{\mathcal{S}_0}$ is:

$$e^{\mathcal{S}_0} = \exp \begin{pmatrix} 0 & g\mathbf{V}\mathbf{\Lambda}\mathbf{V}^T \\ g\mathbf{V}^*\mathbf{\Lambda}\mathbf{V}^\dagger & 0 \end{pmatrix} = \begin{pmatrix} \mathbf{V} & 0 \\ 0 & \mathbf{V}^* \end{pmatrix} \exp \begin{pmatrix} 0 & g\mathbf{\Lambda} \\ g\mathbf{\Lambda} & 0 \end{pmatrix} \begin{pmatrix} \mathbf{V}^\dagger & 0 \\ 0 & \mathbf{V}^T \end{pmatrix} \quad (3.66)$$

¹When we have an integral operator of the type $T : \phi \rightarrow (T\phi)(x) := \int k(x, y)\phi(y)dy$ we can consider it as the continuous version of matrix multiplication: $M : \phi \rightarrow (M\phi)_i := \sum_{ij} M_{ij}\phi_j$.

and we obtain:

$$\begin{pmatrix} \hat{\mathbf{a}}(L) \\ \hat{\mathbf{a}}^\dagger(L) \end{pmatrix} = \begin{pmatrix} \mathbf{V} & 0 \\ 0 & \mathbf{V}^* \end{pmatrix} \begin{pmatrix} \cosh(g\Lambda) & \sinh(g\Lambda) \\ \sinh(g\Lambda) & \cosh(g\Lambda) \end{pmatrix} \begin{pmatrix} \mathbf{V}^\dagger & 0 \\ 0 & \mathbf{V}^T \end{pmatrix} \begin{pmatrix} \hat{\mathbf{a}}(0) \\ \hat{\mathbf{a}}^\dagger(0) \end{pmatrix} \quad (3.67)$$

We define a new basis as:

$$\begin{pmatrix} \hat{\mathbf{s}} \\ \hat{\mathbf{s}}^\dagger \end{pmatrix} = \begin{pmatrix} \mathbf{V}^\dagger & 0 \\ 0 & \mathbf{V}^T \end{pmatrix} \begin{pmatrix} \hat{\mathbf{a}} \\ \hat{\mathbf{a}}^\dagger \end{pmatrix} \quad (3.68)$$

so that in this new basis the previous equation can be expressed as:

$$\begin{pmatrix} \hat{\mathbf{s}}(L) \\ \hat{\mathbf{s}}^\dagger(L) \end{pmatrix} = \begin{pmatrix} \cosh \mathbf{r} & \sinh \mathbf{r} \\ \sinh \mathbf{r} & \cosh \mathbf{r} \end{pmatrix} \begin{pmatrix} \hat{\mathbf{s}}(0) \\ \hat{\mathbf{s}}^\dagger(0) \end{pmatrix} \quad (3.69)$$

where $\mathbf{r} = g\Lambda$. We recall that, as Λ is a diagonal matrix with non-negative entries, the squeezing factors \mathbf{r} will be positive and define p -squeezed states. However, in this general case, the supermodes are defined by the unitary change of basis \mathbf{V} and are in general complex vectors. The supermodes are squeezed along an arbitrary axis, relatively to the pump phase, depending on this basis change.

An interesting case is the one in which the pump has at most a flat spectral phase, i.e. $\alpha_p(\omega) = |\alpha(\omega)|e^{i\phi_p}$. In this case, we can use a trick to deal with a real symmetric JSA and identify the squeezing directions relative to the pump phase. We take out the complex phase from the \mathbf{L} matrix leaving only the $|\alpha(\omega)|$ term to account for the pump. This way, \mathbf{L} is a symmetric real matrix and we can diagonalize it with the spectral theorem as:

$$\mathbf{L} = \mathbf{V}\Lambda\mathbf{V}^T \quad (3.70)$$

where now \mathbf{V} is an orthogonal matrix and Λ is a symmetric matrix that contains eigenvalues in a geometric progression as explained in the previous section. The discretized counterpart of $e^{\mathbf{S}_0}$ is:

$$e^{\mathbf{S}_0} = \exp \begin{pmatrix} 0 & ig\mathbf{V}\Lambda\mathbf{V}^T \\ -ie^{i\phi_p}g\mathbf{V}^*\Lambda\mathbf{V}^\dagger & 0 \end{pmatrix} = \begin{pmatrix} \mathbf{V} & 0 \\ 0 & \mathbf{V}^* \end{pmatrix} \exp \begin{pmatrix} 0 & ie^{i\phi_p}g\Lambda \\ -ie^{-i\phi_p}g\Lambda & 0 \end{pmatrix} \begin{pmatrix} \mathbf{V}^\dagger & 0 \\ 0 & \mathbf{V}^T \end{pmatrix} \quad (3.71)$$

and we obtain:

$$\begin{pmatrix} \hat{\mathbf{a}}(L) \\ \hat{\mathbf{a}}^\dagger(L) \end{pmatrix} = \begin{pmatrix} \mathbf{V} & 0 \\ 0 & \mathbf{V}^* \end{pmatrix} \begin{pmatrix} \cosh(g\Lambda) & ie^{i\phi_p} \sinh(g\Lambda) \\ -ie^{-i\phi_p} \sinh(g\Lambda) & \cosh(g\Lambda) \end{pmatrix} \begin{pmatrix} \mathbf{V}^\dagger & 0 \\ 0 & \mathbf{V}^T \end{pmatrix} \begin{pmatrix} \hat{\mathbf{a}}(0) \\ \hat{\mathbf{a}}^\dagger(0) \end{pmatrix} \quad (3.72)$$

We define a new basis as:

$$\begin{pmatrix} \hat{\mathbf{s}} \\ \hat{\mathbf{s}}^\dagger \end{pmatrix} = \begin{pmatrix} \mathbb{1} \frac{ie^{i\phi_p}}{2} & 0 \\ 0 & -\mathbb{1} \frac{ie^{-i\phi_p}}{2} \end{pmatrix} \begin{pmatrix} \mathbf{V}^\dagger & 0 \\ 0 & \mathbf{V}^T \end{pmatrix} \begin{pmatrix} \hat{\mathbf{a}} \\ \hat{\mathbf{a}}^\dagger \end{pmatrix} \quad (3.73)$$

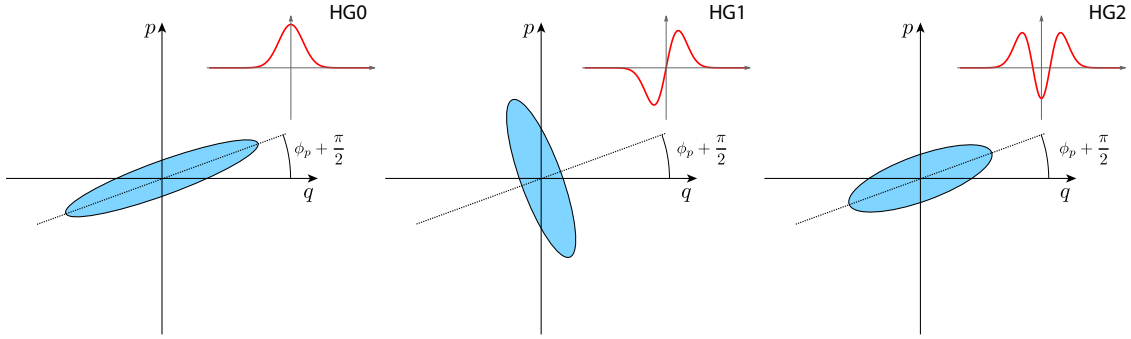


Figure 3.3: Scheme of the typical first three spectral modes at the output of the SPDC process, pumped by a field that shows at most a linear spectral phase and in the Gaussian approximation. The squeezing direction is determined by the pump phase and the squeezing ellipse is rotated by $\pi/2$ in consecutive modes.

so that in this new basis the previous equation can be expressed as:

$$\begin{pmatrix} \hat{s}(L) \\ \hat{s}^\dagger(L) \end{pmatrix} = \begin{pmatrix} \cosh \mathbf{r} & \sinh \mathbf{r} \\ \sinh \mathbf{r} & \cosh \mathbf{r} \end{pmatrix} \begin{pmatrix} \hat{s}(0) \\ \hat{s}^\dagger(0) \end{pmatrix} \quad (3.74)$$

where $\mathbf{r} = g\Lambda$. As shown in Sec. 3.3.2, the Λ eigenvalues alternate between positive and negative values, so between p -squeezing (for positive eigenvalue) and q -squeezing (for negative eigenvalue). However, differently from the previous case of a general complex pump, now we can identify easily the squeezing directions relatively to the pump, as shown in Fig. 3.3. Indeed, as \mathbf{V} is an orthogonal matrix, the supermodes are real eigenvectors up to common $\frac{\pm ie^{i\phi_p}}{2}$ factors.

3.3.4 Hamiltonian derivation

The process can be equivalently described using a Hamiltonian derivation, which is present in most books of quantum optics. In this section, we will sketch the basics of this approach, while skipping the calculations that are analogous to the ones presented in the previous section. The unitary operator acting on the quantum state can already be derived by the results of the previous section. Indeed, it can be shown [Horoshko 19] that a transformation acting on the operators as in 3.69 can be mapped into a unitary operator $\mathcal{U} = e^{-i\mathcal{H}}$ acting on the quantum state, where \mathcal{H} is sometimes called generator or “effective Hamiltonian”. In the case of the transformation under examination, the effective Hamiltonian takes the form of:

$$\mathcal{H} = \frac{i\hbar}{2} (\hat{s}^\dagger \Lambda \hat{s}^{\dagger T} - \hat{s}^T \Lambda \hat{s}) = \sum_i \frac{i\hbar g \Lambda_i}{2} (\hat{s}_i^{\dagger 2} - \hat{s}_i^2) \quad (3.75)$$

From this expression we can recognize the Hamiltonian of the squeezing transformation.

We can also derive the above Hamiltonian directly from the nonlinear interaction Hamiltonian. The total Hamiltonian of the light modes and their interaction can be written as:

$$\hat{H}_{tot} = \hat{H}_0 + \hat{V} \quad (3.76)$$

where \hat{H}_0 is the free Hamiltonian that includes the energies of the free fields (in the form $\omega_k \hat{a}_k^\dagger \hat{a}_k$) and \hat{V} is the three-wave interaction part. When dealing with interacting fields, it is useful to switch to the interaction (or Dirac) picture. The interaction picture is useful because it permits us to unravel part of the dynamics (the part governed by the free Hamiltonian) and concentrate on the dynamics that arises from the interaction among the fields. In this picture, the operators evolve according to the free Hamiltonian, and the overall effect of this transformation is to map the terms \hat{a}_i into:

$$\hat{a}_{i,I}(t) = e^{\frac{i}{\hbar} \hat{H}_0 t} \hat{a}_I(0) e^{-\frac{i}{\hbar} \hat{H}_0 t} = \hat{a}_{i,I}(0) e^{-i\omega_i t} \quad (3.77)$$

where $\hat{a}_{i,I}(0) = \hat{a}_{i,S} = \hat{a}_i$ is the annihilation operator in the “usual” Schrödinger picture. An analogous equation holds for the creation operators. Conversely, the states evolve according to the interacting Hamiltonian as:

$$|\psi(t)\rangle_I = \mathcal{T} e^{-\frac{i}{\hbar} \int_0^t d\tau V_I(\tau)} |\psi(0)\rangle_I \quad (3.78)$$

where the “ I ” subscript indicates that we are working in the interaction picture and where \mathcal{T} is a time-ordering operator¹. More details on the interaction picture can be found in Appendix A.

In the interaction picture, the interacting Hamiltonian is given by²:

$$V_I(t) = \frac{1}{2} \int_{\mathbb{R}} d^3 \mathbf{r} \hat{E}_{2\omega,I}(\mathbf{r}, t) \hat{P}_I(\mathbf{r}, t) \quad (3.79)$$

where $\hat{P}_I(\mathbf{r}, t)$ is the quantized counterpart of the nonlinear polarization introduced in Eq. 3.10. From now on, we drop the I subscripts in the field operators. Often in the literature the fields are rewritten as $\hat{E}(\mathbf{r}, t) = \hat{E}^{(+)}(\mathbf{r}, t) + \hat{E}^{(-)}(\mathbf{r}, t)$. As we are interested only in PDC, we are left with the term:

$$V_I(t) = \frac{\epsilon_0 d_{eff}}{2} \int_{\mathbb{R}} d^3 \mathbf{r} \hat{E}_{2\omega}^{(+)}(\mathbf{r}, t) \hat{E}_{\omega}^{(-)}(\mathbf{r}, t) \hat{E}_{\omega}^{(-)}(\mathbf{r}, t) + \text{h.c.} \quad (3.80)$$

¹The time ordering operator acts as:

$$\mathcal{T}(A(t), B(t')) = \begin{cases} A(t)B(t') & \text{if } t < t' \\ B(t')A(t) & \text{if } t' < t \end{cases}$$

²As reported in Eq. A.21, the connection between the interaction Hamiltonian in the Schrödinger picture and in the interaction picture is given by $\hat{V}_I(t) = e^{\frac{i}{\hbar} \hat{H}_0 t} \hat{V}_S e^{-\frac{i}{\hbar} \hat{H}_0 t}$.

We stress out that we deal with degenerate PDC: the signal and idler field are indistinguishable¹. We use the expression of the electric field defined as:

$$\hat{E}^{(+)}(\mathbf{r}, t) = \mathcal{E}_0 \int_0^\infty d\omega \hat{a}(\omega) e^{i(\mathbf{k}(\omega)\mathbf{r} - \omega t)} \quad (3.81)$$

$$\hat{E}^{(-)}(\mathbf{r}, t) = \mathcal{E}_0 \int_0^\infty d\omega \hat{a}^\dagger(\omega) e^{-i(\mathbf{k}(\omega)\mathbf{r} - \omega t)} \quad (3.82)$$

When performing the time integration of $V_I(\tau)$ in Eq. 3.78, we can push the integral limits to infinity. Indeed, we have:

$$\int_0^t d\tau V_I(\tau) = \int_{-\infty}^\infty d\tau V_I(\tau) \quad (3.83)$$

as $V_I(\tau)$ outside the $[0, t]$ interaction range vanishes. This step is important, as it permits to integrate the time-dependence of the electric field, of the form $e^{i(\omega_p - \omega_s - \omega_i)}$, to obtain the Dirac delta term $\delta(\omega_p - \omega_s - \omega_i)$, that accounts for energy conservation. The calculations are analogous to what has been done in the previous sections. Step-by-step details can be found in [Ou 07] and in [Mosley 07]. Carrying on the calculations will lead us to:

$$\int_{-\infty}^\infty d\tau V_I(\tau) = \frac{g\hbar}{2} \int_{\mathbb{R}^+} d\omega_s d\omega_i L(\omega_s, \omega_i) \hat{a}^\dagger(\omega_s) \hat{a}^\dagger(\omega_i) + \text{h.c.} \quad (3.84)$$

where $L(\omega_s, \omega_i)$ is the JSA already encountered in the previous sections. After switching to the supermode basis by diagonalizing $-iL(\omega_s, \omega_i)$ we get:

$$-\frac{i}{\hbar} \int_{-\infty}^\infty d\tau V_I(\tau) = \frac{g}{2} \sum_i \left(\Lambda_i \hat{s}_i^{\dagger,2} - \Lambda_i \hat{s}_i^2 \right) \quad (3.85)$$

Finally, if we start with a vacuum state in the signal and idler field $|\psi(0)\rangle_I$, the evolution is given by Eq. 3.78 and we obtain:

$$|\psi_{out}\rangle = \prod_i e^{\frac{g}{2} (\Lambda_i \hat{s}_i^{\dagger,2} - \Lambda_i \hat{s}_i^2)} |0\rangle \quad (3.86)$$

In the photon counting regime these equations are usually truncated at first order. From Eq. 3.84 we obtain:

$$|\psi_{out}\rangle \sim |0\rangle - \frac{ig}{2} \int_{\mathbb{R}^+} d\omega_s d\omega_i L(\omega_s, \omega_i) \hat{a}^\dagger(\omega_s) \hat{a}^\dagger(\omega_i) |0\rangle + \text{h.c.} \quad (3.87)$$

¹From the expression of the nonlinear polarization we also note that if we choose a non-degenerate process we have to account for a factor 2, that simplifies with the 1/2 in front of the integral of $V_I(t)$. Indeed, for two polarizations, $\hat{P}_i \propto \sum_{j,k=1}^2 \hat{E}_j \hat{E}_k = \hat{E}_1^2 + \hat{E}_2^2 + 2\hat{E}_1 \hat{E}_2$ where we omitted the nonlinear susceptibility. In our case we deal with a degenerate case: signal and idler are indistinguishable, so depending on the case we keep either the \hat{E}_1^2 term or the \hat{E}_2^2 term and the 1/2 factor does not vanish.

where $|0\rangle$ is the multimode vacuum. At first order, we obtain at the output of the crystal a monochromatic bi-photon state, where the frequencies are determined according to the probability encoded in the JSA. However, if expand the Hamiltonian in the supermode basis, from Eq. 3.86 we obtain:

$$|\psi_{out}\rangle \sim |0\rangle - \frac{g}{2} \sum_i \Lambda_i \hat{s}_i^{\dagger,2} |0\rangle \quad (3.88)$$

Even in this case the output state is a bi-photon state, but in a specific eigenmode temporal shape determined by the Λ_i probability coefficients.

Part II

Experimental Tools

Chapter 4

Experimental setup for squeezing generation

Contents

4.1	Scheme of the setup	84
4.2	The ultrafast light source	86
4.2.1	Mode-locked lasers	86
4.2.2	The Synergy laser	90
4.2.3	Frequency combs	91
4.2.4	Gaussian pulses	92
4.3	Nonlinear ppKTP Waveguides	94
4.3.1	Generalities on waveguides	94
4.3.2	Guided modes in diffused waveguides	95
4.3.3	Spectral modes for type-0	98
4.3.4	Waveguides injection and characterization	101
4.4	Second-Harmonic generation via ppKTP	105
4.4.1	The history of SHG in this setup	105
4.4.2	Simulation of the second-harmonic spectrum	106
4.4.3	Experimental second-harmonic generation	109
4.5	The pulse shaper	111
4.5.1	General introduction	111
4.5.2	Spectral phase and amplitude shaping	112
4.5.3	Characteristics of our pulse shaper	115

Spontaneous parametric down-conversion is the leading process in CV to generate squeezed states and entangled states of light, as seen in the previous part of this work. Squeezed states are a fundamental CV resource, whose application include quantum computing [Bourassa 21] quantum sensing [Aasi 13] and quantum metrology [Nielsen 23].

In CW, squeezing values of up to 15 dB of squeezing have been obtained via degenerate

SPDC at 1064 nm [Vahlbruch 16], and the generation of squeezed states and entangled states has been reported in integrated platforms [Lenzini 18, Mondain 19]. In the pulsed regime, degenerate SPDC results in the generation of multiple squeezed spectral modes, which can be employed to generate entangled networks in the spectral domain [Cai 17, Chen 14].

Multimode squeezing for quantum information processing applications has been presented both in the frequency domain [Yang 21] and in the time domain [Inoue 23]. Here, the goal is the single-pass generation of multimode squeezed states of light that are multiplexed both in time and in frequency. The spectral multimode structure is present in each pulse and, via fast balanced homodyne detection, we can measure squeezing in a pulse-resolved way [Kouadou 23]. Temporal multiplexing allows for the generation of an infinite number of modes (one for each pulse) [Yokoyama 13, Asavanant 19, Larsen 19], while spectral multiplexing enables the reconfigurability of the resource [Cai 17].

In this chapter, we outline the experimental setup that allowed us to carry out the squeezing generation experiment. The waveguide experimental setup has been designed by Tiphaine Kouadou, who has also designed and implemented the fast homodyne detector [Kouadou 21]. Here, I refined the simulations originally used for selecting the nonlinear crystal, enhancing their accuracy and permitting us to gain a better understanding on the nonlinear process. My experimental contribution consisted in building the waveguides setup, along with dealing with the necessary steps that resulted in squeezing generation, from waveguide characterization to performing the measurements in the spectral and time domain, presented in [Kouadou 23]. In addition, I devised and implemented a new second-harmonic generation in the setup.

4.1 Scheme of the setup

Our experimental setup is composed of several modules, each of which plays a critical role in the experiment's success. While we will detail each module later in this chapter, it is useful to present the entire setup as a whole, in order to highlight in advance how the various components are interconnected. In Fig. 4.1 a scheme of the experiment is presented.

Waveguides for SPDC Periodically-poled KTP waveguides crystals are at the core of this single-pass squeezing generation experiment. The nonlinearity of the crystal drives the SPDC process, while the waveguide structure ensures that the generated light remains confined within a narrow section. This confinement enhances the efficiency of the non-linear process and, in our case, it ensures spatial single-mode operation. This last aspect is crucial in preventing the emergence of spatial-spectral correlations, which can occur in bulk setups [LaVolpe 20].

Nonlinear waveguides have to be carefully engineered to deliver multimode squeezed states at their output, and the entire setup must be constructed in accordance with the waveguides requirements. Factors such as the pump beam's characteristics, spatial

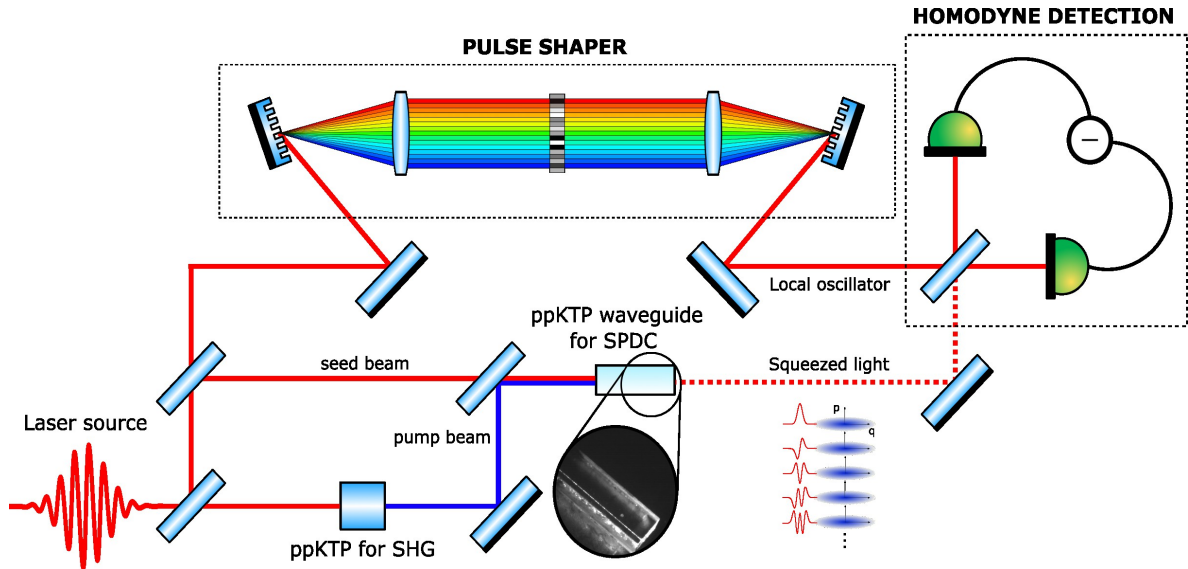


Figure 4.1: Scheme of the waveguides squeezing generation experiment.

alignment with the local oscillator of the homodyne detector, and precise control over alignment parameters are all critical for the success of the experiment.

Laser source The laser beam serves as the common source for the various beams used in the experiment, each with specific purposes and distinct characteristics. After undergoing spatial filtering, the laser beam is split into three main parts: approximately 50 mW are used for seeding the SPDC process (referred to as the *seed beam*), 200 mW are allocated for the local oscillator (LO) in the detection stage, and the remaining power is directed toward driving the SHG process.

Pump beam The majority of the laser beam serves as the pump for the second-harmonic generation (SHG) process. The second-harmonic light is subsequently used to pump the waveguides to drive the SPDC process; for this reason, throughout this work we will often refer to this beam as “pump beam”. The SHG crystal was selected to ensure that the second-harmonic light possesses suitable characteristics for multimode squeezing generation. Factors such as the efficiency of SHG, the width of the output pulse and the spatial properties of the beam were all considered when choosing the crystal. In particular, we will explore how the spectral width of the SHG light plays a crucial role in determining certain key spectral characteristics of the generated squeezed light.

Seed beam The seed beam, much like the SHG pump beam, is directed towards the waveguide module, but its purpose is quite different. It is used exclusively for alignment and for locking purposes and it is intentionally blocked during the measurement stage. Indeed,

both temporal and spatial alignment are crucial in this experiment: squeezed vacuum light is not bright, so its path cannot be easily traced, and the temporal location of its pulses cannot be measured using conventional methods applied to coherent beams. The seed beam essentially acts as a “vessel” for the squeezed beam. When alignment procedures are carried out accurately, the seed pulses follow the same path and occupy the same position as the squeezed pulses. Furthermore, since both the seed and squeezed light are guided within a waveguide structure, they share the same transverse spatial profile; this is an important point for ensuring proper spatial overlap with the local oscillator beam during the homodyne detection stage, as we will discuss in more detail throughout this chapter.

LO beam The local oscillator beam is used in the detection stage of the experiment. It is sent to a pulse-shaper, an optical device designed for spectral-temporal shaping of light pulses. The pulse shaper is controlled by a computer program, and it enables us to imprint a specific temporal profile on the light, within the resolution limits of the pulse shaper.

Since homodyne detection is a projective measurement, the LO is used to select the specific spectral mode that we intend to measure. Our capabilities in this regard are limited by the local oscillator bandwidth; a wider bandwidth grants access to a larger number of modes for measurement. During the alignment phase, the LO beam is combined with the seed beam at the homodyne detection beamsplitter, while when taking measurements the seed is blocked and only the squeezed light is measured alongside with the LO.

4.2 The ultrafast light source

In this section, we explore the temporal and spectral characteristics of a femtosecond light source. Ultrafast light opens the way to a wide range of applications, but it also introduces unique challenges when compared to Continuous-Wave (CW) light. Managing dispersion, ensuring precise temporal alignment, and addressing the complex spectral structure during the measurement stage are prices we have to pay when working in an ultrafast optics experiment. An extensive review on ultrafast light, its applications and its inherent challenges is given in [Weiner 11].

4.2.1 Mode-locked lasers

In a laser operating at steady state, only certain frequencies (known as *longitudinal modes*) are allowed to resonate in the cavity. It follows that we don't have a continuous spectrum but the frequencies are discretized, following:

$$\omega_n = n \frac{2\pi c}{L} = n\omega_r, \quad n \in \mathbb{Z} \quad (4.1)$$

where L is the cavity length. The quantity $\omega_r = \frac{2\pi c}{L}$ is called free-spectral range of the cavity, and it corresponds to the angular frequency of the laser repetition rate. When the

steady-state conditions are valid only for a single longitudinal mode, the laser operates in the continuous-wave (CW) regime, resulting in the emission of a monochromatic light beam. More details on laser essentials are given in Appendix B.1.

A priori each longitudinal mode ω_n can oscillate in the cavity with a random phase ϕ_n , resulting in an electric field

$$E^{(+)} = E_0 \sum e^{i(k_n z - \omega_n t + \phi_n)} \quad (4.2)$$

This results in the intensity fluctuating randomly around its average value $I(t) \propto N|E_0|^2$, where N is the number of longitudinal modes and we assume that each mode has the same amplitude E_0 . This situation is analogous to that of a lightbulb, which is inherently a broadband source but typically does not emit light in the form of distinct pulses. To shift from continuous light emission to light pulses, we introduce one final essential ingredient: *mode-locking*.

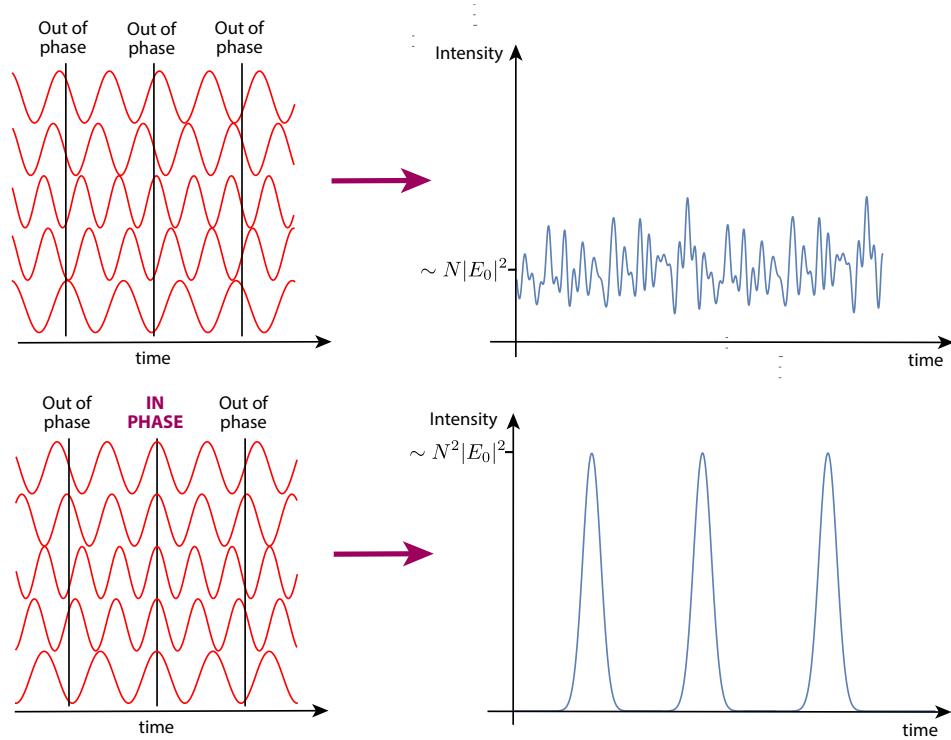


Figure 4.2: Random phase relation (top) and fixed phase relation (bottom) between longitudinal modes. In the first case, the output results in random (but still periodic) intensity fluctuations around the average value. A fixed phase relation permits the formation of a pulse. In both cases, the average value of the intensity is the same.

Mode-locking is a technique that permits the modes to oscillate inside the cavity with a fixed relative phase. In most cases of interest we fix the relative phases such that $\phi_n = \phi$. In

this case, the intensity takes the form:

$$I(t) \propto |E_0|^2 \frac{\sin^2(N\Delta\omega t/2)}{\sin^2(\Delta\omega t/2)} \quad (4.3)$$

where $\Delta\omega$ is the angular frequency spacing between two consecutive longitudinal modes. The average intensity is still proportional to $N|E_0|^2$ but the peak intensity of the pulse is much higher and of the order of $N^2|E_0|^2$ [Weiner 11]. This is shown in Fig. 4.2.

The mode-locking technique permits to generate very short pulses, up to the femtosecond range¹. While not all laser gain media are capable of producing ultrashort femtosecond pulses, specific gain media, paired with mode-locking technique and with extensive research in the cavity configuration, have enabled the generation of remarkably short pulses. Among these media, titanium-doped sapphire (Ti:Sa) lasers have emerged as the leading technology for femtosecond pulse generation in the near-infrared spectrum², achieving pulses as short as 5 femtoseconds [Eli 01].

Mode-locking can be active or passive³. Here, we focus on passive mode-locking, which is achieved by placing in the oscillator cavity a saturable absorber, where the absorption of light is reduced non-linearly if the intensity of light increases. Low intensity CW light will suffer from absorption losses, while pulsed light, with higher peak intensity, will saturate the absorber and reduce this induced losses effect. In particular, the wings of the pulse, of lower intensity, will suffer more losses compared to the pulse peak, which saturates the absorber. This results in pulse shortening, and the saturable absorber acts effectively as an ultrafast shutter. The pulses continue to shorten until a counterbalancing mechanism comes into play. Indeed, as the pulse shortens, its spectral width broadens. When the ultrashort pulse reaches a spectral width comparable to the gain bandwidth, a spectral shortening (temporal-broadening) effect kicks in, inducing losses in the spectral wings that overcome the gain bandwidth. Eventually, the shortening and broadening mechanism balance out and the pulse is stabilized to a specific temporal and spectral width [Agrawal 20, Yefet 13].

The shortest achievable pulses are generated via Kerr-lens mode-locking, a technique that employs the Kerr-lensing effect of the gain medium. This, coupled with either a hard or a soft aperture, two different mode-locking techniques explained below, behaves like a fast saturable absorber. The Kerr effect is a third-order non-linear effect, in which the refractive index of the crystal changes locally non-linearly with the electric field strength:

$$n(\mathbf{r}, t) = n_0 + n_2 I(\mathbf{r}, t) \quad (4.4)$$

¹Mode-locking is not the only technique for pulse generation, but it is the one that permits the generation of the shortest pulses. For instance, Q-switching generated pulses are in the nanosecond range.

²We remind that there is an intrinsic limitation: pulses cannot contain less than one optical cycle. Given a central wavelength $\lambda_0 \sim 800$ nm, the shortest pulse duration is of $t_{min} = 2.67$ fs. However, attosecond pulses can be achieved in the XUV (extreme ultraviolet) range.

³Active mode locking requires an external device, such as amplitude or phase modulator, to modulate the losses synchronously with the resonator round trip. Typically, active mode-locked lasers can generate pulses in the picosecond range.

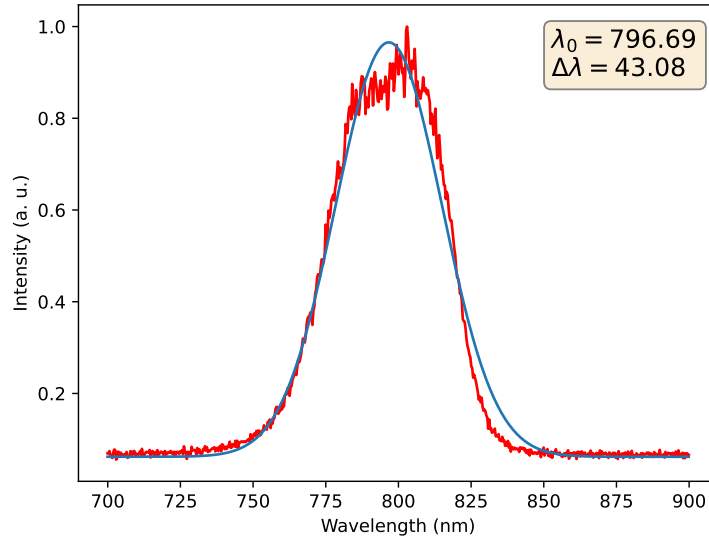


Figure 4.3: Spectrum of our light source.

This gives rise to various effects such as self-phase modulation in the temporal domain and Kerr lensing (or self-focusing) in the spatial domain. As a consequence of this non-linear effect, the intensity of the pump beam being higher along the beam axis results in a bigger change of the refractive index in the center of the beam. The crystal behaves then like a lens, causing focusing or defocusing of the high intensity beam. High intensity beams will thus have a different spatial behaviour than low intensity ones. This difference will be exploited to introduce losses in the CW (low-intensity) operation to promote the ML (mode-locked, high intensity) operation. In the case of hard-aperture mode-locking, we exploit the fact that the size of the CW beam at the output mirror is larger than the size of the ML beam. Adding a slit to induce losses on the CW beam favours ML operation, that soon saturates the gain. In soft-aperture mode-locking, the ML operation is favoured because the pump itself acts as an aperture: inside the crystal the ML beam is smaller than the CW beam and it has a better overlap with the pump, thus favouring its gain over the CW beam. Both methods have the effect of increasing the round-trip gain.

To start the mode-locking operation we kick the end mirror of the cavity, breaking the CW regime and seeding a pulse that saturates the absorber sufficiently to build up, overcoming the CW beam. When the gain is greater than the cavity losses, lasing is possible. The light builds up in the cavity and a steady-state is reached when the gain and losses are equal.

4.2.2 The Synergy laser

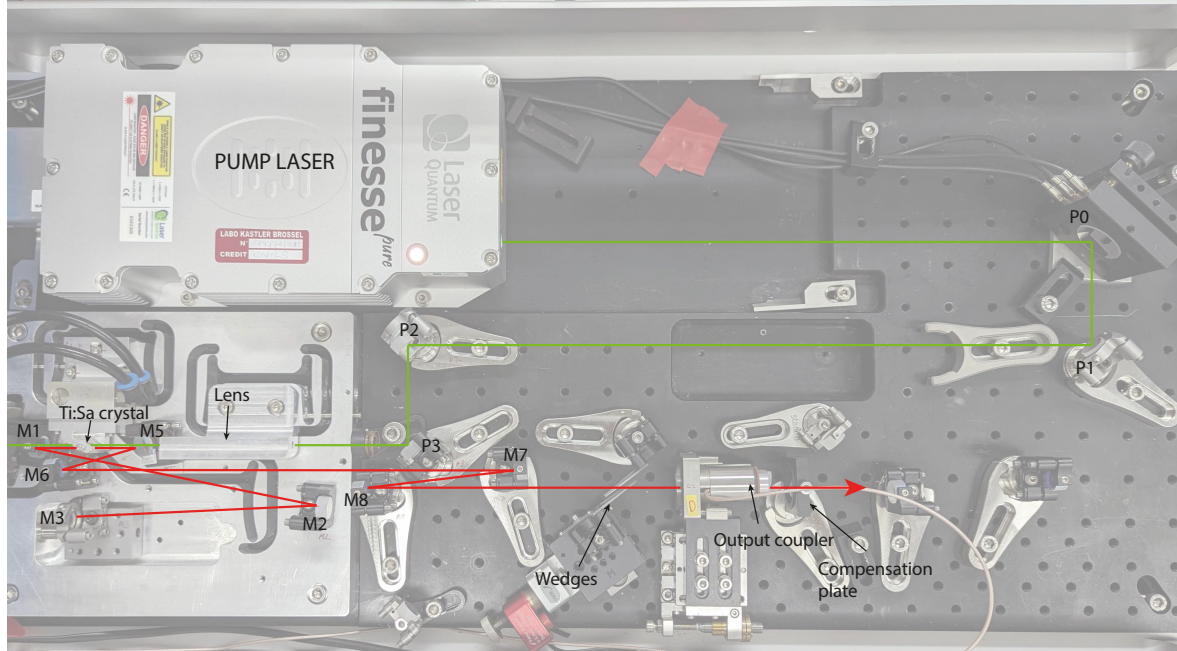


Figure 4.4: Picture of the pump laser and the Ti:Sa laser.

Our light source is a Synergy laser by Femtolaser, a Titanium-Sapphire (Ti:Sa) soft-aperture Kerr-lens mode-locked laser, that delivers near-infrared 22 fs pulses at a repetition rate of $f_r = 156 \text{ MHz}$ ¹. In the frequency domain, the source is a frequency comb (see section 4.2.3) centered at $\lambda_0 = 795 \text{ nm}$ with a FWHM of 42 nm. Depending on the alignment of the laser cavity, these parameters can be slightly shifted. A typical laser spectrum is shown in Fig. 4.3. The oscillator is pumped with 5 W of 532 nm continuous wave light delivered by a Finesse pure from Laser Quantum, a diode-pumped solid state laser.

A scheme of the laser can be seen in Fig. 4.4. The cavity is folded into an X-fold configuration, and the folding angles θ_1 and θ_2 between the curved mirrors M1 and M5 and the crystal compensate for the astigmatism introduced by the Ti:Sa crystal. These angles are calibrated at the factory and the mirrors M1 and M5 must never be realigned. For intracavity dispersion compensation, all the cavity mirrors, except for M1, M5 and the OC, are chirped². For fine-tuning of the intracavity dispersion, a pair of wedges are placed

¹Standard Ti:Sa lasers do not operate at 156 MHz. This unusual repetition rate is due to a customization of our laser cavity, that has been halved by the manufacturer with respect to the standard Synergy laser that operates at 80 MHz. The reason was of practical purpose: this laser has been purchased to serve an older metrology experiment. The higher repetition rate permitted to build a smaller cavity to serve the experiment, as the distance between pulses is only around 2 m. This footnote is specifically intended for the knowledge of future PhD students.

²Chirped mirrors are specifically designed for introducing negative group delay dispersion.

before the OC, and one of them is mounted on a translation plate; adjusting this translation, one can fine tune the width of the output spectrum and restore its nominal alignment values. Finally, a compensation plate (CP) and extra-cavity chirped mirrors are placed in the path of the beam, to get the shortest pulse.

The alignment of the laser cavity is achieved by maximizing the output power by aligning the two injection mirrors P1 and P2 and by aligning the cavity-end mirrors M3 and OC. Cleaning with a mix of acetone and methanol¹ is also part of the routine, as dust on the optics, and especially on the crystal, is very detrimental to lasing. In optimized conditions, 5W of CW pump generate 0.98 W of pulsed light.

The laser output beam doesn't have a proper TEM00 spatial shape. Spatial filtering is needed, in order to obtain a TEM00 mode. To ensure spatial filtering, a couple of curved mirrors and a pinhole of 150 μm are placed in the path of the beam, with a transmission that ranges from 86% to 90%.

4.2.3 Frequency combs

The electric field of an infinite train of pulses can be mathematically described as:

$$E_{train}^{(+)}(t) = \sum_{n=-\infty}^{\infty} E_{pulse}^{(+)}(t - n\tau) = \mathcal{E}_0 \sum_{n=-\infty}^{\infty} \alpha(t - n\tau) e^{-i\omega_0(t-n\tau)} \quad (4.5)$$

where $E_{pulse}^{(+)}(t)$ is defined as in Eq. 1.28, where $\alpha(t)$ is the envelope and ω_0 is the carrier. The temporal spacing between the pulses is denoted as τ and it reads $\tau = 2\pi/\omega_r$, where ω_r is the angular frequency of the laser repetition rate.

The Fourier transform of 4.5 reads²:

$$E_{train}^{(+)}(\omega) = \omega_r E_{pulse}^{(+)}(\omega) \sum_{n=-\infty}^{\infty} \delta(\omega - n\omega_r) \quad (4.6)$$

From this equation, we identify the structure of the so-called *frequency comb* [Fortier 19], that is characterized by a succession of single-frequencies (the *teeth* of the comb) equally spaced by ω_r and modulated by a spectral envelope, defined by the laser characteristics. This comb structure reflects the temporal periodicity of the train of pulses.

This description is accurate for an ideal frequency comb. However, for a realistic description of the comb, chromatic dispersion within the cavity must be considered. This results in a frequency offset ω_{CE} in the frequency domain, and in a phase offset ϕ_{CE} between consecutive pulses. More details on a realistic frequency comb are given in B.2 and [Thiel 15]. A picture of the spectral and temporal features of a realistic frequency comb field can be seen in Fig. 4.5.

¹The two pump mirrors P1 and P2 are dielectric mirrors and should only be cleaned with methanol.

²Here we use the fact that $f(\omega) = \frac{1}{\omega_r} \sum_{n=-\infty}^{\infty} e^{in\omega \frac{2\pi}{\omega_r}} = \sum_{n=-\infty}^{\infty} \delta(\omega - n\omega_r)$.

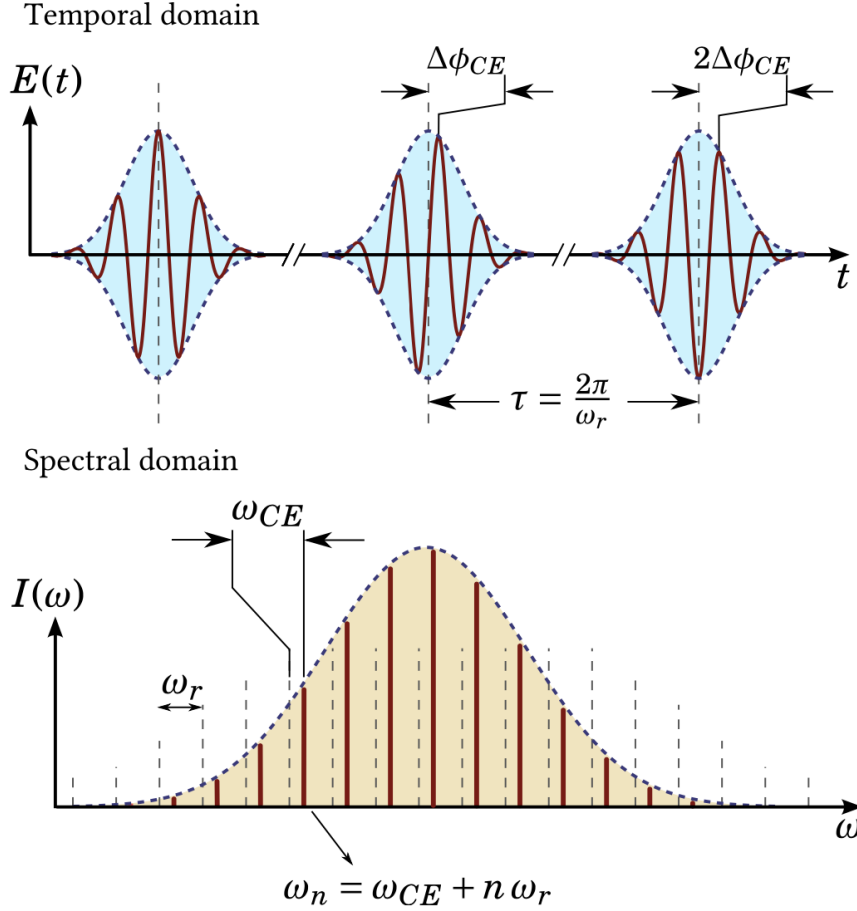


Figure 4.5: Realistic frequency comb in the temporal domain (top) and in the spectral domain (bottom). Picture from [Thiel 15].

4.2.4 Gaussian pulses

In this experiment, we work with pulses that can be approximated by a Gaussian envelope. Although ultrafast Ti:Sa lasers pulses typically exhibit a temporal profile that more closely resembles a hyperbolic secant function, employing Gaussian functions allows us to perform analytical calculations.

We define Gaussian temporal envelopes as a normalized electric field mode $u(t)$ using the following expression:

$$u(t) = C_t \exp\left(-\frac{t^2}{4\Delta t^2}\right) \quad (4.7)$$

where C_t is a constant that accounts for the normalization of the mode and where the time width Δt , sometimes referred to as σ_t , is the standard deviation of the intensity

profile of the field¹. This definition differs from others that are used in the quantum optics community. However, as here we work extensively with spectral-temporal characteristics, it is a convenient choice that ensures the symmetry between the temporal and the spectral domain.

The Fourier transform, with respect to the carrier frequency, of Eq. 4.7 yields the expression:

$$u(\Omega) = C_\omega \exp\left(-\frac{\Omega^2}{4\Delta\omega^2}\right) \quad (4.8)$$

where $\Omega = \omega - \omega_0$, C_ω is the normalization constant and $\Delta\omega$ (also called σ_ω) is the standard deviation of the spectral intensity, that can be directly measured with a spectrometer. As a consequence of the relations between the spectral and the time domain, the following equality holds:

$$\Delta t \Delta\omega = \frac{1}{2} \quad (4.9)$$

We point out that in the case of a pulse with a general temporal shape, this equation represents a lower bound. Pulses that satisfy this equality are said to be Fourier-transform limited. Ultrafast pulses are subjected to dispersion, that results in the altering of the pulse shape. The effect of dispersion, up to the second order, is treated in B.3.

To describe measured intensities, we often use the Full-Width-Half-Maximum instead of the standard deviation. The two are related by

$$\Delta t_{FWHM} = 2\sqrt{2 \ln 2} \Delta t \quad (4.10)$$

and Eq. 4.9 can be rewritten in the FWHM notation as

$$\Delta t_{FWHM} \Delta\omega_{FWHM} \sim 0.441 \quad (4.11)$$

This is known as *time-bandwidth product*².

To conclude this section, we turn our attention to the energy and power of a pulse. In the general case, the average detected power of a laser beam is determined by the equation:

$$P_{avg} = E_p \cdot f_r \quad (4.12)$$

where E_p is the energy of the pulse and f_r is the repetition rate. For Gaussian pulses, the peak power of a pulse can be expressed as:

$$P_{peak} = 0.94 \frac{P_{avg}}{f_r \cdot \Delta t_{FWHM}} \quad (4.13)$$

¹In this specific case, being the mean of the gaussian envelope $\langle t \rangle = 0$, the variance (or second central moment), corresponds to the second moment, i.e. $\langle t^2 \rangle = \int_{\mathbb{R}} dt t^2 |\alpha(t)|^2 = \sigma_t^2$

²The time bandwidth product depends on the pulse shape. As an example, for a sech² pulse it takes the value of 0.315.

As an example of the striking differences of the scales involved between the CW and the pulsed regime, we consider a Fourier-transform limited pulse with the characteristics of our light source. In this case, the peak power can be estimated as $P_{peak} \sim 0.27 \cdot 10^6 \cdot P_{avg}$. For instance, with just 10 mW of average power, our pulses yield a remarkable peak power of 2.7 kW.

4.3 Nonlinear ppKTP Waveguides

In this section, we introduce nonlinear periodically-poled KTP waveguides, the primary component of the squeezing generation experiment. We start by discussing the concept of guided light, which has gained popularity in recent years. This concept is familiar to many, particularly due to the widespread use of optical fiber internet connections in households, made possible by advancements in telecommunications. The particular geometry of our waveguides is studied, along with the nonlinear characteristics of the ppKTP crystal. An important aim of this section is to evaluate the specific requirements that the surrounding components in this setup must meet to facilitate effective squeezing generation. Details on optical waveguides can be found in [Snyder 83, Okamoto 06].

4.3.1 Generalities on waveguides

Waveguides are structures that confine light by exploiting the phenomenon of total internal reflection. Typically, guided light is confined within a region of high refractive index relative to its surroundings, allowing for transmission along the longitudinal direction, denoted often as the z direction. Waveguides can be classified into different types based on their geometrical structure and the profile of their transverse index of refraction $n(x, y)$. Light confinement can be limited to only one transverse direction (*planar* or *slab waveguides*) or to both transverse directions (*non planar waveguides*). Moreover, waveguides can be classified according to their index-profile into *step-index waveguides*, characterized by an abrupt change in refractive index between the core region and its surroundings, or *graded-index waveguides*, where the refractive index changes gradually. Among non-planar waveguides, optical fibers are perhaps the most well-known, being widely used in telecommunications. Other types of non-planar waveguides include buried channel, ridge, rib, and diffused waveguides, as illustrated in Figure 4.6. In the context of this work, we will use diffused waveguides as the chosen type for our experiments.

These various structures and index profiles provide control over the characteristics of the guided modes within the waveguide. Guided modes are transverse profiles of the electric and magnetic fields that remain constant along the propagation direction. The electric and

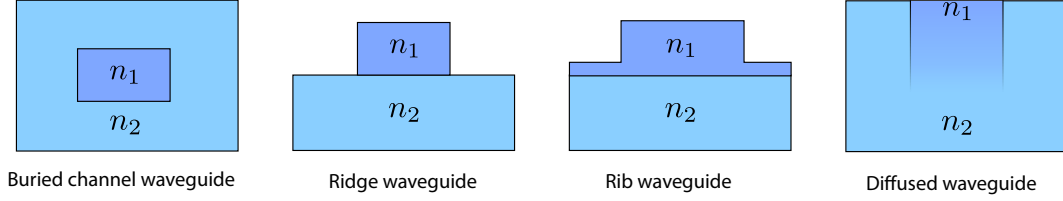


Figure 4.6: Examples of non-planar waveguides.

magnetic field of a guided mode can be written as follows:

$$\mathbf{E}_\nu(\mathbf{r}, t) = \mathbf{E}_\nu(x, y)e^{i(\beta_\nu z - \omega t)} \quad (4.14)$$

$$\mathbf{H}_\nu(\mathbf{r}, t) = \mathbf{H}_\nu(x, y)e^{i(\beta_\nu z - \omega t)} \quad (4.15)$$

where ν is the mode index, $\mathbf{E}_\nu(x, y)$ and $\mathbf{H}_\nu(x, y)$ are the transverse distributions of the electric and magnetic field, and β_ν is the propagation constant of the mode. The propagation constant β_ν , analogously to the wavevector k_z for a plane wave in a medium with refractive index n , describes the change in phase along the propagation direction z . It can be expressed by:

$$\beta_\nu = n_{eff,\nu} \frac{\omega}{c} \quad (4.16)$$

where $n_{eff,\nu}$ is the effective refractive index experienced by the mode within the waveguide.

It is important to note that dielectric waveguides do not support TEM modes, which are modes in which the E_z and B_z components of the electric and magnetic fields both vanish. Instead, waveguides support various types of modes, including: transverse electric (TE) modes ($E_z = 0$ and $B_z \neq 0$), transverse magnetic (TM) modes ($E_z \neq 0$ and $B_z = 0$) and hybrid modes ($E_z \neq 0$ and $B_z \neq 0$). In certain cases, such as for planar waveguides and optical fibers, the solutions to Maxwell's equations can be found analytically and result in pure TE and TM modes. However, in the general case, a pure TE and TM solution does not exist. Instead, guided modes are typically hybrid modes,¹ and the wave equation does not have an analytical solution [Snyder 83, Murphy 01]. Therefore, numerical methods must be employed to analyze the modes of these waveguides.

4.3.2 Guided modes in diffused waveguides

The waveguides that are employed for the SPDC process in this experiment are graded-index periodically-poled KTP waveguides, provided by the company AdvR Inc. These waveguides are organized into chips, with each chip containing six groups of five waveguides, resulting in a total of 30 waveguides. The width of these waveguides varies between 2, 3 or 4 μm and

¹For hybrid modes, often one of the transverse components of the fields is much bigger than the other, and we can approximate them with quasi-TE and quasi-TM modes

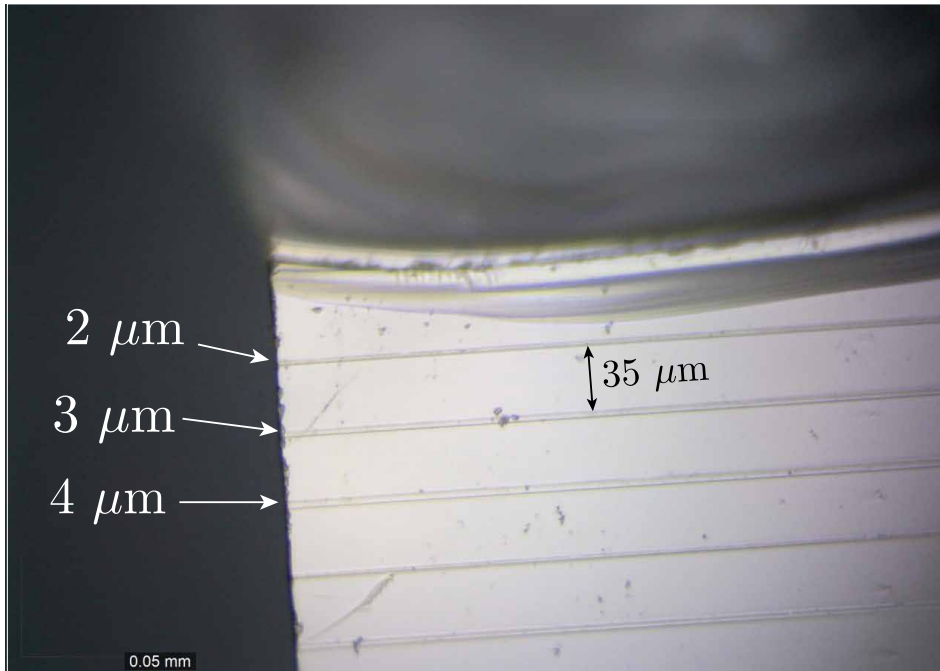


Figure 4.7: High-resolution picture of the first group of the waveguide chip.

there is a separation of $75 \mu\text{m}$ between groups of waveguides, while the distance between waveguides within the same group is $35 \mu\text{m}$. A picture of a group of waveguides is shown in Fig. 4.7. The KTP chip itself has a length of 5.7 mm ; due to fabrication constraints, a smaller chip length is not achievable. However, the periodically poled region is limited to a length of $L = 1 \text{ mm}$, situated at the end of the crystal. Anti-reflection coatings are applied to both the input and output facets of the chip to minimize reflection losses. Moreover, the crystal is x-cut, meaning that light propagates along the x -axis of the crystal. In the rest of this section, we will therefore indicate with x the propagation direction and with (y, z) the transverse directions.

The diffused profile is obtained via Rb^+ ions exchange on the x-cut KTP chip [Bierlein 87]. The ion diffusion into the bulk KTP is responsible for creating a waveguide structure with a graded index profile along the z -axis, denoted with $n(z)$. In this profile, the refractive index decreases with depth, following an exponential law [Roelofs 94]. Since these waveguides lack specific planar or cylindrical symmetry, analytical computations of their eigenmodes are not feasible and numerical techniques must be employed. For this work, a finite-difference method is used to calculate the spatial modes supported by the waveguide [Murphy 01, Fallahkhair 08].

To calculate numerically the spatial modes, the graded-index profile $n(y, z)$ is coarse grained into a finite mesh, with elements of size $\Delta y \cdot \Delta z$ in which the refractive index is constant, as can be seen in Fig. 4.8. The refractive indexes of our waveguides have been

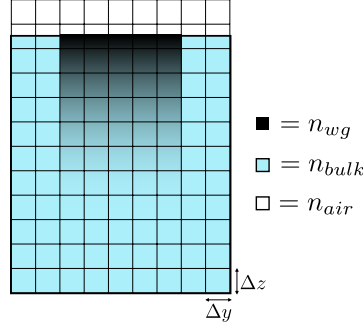


Figure 4.8: Typical finite-difference mesh, where the refractive index profile $n(y, z)$ is divided into pixels of dimensions Δy and Δz , over which the refractive index is constant.

	400nm z	400nm y	800nm z	800nm y
n_{wg}	1.98885	1.86786	1.85681	1.77339
n_{bulk}	1.96405	1.84346	1.84465	1.75653

Table 4.1: Refractive index n_{wg} of the waveguide and n_{bulk} of the bulk for the waveguide chip provided by AdvR Inc. along the axes y and z .

provided by AdvR Inc. for $\lambda = 400$ nm and $\lambda = 800$ nm and are given in Table 4.1. The y -profile follows a step-gradient while the z -profile follows a graded-index, expressed as:

$$n(z) = n_{bulk} + \Delta n e^{-\frac{z}{d}} \quad (4.17)$$

where $\Delta n = n_{wg} - n_{bulk}$ and d is a parameter that depends on the fabrication process that is, unfortunately, unknown. It has been observed that narrower waveguides are deeper than broader ones [Padberg 20].

The normalized propagation constant:

$$b_v = \frac{n_{eff,v}^2 - n_{bulk}^2}{n_{wg}^2 - n_{bulk}^2} \quad (4.18)$$

permits us to calculate the range of modes that can be guided through a waveguide. The condition for guidance reads $0 < b < 1$ and b decreases with the mode order, as β_v does. The more b_v is closer to 1, the better the mode v is guided. With the finite-difference method we can calculate numerically the n_{eff} for each spatial mode supported by the waveguide, until we reach the cut-off condition of $b \leq 0$. The numerical simulations of the guided modes of the waveguide can be seen in Fig. 4.9 and in Fig. 4.10, for a waveguide of width $3 \mu\text{m}$ and $d = 4 \mu\text{m}$. The calculated values of n_{eff} and b for guided modes are provided in Table 4.2.

In the near-infrared at $\lambda = 800$ nm, the waveguide supports the fundamental and the first order mode. While the waveguide isn't strictly single-mode, we have found that it is

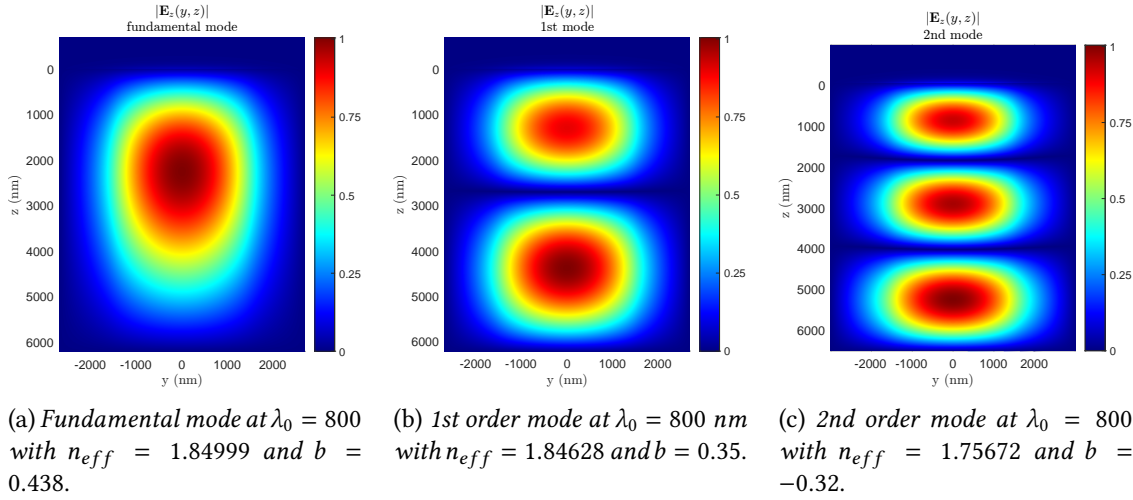


Figure 4.9: Simulation of the guided modes for $d = 4 \mu\text{m}$ and waveguide width of $3 \mu\text{m}$. The mesh graining is $\Delta y = \Delta z = 2$ nm. The waveguide supports the first two modes while the second-order one is non-guided.

possible to achieve a single-mode behavior by adjusting the vertical position of the chip. Indeed, injecting the beam less deeply into the waveguide promotes the selection of the fundamental mode. However, when the beam is injected more deeply, a second lobe faintly appears toward the surface of the waveguide, as depicted in Fig. 4.11.

The situation is quite different for $\lambda = 400$ nm light. At this shorter wavelength, the waveguides become highly multimode, and $b \leq 0$ only applies to modes starting from the 13th order and beyond. As a result, the selection of only the fundamental mode is typically not feasible, and the number of excited spatial modes depends greatly on the alignment of the pump beam. The presence of a large number of pump spatial modes and the challenge of selecting just the fundamental one represent a significant limitation of this system for the SPDC process at these wavelengths.

4.3.3 Spectral modes for type-0

The time-frequency structure of the generated light can be investigated following the theory on SPDC that has been given in section 3.3. For this purpose, we use a software developed by B. Brecht at the University of Paderborn [Brecht 14], which allows us to numerically compute the Joint Spectral Amplitude (JSA) of the process. Specifically, we rely on the so-called metallic waveguide approximation, neglecting the graded-index feature in our simulation. Additionally, our calculations do not account for temperature dependencies.

We begin by defining several key parameters: the transverse dimensions and the length of the waveguide, and the spectral characteristics of the pump. With these parameters in mind, we compute the joint spectral amplitude $L(\omega', \omega)$. We then transform it into its

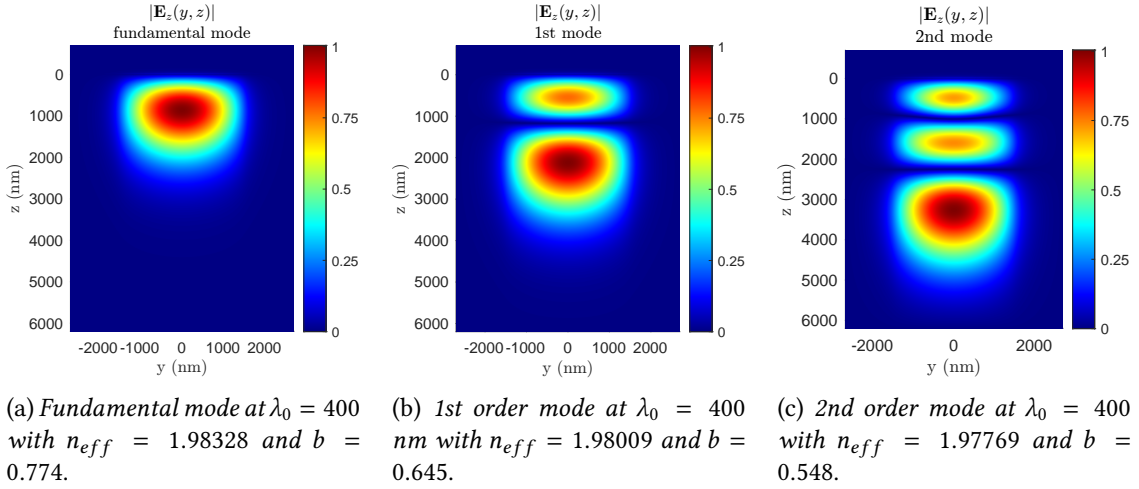
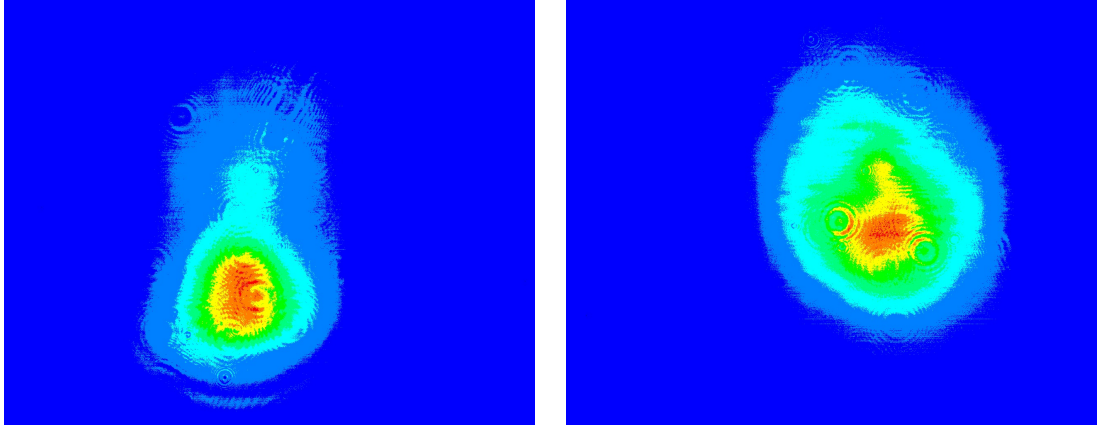


Figure 4.10: Simulation of the guided modes for light at $\lambda_0 = 400$ nm for $d = 4$ μm and waveguide width of 3 μm . The mesh graining is $\Delta y = \Delta z = 2$ nm.



(a) Emergence of the first order mode.

(b) Prevalence of the fundamental mode. The overlap with a TEM_{00} gives $w_x = 1740$ μm and $w_y = 1980$ μm .

Figure 4.11: Experimental waveguide output spatial mode at $\lambda = 795$ nm. Between figure (a) and figure (b) the input lens has been raised by 4 μm , increasing the injection point of the beam.

diagonal form to extract the eigenvalues and the corresponding eigenmodes of the process. As stated in section 3.3, we anticipate the supermodes to be Hermite-Gauss time-frequency modes. To quantify the effective number of modes, we introduce the Schmidt number represented as:

$$K = \frac{1}{\sum_i \Lambda_i^4} \quad (4.19)$$

Mode	$\lambda = 800$		$\lambda = 400$	
	n_{eff}	b	n_{eff}	b
Fundamental	1.84999	0.438	1.98328	0.774
1	1.84628	0.35	1.98009	0.645
2	-	-	1.97769	0.548
3	-	-	1.97658	0.504
4	-	-	1.97564	0.466
5	-	-	1.97351	0.380
6	-	-	1.97343	0.377
7	-	-	1.97123	0.288
8	-	-	1.97068	0.266
9	-	-	1.96925	0.209
10			1.96736	0.133
11			1.96704	0.120
12			1.96436	0.012
13			1.96427	0.009

Table 4.2: Effective refractive index n_{eff} and normalized propagation constant b of guided modes, for a 3- μm -width waveguide with $d = 4 \mu\text{m}$.

where K is the effective number of squeezed modes of the state, while Λ_i are the eigenvalues of the JSA, whose distribution reflects the distribution of squeezing values [Brecht 14, Roman-Rodriguez 21]. In Fig. 4.12 we show the eigenvalue distribution and the first three eigenmodes, that, as expected, turn out to be Hermite-Gauss frequency modes for our current setup, where we satisfy the gaussian pump approximation.

We remind that our primary objective in this context is to generate multimode squeezed states of light. However, in the frequency domain there is a tradeoff between the number of generated squeezed modes and the level of squeezing per mode. In other words, a higher number of modes results in a lower squeezing level per mode, assuming all other parameters, such as process non-linearity and waveguide length, remain constant [Kouadou 23]. For this reason, it is important to understand the relation that exists between waveguide parameters and the number of generated modes. The simulation provides valuable insights into the number of generated squeezed states (in the supermodes basis), the relative squeezing levels in each mode, and the spectral shape and bandwidth of the supermodes.

Once the length of the crystal is fixed, we can only act on the pump to modify the outcome of the generation. Indeed, while we also have the option to choose from different transverse sections (2,3,4 μm), we have observed that this has a negligible impact on the number of modes and their spectral width. In Fig. 4.13 and 4.14, we present the dependence of the number of modes and of the spectral width of the squeezed light on the pump width.

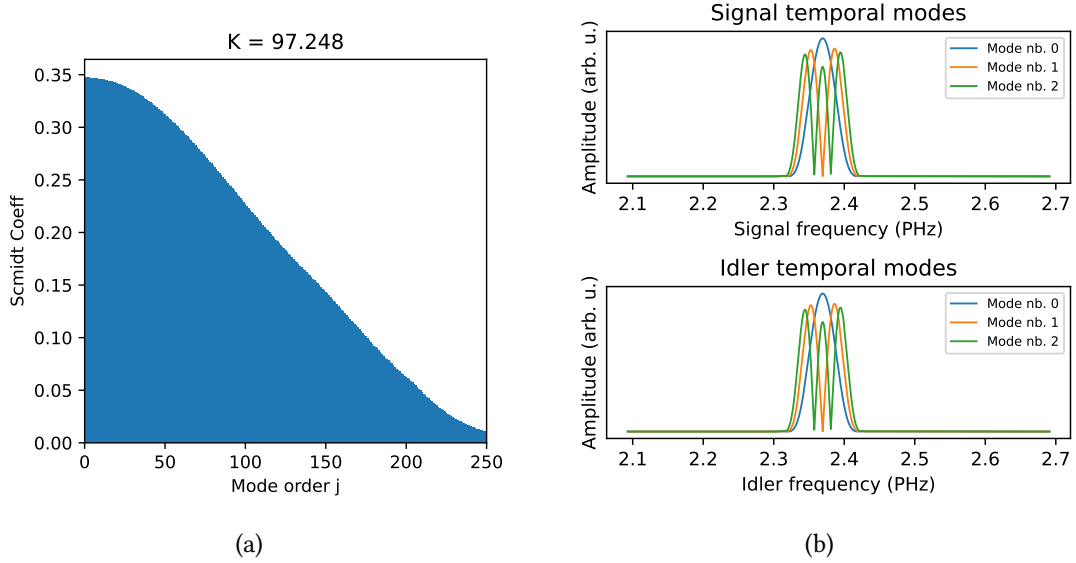


Figure 4.12: (a) Eigenvalues and (b) absolute value of the electric field amplitude of the first three eigenmodes for a type-0 SPDC process in a KTP waveguide of $L = 1$ mm and transverse dimensions $3 \times 5 \mu\text{m}$ in the metallic waveguide approximation. The pump bandwidth here is 0.7 nm (intensity FWHM).

We observe that the number of modes reaches a minimum for a pump width of $\Delta\lambda \sim 0.3$ nm (intensity FWHM). However, this corresponds also to the condition of maximum width for the generated squeezed light, that reads $\Delta\lambda \sim 26.5$ nm. It is worth mentioning that the generated light should not be excessively broad, as this would limit the number of accessible modes during the measurement stage, due to the finite bandwidth of the local oscillator.

The choice of the second-harmonic crystal plays a central role in determining the spectral characteristics of the pump for the SPDC process, which, in turn, determines the number and the spectral properties of the supermodes. This is why a careful choice of the SHG crystal is required. In this work, we settled on a 0.7-nm-wide pump, which provides a suitable balance between the number of generated modes (approximately 98) and their width.

4.3.4 Waveguides injection and characterization

The fabrication process of the waveguide chip is not ideal and this results in potential variations between individual waveguides. Consequently, upon receiving a new waveguide chip, the initial step involves assessing the characteristics of each waveguide, to identify the most suitable waveguide for generating squeezing.

Waveguide injection requires precise positioning tools. The waveguide chip itself is mounted on a 6-axis stage, which is composed of a high-precision 3-axis translation stage

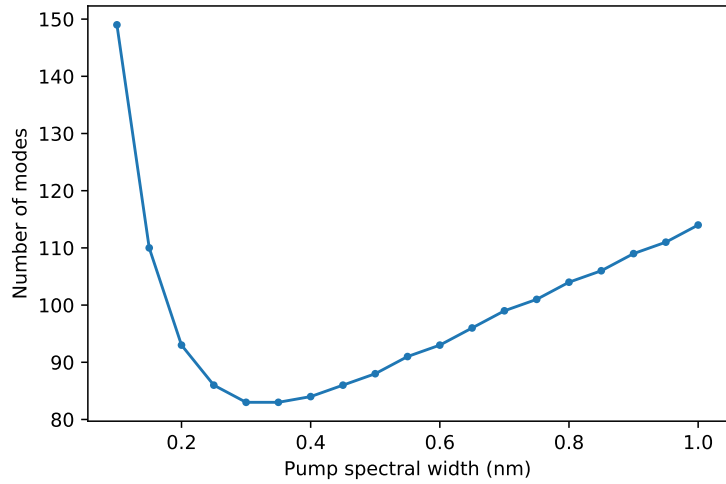


Figure 4.13: Number of generated squeezed modes as a function of the pump width (in FWHM) for a crystal of length $L = 1$ mm and transverse dimensions of $3 \times 5 \mu\text{m}$.

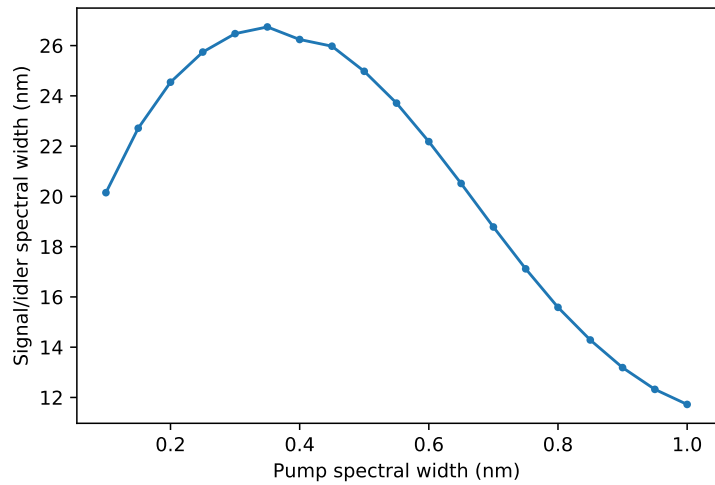


Figure 4.14: FWHM of the intensity of the generated signal/idler field as a function of the pump width (in FWHM) for a crystal of length $L = 1$ mm and transverse dimensions of $3 \times 5 \mu\text{m}$.

and a 3-axis rotation stage. The input lens is mounted on 3-axis translation stage, while the output lens only translates along the z -direction. Moreover, both the input and the output lens frames have xy alignments screws. The waveguide chip is positioned on a temperature-controlled oven, where the temperature is set at $T = 89^\circ\text{C}$. This is the working temperature provided by AdvR Inc., which corresponds to the temperature for achieving maximum SHG efficiency. However, this temperature setting may require adjustments when working with more than one waveguide, depending on the specific characteristics of each chip, as discussed in detail in Chapter 6.

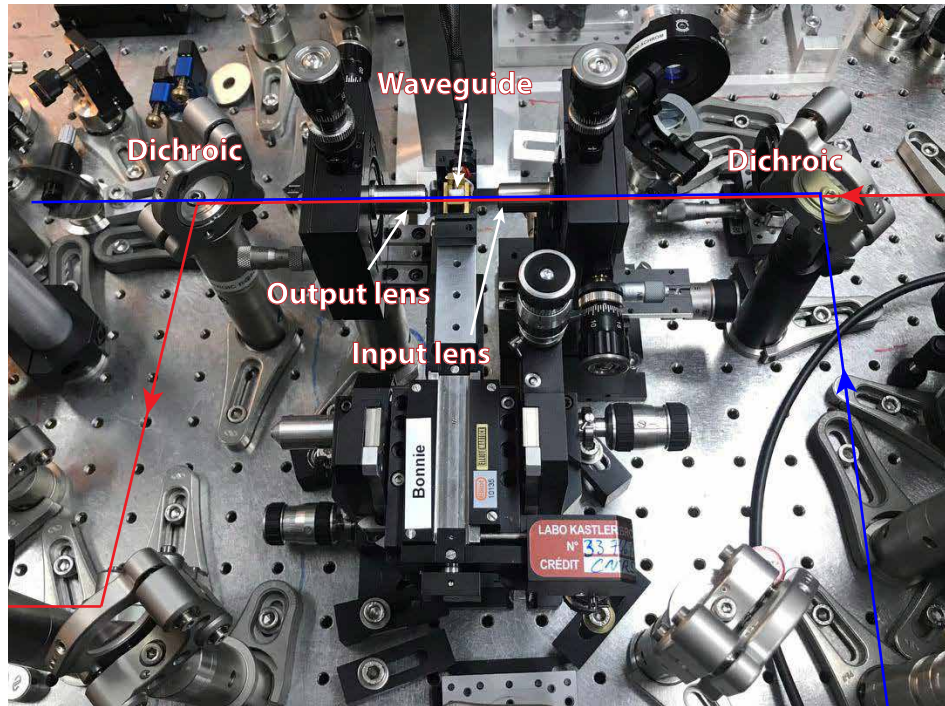


Figure 4.15: Setup for the injection of waveguides. The input dichroic is used to mix the pump and seed beam, while the output dichroic is used to discard the pump.

Due to the beam's small waist in the waveguide, typically a few micrometers in size, the focal lengths required for focusing the seed beam into the waveguide are very short, on the order of approximately 10 mm. In our setup, we have chosen an achromatic lens with $f = 15$ mm as the input lens, that allows for the simultaneous injection of both the pump beam and the seed beam. For the output lens, we use an aspheric lens with a focal length of $f = 11$ mm, equipped with an anti-reflective (AR) coating suitable for infrared light. The numerical aperture of the output lens is $\text{NA} = 0.30$. A high numerical aperture of the output lens is an important parameter for efficiently collecting all the light emitted from the waveguide. A picture of the experimental setup is shown in Figure 4.15.

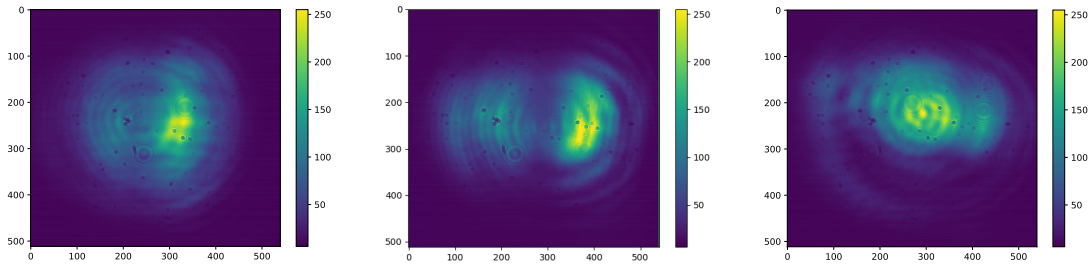


Figure 4.16: Example of the spatial modes in waveguide 14 ($3\ \mu\text{m}$), 16 ($2\ \mu\text{m}$), 24 ($4\ \mu\text{m}$).

Another critical parameter is the distance, denoted as d , between the output lens and the output facet of the waveguide. Even a slight deviation from the ideal position of $d = f = 11\ \text{mm}$ can result in a non-collimated beam. Achieving precise alignment of this parameter can be challenging, as it requires a high degree of precision. To address this, we employ a technique that we refer to as “back-propagation”, which involves injecting an infrared beam into the output facet. To do this, the LO beam is deflected using two flip-mirrors and directed into the output facet. The optimal position for d is determined when the transmission is maximized, meaning that it matches the focal length of the output lens.

Once light is injected, we begin by testing the input-output transmission of the waveguides. This is accomplished by simply measuring the ratio of output power to input power. Although there is some minor variation between different waveguides, they perform similarly¹, with transmission $>50\%$.

Next, we proceed to test the spatial modes of the waveguide, searching for the vertical position that enables single-mode propagation. This is an area where the waveguides differ significantly among each other. To give an example of the variety of modes that we may encounter when translating from one waveguide to another, see Fig. 4.16. Our goal in this step is to select waveguides in which the spatial modes closely resemble a gaussian shape, ensuring better overlap with the LO.

Finally, we examine the properties of the second-harmonic beam generated in the waveguide from the seed beam, verifying that it exhibits the typical sinc spectral shape associated to a second-harmonic beam. Moreover, measuring the efficiency of the waveguide second-harmonic generation we can make a rough estimation of the effective non-linearity of the process within the waveguide. However, this is assessed more accurately through parametric amplification, a topic we will explore in section 5.1.1.

We conclude this section by providing some general insights on laser-induced damage threshold (LIDT) for KTP. The laser-induced damage threshold (LIDT) of the waveguide

¹An exception is waveguide 29 and 30, which are not accessible, due to the crystal being damaged on the side.

is unknown, as it is far too dependent on the characteristics of the light source for the provider to be able to assess it correctly. Existing studies on the damage threshold of KTP are usually available regarding nanosecond or picosecond pulses and 1064 nm or 532 nm wavelength [Hildenbrand 08], with few studies exploring femtosecond pulses [Bach 16]. The surface LIDT is dependent on the AR coating, typically lower in coated optics compared to uncoated optics, which more closely align with the bulk material's LIDT [Bloembergen 74]. Moreover, as a general guideline, while keeping other parameters constant, the LIDT tends to decrease with longer wavelengths, a trend observed in various nonlinear crystals. [Yoshida 06]. Different damage mechanisms come into play depending on the pulse duration. For longer pulses, in the picosecond range, thermal breakdown resulting from multiphoton-absorption and avalanche ionization is the main cause of damage [Bloembergen 74]. In contrast, femtosecond pulses lead to optical damage through Coulomb explosion, where the buildup of electrostatic forces breaks the chemical bonds and fractures the crystal lattice [Wang 15].

4.4 Second-Harmonic generation via ppKTP

In this section, we provide an experimental implementation of the theory of second-harmonic generation (SHG) described in section 3.2. Understanding this process and the various parameters at play is important because we require the SHG light to have certain characteristics for it to be suitable to pump the SPDC process for squeezing generation.

Here, we present our experimental procedure for generating a light beam centered at 397.5 nm from a 795-nm source light. Additionally, we explore the spectral properties of the second-harmonic light, in relation to the characteristics of the nonlinear crystal.

4.4.1 The history of SHG in this setup

Initially, SHG in our setup was achieved using a BiBO crystal and relied on birefringent phase-matching [LaVolpe 19]. This method was employed in the early stages of our squeezing generation experiment. At that time, the second-harmonic beam had a spectral width of approximately $\Delta\lambda = 2.2$ nm (in FWHM of the intensity). Using this pump configuration for SPDC resulted in the generation of approximately 170 squeezed modes. Squeezing was experimentally observed in this configuration, with the leading mode exhibiting a squeezing level of 0.4 dB.

In order to reduce the number of modes, and to enhance the squeezing level, a spectral filter was placed in the second-harmonic light path, resulting in a narrower pump with spectral width of 0.7 nm (FWHM), corresponding to ~ 100 generated squeezed modes. However, this substantially reduced the average power of the pump, limiting it to a maximum value of ~ 6 mW of second-harmonic light. While this average power may suffice

for a single waveguide, it falls short if we intend to use multiple waveguide sources for implementing an entangled network, a topic that will be discussed in Chapter 6.

Additionally, the spatial properties of the second-harmonic beam generated by the BiBO crystal were ill-suited for injection into the waveguides due to birefringence-induced spatial walk-off. This walk-off effect, caused by the beam's non-collinear propagation through the crystal, resulted in an elliptical output beam with spatial chirp¹. Although some compensation for ellipticity was achieved using an anamorphic prism pair, the spatial chirp remained problematic.

A new SHG method was chosen to better align with the characteristics of the waveguide experiment, and periodically-poled KTP (ppKTP) was selected for SHG. Periodically-poled crystals, as previously explained in section 3.2.3, employ the quasi-phase matching technique to enable efficient SHG. The selection of ppKTP was based on three primary considerations. First, periodically-poled crystals allow the beam to propagate along a principal axis of the crystal, preventing unwanted spatial walk-off or spatial chirp effects associated with propagation in different directions in birefringent materials. Second, ppKTP has a high nonlinear coefficient for type-0 SHG process, resulting in high SHG efficiency. Finally, ppKTP offers a very narrow phase-matching bandwidth, as we will show in the next section, which aligns well with our experimental requirements. Indeed, we specifically require a narrow pump for the SPDC process to limit the number of generated spectral modes.

4.4.2 Simulation of the second-harmonic spectrum

The process we are interested in is type-0 SHG, primarily because it exhibits the highest nonlinear coefficient. We remind that in type-0 SHG, the interacting fields are all polarized along the z -axis of the crystal, as explained in section 3.2.

The refractive index along the crystal's z -axis is calculated using the Sellmeier equations for KTP [Kato 02]. The equation is given by:

$$n_z(\lambda) = \sqrt{a_k + \frac{b_k}{1 - \frac{c_k}{\lambda^2}} + \frac{d_k}{1 - \frac{e_k}{\lambda^2}} - f_k \lambda^2} \quad (4.20)$$

where the coefficients read $a_k = 2.12725$, $b_k = 1.18431$, $c_k = 5.14852 \cdot 10^2$, $d_k = 0.6603$, $e_k = 100.00507$ and $f_k = 9.68956 \cdot 10^3$ and where λ is in μm .

The poling period, denoted as Λ , is a crucial parameter for achieving quasi-phase matching in the crystal. It can be calculated using Eq. 3.43, and the calculated value is:

$$\Lambda = \frac{\pi c}{\omega_0} (n_{2\omega}(2\omega_0) - n_{\omega}(\omega_0)) = 3.19 \mu m \quad (4.21)$$

¹Spatial chirp refers to a specific type of spatiotemporal coupling in which various temporal frequencies are distributed or separated along a single transverse coordinate.

for a fundamental field centered at $\lambda_0 = 795$ nm and a second-harmonic field centered at $\lambda_0 = 397.5$ nm.

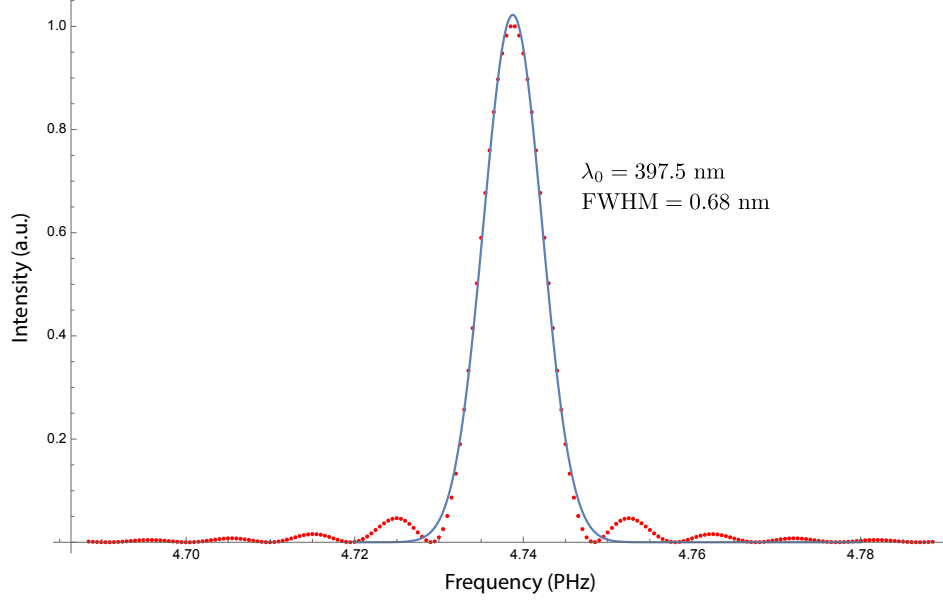


Figure 4.17: Simulation of the output second-harmonic generation spectrum for a 0.4 mm long ppKTP crystal, with a superimposed Gaussian fit in blue. The input field is centered at 795 nm and has a spectral width of 44 nm (intensity FWHM).

Adding the poling period term guarantees quasi phase-matching for the frequencies $2\omega_0$ and ω_0 , i.e. $\Delta k_{0th} \approx 0$. As we have a range of frequencies, being in the pulsed regime, we need now to look at the first order. Assuming $\Delta k_{0th} = 0$ and neglecting higher-order dispersion terms, from Eq. 3.33 we retrieve the phase mismatch at first order, that we rewrite here:

$$\Delta k(\omega) = \left(\frac{1}{v_g(2\omega_0)} - \frac{1}{v_g(\omega_0)} \right) (\omega - 2\omega_0) \quad (4.22)$$

where v_g indicates the group velocity, the velocity with which the pulse envelope propagates in the crystal. The group velocity for a pulse polarized along the z -axis is defined, as a function of the wavelength, as:

$$v_{g,z}(\lambda) = \frac{c}{n_{g,z}(\lambda)} = \frac{c}{n_z(\lambda) - \lambda \frac{\partial n_z}{\partial \lambda}(\lambda)} \quad (4.23)$$

where $n_{g,z}(\lambda)$ is the group velocity index and $n_z(\lambda)$ and $\frac{\partial n_z}{\partial \lambda}$ can be retrieved from Eq. 4.20. This permits us to calculate the phase-mismatch $\Delta k(\omega)$ and, consequently, the phase matching function $\Phi(\omega)$ defined in Eq. 3.29. From Eq. 3.41, we can calculate the field

Length (mm)	$\Delta\lambda$ (nm) (Simulated)	$\Delta\lambda$ (nm) (Experimental)
0.3	0.91	0.88
0.4	0.68	0.58
0.6	0.46	0.42
0.8	0.34	0.30
1	0.27	0.27

Table 4.3: Experimental and simulated width (intensity FWHM) of the second harmonic light intensity as a function of the ppKTP crystal length. The experimental results have been obtained using a crystal with $\Lambda = 3.15 \mu\text{m}$ and an input field centered at 796 nm with FWHM of 42 nm.

$A_{2\omega}(L, \omega)$ generated at the output of a crystal of length L . In Fig. 4.17, the expected output for a 0.4-mm-long crystal is shown.

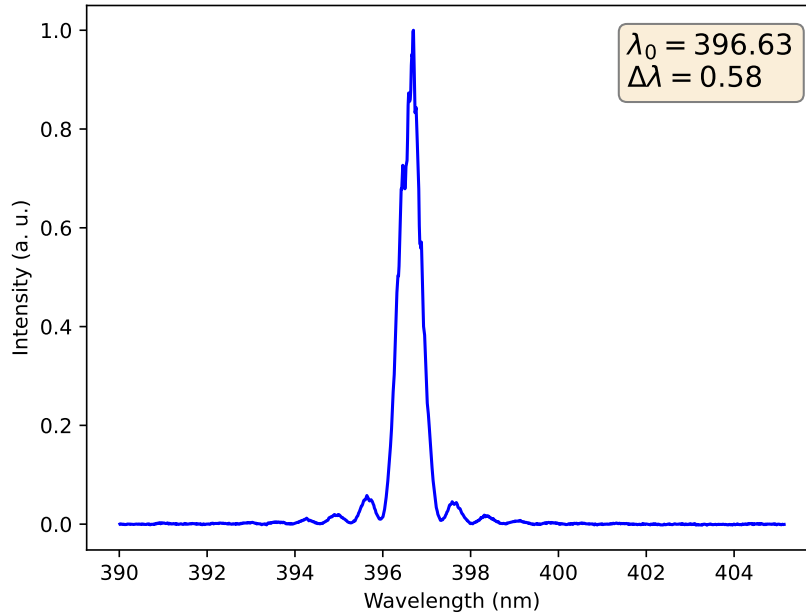


Figure 4.18: Experimental output SHG spectrum for a 0.4 mm long ppKTP crystal, in response to a fundamental field centered at $\lambda_0 = 795 \text{ nm}$ with a FWHM of 44 nm. The generated field features a central wavelength of 396.6 nm and a FWHM of 0.58 nm.

4.4.3 Experimental second-harmonic generation

The simulations show that second-harmonic light generated from ppKTP crystals features a narrow spectrum, typically with a FWHM shorter than 1 nm, confirming that the spectral characteristics of the ppKTP-generated second-harmonic beam are suitable for our experiment. The ppKTP crystals used in this experiment were supplied by Raicol Crystals and are employed in a type-0 nonlinear process. To achieve efficient SHG, both the 795-nm pump beam and the 397.5-nm second harmonic light must be polarized along the z axis of the crystal. In our experimental configuration, this z -axis polarization corresponds to a vertical polarization direction. Several ppKTP crystals have been tested in the lab, and the results are shown in Table 4.3, where they are compared with the results of the simulations.

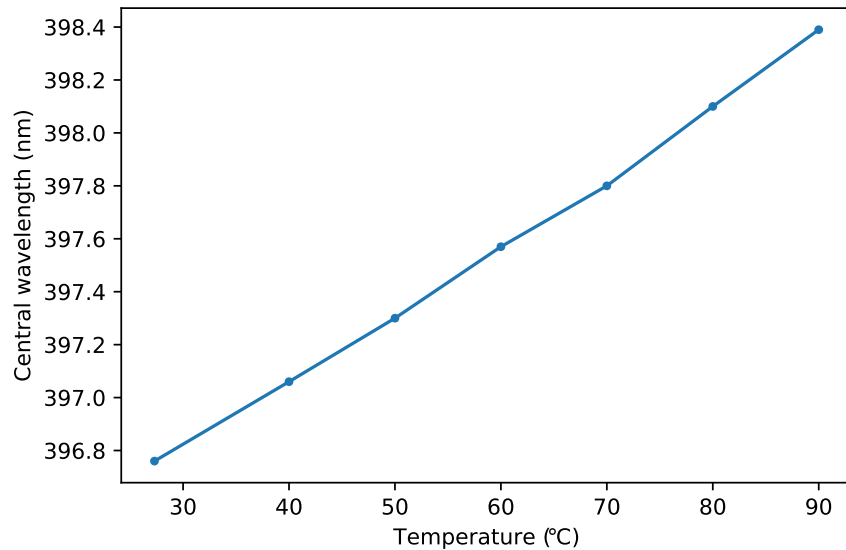


Figure 4.19: Dependence of the central wavelength of the SHG light with respect to the temperature of the crystal, with a fundamental field centered at 794 nm. The dependence is linear with a slope of 0.026 nm/°C

The poling period provided by Raicol Crystals is specified as $\Lambda = 3.15 \mu\text{m}$, only slightly different from the result of Eq. 4.21. The discrepancy may be attributed to variations in the specific models or characteristics of the KTP crystals used by Raicol Crystals in comparison to the reference in [Kato 02]. However, these small discrepancies do not significantly affect the results of SHG and may, at most, cause a shift in the central wavelength of the generated field. This shift can be adjusted by fine-tuning the phase-matching function, which is accomplished by altering the crystal's temperature.

We can finely tune the temperature by means of an oven that heats up the SHG crystal.

Increasing the temperature shifts linearly the central wavelength of the SHG light towards a bigger wavelength. This is known as non-critical phase matching and it employs the fact that the refractive indices are dependent on the temperature. We tested experimentally the dependence of the central wavelength to the temperature in our crystals. We measured that a change in temperature of $\Delta T = 10$ °C corresponds to a central wavelength shift of $\Delta\lambda = 0.26$ nm, as shown in Fig. 4.19. A change in efficiency can also be seen in the general case, but for our crystal it was not observed, probably due to the input pump being broad. The width of the second-harmonic light, at first order, is not affected by the temperature.

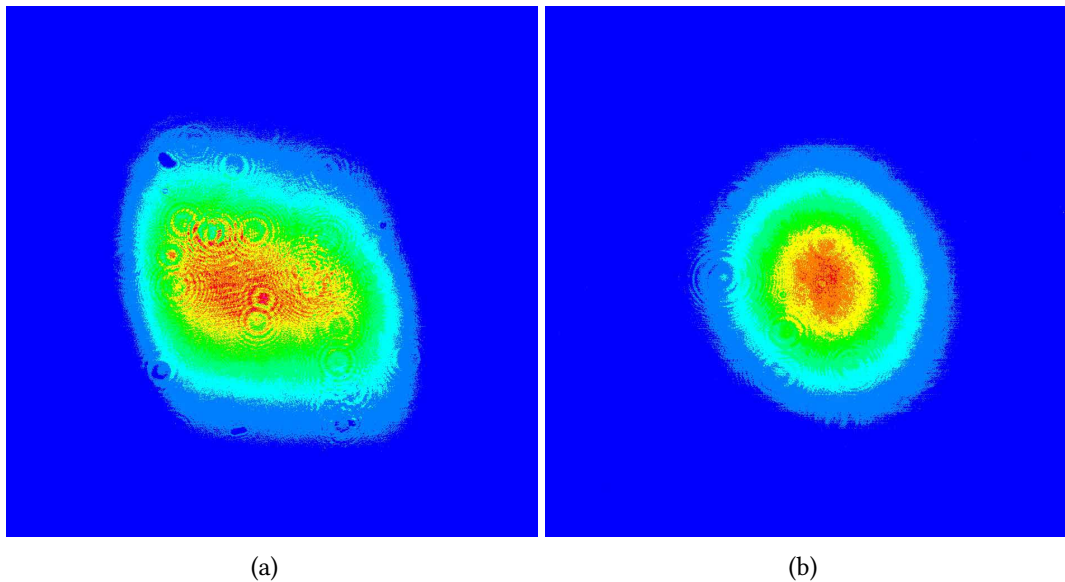


Figure 4.20: Experimental spatial transverse profile of the second-harmonic beam, generated from a) a 1-mm BiBO crystal employing bi-refrangent phase-matching and b) a KTP crystal.

Other than the spectral properties of the second-harmonic light, also the spatial characteristics of the beam have been analyzed. The spatial profile is an important feature for injection in waveguides, and we especially wish to avoid spatial chirp phenomena, that can be present in the case of birefringent phase-matching. The comparison between the spatial profile of the beam generated from the ppKTP crystals and one generated from a 1-mm BiBO crystal (via birefringent phase-matching) are shown in Fig. 4.20. We observe that the ppKTP beam approximates more closely a Gaussian profile, while in contrast the BiBO-generated beam shows distortion, due to spatial walk-off. In addition, spatial chirp has not been observed in the case of the ppKTP crystals, differently from the BiBO case, where spatial chirp was observed, primarily in the vertical direction [LaVolpe 19].

We conclude that the most suitable crystals for squeezing generation are the 0.4 and the 0.6 crystals, that show a good compromise between the efficiency, the peak power of

the pulse and the number and, as seen in in section 4.3.3, the spectral width of generated squeezed modes. In response to an input power of 330 mW, the 0.4 and 0.6 show a SHG of respectively 55 mW and 65 mW, which is enough for providing pumping beams for multiple waveguides.

We make a final remark. The generated SHG pulses, which are to be used to pump for the SPDC process, cannot be reduced to a Fourier transform limited form¹, due to the difficult task of building a pulse compressor for 397.5-nm light. Measuring the pulse duration for a blue pulse with our characteristics is not possible in the current setup. In fact, commercially available ultrashort pulses measurement techniques [Trebino 00] require larger power to work at this wavelength. Spectral interference techniques with a reference pulse are another alternative [Ansquer 22, Thiel 15], but given the narrow spectrum of our second-harmonic light, they would require a spectrometer with a better resolution than the one that we have in the setup.

4.5 The pulse shaper

In this section, we describe the basics of ultrafast pulse shaping, i.e. the temporal and spectral shaping of femtosecond pulses. As discussed in previous chapters, the quantum features of interest are associated with Hermite-Gauss (HG) spectral-temporal modes. Since homodyne detection is a projective measurement, it is necessary to effectively shape the time-frequency modes of the local oscillator, in order to access individual HG modes of light, or their linear combinations. Pulse shaping emerges as a valuable tool for accessing the quantum properties stored in temporal-frequency modes. This technology is well-established in the femtosecond regime and it relies on Fourier-transform techniques. An extensive review on ultrafast pulse shaping can be found in [Monmayrant 10, Weiner 11].

4.5.1 General introduction

Pulse shaping can be achieved by applying a linear-time invariant filter on an input pulse, whose behaviour is described by the convolution:

$$E_{out}(t) = h(t) * E_{in}(t) = \int_{\mathbb{R}} d\tau E_{in}(\tau)h(t - \tau) \quad (4.24)$$

For a given input signal $E_{in}(t)$, the output signal $E_{out}(t)$ is entirely determined by the response function $h(\tau)$. The limits of a pulse shaping device are defined by how accurately we can implement $h(t)$ and by how quickly our response function can operate. Creating

¹The SPDC pump will have a quadratic spectral phase resulting from the propagation of the beam in various media. These media include the ppKTP SHG crystal, the waveguide injection lens and the waveguide ppKTP crystal, along with various optics placed on the pump path, such as mirrors and lenses.

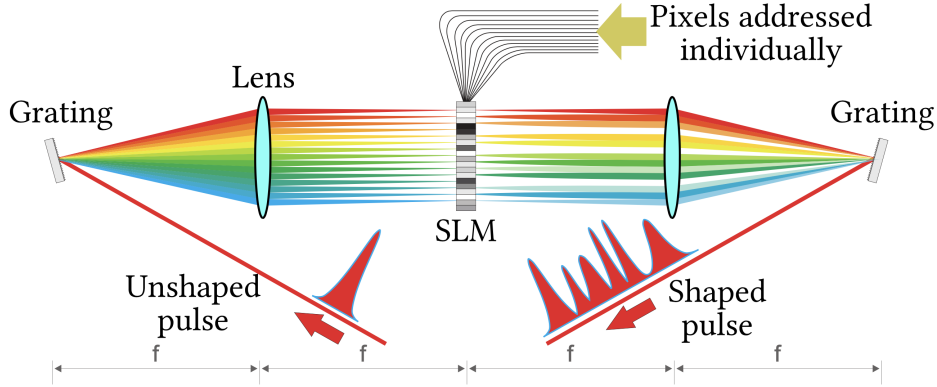


Figure 4.21: Scheme of a the femtosecond pulse shaper.

an appropriate $h(t)$ in the time domain for shaping femtosecond pulses is extremely complex [Monmayrant 10]. Therefore, we turn to the frequency domain to manipulate ultrashort light pulses. In the frequency domain, linear filter input-output equations take the form:

$$E_{out}(\omega) = h(\omega)E_{in}(\omega) \quad (4.25)$$

Successfully implementing $h(\omega)$ to achieve the desired $E_{out}(\omega)$ leads to the realization of $h(t)$ in order to attain the desired $E_{out}(t)$.

To implement a suitable frequency response $h(\omega)$, we build a dispersion-free 4-f line scheme, with two lenses, two diffraction gratings and a spatial light modulator (SLM), as shown in picture 4.21. The first diffraction grating is used to spatially disperse the various frequency components, and the first lens collimates them on the SLM screen, where each component is addressed by individual pixels. This way, the phase of each spectral component can be tuned. We will see that using a 2D pixel configuration enables us to tune also the spectral amplitude. After being diffracted by the SLM, the beam is refocused onto the grating and recombined [Weiner 88].

4.5.2 Spectral phase and amplitude shaping

The spectral phase $\phi_i(\omega)$ of each spectral component i can be tuned by changing the voltage applied to the liquid crystals of the SLM, as shown in Fig. 4.22. Indeed, the molecules of the liquid crystal rotate according to the applied voltage, modifying the refractive index of the medium. Applying different voltages to different pixels, each spectral component will have a different spectral phase, resulting in the desired outcome for the overall spectral phase $\phi(\omega)$ after the recombination of the beam.

In principle, a LC (liquid crystals) SLM acts like a phase modulator, but not as an amplitude modulator. However, using a 2D-LC-SLM we can achieve also amplitude modulation of the pulse [Vaughan 05]. For this purpose, the various spectral components

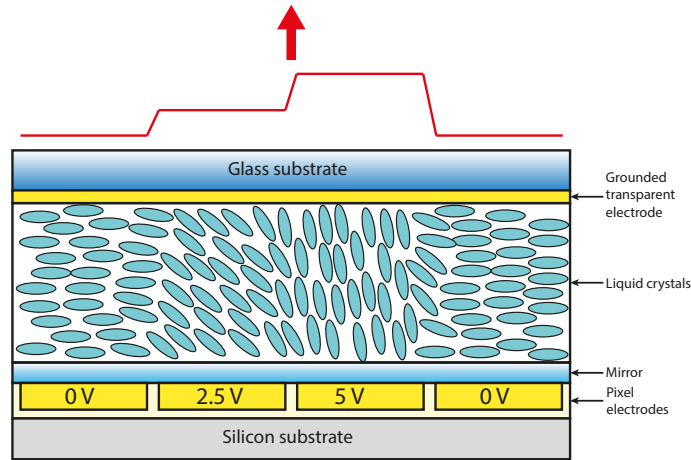


Figure 4.22: Structure of SLM pixels.

are spatially dispersed on the horizontal direction, and we employ the vertical direction of the SLM for amplitude modulation, by applying a blazed grating phase mask, that effectively acts as a physical blazed grating.

A blazed grating is a particular type of diffraction grating, that features a sawtooth pattern, designed to optimize diffraction efficiency in a specific diffraction order. As in every blazed grating, the diffraction angles depend on the period d of the pattern, while we can tune the intensity of light present in diffraction order 1 by acting on the depth A of the sawtooth function. In our case, we select only the first order of diffraction with spatial filtering. When the pattern has a depth of $A = 1$, corresponding to a phase difference along a tooth of $\Delta\phi = 2\pi$, the intensity in the first order of diffraction is maximized. Moreover, the sawtooth pattern can also be shifted as a whole vertically, creating a global phase shift ϕ_0 of the beam, resulting in an output spectral phase of $\phi(\omega) = \phi_0$. This is summarized in Fig. 4.23. Adding a global phase to the beam doesn't seem very interesting, but this property is actually very promising if we are able to address each wavelength, i.e. each pixel column, separately. Indeed, shifting the sawtooth pattern differently for each pixel column permits us to tune the phase for each spectral component. For example, a linear shift of the sawtooth pattern has the effect of introducing a first-order spectral phase of the form $\phi(\omega) = \phi_1\omega$, where $\phi_1 = d\phi/d\omega$. Quadratic and cubic shifts are also possible, so that we can introduce (or compensate) a quadratic or a cubic spectral phase in our beam. Examples of different patterns of the phase mask are shown in Fig. 4.24. Additional details can be found in [Jacquard 17].

To summarize, the capability of controlling the amplitude and the phase of the grating mask permits us to control the amplitude $A(\omega)$ and the spectral phase $\phi(\omega)$ of the light diffracted into the first order. This enables us to shape the pulse at will, within the limits of the pulse shaper performances.

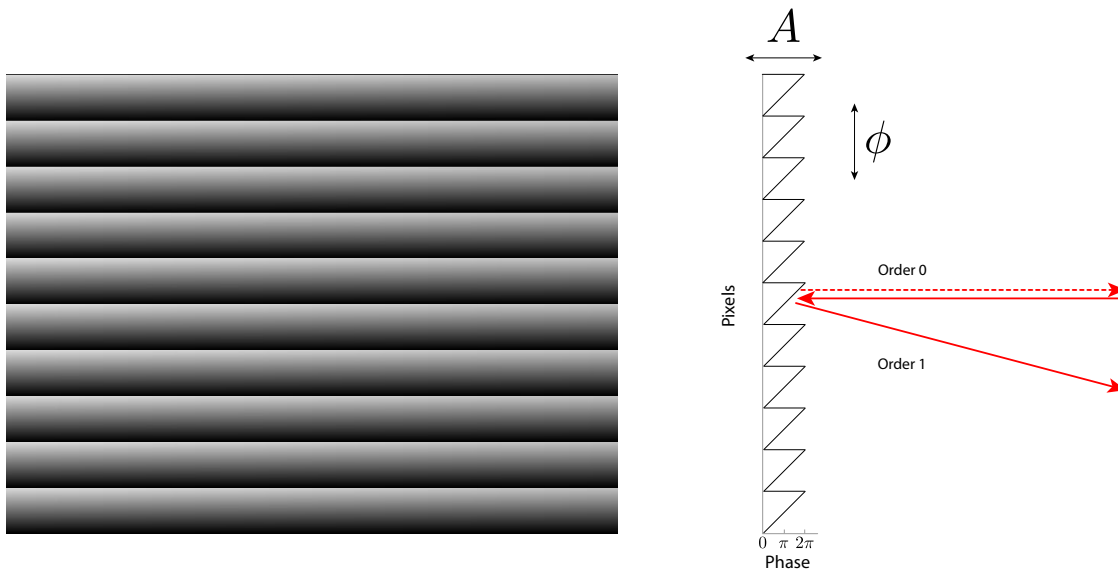


Figure 4.23: SLM blazed grating phase (left) and its effect on the incoming beam (right). The depth A of the sawtooth pattern accounts for the spectral amplitude, while the phase shift ϕ accounts for the spectral phase.

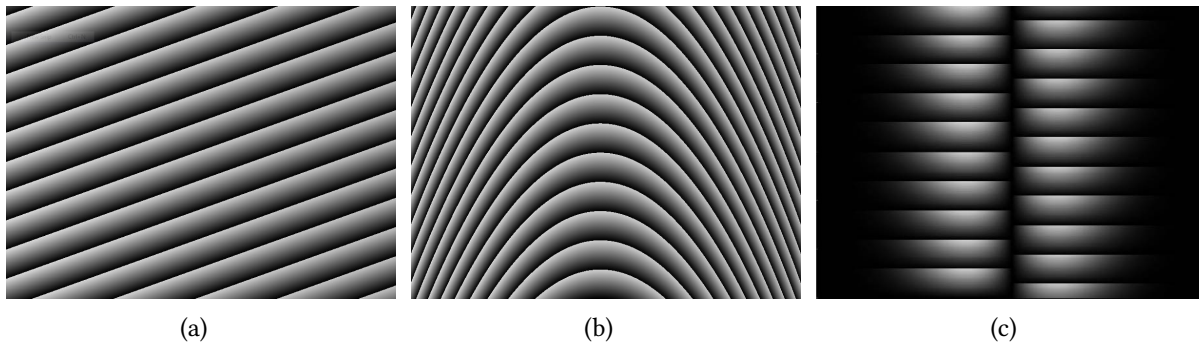


Figure 4.24: Different phase masks for the pulse shaper, that imprint different spectral phases and amplitudes to the output beam. (a) linear spectral phase (delay), (b) quadratic spectral phase (spectral chirp), (c) HG1 mask. Note that in (a) and (b) we don't act on the spectral amplitude.

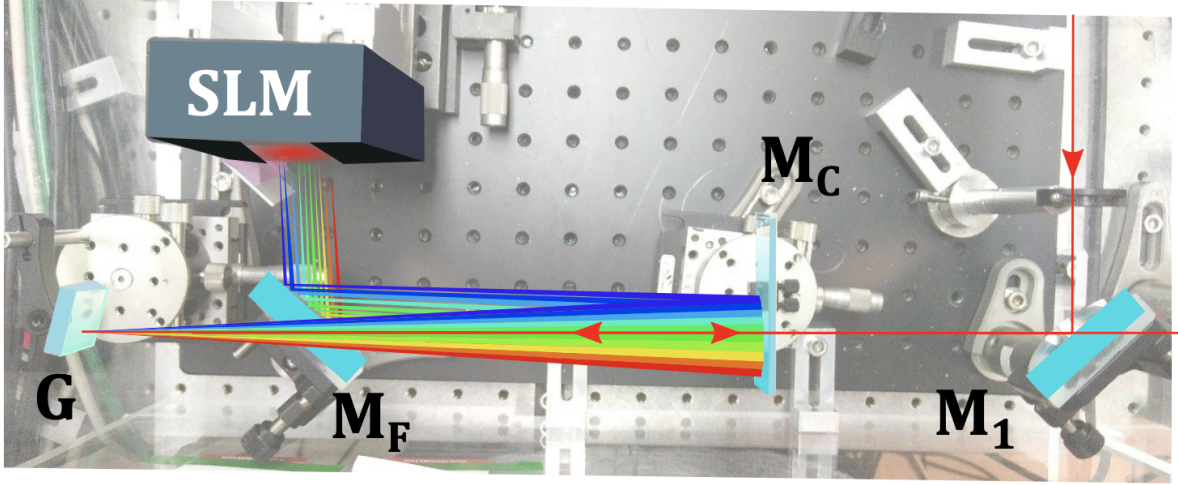


Figure 4.25: Pulse shaper in our setup, where G is a blazed grating, M_F is a HR mirror used for folding, M_C is cylindrical mirror used both for focusing and collimating the beam and M_1 is a half-cut mirror, that reflects the incoming beam while permitting to the output beam to be directed towards spatial filtering.

4.5.3 Characteristics of our pulse shaper

The pulse-shaper in our experiment is configured in a folded geometry, as shown in Fig. 4.25, where a grating G with groove density¹ $g = 600$ grooves/mm and a cylindrical mirror of focal length $f = 250$ mm are employed to disperse the wavelength on the SLM pixels. Subsequently, the beam is diffracted by the sawtooth pattern of the SLM, it encounters the same cylindrical mirror and grating of the incoming beam and it is therefore recombined and collimated. The SLM has a vertical tilt, so that the output beam can be easily separated from the incoming beam. The SLM is a 2D-LCOS-SLM X10468 (Liquid Crystal On Silicon) from Hamamatsu. The waist of the incoming beam is expanded to the $w_{in} = 2.6$ mm value by three curved mirrors placed before the pulse shaper. In Table 4.4 we collect the parameters of our pulse shaper and of the incoming beam in our setup. From all these parameters, it is possible to calculate the performances of our pulse shaper and assess how well it can shape our 22-femtosecond light.

The performances of the pulse shaper are limited both by the finite pixel size and by the finite size, due to diffraction, of each spectral component on the SLM. The size of the beam spot on the SLM in intensity FWHM is given by:

$$\Delta x_0 = 2 \ln 2 \frac{\cos \theta_{in} f \lambda_0}{\cos \theta_{out} \pi \Delta x_{in}} \quad (4.26)$$

¹Sometimes in the literature the grating period instead of the grating density is used. One is the inverse of the other.

pulse shaper geometry		beam characteristics	
LCD size	15.8 mm	λ_0	795 nm
pizel size	0.02 mm	$\Delta\lambda$	42 nm
f	250 mm	ω_{in}	2.62 mm
g	600 gr/mm		
θ_{in}	16°		
θ_{out}	10°		

Table 4.4: Parameters of the pulse shaper geometry and the incoming beam. In the pulse shaper, f is the focal length of the cylindrical mirror, g is the density of grooves of the grating, θ_{in} and θ_{out} are the angles of the incoming and diffracted beam on the grating. For the beam λ_0 is the central wavelength, $\Delta\lambda$ is the spectral width and ω_{in} is the waist of the incoming beam on the SLM.

where $\Delta x_{in} = w_{in} \sqrt{2 \ln 2}$ is the size of the incoming beam (in intensity FWHM), as prescribed from Eq. 1.26. According to the parameters of our setup, we obtain $\Delta x_0 = 27.7 \mu\text{m}$, that with respect to the pixel size reads $\Delta x_0 = 1.38$ pixels. We conclude that the limiting factor for the resolution of our pulse shaper is the finite size of the beam due to diffraction, not the pixel size¹. We define the coefficient α : d

$$\alpha = \frac{\lambda_0^2 f g}{2\pi c \cos \theta_{out}} \quad (4.27)$$

that, substituting our parameters, reads $\alpha = 5.11 \cdot 10^{-14}$ mm·s. The frequency resolution is given by:

$$\delta\omega = \frac{\Delta x_0}{\alpha} \quad (4.28)$$

For our setup, the frequency resolution reads $\delta\omega = 0.543$ THz; this represents the smallest feature that can be imprinted in the light beam by the pulse shaper.

It is interesting to calculate a parameter known as *optical complexity*, that evaluates the ratio between the biggest features and the smallest features that can be cast onto light. This gives us an indication of the number of Hermite-Gauss modes that we are able to shape. Optical complexity is defined as:

$$\eta_{opt} = \frac{\Delta\omega}{\delta\omega} = \frac{\Delta\lambda}{\delta\lambda} \quad (4.29)$$

¹If $\Delta x_0 < \Delta x_{px}$, where Δx_{px} is the size of the pixel, then the pixel size is the parameter limiting the resolution of our pulse shaper. In such case, the calculations of this section are to be carried on with the value Δx_{px} substituting Δx_0 in the equations. The complexity that we calculate in this case is called *pixel complexity* and it is designated as η_{px} [Michel 21]

where in our case $\Delta\omega = 125$ THz (which corresponds to $\Delta\lambda = 42$ nm). We obtain an optical complexity of $\eta_{opt} \sim 231$. More details on the pulse-shaper used in this experiment, such as its optimization and its alignment, can be found in [Kouadou 21, LaVolpe 19].

Chapter 5

Measuring multimode squeezing multiplexed in time and frequency

Contents

5.1 Alignment procedure	119
5.1.1 Parametric amplification	120
5.1.2 Visibility between seed and LO	122
5.2 Measuring squeezing	125
5.2.1 Sidebands measurement	125
5.2.2 Temporal measurement: alignment and mode definition	126
5.2.3 Temporal measurement: measurement and results	128
5.3 Covariance matrix reconstruction	130
5.3.1 Covariance matrix measurement	131
5.3.2 Supermodes reconstruction	134
5.3.3 Bipartite entanglement in the frexel basis	136

After describing in detail all the experimental components, here we elaborate on how these components work together to measure multimode squeezing in time and frequency. We will cover the alignment steps, emphasizing the most important alignment parameters, and ultimately we will present the experimental results for both spectral homodyne detection and time-resolved homodyne detection, whose principles have been discussed in section 2.3. These results have been published in [Kouadou 23], where me and Tiphaine Kouadou share the first co-authorship.

5.1 Alignment procedure

In section 4.1, we mentioned that temporal and spatial alignment, performed using the seed beam, is a crucial step of the experiment. In this section, we outline the main alignment steps

that are needed to achieve temporal and spatial matching. This requires careful adjustment of many different experimental parameters.

5.1.1 Parametric amplification

The parametric amplification process, detailed in section 3.3, plays a fundamental role in the alignment procedure. We recall that this process, also known as parametric down-conversion (PDC), is a three-wave mixing process involving the interaction of three fields: the signal, the idler, and the pump beam. In our case, we are dealing with a degenerate process, meaning that the signal and idler fields are indistinguishable. In this work, when dealing with degenerate parametric amplification, we will refer to this beam as the *seed* beam. For the process to take place, both the seed and the pump beam are injected into the waveguide. During the actual squeezing measurement, blocking the seed and allowing only the pump beam to be injected in the waveguide leads to spontaneous parametric down-conversion (SPDC) and the generation of squeezed light. Degenerate PDC is phase sensitive: scanning the phase of one of the two beams, either the seed or the pump, results in oscillations in the intensity of the seed beam, shifting between points of maximum amplification and deamplification.

For parametric amplification to take place we need to meet two requirements: 1) the pump and seed beams must be collinear within the nonlinear crystal (spatial matching), and 2) their pulses must arrive simultaneously in the crystal (temporal matching). To achieve spatial matching, we must carefully select the input lens in order to minimize the focal shift between the pump and the seed wavelengths. We employ an achromatic lens with a focal length of 15 mm, as discussed in section 4.3.4. This lens exhibits a minimal relative focal shift of only 0.003 mm between the two wavelengths¹. The blue and infrared light are directed towards the input lens using a dichroic mirror, that transmits the seed wavelength and reflects the pump wavelength, as it is shown in Fig. 4.15.

The alignment procedure follows. First, the seed is injected into the waveguide and the output power is optimized, to achieve a typical transmission of 55%. Next, the 397.5 nm pump light is superposed with the seed. The combined beam is then vertically adjusted by raising the input lens by 4 μm . This vertical displacement has been chosen to promote the best single-mode operation for the infrared beam. After coarse spatial alignment is achieved, we concentrate on temporal matching. While temporal matching, on a day-to-day basis, is easy to retrieve, finding it from scratch can be quite challenging. Usually, for matching pulses of light we use interference patterns. However, we cannot directly interfere the seed and the pump and we have to find a workaround. We begin by roughly matching the seed and the pump paths using a fast photodiode. This method, while not very precise for femtosecond pulses, allows us to reach a configuration where the two pulses are separated

¹In previous tests, we experimented with a short focal aspheric lens that had a focal shift of 0.4 mm between 397.5 nm and 795 nm light. However, this focal shift was found to be detrimental for the injection process.

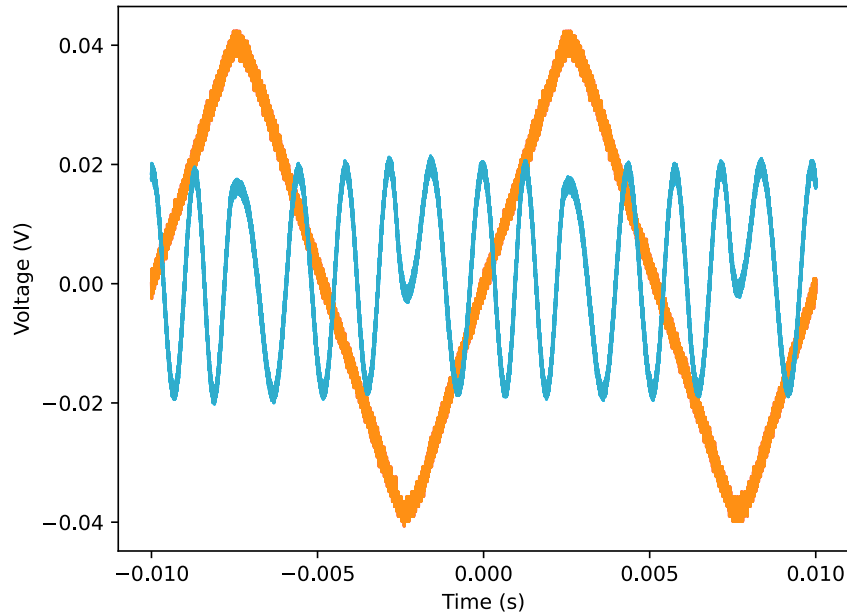


Figure 5.1: Typical curve of phase sensitive parametric amplification. The orange curve is the voltage ramp of the piezo actuator that scans the seed phase, while the blue curve is the seed intensity signal detected by a photodiode.

by a few centimetres. For fine alignment, we employ an interference effect at 397.5 nm. We replace the waveguide crystal with a bulk non-linear BiBO crystal, which is phase-matched for our wavelengths, and we send both the pump and the seed into it. The seed will stimulate the generation of a second-harmonic beam that will interfere with the pump beam. When using this method, we need to ensure that the spectral shapes of the pump and the generated SHG beam overlap, at least to some extent. To accomplish this, a 0.5-nm spectral filter is employed to select a common spectral band and eliminate portions of the spectra that are not in common, as they would add noise to the interference effect. We scan a translation stage placed on the seed path until interference patterns appear between the pump and the seed-generated second-harmonic beam; this indicates that the seed and the pump beams are temporally matched. The BiBO can be removed and the waveguide can be placed in its original position.

Daily alignment doesn't require this step. To achieve temporal matching on a day-to-day basis we adjust the seed translation stage until we observe the parametric amplification signal, directly assessed by measuring the intensity of the seed through a photodiode, while scanning the seed (or pump) phase at 100 Hz. A typical parametric amplification curve is shown in Fig. 5.1.

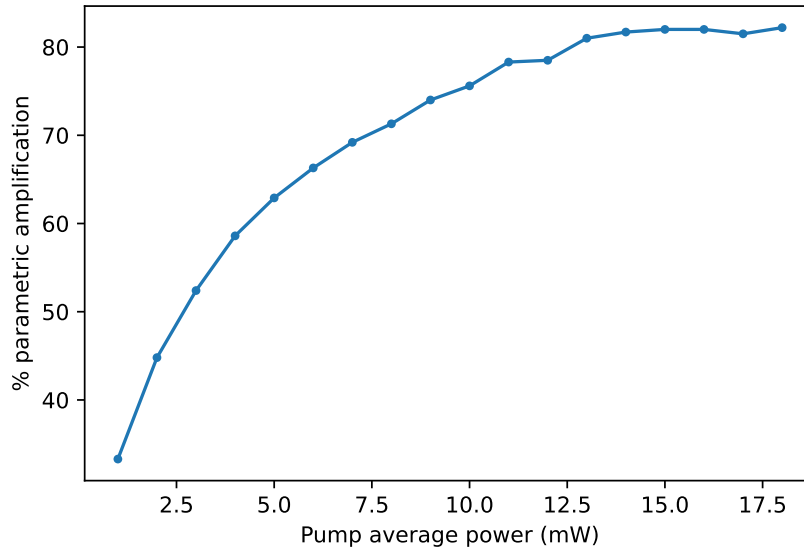


Figure 5.2: Dependence of the parametric amplification with pump input power, measured in waveguide 25.

After coarse temporal and spatial matching, the alignment is optimized by acting on the injection mirrors and on the seed translation stage several times, with the aim of maximizing the parametric amplification signal. Additionally, we make adjustments to the temperature of the SHG crystal to select the optimal central wavelength for the pump that better corresponds to the phase-matching conditions of the waveguide.

As a quantitative measure of parametric amplification we use the ratio between the signal peak-to-peak and the mean field. In the waveguide we are currently employing for squeezing generation, number 26, this can reach a value of 70% with 10 mW of input power. This value is highly dependent on the waveguide that we choose for the non-linear process; usually, smaller waveguides have higher parametric amplification gain. The typical dependence of the parametric amplification gain as a function of the pump power is shown in Fig. 5.2.

5.1.2 Visibility between seed and LO

Once temporal and spatial matching between the seed and the pump is achieved, we turn our attention to the detection process. Even this second alignment step has the purpose of ensuring temporal and spatial matching, but this time between the LO and the seed.

To reach this purpose, we measure the interference fringes between the seed and the LO at the output of the homodyne detector beam-splitter. We focus on maximizing the so-called

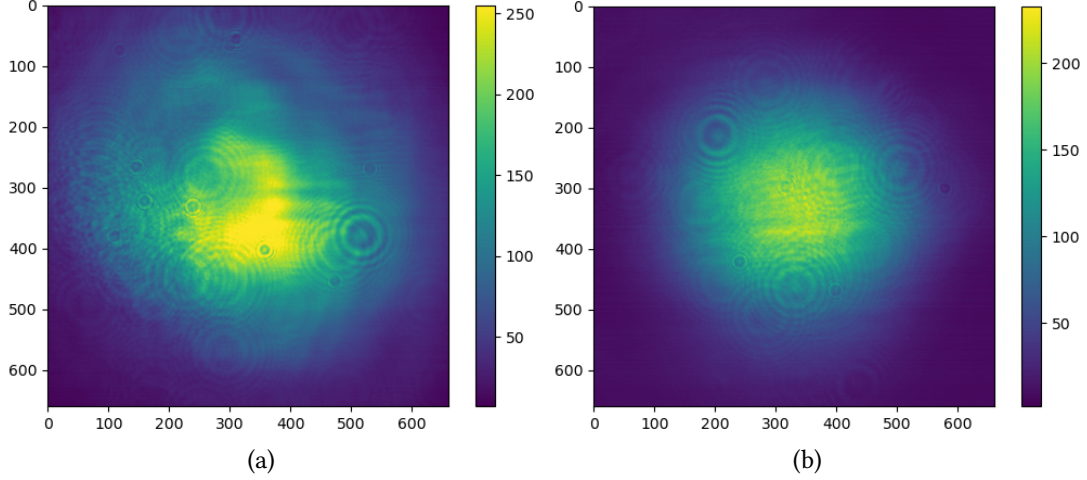


Figure 5.3: Seed (a) and LO (b) transverse spatial modes. The spatial overlap calculated numerically is 96%. When measuring visibility, the spatial overlap calculated numerically is to be considered as an upper bound.

visibility (sometimes referred to as *contrast*) of the interference fringes. The fringe visibility is defined as:

$$\mathcal{V} = \frac{I_{max} - I_{min}}{I_{max} + I_{min}} \quad (5.1)$$

where I_{max} and I_{min} are respectively the maximum and the minimum of the intensity oscillations. The visibility falls within the range $0 < \mathcal{V} < 1$ and it depends on both the LO and the seed characteristics, as expressed by:

$$\mathcal{V} = \frac{2\sqrt{I_s I_{LO}}}{I_s + I_{LO}} \Gamma \quad (5.2)$$

where I_s and I_{LO} are the intensity of the seed and the LO respectively. In this equation, Γ is a factor that accounts for the spectral and spatial matching of the two fields, defined as:

$$\Gamma = \left(\int_S dS f_s(\mathbf{x})^* f_{LO}(\mathbf{x}) \right) \left(\int_{\mathbb{R}} d\Omega u_s(\Omega)^* u_{LO}(\Omega) \right) = \gamma_S \cdot \gamma_{\Omega} \quad (5.3)$$

where γ_S and γ_{Ω} account respectively for the spatial and spectral overlap [Thiel 15]. Here, we make the assumption that the input field modes are factorized in transverse and longitudinal modes, denoted respectively with $f(\mathbf{x})$ and $u(\Omega)$, as defined in Eq. 1.19. Perfect spatial and spectral matching is achieved for $\gamma_S = \gamma_{\Omega} = 1$.

The alignment procedure begins by overlapping the seed beam and the LO beam on the 50:50 beam-splitter of the homodyne detection setup, shown in Fig. 5.4, and searching for interference fringes. Temporal matching between the seed and the LO is necessary, and it can be achieved by measuring the beams with a fast photodiode, to ensure that the

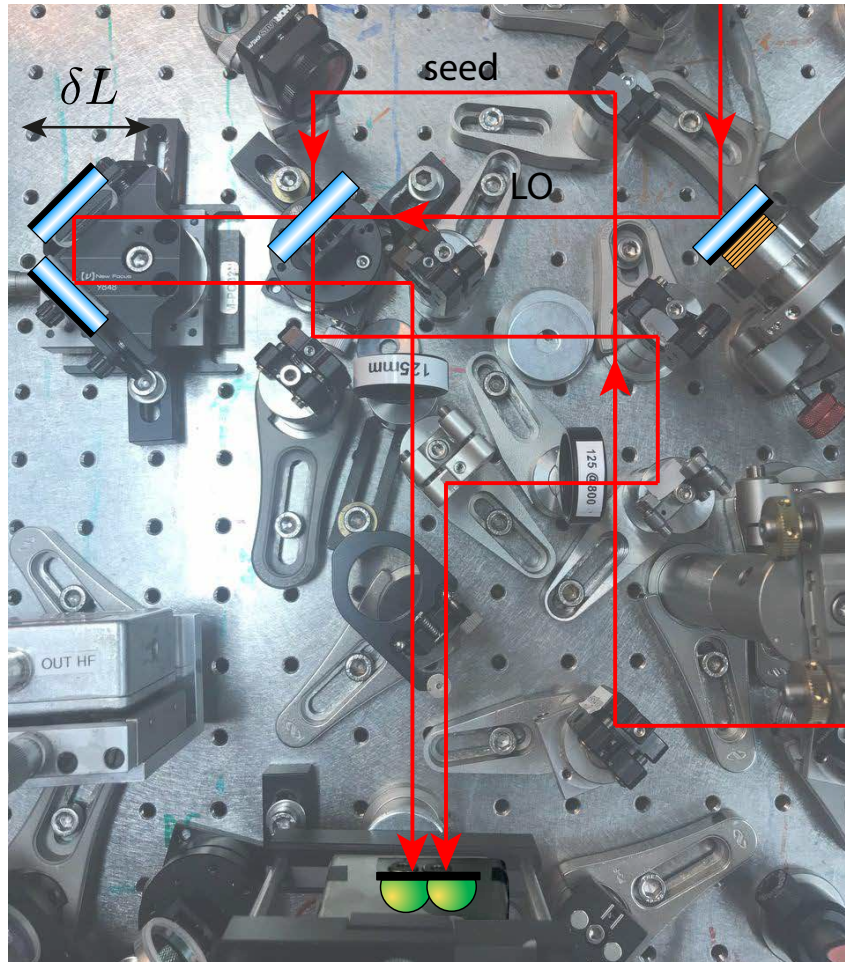


Figure 5.4: Homodyne detection setup. The seed and LO are mixed on a 50:50 beam splitter and a piezo actuator is placed on the LO path. The translation stage placed after the beam-splitter ensures that the pulses reach the photodiodes at the same time; this is an important point for the temporal squeezing measurement.

pulses from both beams arrive at the beam-splitter simultaneously. Fine-tuning the temporal alignment is performed by adjusting a translation stage along the LO path. Spatial mode matching is equally important. To achieve this, a telescope is placed in the LO beam's path, to resize it to match the dimensions of the seed beam. The two transverse beam profiles are then overlapped, and their average power levels are balanced.

We scan the phase of the LO at 300 mHz via a piezoelectric actuator placed in the LO path and we use a camera to observe the superposed transverse profiles of the seed and LO beams. Once the interference fringes appear, we adjust position of the beams to optimize the

visibility¹, until we reach the point in which we observe the transverse profile “blinking”. We then observe the intensity oscillations, measured with a photodiode, using an oscilloscope. We place a 3-nm bandpass filter in front of the photodiode, to minimize spectral mismatch effects on the visibility. Indeed, our primary focus in this step is on spatial matching, as the seed and the generated light share the same spatial mode (the fundamental guided mode) but do not have the same spectral structure. Spectral matching between the LO and the squeezed light will need to be optimized at a later stage.

Since the output lens has a short focal length, the seed beam diverges rapidly. However, in our setup configuration, the homodyne beam-splitter is at a distance of less than 1 m from the output of the waveguide, and it is not necessary to re-collimate the beam. After the beam-splitter, the modes have a high spatial overlap, as seen in Fig. 5.3. With careful alignment and the 3-nm spectral filter in place, we can reach a visibility of $\mathcal{V} = 0.9$.

5.2 Measuring squeezing

5.2.1 Sidebands measurement

In this work, we use the terms “sidebands squeezing” or “sidebands squeezing measurement” to describe the measurement of squeezed light conducted with the spectrum analyzer. As detailed in section 2.3.4, this type of measurement lacks the complete information about the quantum state, preventing quantum state reconstruction. However, when dealing with a squeezed vacuum state and aiming to retrieve only the level of squeezing, this method is suitable.

After completing the alignment steps outlined in the previous section, the seed is blocked, so that we transition from a PDC process to a SPDC process and to the consequent generation of squeezed light in Hermite-Gauss spectral modes. If the alignment has been done correctly, the pump is matched with the seed, the seed is matched with the LO, and as a consequence the multimode squeezed light (generated from the pump) matches with the LO. This involves both spatial and pulse matching, while spectral matching will be achieved later, as we will explain.

We shape the local oscillator as the Hermite-Gauss spectral mode of interest, choosing a specific width to maximize the squeezing level. Initially, we measure the shot noise level, i.e. the variance of the vacuum, by blocking the signal path and allowing only the LO to shine on the photodetectors. Then, we let the down-converted light mix with the LO and we observe the typical squeezing oscillations, as depicted in Fig. 5.5. We sweep the phase of the local oscillator with a piezoelectric actuator on the LO path at 300 mHz to access the variance of the generalized quadrature \hat{x}^ϕ . We label the quadrature with the lowest level of noise as p , the squeezed quadrature, and the quadrature with the highest level of noise as q , the antisqueezed quadrature. Finally, the squeezing level is optimized by adjusting with

¹The visibility is increased the more the fringes are big and spaced.

the pulse-shaper the spectral characteristics of the LO beam, such as central wavelength, mode width and spectral phase. Typical squeezing and antisqueezing values can be found in Table 5.1.

A comment on the results is required at this point. Despite tailoring the width of the pump to minimize the number of spectral modes generated in our setup, as discussed in section 4.3.3, the number of modes remains considerably high. For this reason, the squeezing per mode is expected to be low, even with the experiment being low-loss. Phase-matching function engineering, such as spatial modulation of the poling of the crystal, is an option and is currently investigated to reduce the number of generated modes [Dosseva 16, Ramos-Israde 21].

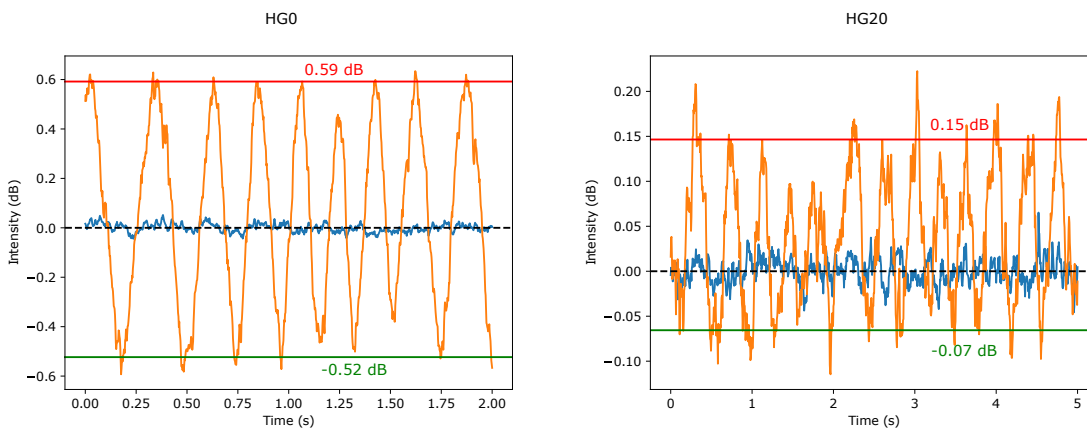


Figure 5.5: Typical squeezing oscillations (orange) obtained for the mode HG0 (left) and HG20 (right), the highest-order mode measured. The blue curve represents the shot noise averaged over multiple acquisitions, and the dashed black line is its mean value.

5.2.2 Temporal measurement: alignment and mode definition

The central result of this work is the simultaneous multiplexing of the spectral and the temporal degrees of freedom. To achieve this result, we need a time-resolving measurement device, such an oscilloscope, as we will work with the temporal modes $\hat{a}(t)$ defined by the pulse. We also need an ultrafast homodyne detector, with a bandwidth of at least 156 MHz. This detector has been implemented in our lab by Tiphaine Kouadou and it is one of the main subjects of her PhD manuscript [Kouadou 21].

When we measure squeezing in the time domain, we have to choose a real function $\varphi(t)$ that defines the mode of interest [Lvovsky 16]. The corresponding mode operators are defined as:

$$\hat{A} = \int_{\mathbb{R}} dt \varphi(t) \hat{a}(t) \quad (5.4)$$

mode	squeezing		anti-squeezing	
	average (dB)	error interval (dB)	average (dB)	error interval (dB)
HG0	-0.47	[-0.50, -0.44]	0.56	[0.55, 0.59]
HG1	-0.33	[-0.36, -0.30]	0.44	[0.40, 0.48]
HG2	-0.24	[-0.27, -0.21]	0.34	[0.27, 0.41]
HG3	-0.20	[-0.23, -0.17]	0.27	[0.23, 0.30]
HG4	-0.19	[-0.22, -0.16]	0.31	[0.27, 0.34]
HG5	-0.19	[-0.21, -0.17]	0.30	[0.28, 0.32]
HG6	-0.19	[-0.21, -0.16]	0.27	[0.24, 0.31]
HG7	-0.13	[-0.16, -0.09]	0.25	[0.23, 0.27]
HG8	-0.14	[-0.15, -0.13]	0.25	[0.22, 0.28]
HG15	-0.08	[-0.11, -0.06]	0.15	[0.13, 0.18]
HG20	-0.07	[-0.09, -0.05]	0.13	[0.11, 0.16]

Table 5.1: Typical values of squeezing in our setup for the squeezed and antisqueezed quadrature at sidebands frequency $\Omega = 50$ MHz. These values have been obtained with a 0.7-nm-wide pump and with an average pumping power of 6 mW.

and the associated generalized quadrature as:

$$\hat{X}^\phi = \int_{\mathbb{R}} dt \varphi(t) \hat{x}^\phi(t) \quad (5.5)$$

where $\hat{x}^\phi(t)$ is the generalized quadrature at time t , defined in Eq. 2.69. Here, $\varphi(t)$ represents the temporal response of the system, that is mainly limited by the electronics response. This is in any case shorter than the time between two pulses, so that we are not mixing signals from consecutive pulses. We will define the modes identified by the \hat{A} operators as *pulsed modes*. The homodyne detector produces an electrical pulse, the shape of which is defined by the response function. The magnitude of this pulse is directly proportional to the quadrature of interest [Lvovsky 16]. A theoretical analysis on the dependence of the measured mode with the characteristics of the detector, such as response function and bandwidth, can be found in [Kumar 12].

Time-resolved measurements are highly sensitive to the alignment of the homodyne detector and the bias voltage of the photodiodes. We start the alignment by balancing the power of the detected beams, by fine-rotating the beam splitter of the homodyne, and by aligning the beams to hit the center of the photodiodes. We verify and adjust the alignment by examining the DC output of the detector, aiming for a DC value of $V_{DC} \sim 0$ V¹. We

¹Usually, an offset value of the order of a few mW is observed without shining light on the detector, so this is the value we should aim at when we align.

then analyze the AC signal with the spectrum analyzer, focusing on the Common Mode Rejection Ratio (CMRR) at 156 MHz. The CMRR quantifies the efficiency of the subtraction of the photocurrents; a less intense CMRR peak indicates better subtraction. To minimize the CMRR we act on various parameters. We ensure that the pulses arrive simultaneously on both photodiodes by adjusting a translation stage, present in one of the two arms. Additionally, we adjust the bias voltage of the two photodiodes and fine-tune the alignment mirrors. These parameters require multiple adjustments to find the optimal configuration where the common mode rejection ratio is minimized. Empirically, we observe that when this occurs, the peak of the CMRR starts to oscillate. As a final check, by blocking first one photodiode and then the other, we confirm that the two peaks at 156 MHz from the two photodiodes have the same intensity.

After taking care of the minimization of the CMRR and the alignment of the detector, we can begin the measurement procedure. For each squeezed pulse of light i , our goal is to measure the quadrature:

$$\hat{X}_i^\phi \propto \int_{t_i}^{t_i+T} dt \varphi(t) \hat{x}^\phi(t) \quad (5.6)$$

where T is a time window containing the pulse. Each pulse then yields one quadrature value. Our initial step is to identify the time windows that are associated with the squeezed pulses. To accomplish this, we let the light shine only on the positive photodiode¹ and we mark the positions of the time windows corresponding to individual light pulses, as shown in Fig. 5.6. They will serve as a time reference for calculating quadratures of individual pulses during the squeezing measurement.

5.2.3 Temporal measurement: measurement and results

The AC output signal of the homodyne detector is sent through a notch filter, to get rid of the 156 MHz component, and an amplifier. It is then split, with one branch directed to the spectrum analyzer and the other to the oscilloscope. Since we do not lock the detected quadrature, the spectrum analyser is used to determine if we are probing the squeezed quadrature, the antisqueezed quadrature or any generalized quadrature in between. The trigger of the oscilloscope is set into “single” mode and synchronized with the spectrum analyzer; this allows us to freeze and save a “screenshot” of the subtracted intensity current that corresponds to the quadrature displayed on the spectrum analyzer screen. Generally, we set a longer sweep time for the spectrum analyser, ranging between 0.5 s and 1 s. This ensures that the 50-100 μ s of intensity noise recorded by the oscilloscope correspond to the first few points plotted on the spectrum analyzer. Measurements corresponding to intermediate values are discarded, and only data related to the squeezed and antisqueezed quadratures are retained. We collect also data relative to the vacuum (shot) noise, for

¹The positive (resp. negative) photodiode is the photodiode that displays a positive (resp. negative) voltage value when we let light shine on it.

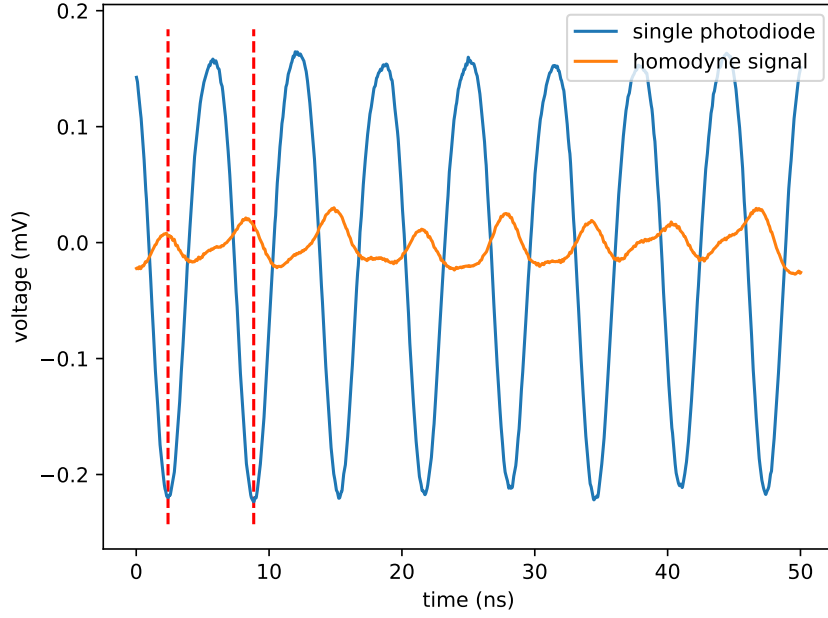


Figure 5.6: 50 ns detail on a data acquisition with the oscilloscope, where we collected 2M samples in a time span of 100 μ s, corresponding to 15559 pulses. The signal of the positive photodiode is used to identify the time windows that correspond to the pulses. A single quadrature value is obtained by integrating the homodyne signal (orange) over the time of a single pulse (dashed red lines).

normalization purposes. Each quadrature is obtained by adding the voltage points relative to each pulse. If we collect 2M samples in a time span of 100 μ s, corresponding to 15559 pulses, each pulse has approximately 128 voltage samples.

This procedure leads us to collect N quadratures, where N is the number of pulses, for each measurement of squeezing, antisqueezing or vacuum. The quadratures must be normalized and displaced with vacuum as follows:

$$x_i \rightarrow \frac{x_i - \mu_{shot}}{\sigma_{shot}} \quad (5.7)$$

where the vector \mathbf{x} refers either to the squeezing or antisqueezing quadrature vector, and μ_{shot} and σ_{shot} are the mean and the variance of the shot noise. In Fig. 5.7 a typical histogram of the quadratures is plotted. As expected, the variance of the squeezed quadrature is smaller than the variance of the shot noise; the opposite is true for the antisqueezed quadrature.

By changing the shape of the local oscillator, we can access higher-order Hermite-Gauss modes. We measured squeezing pulse-by-pulse in 7 Hermite-Gauss modes, up to HG6. The results are shown in Fig. 5.8, where they are compared with the squeezing values obtained

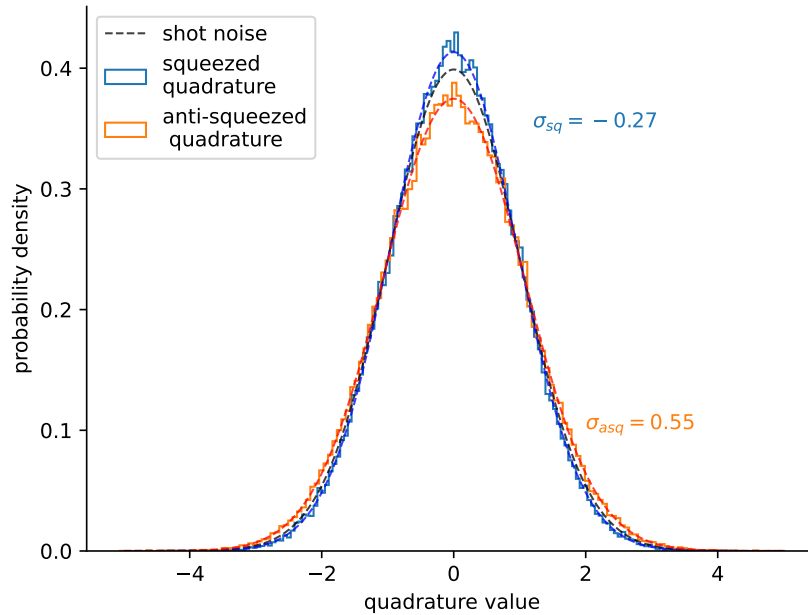


Figure 5.7: Histogram depicting squeezing and antisqueezing values, normalized by the relative shot noise curve, for the mode HG0. For each curve we collected 10^6 quadrature values. The variance of the plotted data gives the squeezing and antisqueezing values, that in this case are around 0.55 dB for antisqueezing and -0.27 dB for squeezing.

with the sidebands measurement of section 5.2.1, performed with the spectrum analyzer and non-pulse-resolved. These results demonstrate that the squeezing values obtained with the two methods are consistent and confirm that the multimode spectral structure is present in each individual pulse, and we can access it with our homodyne detector. This enables the possibility to multiplex simultaneously spectral and pulsed modes of light.

5.3 Covariance matrix reconstruction

In this section, we detail the experimental procedure used to reconstruct the covariance matrix of the multimode quantum state in the frequency pixel basis. We will demonstrate how the squeezing values obtained in the previous section can be recovered by diagonalizing this matrix. Finally, we will evaluate the non-separability between different bipartitions of the state.

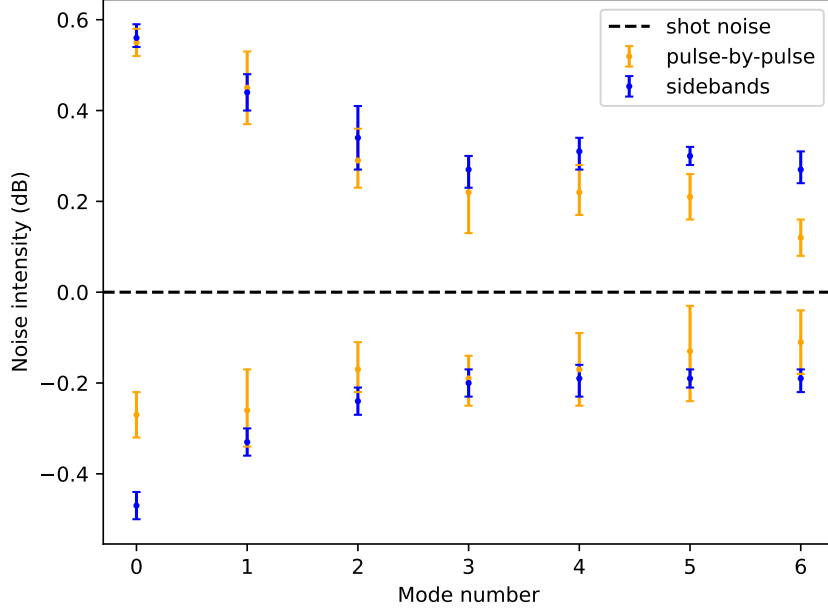


Figure 5.8: Comparison of squeezing and antisqueezing measurements for the first 7 Hermite-Gauss supermodes. The two sets of measurements share the same basis but use different techniques and devices: spectrum analyser for the sidebands squeezing measurement (blue) and oscilloscope for the pulse-by-pulse measurement (orange).

5.3.1 Covariance matrix measurement

Differently from the most general definition of the covariance matrix, from Eq. 2.3, here we make the assumption that the q and p quadratures are uncorrelated, so that the terms of the type $\langle \{\hat{q}_i \hat{p}_j\} \rangle$ are null. This assumption holds if the pump is real, i.e. the higher order phases are negligible [Michel 21]. In this case, the covariance matrix takes a block-diagonal form:

$$\mathbf{V} = \begin{pmatrix} \mathbf{V}_{qq} & 0 \\ 0 & \mathbf{V}_{pp} \end{pmatrix} \quad (5.8)$$

where

$$\mathbf{V}_{xx} = \begin{pmatrix} \Delta^2 x_1 & \langle x_1 x_2 \rangle & \dots \\ \langle x_1 x_2 \rangle & \Delta^2 x_2 & \\ \vdots & & \ddots \end{pmatrix} \quad (5.9)$$

with $x = \{q, p\}$. Considering n modes and the symmetry of \mathbf{V}_{qq} and \mathbf{V}_{pp} , we need to determine $n(n+1)$ terms to reconstruct the covariance matrix.

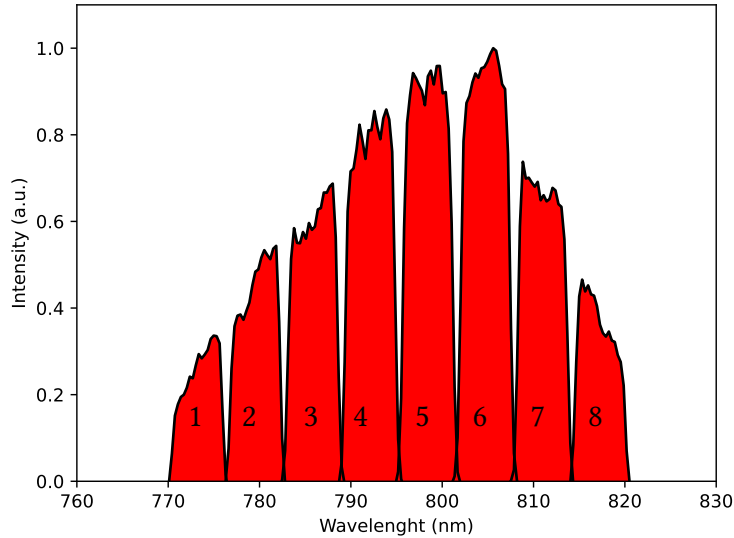


Figure 5.9: Frexel modes used for the measurement of the covariance matrix. Each frexel is 5 nm wide.

From now on we will define the frequency pixel modes as *frexel* modes. We define a frexel mode by dividing our 42-nm spectrum into 8 frexels, of 5-nm width, as shown in Fig. 5.9. Additionally, we make sure that the spectral overlap between two frexels is negligible.

Each term is measured through homodyne detection, and by scanning the phase of the local oscillator we can access to the quadrature q^ϕ for every value of ϕ . We note that, if the spectral phase is flat, the squeezed (or antisqueezed) quadrature is the same for each mode [Michel 21, Medeiros de Araujo 12]. We choose to define q as the quadrature with less noise, so that p is the quadrature with more noise. This choice arbitrary, and a different choice leads to equivalent results. To reconstruct the covariance matrix for n modes we need $n(n+1)/2$ homodyne traces.

The diagonal terms are measured by sending with the local oscillator individual frexels. This permits us to measure $\Delta^2 q_i$ and $\Delta^2 p_i$, which are the minimum and the maximum of the homodyne trace obtained from frexel i . To measure the off-diagonal terms, we measure the quadratures of the mode obtained by combining the frexels i and j . We define the quadrature operators of the mode $i+j$ as $\hat{x}_{i+j} = (\hat{x}_i + \hat{x}_j)/\sqrt{2}$, provided that the optical power detected

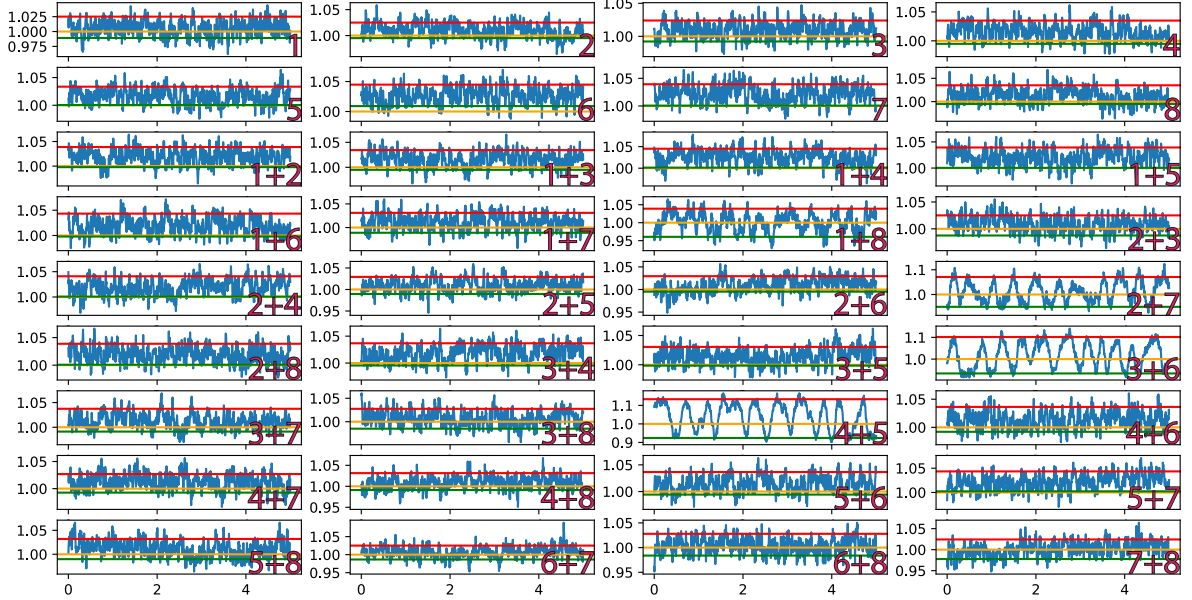


Figure 5.10: 36 homodyne traces for the reconstruction of the 8-frexel covariance matrix. The only traces that show non-vacuum fluctuations are the 1 + 8, 2 + 7, 3 + 6 and 4 + 5 traces. In the plots, the yellow line is the shot noise level, while the green and the red lines represent respectively the value of the q and the p quadrature variance. The measurement time is 5 seconds for each trace. We sweep the LO phase at 300 mHz.

by the frexels i and j is the same¹. The $\langle x_i x_j \rangle$ terms of the covariance matrix are given by:

$$\langle x_i x_j \rangle = \left[\Delta^2 x_{i+j} - \frac{\Delta^2 x_i + \Delta^2 x_j}{2} \right] \quad (5.10)$$

assuming the mean value of the quadratures vanishes, i.e. $\langle q_i \rangle = \langle p_i \rangle = 0$. From this equation we see that to obtain the $\langle x_i x_j \rangle$ term we need the information of the quadrature variance of both the combined mode $i + j$ and the frexels i and j .

The subtracted photocurrent for the mode k (in our case a frexel or combinations of frexel modes) is written as:

$$\hat{i}_{-,k}(\phi) = |\alpha_{LO}| (\cos \phi \hat{q}_k + \sin \phi \hat{p}_k) + \hat{e} \quad (5.11)$$

and its variance reads:

$$\Delta^2 i_{-,k}(\phi) = |\alpha_{LO}|^2 (\cos^2 \phi \Delta^2 q_k + \sin^2 \phi \Delta^2 p_k) + \Delta^2 e \quad (5.12)$$

¹We indeed need the mode (and the respective quadratures) to be normalized. In the general case, we use the normalization $\hat{x}_{i+j} = (\sqrt{P_i} \hat{x}_i + \sqrt{P_j} \hat{x}_j) / \sqrt{P_i + P_j}$, where P_i indicates the average power of frexel i .

where \hat{e} is the electronic noise of the detector and $|\alpha_{LO}|$ is the intensity of the LO. To access the information on the quadratures q_k and p_k we need to get rid of the electronic noise and the shot noise and correct the signal accordingly. If no light is shined on the photodetector, Eq. 5.12 reduces to

$$V^{el} = \Delta^2 i_{-,k}^{el} = \Delta^2 e \quad (5.13)$$

while sending only the LO and blocking the signal gives us:

$$V_k^{shot} = \Delta^2 i_{-,k}^{shot} = |\alpha_{LO}|^2 + \Delta^2 e \quad (5.14)$$

Following these considerations, at the beginning of each measurement round we measure the electronic noise of the detector by blocking both photodiodes of the detector. Then, by blocking only the signal light while letting the LO light hit the photodiodes, we take the shot noise for each frexel or combination of two frexels. In order to correct the signal trace, both the electronic noise and the shot noise trace will be needed. Lastly, we measure the signal variance $V_k(\phi) = \Delta^2 i_{-,k}(\phi)$ by sweeping the phase of the LO with a piezoelectric actuator to have access to both the q and the p quadrature. The corrected signal reads:

$$V_k^{corr}(\phi) = \frac{V_k(\phi) - V^{el}}{V_k^{shot} - V^{el}} = \cos^2 \phi \Delta^2 q_k + \sin^2 \phi \Delta^2 p_k \quad (5.15)$$

In Fig. 5.10 we show the 36 corrected homodyne traces that correspond to the measurement of a 8-frexel covariance matrix, obtained using a spectrum analyzer as measurement device.

From the homodyne traces, we retrieve the variances that we require for the reconstruction of the covariance matrix. Typically, multiple acquisitions are taken for each covariance matrix. An example of reconstructed covariance matrix can be seen in Fig 5.11. The diagonal elements of the matrix display the noise within individual frequency bands, whereas the off-diagonal terms unveil correlations between distinct frequency bands. Notably, the covariance matrix highlights correlations between frexel pairs 1-8, 2-7, 3-6, and 4-5, consistently with our observations in the homodyne traces depicted in Fig. 5.10. The correlations observed along the antidiagonal are characteristic of the narrow JSA of the generated photon-pair from our type-0 SPDC.

Finally, as the squeezing and antisqueezing values are comparable, we expect our experiment to be low-loss. We can confirm it by checking the purity of the state, as losses are the main mechanism that impacts it. For a multimode Gaussian state, the purity is assessed using Eq. 2.6. From the measurement of the covariance matrix, we can infer that the purity of the multimode quantum state generated by our source reads $\mu_\rho \sim 96\%$.

5.3.2 Supermodes reconstruction

In the previous section, we measured the covariance matrix in the frexel basis, which is the most natural basis for describing the SPDC process and for assessing bipartite entanglement

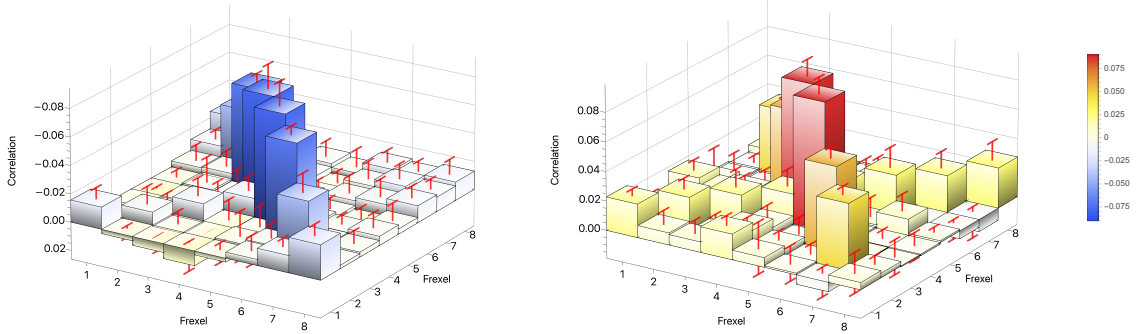


Figure 5.11: Experimental matrices $\mathbf{V}_{qq} - \mathbb{1}$ (left) and $\mathbf{V}_{pp} - \mathbb{1}$ (right) that show the correlations among the 8 frexels, where the identity has been subtracted for better visibility of the off-diagonal elements. The z-axis of the q matrix is reversed to properly show the anti-diagonal. This covariance matrix is the result of 5 acquisition rounds.

of the state. By diagonalizing the covariance matrix, we expect to recover the squeezing values (eigenvalues) and the supermodes (eigenmodes) of the state. We denote \mathbf{V}_{xx}^{HG} and \mathbf{V}_{xx}^{fr} as the x -block of the covariance matrix expressed in the supermodes and frexel basis, respectively. We expect $\mathbf{V}_{qq}^{HG} = \left(\mathbf{V}_{pp}^{HG}\right)^{-1}$, which follows from the definition of the covariance matrix of a multimode squeezed state. Moreover, we expect the eigenmodes of the two matrices to be equal. However, there are slight differences, likely stemming from low signal-to-noise ratio. We can verify this by expressing \mathbf{V}_{qq} first in a basis of its own eigenmodes (where it is obviously diagonal), then in a basis of the eigenmodes of \mathbf{V}_{pp} . The discrepancies are shown in Fig. 5.12.

To define a basis, we choose the eigenvectors corresponding to the 8 highest eigenvalues of both matrices combining them to form a new basis. While this new basis is not orthogonal, we can apply Gram–Schmidt orthogonalization to obtain an orthogonal basis. It is to note that this new basis does not consist of eigenvectors of either \mathbf{V}_{qq} or \mathbf{V}_{pp} , but it incorporates information from both quadrature measurements. Alternatively, we could have opted for a basis of eigenvectors of one of the two matrices, but this approach might introduce more bias towards the measurement of one of the two quadratures.

The diagonal elements relative to the basis change of \mathbf{V}_{qq}^{fr} and \mathbf{V}_{pp}^{fr} into “quasi-diagonal” matrices are shown in Fig 5.13. These can be interpreted as an approximation of the squeezing values of the uncorrelated modes of the system. A comparison between the squeezing values obtained by directly measuring the HG modes (as in section 5.2.1) and the ones derived from the measurement of the covariance matrix in the frexel basis is shown in Fig. 5.14. The uncorrelated modes of the system are approximated by vectors shown in Fig. 5.15. Some comments about what we expect from our system and the results that we obtained are in order.

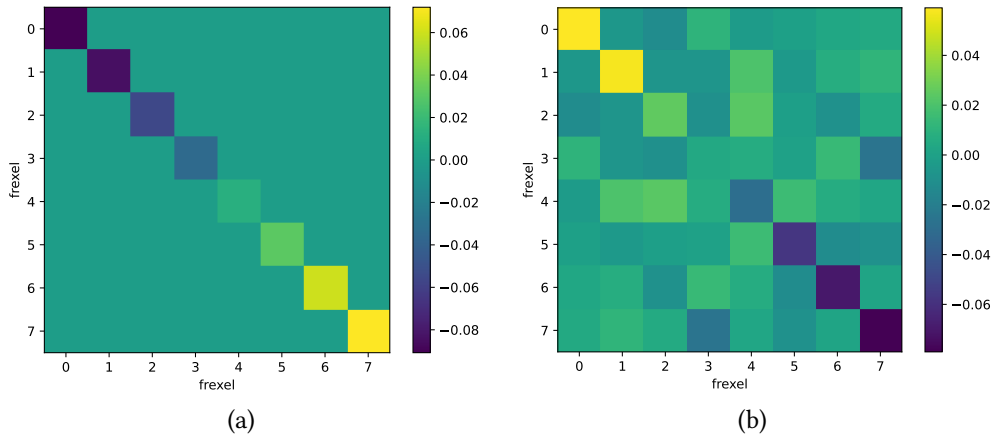


Figure 5.12: a) Plot of the $V_{qq} - \mathbb{1}$ matrix rewritten in the basis of its own eigenvectors. We trivially obtain a diagonal matrix. b) Plot of the $V_{qq} - \mathbb{1}$ matrix rewritten in the basis of the eigenvectors of V_{pp} . In the ideal, theoretical case we should obtain a diagonal matrix, as the eigenvectors of V_{pp} and V_{qq} should be equal. In both a) and b) an identity matrix has been subtracted for better visibility of the correlations.

We expect the recovered uncorrelated modes to be HG modes, or more precisely a “discretized” version of them. Moreover, we expect the squeezing values to exhibit an alternating pattern between squeezing in q and in p , as explained in section 3.3. In Fig. 5.13, we observe the expected alternating pattern, except for the first two values, which both show squeezing in the q quadrature. This deviation can be explained by examining the corresponding vectors in Fig. 5.15. The vectors appear to be shuffled and not in the typical order of HG modes. For instance, the discretized version of HG1 appears to be in the third position instead of the expected second position. In particular, mode 0 and the mode 7 are placed in the correct order, while the modes 1-2, 3-4 and 5-6 have switched order. This is probably due to the low signal-to-noise ratio, that makes it difficult to discriminate between squeezing values that are close in magnitude. This is especially true in our case, as we expect a flat spectrum of squeezing values, according to the simulations shown in Section 4.3.3 and the results of section 5.2.1.

5.3.3 Bipartite entanglement in the frexel basis

The frexel basis is the most natural basis for assessing entanglement between frequency bands, as it reflects the monochromatic frequency distribution of the JSA. However, it is obviously a coarse-grained measurement, since we cannot realistically access monochromatic components. Here we use the covariance matrix of the state, measured in the frexel basis, to evaluate bipartite entanglement between any bipartition of the 8 frequency bands.

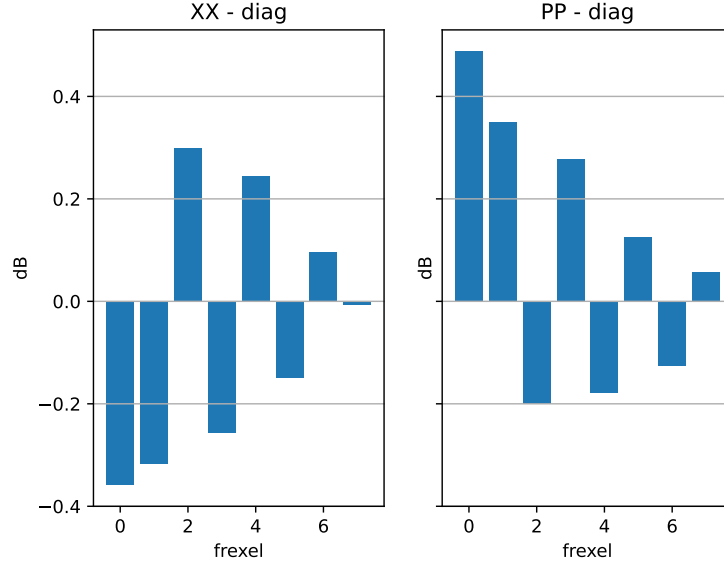


Figure 5.13: Diagonal of the \mathbf{V}_{qq} and \mathbf{V}_{pp} “quasi-diagonal” matrices, in the orthonormal basis implemented by the Gram-Schmidt process. These values correspond to the average value of the squeezing of the supermodes.

First of all, we need to verify that the covariance matrix we have measured is a real positive semi-definite matrix that satisfies the uncertainty relations of Eq. 2.4, i.e. $\mathbf{V} - i\mathbf{J} \geq 0$, where \mathbf{J} is the $2n \times 2n$ symplectic form defined in Eq. 2.5. In some cases, slow drifts occur during the acquisition, so that the covariance matrix is slightly unphysical [Gerke 15]. To correct for this, we add vacuum noise to the measured covariance matrix as follows:

$$\mathbf{V} \rightarrow \mathbf{V} + c\mathbb{1} \quad (5.16)$$

where c is adjusted so that Eq. 2.4 is satisfied. The corrected version of the covariance matrix will be the one used to carry out calculations in the remaining part of this section.

To assess bipartite entanglement, we use the Peres-Horodecki separability criterion for CV systems [Simon 00], that is based on the positivity of the density operator under the partial transposition of one of the two subsystems. The positive partial transpose (PPT) criterion is a necessary and sufficient condition for the separability of bipartite Gaussian states. We stress again that this criterion does not evaluate multipartite entanglement but rather the entanglement between bipartitions of the system. Once we have chosen the bipartition for which we want to evaluate the entanglement, we apply the partial transpose operation, whose effect is a mirror reflection in phase space for the p quadrature of one of the two subsystems, that reads:

$$W(q_1, q_2, p_1, p_2) \xrightarrow{PT} W(q_1, q_2, p_1, -p_2) \quad (5.17)$$

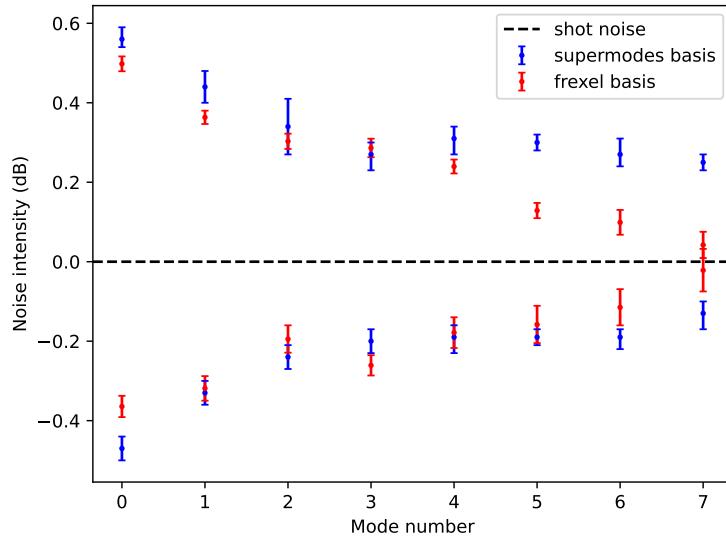


Figure 5.14: Comparison between squeezing and antisqueezing values measured in the Hermite-Gauss basis supermodes (blue) and those derived from the reconstruction of the covariance matrix measured in the frexel basis (red). Both sets of measurements employ the same technique (non-time resolved sideband squeezing measurement) and device (spectrum analyzer) but differ in the measurement basis.

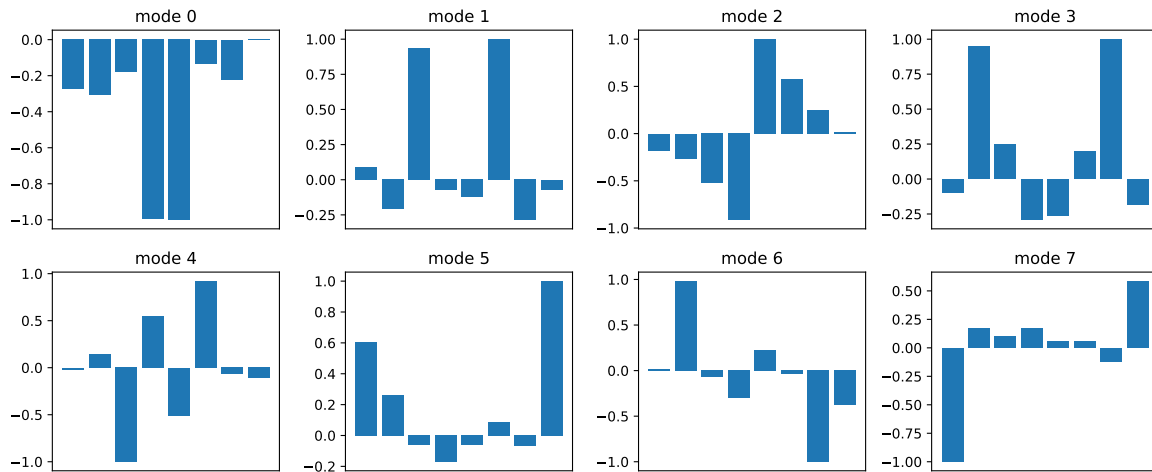


Figure 5.15: Orthonormal basis vectors obtained by the Gram-Schmidt process, that approximate the uncorrelated modes of the system. While we expect these modes to have the HG shape and to be ordered accordingly, the modes that we obtained appeared reshuffled, probably due to the low signal-to-noise ratio.

This corresponds to a transformation that inverts the p coordinate of the transposed system in the quadrature vector, as:

$$\mathbf{x} \xrightarrow{PT} \Lambda \mathbf{x} \quad (5.18)$$

where $\mathbf{x} = (\mathbf{q}, \mathbf{p})$ and where Λ is a diagonal matrix with +1 or -1 entries, where the -1 entries correspond to the p quadrature of the transposed subsystem. This transformation maps the covariance matrix into:

$$\tilde{\mathbf{V}} = \Lambda \mathbf{V} \Lambda \quad (5.19)$$

The PPT necessary condition for separability is:

$$\mathbf{P} = \tilde{\mathbf{V}} - i\mathbf{J} \geq 0 \quad (5.20)$$

If this condition is not fulfilled, the two partitions are entangled.

For a 8-frexel system, there are 127 possible bipartitions, representing different ways of dividing the 8 frexels into two sets. Examples of bipartitions include {2} and {1, 3, 4, 5, 6, 7, 8} or {1, 2, 3, 4} and {5, 6, 7, 8}. We define the *PPT value* as the smallest eigenvalue of a given bipartition. In Fig. 5.16, we show the PPT values for the 127 bipartitions of our system, indicating that approximately 90% of them exhibit inseparability.

The PPT values can be categorized into four distinct bands based on the degree of entanglement: a lower band, a lower-intermediate band, an upper-intermediate band, and an upper band. There is a correlation between the partitioning choice and the PPT band to which the partition belongs. Specifically:

- lower band: frexels 4 and 5 are separated in two different bipartitions
- lower-intermediate band: frexels 3 and 6 are separated in two different bipartitions, but 4-5 are in the same
- upper-intermediate band: frexels 2 and 7 are separated in two different bipartitions, but 4-5 and 3-6 are in the same
- upper band: 2-7, 4-5 and 3-6 are in the same bipartitions

The pair of frexels 1-8 does not play a significant role, and the upper band contains partitions that are mostly non-entangled.

The different distribution of the degree of entanglement reflects the narrow type-0 JSA of the entangled photon-pairs generated in our setup. Indeed, the quantum correlations, as also shown in the covariance matrix, are mostly shared between frequency bands positioned symmetrically in relation to the central optical frequency, i.e. 4-5, 3-6 and 2-7. For this reason, bipartitions that do not separate these pairs of frexels are not necessarily entangled.

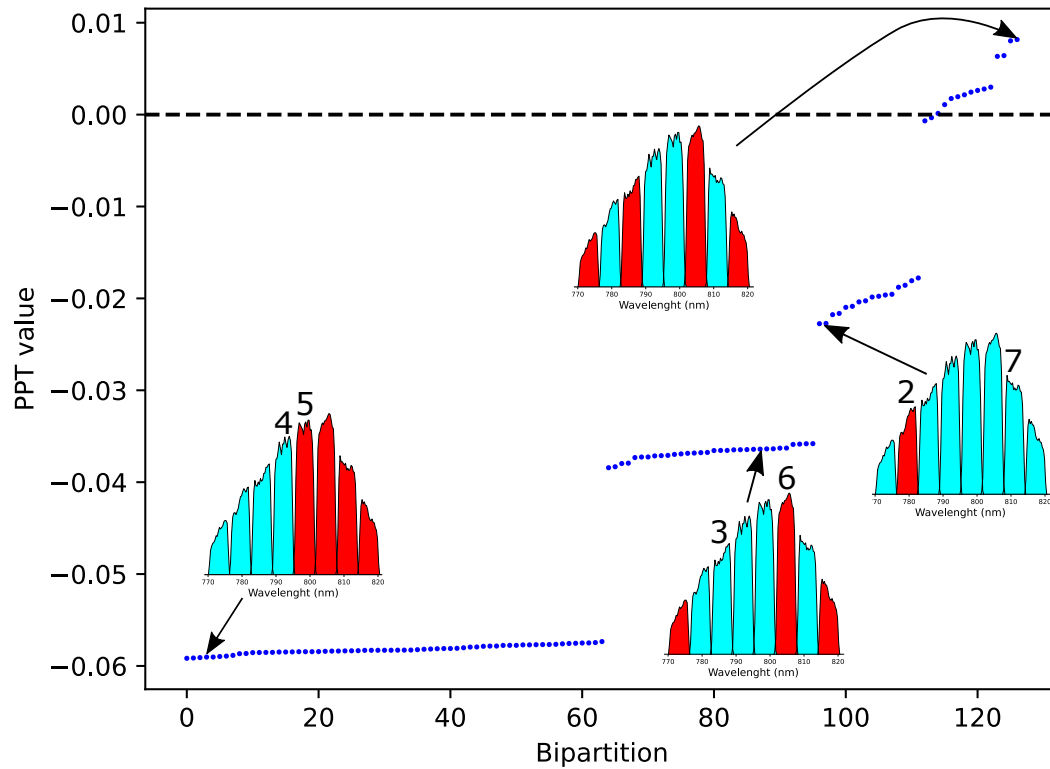


Figure 5.16: PPT inseparability value (lowest eigenvalue of the PPT matrix) for all of the 127 possible bipartitions of 8 frexels, ordered from the smallest to the highest. All the bipartitions below the dashed line (negative PPT value) are entangled. 4 distinct bands of values are distinguishable, depending on which pair of frexels are separated into two different bipartitions (4-5, 3-6, 2-7 or none of them).

Chapter 6

Towards a time-frequency multiplexed CV network

Contents

6.1 Time-frequency multiplexed cluster state	141
6.1.1 Building a multiplexed network	141
6.1.2 Second waveguide	143
6.1.3 Implementation of an EPR state	145
6.2 Locking system	146
6.2.1 The PID controller	147
6.2.2 DC lock and AC lock	148
6.2.3 Experimental implementation of phase locks	150
6.2.4 Measurement-hold phase	154

In this work, we demonstrated the generation of multimode squeezed states that are multiplexed both in the temporal and spectral degrees of freedom: the temporal multiplexing is achieved by measuring squeezing in individual pulses at a repetition rate of 156 MHz, while 21 squeezed spectral modes have been measured for each pulse. The next step is to employ this multimode squeezed source to build time-frequency multiplexed cluster states. In this chapter we will describe the setup for the implementation of the resource of interest.

6.1 Time-frequency multiplexed cluster state

6.1.1 Building a multiplexed network

Large-scale CV cluster states have already been built in the temporal domain, both in a 2D [Yokoyama 13] and in a 3D configuration [Larsen 19, Asavanant 19]. The simpler 2D scheme, shown in Fig. 6.1, involves the use of two squeezed light sources and a linear

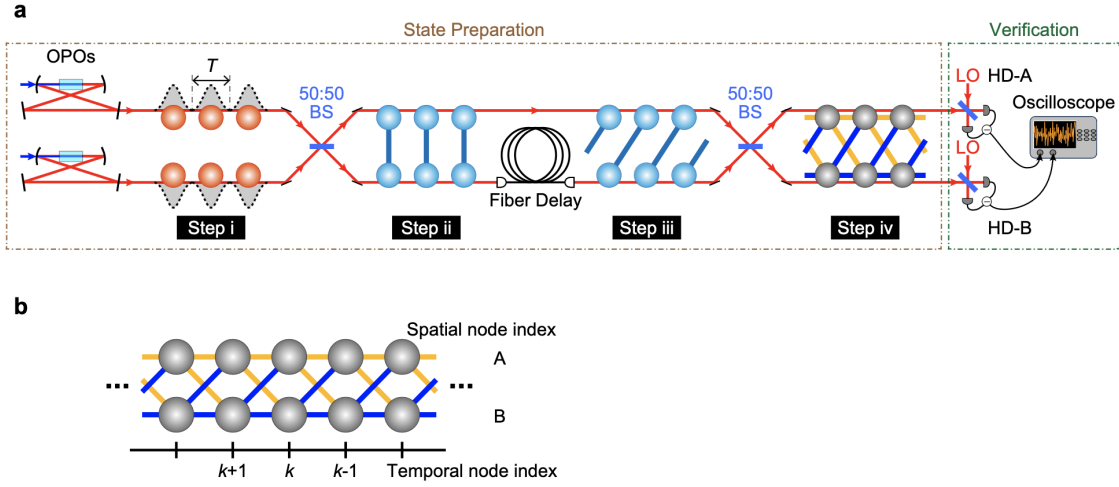


Figure 6.1: Implementation of a dual-rail cluster state, from [Yokoyama 13]. Squeezed light is generated at the output of the two OPO and it is subsequently mixed on a 50:50 beam-splitter for the generation of EPR states. A delay and another beam-splitter enable the generation of the dual-rail cluster state.

interferometer to implement the cluster state, and of two homodyne detectors to measure it. The linear interferometer consists of a first beam-splitter, a delay-line, and a second beam-splitter. The first beamsplitter is used to create an EPR state from the two squeezed states, while the delay line and the second beam-splitter are used to entangle successive nodes and implement a cluster state with the so-called *dual-rail* shape.

Our setup differs in two main aspects. First, instead of CW light, we employ pulsed light, which grants us access to the spectral multimode degree of freedom. Second, instead of using an OPO as the source of squeezed light we employ waveguides. This allows us to use the natural time slot of the laser pulse and to implement entangled states at the repetition rate of the laser.

The state generated at the output of the waveguides consists of a series of n independent squeezed states in the supermode basis. Combining these states on a 50:50 beam splitter leads to the implementation of n EPR states, as shown in Fig. 6.2. This occurs because the squeezed states of the two waveguides are mixed mode-wise. Indeed, orthogonal modes in the spectral basis cannot be mixed via a linear optics interferometer. This kind of mixing can only be achieved through a non-linear effect, as demonstrated in the case of the *quantum pulse gate* [Eckstein 11].

Similarly, by employing the interferometer illustrated in Fig. 6.1, it becomes possible to create n dual-rail cluster states, one for each mode within the supermode basis. However, linear combinations of spectral modes can be easily implemented at the measurement stage, by changing the measurement basis [Cai 17]. This allows us to reconfigure the spectral layer

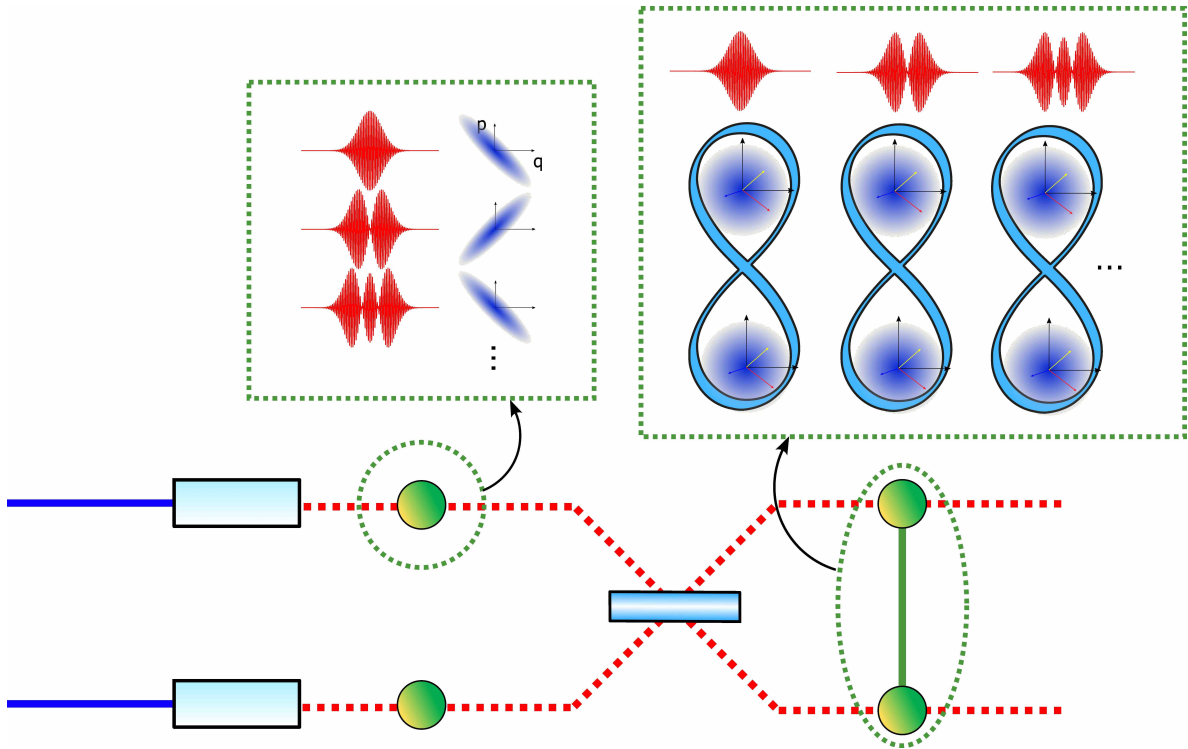


Figure 6.2: The two multimode squeezed vacuum states generated in the supermode basis at the output of the two waveguides are mixed on a 50:50 beam splitter. This results in the implementation of mode-wise EPR states.

effectively, resulting in a 3D cluster state that is multiplexed in both time and frequency. One axis corresponds to the temporal degree of freedom, and at each pulse-time t a 2D spectral layer is present.

6.1.2 Second waveguide

In the previous section, we discussed the necessity of a second source of squeezed light to construct a cluster state in the temporal domain. To fulfil this requirement, we use a second waveguide chip, manufactured within the same batch as the first one, ensuring that they possess similar characteristics. We evaluated the performances of the second waveguide chip, by employing the same procedures already used for the first chip. More precisely, our objective was to identify a suitable waveguide for both the generation of squeezing and the overlap with the light beam from the first waveguide chip.

We focus our attention especially on the output mode of the seed, as in this case we are not only seeking a spatial mode with a good overlap with the local oscillator (LO) but also one that could effectively match with the seed of the first waveguide. Even in this case, the

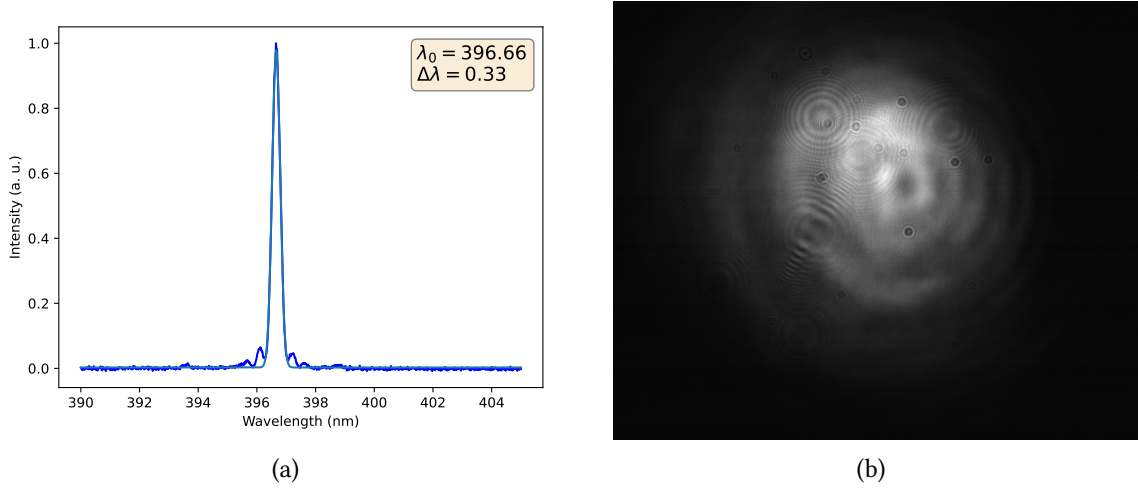


Figure 6.3: (a) Spectrum of the SHG for $T = 90^\circ\text{C}$, overlapped with its gaussian fit and (b) fundamental spatial mode of waveguide 26 of the second chip.

choice falls on waveguide 26, whose mode can be seen in Fig. 6.3b.

However, the two waveguide chips present a substantial difference that needs to be addressed. Indeed, we observed a discrepancy between the central wavelengths of the SHG produced by the two waveguide chips, as shown in Table 6.1. This indicates that the phase-matching functions of the two chips are not centered at the same wavelength. In particular, at the theoretical point of maximal SHG efficiency (90°C), there is a difference of approximately $\Delta\lambda_0 \sim 0.55$ nm. While 0.55 nm does not seem like a substantial difference, we recall that our pump has a comparable width. In the case of a very narrow pump and a very narrow phase-matching function, even such a small difference can significantly affect the efficiency of the process. Indeed, the efficiency of the parametric amplification process is contingent upon how well the pump (and the seed) align with the phase-matching function of the waveguide crystal. Since the two phase-matching functions are slightly different, they require a pump centered at a different wavelength to optimize the parametric amplification. However, given that the pump for the SPDC process is necessarily the same, originating from the SHG process described in section 4.4, tuning the wavelength of the pump to optimize the parametric amplification for one chip results in suboptimal amplification for the other chip, and vice versa.

A possible solution is to adjust the temperature of the waveguide chips to strike a balance, ensuring that the pump aligns well with both chips. We will deviate from the temperature providing best SHG efficiency (90°C) and aim to set the central wavelength of the SHG to $\lambda_0 = 397$ nm for both waveguides. This is achieved by tuning the temperature of the first chip to around 80°C and the temperature of the second chip to around 105°C . The temperature of the ppKTP SHG crystal that generates the pump beam will be adjusted

Temperature (°C)	λ_0 SHG chip1 (nm)	λ_0 SHG chip2 (nm)
90	397.2	396.65
80	396.95	396.45
70	396.6	396.25
60	396.45	396.01
50	396.16	395.83
40	395.96	395.56
30	395.75	395.23

Table 6.1: Central wavelength λ_0 of the SHG generated by the two waveguides chip in waveguide 26. The pump is at $\lambda_0 = 794$ nm.

as to achieve a $\lambda_0 = 397$ nm output.

6.1.3 Implementation of an EPR state

The two waveguides are used as squeezed light sources to build first an EPR pair, then an entangled network. In this section, we focus on the EPR state implementation, whose setup can be seen in Fig. 6.4. The initial challenge involves combining the two squeezed light beams at the first beam splitter. Indeed, we have to take care of: 1) achieving optimal spatial overlap between the two modes to maximize the entanglement level of the resulting state, and 2) ensuring that the two beams interfere with a precise phase relation to generate an EPR pair, necessitating phase-locking.

The divergence of the seed beams after passing through the two output lenses of the waveguide setup may affect the spatial overlap, as one beam may be larger than the other at the beam-splitter level. To overcome this problem, we adjusted the geometry of the setup to ensure that the two paths at the waveguide outputs are nearly equal. This also required careful temporal matching; the pump paths have been adjusted so that the pump pulses are injected into the waveguide simultaneously. This guarantees that, at the beam-splitter level, the spatial modes of the two seeds have the same width and divergence.

The second challenge arises from the fact that the squeezing ellipses of the two beams rotate as they propagate¹, as shown in Fig. 6.4. In order to generate the EPR state, we require them to interfere with a relative angle of $\phi = \pi/2$, as explained in section 1.5.4. Deviating from this angle results in a reduction of entanglement in the resulting EPR state, with complete loss of entanglement occurring at $\phi = 0$ or $\phi = \pi$ angles. To maintain the fixed phase relation at $\pi/2$, we employ three phase locks, that will be detailed in section 6.2.

The EPR state generated at the output of the beam splitter is sent to two homodyne

¹In the phasor diagram description, it is often used the rotating frame at frequency ω_0 . Here, we take into account also the evolution of the $e^{i\omega_0 t}$ term of the electric field.

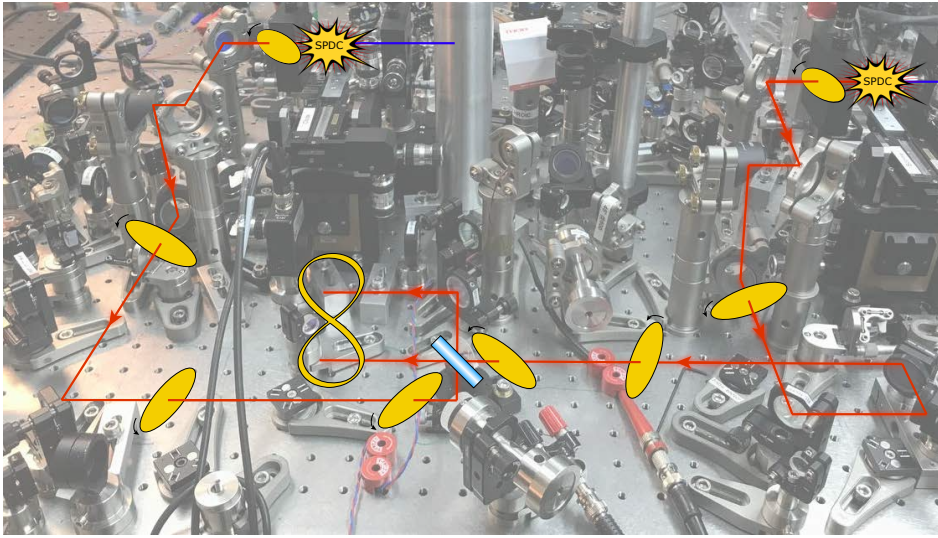


Figure 6.4: Experimental setup that shows both the generation and the interference of the two squeezed beams, with the consequent implementation of an EPR pair. Note that the squeezing ellipse rotates along the propagation axis, and the creation of an EPR pair is contingent on a $\pi/2$ relative phase between the squeezing ellipses of the two beams.

detectors. The goal is to be able to measure the combination of quadratures $x_1 - x_2$, $x_1 + x_2$, $p_1 - p_2$, $p_1 + p_2$; while $x_1 - x_2$ and $p_1 + p_2$ will exhibit noise fluctuations below the shot noise limit, the pair $x_1 + x_2$ and $p_1 - p_2$ will exhibit fluctuations above the shot noise limit, as reported in section 1.5.4. The measurement of these linear combinations requires phase-locking at the homodyne detection stage, that still needs to be implemented and investigated in detail.

For alignment purposes, we have established an alternative path with flip mirrors, that directs the output beams of the two waveguides to the homodyne detectors without passing through the mixing stage. Indeed, before proceeding with the mixing process, it is necessary to confirm the successful generation of squeezed light in both waveguides and ensure that the alignment is optimized to maximize the level of squeezing.

6.2 Locking system

As previously mentioned, this experiment necessitates phase locking, which involves stabilizing the relative phases of the various beams. This is important both during the cluster state implementation stage and in the measurement stage. In this section we will go through the details and the techniques used for phase locking.

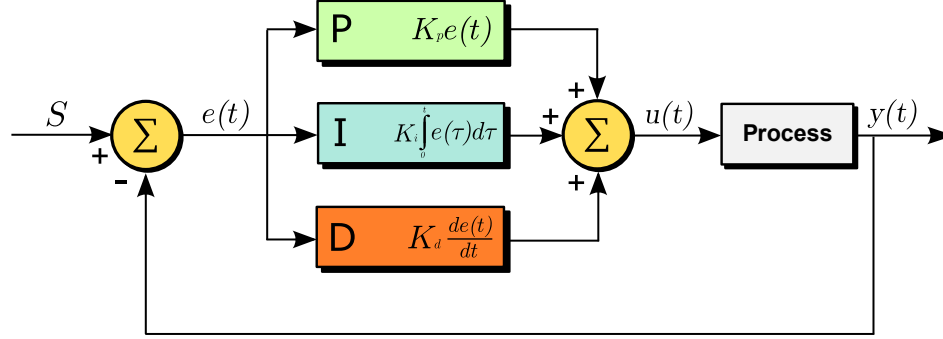


Figure 6.5: Scheme of a PID controller.

6.2.1 The PID controller

Phase-locking is accomplished through a feedback loop mechanism that is controlled by a PID (Proportional-Integral-Derivative) controller, whose scheme is shown in Fig. 6.5. The loop works as follows. The PID receives an electronic signal, that we call *process variable signal* $y(t)$; this signal contains information about the phase fluctuations and modulations within our system. Our objective is to “lock” the system to a specific point on the process variable signal, referred to as the *setpoint* S . The PID generates an *error signal* $e(t) = S - y(t)$, that represents the deviation between the desired setpoint and the variable of interest in our system - the phase, in our case. The larger the phase deviates from the desired setpoint, the larger the PID error signal becomes.

The PID error signal is handled by the proportional unit (P), the integral unit (I) and the derivative unit (D) of the PID controller, which collectively generate the output signal:

$$u(t) = K_P e(t) + K_I \int_0^t d\tau e(\tau) + K_D \frac{de(t)}{dt} \quad (6.1)$$

Here, K_P is the proportional gain, K_I is the integral gain and K_D is the derivative gain. These are tuning parameters that influence the output of the controller. The response signal $u(t)$ then acts on the piezoelectric actuator of the pump beam, modifying the phase of the beam. As a result, both the process variable signal $y(t)$ and the error signal $e(t)$ are affected. The PID controller continuously processes the error signal and acts on the piezo actuator to minimize the error signal, bringing the phase closer to the setpoint S . The aim of this feedback loop is to maintain $e(t) \sim 0$ and $y(t) \sim S$.

The P, I, and D modules of the PID controller have distinct roles in the control process [Aström 95, Aström 08]. The P module generates an output that is proportional to the error signal magnitude. However, its influence diminishes as the process approaches the setpoint. The integral module, on the other hand, produces an output that depends on both the duration and magnitude of the error signal. It accumulates gradually and increases as long as an error persists, making it effective for addressing persistent errors over time. The

output of the derivative module is proportional to the rate of change of the error signal. It anticipates future changes in the error and contributes to the controller output accordingly. By adjusting the contributions of these three components, the PID controller can achieve stable and precise control of the phase of the process, effectively “locking” it to a fixed setpoint.

In our setup, we only have control over the K_P and K_I parameters, but this is sufficient for phase-locking. Typically, the K_P and K_I values require manual adjustment, because there is no established analytical method for determining the precise settings. Therefore, we adopt the approach that follows the so-called Ziegler-Nichols rules [Tho 23, Ogata 10]. Initially, we set all values to zero. Then, we gradually increase the K_P gain until we observe oscillations in the signal and we can audibly hear the piezo actuator. We identify this value with the critical proportional gain K_{cr} and we denote the period of the oscillations with P_{cr} . The final K_P value is set at roughly half of this observed level, precisely $K_P = 0.45K_{cr}$. Typically, when only the proportional gain K_P is used, we may observe an offset between the value of the phase variable and the setpoint S , called steady-state error. Enabling the integral correction allows us to compensate for this error, as the role of the integral module is to address persistent errors. We proceed by increasing the K_I value until we observe steady-state error compensation. However, increasing this value too much can result in instability and oscillations around the setpoint. A more rigorous application of the Ziegler-Nichols rules prescribes precisely setting the K_I to $K_I = 1.2K_P/P_{cr}$. Once the K_P and K_I value are determined, we can successfully achieve phase-locking.

To conclude this section, we highlight an important point. For the PID controller to efficiently achieve a stable lock, the error signal must possess specific characteristics. In particular, we require that the error signal displays a nearly linear behavior around the lock point. Additionally, a sharp signal, characterized by steep slopes, indicates high sensitivity to phase errors and ensures a fast response from the controller. For this reason, a lock point cannot coincide with a stationary point of the process variable signal, such as a maximum or a minimum. To facilitate locking at these points, we must modify the signal as discussed in the next section.

6.2.2 DC lock and AC lock

In this work, we will employ two locking techniques, which we respectively refer to as *DC lock* and *AC lock*. The signals we employ and manipulate for locking purposes in this setup are photocurrents directly detected by photodiodes.

In the DC lock or side-of-fringe lock technique, we identify the original signal, that has been directly detected by the photodiode, with the process variable signal $y(t)$ for the PID module, introduced in the previous section. We take the DC (low-frequency) output of the photodiode, and we set the setpoint S at the value of the DC signal we want to lock onto, as shown in Fig. 6.6a. The error signal $e(t) = y(t) - S$ is fed to the PID, and its response signal $u(t)$ acts on the setup to directly modify $y(t)$.

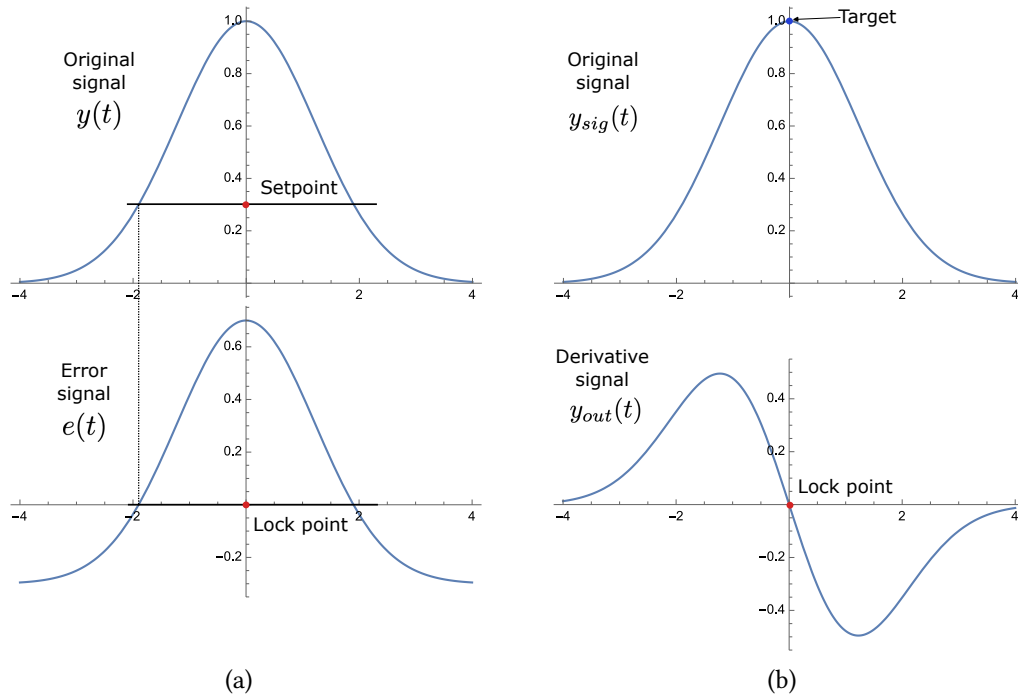


Figure 6.6: Left figure: schematics of DC lock, right figure: schematics of AC lock. In the AC lock the setpoint is usually $S = 0$, and the derivative signal y_{out} is used as error signal $e(t) = y_{out}(t)$.

The DC lock is simple to implement, as we only need to connect the photodiode to the PID module and set the lock point. However, it comes with an important drawback: the impossibility of locking close to or at the peaks of the signal. Indeed, as the name suggests, we can use this technique when our setpoint is located on a slope, as shown in Fig. 6.6a. Moreover, this type of lock is sensitive to intensity fluctuations that change the mean value of the optical field¹.

The AC lock or top-of-fringe lock is a technique that permits to lock the phase at the peaks of the signal, as the name suggests. It offers greater stability compared to its DC counterpart because it is not affected by intensity fluctuations of the signal. However, setting up an AC lock involves more complex signal processing. This is the technique we will use to lock the phase in the parametric amplification process.

Establishing an AC lock involves several signal processing steps, whose purpose is to transform the original process variable signal, here denoted as $y_{sig}(t)$, into its derivative. This transformation has the effect of converting the curve around a maximum or minimum

¹As our setpoint is usually located at the average value of the field, to avoid this problem we may be tempted to take the AC output of the photodiode and lock at $S = 0$. This would permit to be unaffected by mean field fluctuations. However, in so doing, we would filter out the slow contributions of the phase noise, present only in the DC output, which is precisely what we are interested in and what we want to compensate.

into steep slopes, where we can place lock points. By feeding the derivative signal to the PID control, we can effectively lock onto the signal peaks of the original signal, as illustrated in Fig. 6.6b.

We proceed as follows:

- Modulation stage: the original signal $y_{sig}(t)$ is modulated with a sinusoidal signal at a frequency Ω_{m1} , resulting in the signal $y_{mod}(t)$. In the electronic frequency domain, this modulation shifts the noise information from the DC (low-frequency) range into sidebands around Ω_{m1} .
- Demodulation stage: the signal $y_{mod}(t)$ is multiplied by a sinusoidal signal $y_{demod}(t)$ that oscillates at the same frequency Ω_{m1} using an electronic mixer. This yields the signal $y_{out}(t) = y_{sig}(t) \cdot y_{demod}(t)$. In the spectral domain, this operation replicates the phase noise sidebands, already present around Ω_{m1} , also at 0 Hz and at $2\Omega_{m1}$.
- Filtering stage: a low-pass filter with a cutoff frequency $\Omega_{LPF} < \Omega_{m1}$ is added after the mixer to select only the DC-low frequency sidebands.

Finally, the signal is amplified and fed to the PID, for feedback control. The signal $y_{out}(t)$ produced by this process is proportional to the derivative of the original signal $y_{sig}(t)$. The mathematical details are presented in Appendix C. By locking at the zero-crossing points ($S = 0$) of the $y_{out}(t)$ signal, we effectively achieve locking at the minima or maxima of the original signal.

6.2.3 Experimental implementation of phase locks

In the experimental implementation of phase locks, we first need to extract a portion of the signal that we intend to lock onto. This is done by placing two 95:5 beam-splitters after each waveguide chip on the seed path, to retrieve the parametric amplification signal, and one 95:5 beam-splitter after the beam-splitter used for the EPR implementation, to retrieve the interference signal of the two seeds.

Stabilizing the parametric processes in both waveguides, specifically at either an amplification or deamplification point (i.e. antisqueezing or squeezing point), requires locking at the maximum or minimum of the signal. As already discussed, in this case we need to resort to the AC locking technique. The third lock is used to stabilize the relative phases of the two seeds at $\pi/2$ within the interference pattern. In this case, we can directly use the signal detected by the photodiode, and implement a simpler DC lock. If the objective is to build a cluster state, the same $\pi/2$ DC lock is implemented on a second beam-splitter.

For each AC lock we want to implement we introduce additional components into our setup: a piezoelectric actuator on the pump beam (in addition to the one present in the seed beam), a frequency generator with two channels that allows for tuning the electronic phase between the channels, a mixer, an amplifier, and a low-pass filter. A schematic of the AC

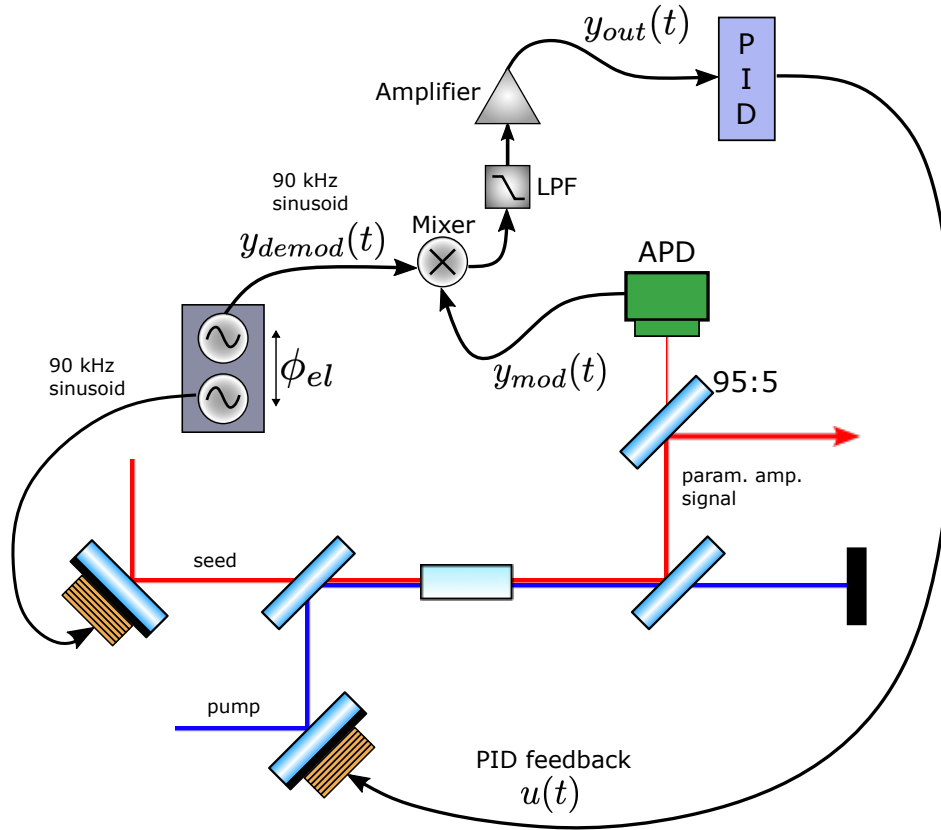


Figure 6.7: Scheme of the AC locking system implemented into our experiment. The parametric amplification signal, optically modulated at 90 kHz, is detected through a photodetector to yield $y_{mod}(t)$. This signal is multiplied with $y_{demod}(t)$, a 90 kHz sinusoid, through a mixer and the output is filtered with a low-pass filter (LPF) and amplified. The resulting signal $y_{out}(t)$ is fed to the PID controller to generate a feedback signal $u(t)$ on the pump phase. The phase ϕ_{el} between the modulation and demodulation channel is tuned to maximize the error signal.

lock setup and how it provides feedback to the experiment is depicted in Fig. 6.7. The piezo on the pump beam is used to drive the 100 Hz ramp of the parametric amplification process, while the piezo on the seed path modulates the seed beam phase with a sinusoidal signal at $\Omega_{m1} = 90 \text{ kHz}$ ¹.

The intrinsic phase fluctuations of the light, along with the 100 Hz and 90 kHz phase oscillations, are converted into intensity fluctuations through the parametric process, and they can then be detected by a photodetector, which generates the AC output signal $y_{mod}(t)$.

¹This value of Ω_{m1} is not the only possible choice; in general, we will choose a resonant frequency of the piezo+mirror+mount system.

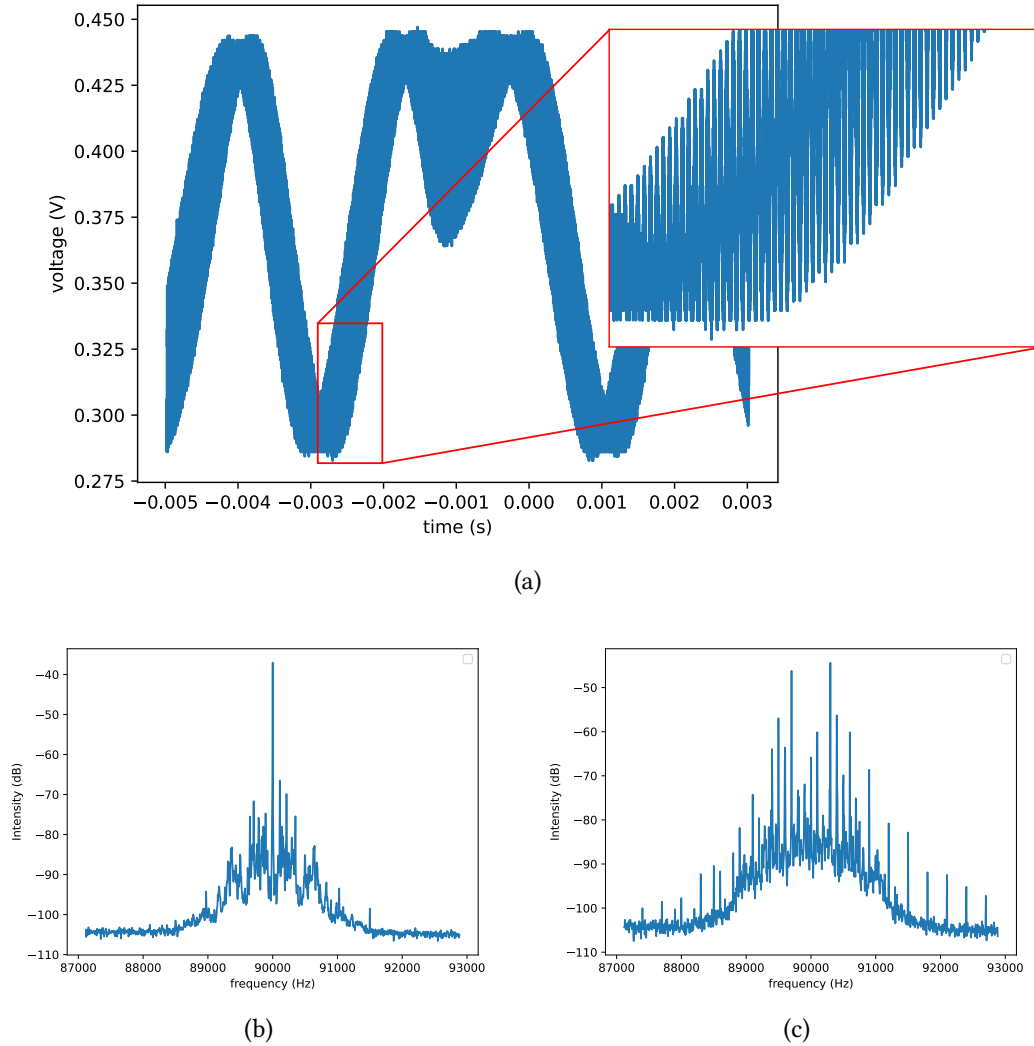


Figure 6.8: In (a) the temporal evolution of the photodiode signal is plotted and in the inset we can clearly see the 90 kHz modulation. (b) Frequency spectrum of the electronic signal generated from the photodiode, where both the 90 kHz modulation and the phase noise are present. Note that the phase noise is centered around $\Omega_{m1} = 90$ kHz. The effect on the 100 Hz ramp is added in (c), where sidebands of the order of ~ 300 Hz (that reflects the number of oscillations present in a single ramp period) are present.

We remind here that direct detection can only capture amplitude fluctuations $\delta q(t)$ (see section 2.3.1), therefore a parametric or an interference effect are needed to convert the phase fluctuations $\delta p(t)$ into amplitude ones $\delta q(t)$. The resulting optically modulated signal is shown in Fig. 6.8a.

During an actual measurement, the 100 Hz ramp will be off, and the photocurrent signal will contain only the phase fluctuations that we aim to compensate and the Ω_{m1} kHz signal. Due to the optical Ω_{m1} modulation, the phase noise, in the electronic frequency domain, will be present in the sidebands around Ω_{m1} , as previously explained and shown in Fig. 6.8b and 6.8c. In contrast, without modulation, the phase noise information is concentrated in the DC component.

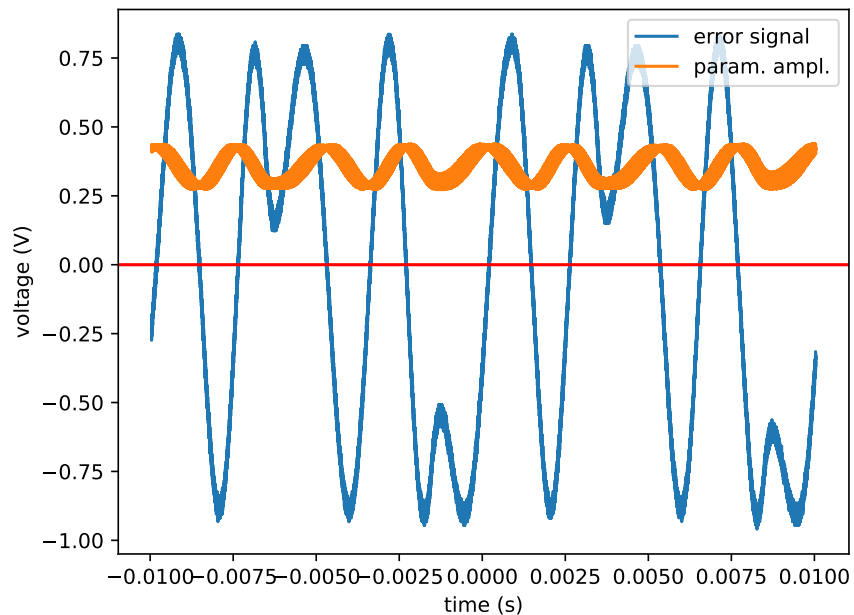


Figure 6.9: Experimental signals of the parametric amplification optically modulated at 90 kHz (orange) and of the corresponding error signal $y_{out}(t)$ (blue). Note that the error signal crosses zero when the parametric amplification reaches a peak.

After the demodulation and the filtering stages, where we use a low-pass-filter with a 30 kHz cutoff frequency, the signal is amplified and sent to the PID controller. In Fig. 6.9, we show the experimental photodiode signal $y_{mod}(t)$ as well as the error signal that results from the modulation-demodulation-LPF chain. The response signal $u(t)$ of the PID is sent to the pump piezo actuator, to correct for phase fluctuations.

The amplitude of the error signal depends on the relative phase between the modulation

and demodulation channels. This phase can be tuned by ensuring that both the piezo modulation signal and the corresponding demodulation signal stem from the same function generator. Tuning the relative phase between the two output channels grants control on the amplitude of the error signal. Typically, we fix the phase of one channel and we scan the phase of the other channel, searching for the phase value ϕ_{min} at which the error signal vanishes and then setting the phase at $\phi_{min} + \pi/2$. Indeed, the phases $\phi_{min} \pm n\pi$ will all correspond to vanishing error signals, while the phases $\phi_{max,\pm} = \phi_{min} \pm \pi/2$ are the phase values for which the error signal is maximal.

We conclude the review of the AC lock by addressing a difficulty encountered during its implementation that remains, at present day, unresolved. Theoretically, the AC lock is designed to be insensitive to mean value fluctuations. This property is advantageous, as it contributes to increased lock stability. However, in our setup we observe a residual DC signal that manages to reach the amplification stage, resulting in an amplified DC offset within the error signal. This presents a significant issue, because our error signal must lock precisely at zero. While we can mitigate this by adjusting the offset of the amplifier at the outset of each experimental run, it remains a vulnerability in our locking system, as our lock point becomes susceptible to gradual drifts in this residual DC signal.

After stabilizing both parametric processes of the two waveguides, we proceed to lock the seed phases at the 50:50 beam splitter level. We remind that our goal is to lock the relative phases of the two beams at $\phi = \pm\pi/2$. In an interference signal, provided it is well-aligned and the visibility is maximized, this corresponds to setting the setpoint S at the average value of the signal, which corresponds to a steep slope. Therefore, we can safely employ the simpler DC lock. The interference signal of the two seed beams is measured by a photodiode and, in this case, the resulting signal $y(t)$ is directly sent to the PID, without additional processing. The response signal $u(t)$ is sent to a piezo actuator placed onto the seed path to finally achieve locking.

6.2.4 Measurement-hold phase

The phase-locking system, which involves the detection of the seed at various points in the experiment, plays a crucial role in aligning the phases within the setup. However, if our goal is to measure squeezed vacuum light, we must get rid of the seed beam during the measurement. Therefore, during a measurement run, we need to distinguish between two distinct phases: 1) a locking phase, where all beams are precisely aligned to facilitate the implementation of the EPR state (or of the cluster state) and its subsequent measurement, and 2) an actual measurement phase. In the measurement phase, the seed beam is blocked, allowing only the vacuum squeezed light to illuminate the homodyne detector. The transition between the lock and measurement phases must occur rapidly to outpace the phase fluctuations in our beam.

In Fig. 6.10, we can observe the typical phase noise characteristic of our setup, with the majority of the noise occurring in the 1 kHz range. To accommodate these

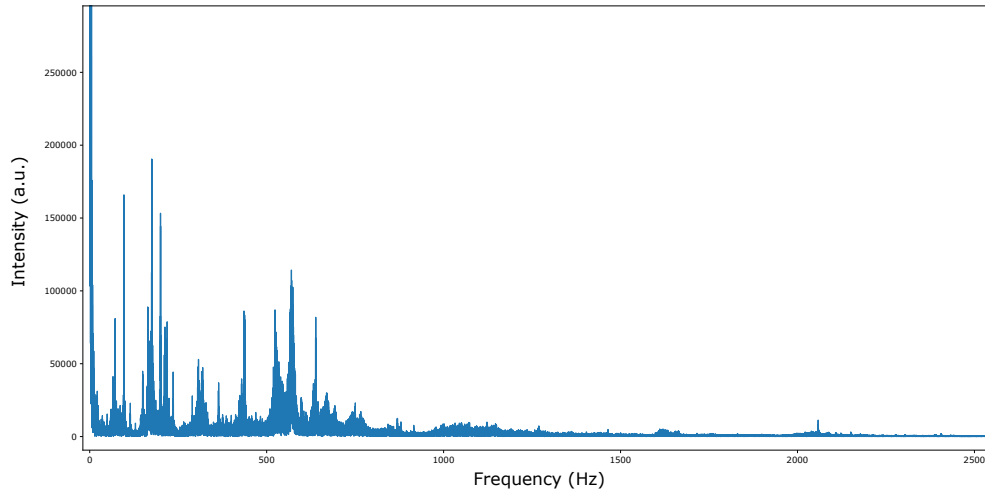


Figure 6.10: Characteristic phase noise in our setup, obtained by taking the FFT of the oscilloscope measurement of light hitting a photodiode. Most of the phase noise is contained in the range 0-1kHz.

lock-measurement cycles effectively, we have selected a chopping wheel (specifically, the MC1F100 from Thorlabs) capable of defining cycles with frequencies up to $f_{chop} = 10$ kHz. This choice is deliberate because if f_{chop} was smaller or comparable to the phase noise, the phase could drift too quickly during the measurement stage, making it challenging to correct during the lock stage.

Part III

Quantum Information Processing with Squeezed Light

Chapter 7

Continuous-Time Quantum Walks in a photonics setup

Contents

7.1 Quantum Walks	160
7.1.1 Random walks on graphs	160
7.1.2 Continuous-time Quantum Walks for spatial search	161
7.1.3 Quantum Walk search in a complete graph	164
7.2 Mapping from theory to experiment	168
7.2.1 Encoding qudits in photon-subtracted squeezed states	168
7.2.2 Encoding of the states and operations for the walk	169
7.3 Photonic implementation of Quantum Walks	171
7.3.1 Building an interferometer	171
7.3.2 A simple instructive attempt	173
7.3.3 Interferometer for quantum search	175
7.3.4 Fidelity with the target state of the walk	178
7.3.5 Generalities on a realistic experimental implementation	180

Quantum walks, the quantum analogue of classical random walks, serve as tools for quantum information processing, offering a framework for implementing quantum algorithms that can provide quantum speed-up for specific problems. In this study, we specifically focus on the quantum walk version of the well-known Grover search algorithm [Grover 96]. Our focus is on continuous-time quantum walks (CTWQ), where time is treated as a continuous parameter, in contrast to the discrete-time version, that involves discrete time steps. The primary goal of this research is to identify an implementation of CTQW that incorporates operations that are feasible in an optical setup.

7.1 Quantum Walks

In this section, we provide a concise theoretical overview of continuous-time quantum walks applied to quantum search. Since quantum walks are often described as the quantum counterpart of classical random walks, we begin our study from the classical description and we later switch to the quantum domain. Here, quantum walks are investigated for the specific search task and in particular we will opt for a specific topology of the walk, that corresponds to the unstructured Grover search, to facilitate the implementation of spatial search. Although different topologies reflecting diverse information structures can also be implemented, exploring them falls beyond the scope of this thesis.

7.1.1 Random walks on graphs

Random walks are stochastic processes that find applications across various fields, providing insights into the dynamics of various systems. They serve as valuable tools in statistical physics, economics, biology, and computer science [Révész 13, Weiss 94]. In computer science, random walks play a crucial role, particularly in modelling Markov chains [Levin 17], which underpin numerous applications, especially those involving graph-based processes. In physics, random walks are used to model Brownian motion, capturing the random movement of particles suspended in a fluid [Weiss 94].

Here, we are interested in graph-based random walks. A graph \mathcal{G} is characterized by a finite set of vertices $V = \{1, 2, \dots, N\}$ and a finite set of links (or *edges*) E , represented by pairs of the form $e = (i, j)$, that indicate the connections between nodes. The degree $d(j)$ of a node j is the number of edges to which the node is connected. The adjacency matrix of the graph $\mathcal{G} = (V, E)$ is defined by:

$$A_{ij} = \begin{cases} 1 & \text{if } (i, j) \in E \\ 0 & \text{otherwise} \end{cases} \quad (7.1)$$

and it contains all the information regarding the connectivity and topology of the graph. Moreover, we define the Laplacian matrix as¹:

$$\mathbf{L} = \mathbf{A} - \mathbf{D} \quad (7.2)$$

where \mathbf{D} is a diagonal matrix with $D_{jj} = d(j)$. The Laplacian matrix serves as the driving term for the random walk. The Laplacian matrix, as the name suggests, embodies the discretization of the Laplace operator ∇^2 , present in the kinetic energy term of a particle trapped in a lattice [Wong 16].

A random walk on a graph is a stochastic process in which, at each time step t_i , we investigate the random variable X_i , associated with the position of a so-called *walker*. In

¹Here, we use the notation of ref. [Childs 04a] and [Wong 16]. A different notation, where $\mathbf{L} = \mathbf{D} - \mathbf{A}$, is often used.

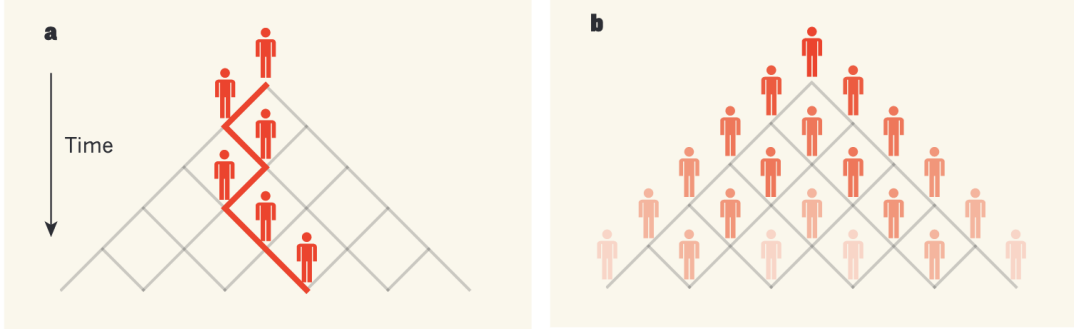


Figure 7.1: a) Classical random walk, where the walker moves left or right at each step. b) Quantum walk, where the walker moves in a superposition of left or right. The wavefunction of the walker can interfere destructively, impacting the probability of finding the walker in a specific vertex and leading to different results than the classical counterpart. Picture from [Matthews 12].

a discrete-time random walk, the walker is situated in a specific site of a lattice and has a certain probability of jumping to a neighbouring site at every time-step t_i . Conversely, a continuous-time random walk involves infinitesimal time-steps dt , and we then define the *hopping rate* γ , that represents the probability per unit time for the walker to move to a connected vertex. Both of these processes can be envisioned as the deterministic evolution of a probability density defined over the graph.

In this work we focus on continuous-time walks. Defining $p_i(t)$ as the probability that the walker is in vertex i at time t , we can derive the equation:

$$\frac{dp_j(t)}{dt} = \gamma \sum_i L_{ji} p_i(t) \quad (7.3)$$

Note that, as by construction $\sum_j L_{ji} = 0$, probabilities are conserved, i.e. $\sum_j \frac{dp_j(t)}{dt} = 0$. We are left with a set of N differential equations, that can be solved to yield the probability vector $\mathbf{p}(t) = (p_1(t), \dots, p_N(t))$:

$$\mathbf{p}(t) = e^{\gamma L t} \mathbf{p}(0) \quad (7.4)$$

From this equation, we identify the Laplacian matrix of the graph as the generator of time evolution.

7.1.2 Continuous-time Quantum Walks for spatial search

In the context of quantum walks, the fundamental concept of random walks is retained, but instead of a classical probability distribution we deal with a quantum state and its complex amplitudes. The behavior of a quantum walk, however, diverges significantly to that of a random walk, due to the quantum interference effect [Matthews 12], as shown in Fig. 7.1.

This distinctive feature allows us to devise quantum algorithms based on quantum walks that exhibit a substantial speed-up compared to classical counterparts.

In the quantum scenario, the Hilbert space of the quantum walk is N -dimensional and is spanned by states $|j\rangle$, that represent vertices of the graph. The walker is described by a quantum state $|\psi(t)\rangle$ and instead of dealing with probabilities, we work with complex amplitudes denoted as $p_j = |\langle j|\psi(t)\rangle|^2$. The evolution of the state is dictated by the Schrödinger equation, where probability amplitudes evolve as follows:

$$i\frac{dp_j}{dt} = \sum_i H_{ji}p_i \quad (7.5)$$

Comparing this equation with Eq. 7.3, we can recognize the quantum version of the random walk, with the Hamiltonian evolution defined by the matrix $\mathbf{H} = -\gamma\mathbf{L}$. Different choices of Hamiltonian are possible, leading to the same dynamics, provided that the graph is regular [Wong 16].

The quantum walk described above adheres to the topology of a given graph without targeting a specific task. However, we can modify the Hamiltonian of the graph to serve a specific purpose. Here, we specifically revise quantum walks for spatial search, exploring how the walk can be employed to execute quantum search on a graph. A well-known quantum search algorithm is the *Grover search algorithm* [Grover 96], designed to address the problem of locating a particular item, labeled as w , in a list of N unsorted items. While classical algorithms typically require $O(N)$ queries to find the marked item, the Grover search algorithm exhibits a quadratic speedup, accomplishing the task with $O(\sqrt{N})$ queries, and this has been proved to be asymptotically optimal [Bennett 97]. Quantum walks can be implemented in a graph that reflects the structure of the database. A detailed reference on search by quantum walks, that provides the theoretical framework that we outline here, can be found in [Childs 04a].

To implement the spatial search with a quantum walk, the evolution must be directed towards the vertex $|w\rangle$. We define the *oracle Hamiltonian*:

$$\hat{H}_w = -|w\rangle\langle w| \quad (7.6)$$

and we modify the walk Hamiltonian as:

$$\hat{H} = -\gamma\hat{L} + \hat{H}_w \quad (7.7)$$

We initialize the walker in the state defined as:

$$|s\rangle = \frac{1}{\sqrt{N}} \sum_j |j\rangle \quad (7.8)$$

which represents an equal superposition of all the vertices in the graph, and we let the state evolve for a certain time T . Our goal is to find the smallest T for which $|\psi(T)\rangle$ is as close to

$|w\rangle$ as possible, resulting in the quantity:

$$p_w = |\langle w|\psi(T)\rangle|^2 \quad (7.9)$$

being as close to 1 as possible.

In general, we have no guarantee of the success of the algorithm for a given topology. However, insights into the success probability, given γ and T , can be obtained from the spectrum of the Hamiltonian and, consequently, from a given shape of the graph [Childs 04a]. Here, we work with $N \gg 1$. We point out that $|s\rangle$ and $|w\rangle$ are not orthogonal, i.e.

$$\langle s|w\rangle = \frac{1}{\sqrt{N}} \quad (7.10)$$

but for $N \gg 1$ we can recover orthogonality.

We start by noting that $|s\rangle$ is the ground state of the Laplacian (a positive-definite operator), as $\hat{L}|s\rangle = 0$. It follows that, for $\gamma \rightarrow \infty$, the ground state $|v_0\rangle$ of \hat{H} is $|v_0\rangle \sim |s\rangle$. Conversely, for $\gamma \rightarrow 0$, the contribution of \hat{L} in the Hamiltonian of Eq. 7.7 is negligible, and we obtain $|v_0\rangle \sim |w\rangle$. The ground state of \hat{H} switches from $|w\rangle$ to $|s\rangle$ as we increase the value of γ to infinity. It is then reasonable to conclude that, since $|s\rangle$ and $|w\rangle$ are almost orthogonal, there must be a certain value of γ for which the ground state has a substantial overlap with both $|s\rangle$ and $|w\rangle$.

A similar reasoning can be applied to the first excited state $|v_1\rangle$. For $\gamma \rightarrow 0$, the lowest energy state after the ground state must be $|s\rangle$. Indeed, following the orthogonality of $|v_0\rangle \sim |w\rangle$ and $|v_1\rangle$, it follows that $\hat{H}|v_1\rangle = -\gamma\hat{L}|v_1\rangle$. As $|w\rangle$ is the ground state of \hat{L} for $\gamma \rightarrow 0$, it follows that $|v_1\rangle \sim |s\rangle$. For the case $\gamma \rightarrow \infty$ the same cannot be inferred, but we expect the overlap $|\langle w|v_1\rangle|^2$ to increase with respect to the $\gamma \rightarrow 0$ case, for which it is vanishing. If the first excited state has some considerable overlap with both $|s\rangle$ and $|w\rangle$, for the same values of γ obtained for the ground state, then the Hamiltonian will drive transitions from $|s\rangle$ to $|w\rangle$ in a time of the order $1/(E_1 - E_2)$ [Childs 04b].

The spatial search is optimal if the ground state and the first excited state show the same overlap with $|s\rangle$ and $|w\rangle$, for a specific value of γ . Indeed, in the case where the two eigenstates of the Hamiltonian satisfy:

$$|v_0\rangle \sim \frac{|s\rangle - |w\rangle}{\sqrt{2}} \quad (7.11)$$

$$|v_1\rangle \sim \frac{|s\rangle + |w\rangle}{\sqrt{2}} \quad (7.12)$$

we can calculate the evolved state at time t , starting from the initial state $|\psi(0)\rangle = |s\rangle$:

$$|\psi(t)\rangle = e^{-i\hat{H}t}|s\rangle = \frac{e^{-iE_0t}}{\sqrt{2}} \left[|v_0\rangle - \frac{e^{-i(E_1-E_0)t}}{2} |v_1\rangle \right] \quad (7.13)$$

For time $t^* = \pi/(E_1 - E_2)$, the evolution yields:

$$|\psi(t^*)\rangle = e^{-iE_0 t} \frac{|v_0\rangle + |v_1\rangle}{\sqrt{2}} = e^{-iE_0 t} |w\rangle \quad (7.14)$$

Therefore, the quantum walk converges to the target state with probability $p_w = 1$.

This condition has been found for the complete graph, where all the vertices are interconnected, and the n -dimensional hypercube, with $N = 2^n$ vertices. Moreover, for d -dimensional periodic lattices, where d is fixed independently on N , the algorithm succeeds in the case $d > 4$, while for $d = 4$ it provides a speedup of $O(\sqrt{N \log N})$ and for $d < 4$ it provides no speedup.

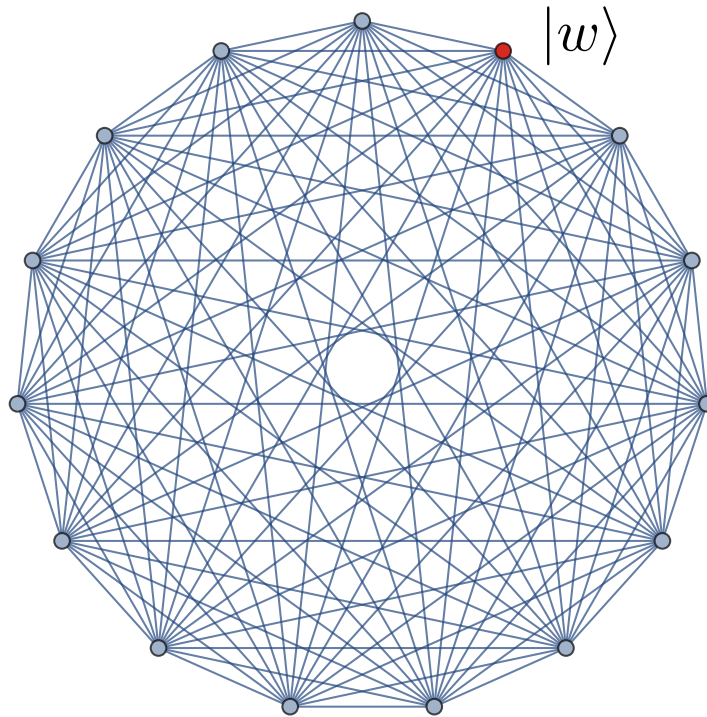


Figure 7.2: Complete graph with $N = 15$, where a vertex has been marked as the target state of the quantum search.

7.1.3 Quantum Walk search in a complete graph

In this manuscript we will be interested in the complete graph, whose topology is illustrated in Fig. 7.2, which is the direct analogue of the Grover search, as it can be used to represent an unstructured database [Farhi 96]. Alternative topologies would correspond to different database structures.

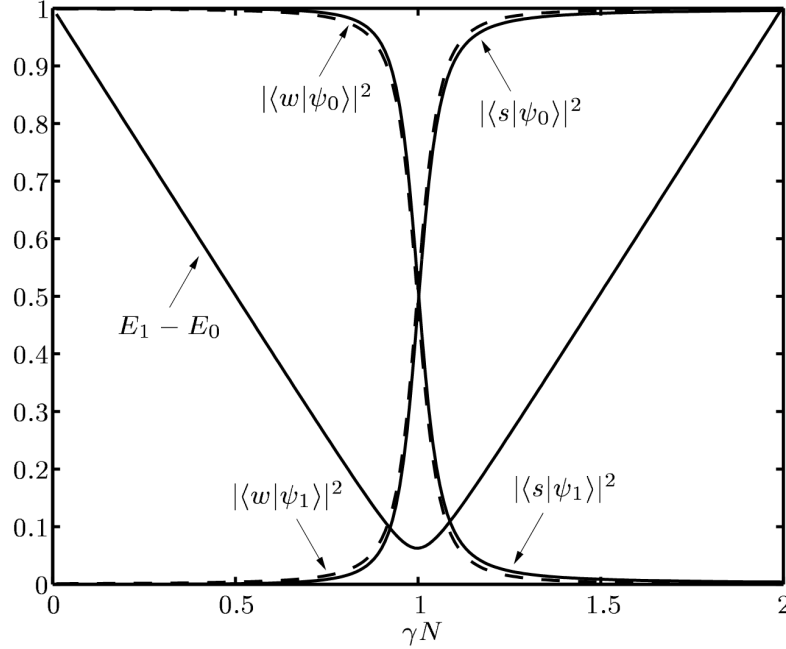


Figure 7.3: Energy gap and overlaps for the complete graph with $N = 1024$, from [Childs 04a]. We see from this graph that the condition $\gamma N = 1$ is optimal for the success of the walk.

The Hamiltonian for the quantum search algorithm in a complete graph is¹:

$$\hat{H} = -\gamma N |s\rangle \langle s| - |w\rangle \langle w| \quad (7.15)$$

In Fig. 7.3, the overlaps between the $|w\rangle$ and $|s\rangle$ states and the ground and first excited state are shown, and we conclude that for $\gamma N = 1$ the quantum walk is optimal. Therefore, from now on we will set $\gamma N = 1$.

The complete graph is a useful topology because, regardless of the number of nodes, we can exploit the graph symmetry to restrict the dynamics to a 2-dimensional subspace [Novo 15]. We identify the basis vectors of the 2-dimensional subspace as all the unmarked vertices on one hand, and as all the marked one(s), identified with w . If w is a single node in the graph, we define:

$$|e_1\rangle = \frac{1}{\sqrt{N-1}}(1, 1, \dots, 1, 0, 1 \dots) = \begin{pmatrix} 1 \\ 0 \end{pmatrix}$$

$$|e_2\rangle = |w\rangle = (0, 0, \dots, 0, 1, 0 \dots) = \begin{pmatrix} 0 \\ 1 \end{pmatrix}$$

¹To obtain this Hamiltonian, the term $N\mathbb{1}$, that does not modify the dynamics, has been added to the Laplacian.

where $|e_1\rangle$ and $|e_2\rangle$ are the basis vectors. In this new basis, the vectors $|s\rangle$ and $|w\rangle$ read:

$$|s\rangle = \frac{\sqrt{N-1}|e_1\rangle + |e_2\rangle}{\sqrt{N}} = \frac{1}{\sqrt{N}} \begin{pmatrix} \sqrt{N-1} \\ 1 \end{pmatrix}$$

$$|w\rangle = |e_2\rangle = \begin{pmatrix} 0 \\ 1 \end{pmatrix}$$

and the Hamiltonian of Eq. 7.15 in the $\{e_1, e_2\}$ basis can be written as:

$$\hat{H} = -|s\rangle\langle s| - |w\rangle\langle w| = -\frac{N-1}{N}|e_1\rangle\langle e_1| - \frac{\sqrt{N-1}}{N}|e_1\rangle\langle e_2| - \quad (7.16)$$

$$\frac{\sqrt{N-1}}{N}|e_2\rangle\langle e_1| - \frac{N+1}{N}|e_2\rangle\langle e_2| \quad (7.17)$$

and in matrix form:

$$H = -\frac{1}{N} \begin{pmatrix} N-1 & \sqrt{N-1} \\ \sqrt{N-1} & N+1 \end{pmatrix} \quad (7.18)$$

The eigenvalues of this Hamiltonian are:

$$E_0 = -1 - \frac{1}{\sqrt{N}} \quad (7.19)$$

$$E_1 = -1 + \frac{1}{\sqrt{N}} \quad (7.20)$$

and the energy gap is $\Delta E = 2/\sqrt{N}$. Moreover, the eigenvectors read:

$$|v_0\rangle = \begin{pmatrix} \frac{\sqrt{N-1}}{\sqrt{N+1}} \\ 1 \end{pmatrix} \propto \frac{|s\rangle + |w\rangle}{\sqrt{2}} \quad (7.21)$$

$$|v_1\rangle = -\begin{pmatrix} \frac{\sqrt{N-1}}{\sqrt{N-1}} \\ 1 \end{pmatrix} \propto \frac{|s\rangle - |w\rangle}{\sqrt{2}} \quad (7.22)$$

We then expect the Quantum Walk Hamiltonian to rotate from $|s\rangle$ to $|w\rangle$ in a time of order $1/(E_1 - E_0)$. In the case of the complete graph, this time is:

$$t^* = \frac{\pi\sqrt{N}}{2} \quad (7.23)$$

This can be verified as follows. Along with the identity matrix, the Pauli matrices $\{\sigma_i\}_{i=1,2,3}$ constitute an orthonormal basis within the Hilbert space of 2×2 complex matrices. The quantum walk Hamiltonian can then be expressed in the $\{\mathbb{1}, \sigma_i\}$ basis with the following formula:

$$H = \sum_{\mu=0,1,2,3} \alpha_\mu \sigma_\mu \quad (7.24)$$

where we define $\sigma_0 = \mathbb{1}$ and where $\alpha_\mu = \frac{1}{2}\text{Tr}(H\sigma_\mu)$. From the definition of Eq. 7.18, it follows that $\alpha_0 = -1$, $\alpha_1 = -\frac{\sqrt{N-1}}{N}$, $\alpha_2 = 0$ and $\alpha_3 = 1/N$. The Hamiltonian of the walk can then be expressed in the Pauli basis as:

$$H = -\mathbb{1} - \frac{\sqrt{N-1}}{N}\sigma_x + \frac{1}{N}\sigma_z = -\mathbb{1} + \vec{v} \cdot \vec{\sigma} \quad (7.25)$$

where $\vec{v} = (-\frac{\sqrt{N-1}}{N}, 0, \frac{1}{N})$ and $\vec{\sigma}$ is the Pauli matrices vector. We define $\hat{k} = \vec{v}/\|\vec{v}\|$, where $\|\vec{v}\| = \frac{1}{\sqrt{N}}$, so that $\vec{v} \cdot \vec{\sigma} = \|\vec{v}\|\hat{k} \cdot \hat{\sigma}$. The unitary evolution operator associated to the quantum walk Hamiltonian can be written as:

$$\hat{U}(t) = e^{-i\hat{H}t} = e^{-i\mathbb{1}t} e^{-i\|\vec{v}\|\hat{k} \cdot \hat{\sigma}t} \quad (7.26)$$

This form is useful because it permits us to apply the well-known formula of Pauli-vector exponentiation:

$$e^{i\theta\hat{k} \cdot \hat{\sigma}} = \cos \theta \mathbb{1} + i \sin \theta \hat{k} \cdot \hat{\sigma} \quad (7.27)$$

that allows us to rewrite the evolution of the walk as a linear combination of Pauli matrices, plus the identity. Identifying $\theta = \|\vec{v}\|t = t/\sqrt{N}$ and $\hat{k} = (-\sqrt{\frac{N-1}{N}}, 0, \frac{1}{\sqrt{N}})$, we obtain:

$$\hat{U}(t) = e^{-i\mathbb{1}t} \left[\cos \theta \mathbb{1} + i \sin \theta \sqrt{\frac{N-1}{N}} \sigma_x - i \frac{\sin \theta}{\sqrt{N}} \sigma_z \right] \quad (7.28)$$

The characteristic time for the walk is $t^* = \pi\sqrt{N}/2$, as reported in Eq. 7.23, which corresponds to $\theta = \pi/2$. At t^* , the evolution operator is given by:

$$\hat{U}(t^*) = e^{-i\mathbb{1}\pi\sqrt{N}/2} i \left[\sqrt{\frac{N-1}{N}} \sigma_x - \frac{1}{\sqrt{N}} \sigma_z \right] \quad (7.29)$$

We can verify that applying this unitary evolution to $|s\rangle$ leads exactly to $|w\rangle$, up to an overall complex phase. The probability of finding the walker in the target state at time t^* is:

$$|\langle w|\hat{U}(t^*)|s\rangle|^2 = 1 \quad (7.30)$$

From Eq. 7.29, we can make an important approximation, that will be used throughout this thesis. Indeed, for $N \gg 1$, the unitary operation at time t^* is given simply by:

$$\hat{U}(t^*) \sim \sigma_x \quad (7.31)$$

7.2 Mapping from theory to experiment

7.2.1 Encoding qudits in photon-subtracted squeezed states

Continuous-time quantum walks (CTQW) on a graph are implemented in a finite N -dimensional Hilbert space, spanned by basis states $|j\rangle$, which we identify with the vertices of our graph. Our first step is to map the physical entities of our experiment to the theoretical framework of CTQW.

The first challenge we encounter is mapping the uncountable nature of the continuous variables in our experiment to the finite number of graph vertices. In other words, we aim to find a suitable mapping between the states generated in our experiment and the states required in quantum walks theory. In our case, this mapping involves encoding discrete variables into infinite-dimensional systems represented by continuous variables. The encoding of DV into CV is not a new concept. One notorious example of this involves GKP (Gottesman-Kitaev-Preskill) states [Gottesman 01], where the infinite-dimensional Hilbert space of a quantum harmonic oscillator is used to encode a qubit. Here, we use an encoding proposed in [Arzani 19a]. Such encoding employs squeezing and photon subtractions as tools to map states generated in our optical platform to multiple qubits or to qudits.

We start with a multimode squeezed vacuum state:

$$|MMSV\rangle = \otimes_{j=1}^N |r_j\rangle_j = \otimes_{j=1}^N \hat{S}(r_j)_j |\emptyset\rangle \quad (7.32)$$

where $|r_j\rangle_j$ are squeezed vacuum states in the optical mode \mathbf{f}_j ¹ with squeezing parameters r_j , implemented by acting on the multimode vacuum with independent squeezing operators $\hat{S}(r_j)_j$. Here, the multimode vacuum $|0, 0, \dots, 0\rangle$ is indicated with $|\emptyset\rangle$ not to confuse it with the logical qudit $|0\rangle$. The state $|MMSV\rangle$ is what we obtain at the output of the nonlinear SPDC process. Indeed, in our setup we have a set of independently squeezed pulsed-modes and a set of independently squeezed Hermite-Gauss frequency modes, as shown in Chapter 5.

The next step is applying a photon annihilation operator, or suitable linear combinations, to the multimode squeezed vacuum state. We define the operator:

$$\hat{b} = \sum_j c_j \hat{a}_j \quad (7.33)$$

where $\sum_j |c_j|^2 = 1$. Applying \hat{b} to the $|MMSV\rangle$ state, we obtain:

$$|MMPS\rangle = \hat{b} |MMSV\rangle = c_0 \hat{a}_0 |MMSV\rangle + c_1 \hat{a}_1 |MMSV\rangle + \dots \quad (7.34)$$

¹In another notation used in previous chapters we indicated them as $|r_j : f_j\rangle$.

or, rewritten in a compact form:

$$|MMPS\rangle = \sum_j \gamma_j |s_j\rangle_j \otimes_{i \neq j} |r_i\rangle_i \quad (7.35)$$

We denote $|MMPS\rangle$ as a multimode photon-subtracted state, which represents a multimode squeezed vacuum state where a photon has been subtracted from a superposition of the $\{\mathbf{f}_j\}$ modes [Averchenko 14, Averchenko 16]. Here, $\gamma_j = c_j/\mathcal{N}_j$ and we define the photon-subtracted state in mode \mathbf{f}_j as:

$$|s_j\rangle_j = \mathcal{N}_j \hat{a}_j |r_j\rangle_j \quad (7.36)$$

where $\mathcal{N}_j = 1/\sinh(r_j)$ is a normalization factor. We define:

$$|j\rangle = |s_j\rangle_j \otimes_{i \neq j} |r_i\rangle_i \quad (7.37)$$

that, written explicitly, read:

$$\begin{aligned} |0\rangle &= \mathcal{N}_0 \hat{a}_0 |MMSV\rangle \\ |1\rangle &= \mathcal{N}_1 \hat{a}_1 |MMSV\rangle \\ &\dots \\ |i\rangle &= \mathcal{N}_i \hat{a}_i |MMSV\rangle \\ &\dots \\ |N\rangle &= \mathcal{N}_N \hat{a}_N |MMSV\rangle \end{aligned} \quad (7.38)$$

The $|i\rangle$ state represents a multimode squeezed vacuum state where a photon has been subtracted from mode \mathbf{f}_i . We can rewrite the $|MMPS\rangle$ state from Eq. 7.35 as:

$$|MMPS\rangle = \sum_j \gamma_j |j\rangle \quad (7.39)$$

The $|j\rangle$ states are orthogonal and we refer to the $|j\rangle$ basis as the *computational basis*. By tailoring appropriately the photon subtraction on multimode squeezed vacuum, we can effectively encode qudits in infinite-dimensional bosonic systems. This is the encoding we employ to apply the theory of quantum walks in our setup. Additional details on the encoding can be found in [Arzani 19a].

7.2.2 Encoding of the states and operations for the walk

Here we investigate how the quantum states relevant for the quantum walk in a complete graph can be expressed according to the encoding presented in section 7.2.1. In particular, we focus on the states $|s\rangle$ and $|w\rangle$, i.e. the superposition of all the vertices and the marked vertex. These states are expressed as follows:

$$|w\rangle = \mathcal{N} \hat{a}_w |MMSV\rangle \quad (7.40)$$

$$|s\rangle = \mathcal{N} \hat{a}_s |MMSV\rangle \quad (7.41)$$

Here, \hat{a}_w is the annihilation operator of a photon in mode \mathbf{f}_w and \hat{a}_s is defined as the operator that annihilates a photon in the superposition of all the modes, namely:

$$\hat{a}_s = \frac{\hat{a}_0 + \cdots + \hat{a}_N}{\sqrt{N}} \quad (7.42)$$

In these equations we assumed, for simplicity, that the squeezing levels are equal, i.e. $r_j = r$ for every mode j , so that $\mathcal{N} = \mathcal{N}_j$ ¹.

The \hat{a}_w and \hat{a}_s operators in general do not commute, as it is evident from the computation of their commutator:

$$[\hat{a}_w, \hat{a}_s^\dagger] = \left[\hat{a}_w, \frac{1}{\sqrt{N}} \sum_i \hat{a}_i^\dagger \right] = \frac{1}{\sqrt{N}} \mathbb{1} \quad (7.43)$$

However, in the limit of large N , we recover the commutativity of the \hat{a}_w and \hat{a}_s^\dagger operators, as $[\hat{a}_w, \hat{a}_s^\dagger] \sim 0$.

Now that we have mapped the states of the walk into states that we can generate in our optical table, we aim to do the same thing with operators. We saw previously that the unitary of the walk can be expressed, for a complete graph, as a linear combination of Pauli matrices and the identity matrix, as seen in Eq. 7.28. The mapping from operators of the form $|s\rangle\langle w|$ to the experimental operations is defined by their action on the Hilbert space where the quantum walk takes place. From the definition of the states $|s\rangle$ and $|w\rangle$, we require:

$$(|s\rangle\langle w|) |s\rangle = \frac{|s\rangle}{\sqrt{N}} \quad (7.44)$$

$$(|s\rangle\langle w|) |w\rangle = |s\rangle \quad (7.45)$$

Similar relations hold for $|w\rangle\langle s|$, $|i\rangle\langle j|$ and so on. These operators are of the type:

$$|s\rangle\langle w| \Big|_{\mathcal{H}_{QW}} = \hat{S} \hat{a}_s^\dagger \hat{a}_w \hat{S}^\dagger \Big|_{\mathcal{H}_{QW}} \quad (7.46)$$

where \hat{S} represents the multimode squeezing operator. Indeed, it can be shown that operators of this form fulfil the defining relations 7.44 and 7.45. An analogous definition holds for other operators of the same form.

From Eq. 7.31 and considering the mapping of Eq. 7.46, the evolution operator at time t^* (the characteristic time of the walk) reads:

$$\hat{U}(t^*) \sim \hat{S} \hat{a}_s^\dagger \hat{a}_w \hat{S}^\dagger + \hat{S} \hat{a}_w^\dagger \hat{a}_s \hat{S}^\dagger \quad (7.47)$$

¹This is a reasonable physical assumption in some cases, for example if our modes are time-bin modes. This assumption in general fails if we use frequency modes, that have an unequal level of squeezing, as seen in the previous chapters. In that case, the operator \hat{a}_s needs to be redefined to account for the difference in the \mathcal{N}_i constants.

in the limit of large N . Taking into account the equations¹:

$$\hat{S}^\dagger \hat{a} \hat{S} = \cosh r \hat{a} - \sinh r \hat{a}^\dagger \quad (7.48)$$

$$\hat{S}^\dagger \hat{a}^\dagger \hat{S} = \cosh r \hat{a}^\dagger - \sinh r \hat{a} \quad (7.49)$$

the unitary operator at time t^* can be expressed as:

$$\hat{U}(t^*) \sim \cosh 2r (\hat{a}_s^\dagger \hat{a}_w + \hat{a}_w^\dagger \hat{a}_s) + \sinh 2r (\hat{a}_s^\dagger \hat{a}_w^\dagger + \hat{a}_w \hat{a}_s) \quad (7.50)$$

Eq. 7.50 and Eq. 7.47 are equivalent for the purpose of the quantum walk, but their experimental implementation is not. Both of them require photon subtractions and photon additions, but Eq. 7.47 requires also online squeezing, which is experimentally demanding. Therefore, we will focus on the implementation that stems from Eq. 7.50.

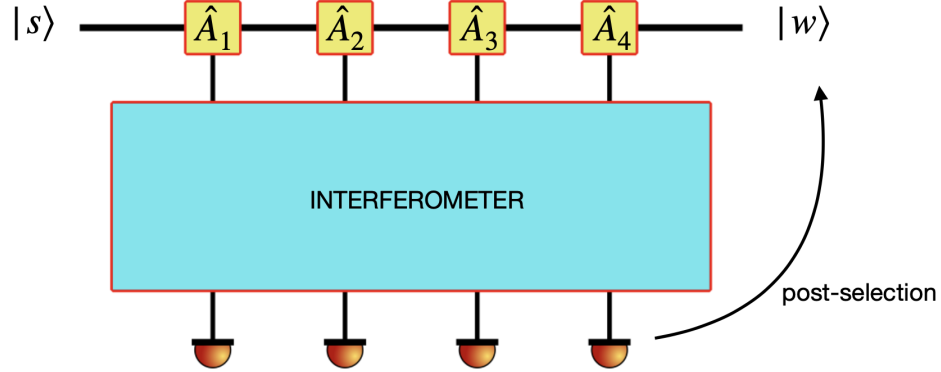


Figure 7.4: Basic scheme for the implementation of the quantum walk, involving the interference of photons released when the operations of the main path are successful. This is followed by detection and post-selection.

7.3 Photonic implementation of Quantum Walks

7.3.1 Building an interferometer

Realizing a unitary transformation as described in Eq. 7.50, requires the quantum interference of different operations. This can be achieved through an interferometric scheme shown in Fig 7.4, comprising several steps. Different quantum operations, denoted as \hat{A}_i , are applied along the optical path, leading to the emission of a photon inside an

¹These equations are analogous to the ones derived in Eq. 1.112 and 1.111, but here we use a different convention, that can be found for example in [Lvovsky 16].

interferometer. These operations could include photon addition or photon subtraction, that can be implemented in an heralded setting with the following unitaries:

$$\hat{U}_{ps} = e^{i\lambda(\hat{a}\hat{b}^\dagger + \hat{a}^\dagger\hat{b})} \quad (7.51)$$

and

$$\hat{U}_{pa} = e^{i\mu(\hat{a}\hat{b} - \hat{a}^\dagger\hat{b}^\dagger)} \quad (7.52)$$

where we herald on single-photon counting on the mode b [Jacquard 17, Kim 08]. For $\mu, \lambda \ll 1$ we can expand these operators in the first order. As a consequence, quantum interference occurs in the interferometer, and it is followed by single photon detection and post-selection. Our goal is to find the operations \hat{A}_i and the interferometer configuration that permit us to implement the unitary of Eq. 7.50.

To understand the concept, and in particular the role of the interferometer, we review a simple interferometer, with two quantum operations \hat{A}_1 and \hat{A}_2 applied on the optical path. We assume that these operations, when effective, release a photon in the interferometer with a certain probability λ . The scheme of the setup is shown in Fig. 7.5. An analogous setup, that involves the interference of two photon subtraction operations, has already been tested to prove the commutation relations of bosonic creation and annihilation operators [Kim 08, Parigi 07].

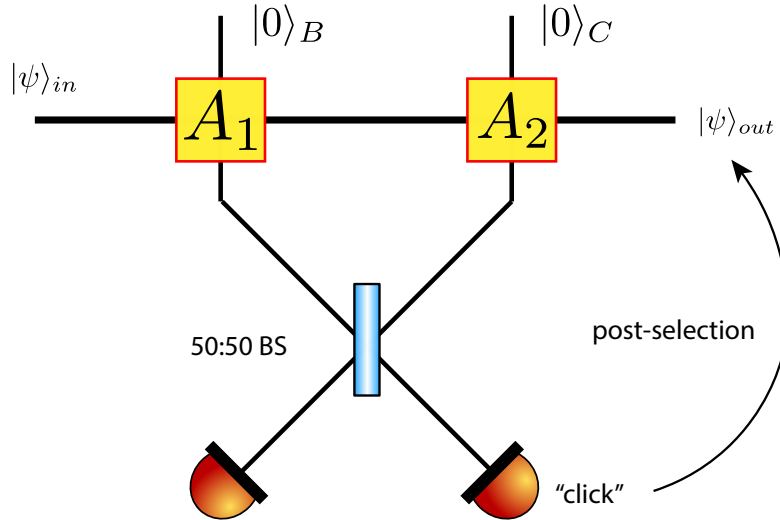


Figure 7.5: Example of simple scheme for the interference of the operations \hat{A}_1 and \hat{A}_2 .

The action of both operations on the input state $|\psi\rangle$ results in the state:

$$|\psi\rangle_A |0\rangle_B |0\rangle_C \rightarrow \mathbb{1} |\psi\rangle_A |0\rangle_B |0\rangle_C + i\lambda\hat{A}_1 |\psi\rangle_A |1\rangle_B |0\rangle_C + i\lambda\hat{A}_2 |\psi\rangle_A |0\rangle_B |1\rangle_C + \mathcal{O}(\lambda^2) \quad (7.53)$$

where with the subscript A, B, C we indicate the three different paths. Here, the term $\mathbb{1}$ represents the instance in which no operation is effective and no photon is released in the interferometer, while the other two terms represent the success of one of the two operations with probability λ , paired with the releasing of a photon in the B or C arm of the interferometer.

The action of the 50:50 beam splitter on the B, C subsystems is the following:

$$|1\rangle_B |0\rangle_C \rightarrow \frac{|1\rangle_B |0\rangle_C + |0\rangle_B |1\rangle_C}{\sqrt{2}} \quad (7.54)$$

$$|0\rangle_B |1\rangle_C \rightarrow \frac{-|1\rangle_B |0\rangle_C + |0\rangle_B |1\rangle_C}{\sqrt{2}} \quad (7.55)$$

If $\lambda \ll 1$, the resulting state turns out to be:

$$\begin{aligned} |\psi\rangle_A |0\rangle_B |0\rangle_C \rightarrow \mathbb{1} |\psi\rangle_A |0\rangle_B |0\rangle_C + \frac{i\lambda}{\sqrt{2}} (\hat{A}_1 - \hat{A}_2) |\psi\rangle_A |1\rangle_B |0\rangle_C + \\ \frac{i\lambda}{\sqrt{2}} (\hat{A}_1 + \hat{A}_2) |\psi\rangle_A |0\rangle_B |1\rangle_C \end{aligned} \quad (7.56)$$

This results show us that if we detect a photon in the B output of the beam-splitter, the operation $(\hat{A}_1 - \hat{A}_2)$ is applied on the input state, while if we detect a photon in the C output arm we are applying $(\hat{A}_1 + \hat{A}_2)$. Post-selecting on the detector clicks, allows us to select only the states we are interested in. For example, after post-selection on B -detector clicks, the output state is:

$$|\psi\rangle_{out} = C(\hat{A}_1 - \hat{A}_2) |\psi\rangle_{in} \quad (7.57)$$

where C is a normalization factor. Note that the B and C subsystems have been traced out as a consequence of the destructive measurement and post-selection.

To obtain this result, we assumed that higher-order terms were negligible. Higher-order terms are connected to the simultaneous presence of two photons in the interferometer. As our detectors are on-off detectors and not photon counting detectors, this will non-negligibly impact the purity of the post-selected state.

7.3.2 A simple instructive attempt

The goal here is to simulate the quantum walk for search algorithm at the specific time $t = t^*$. We start with an input state $|\psi_{in}\rangle = |s\rangle$, where $|s\rangle$ is defined in Eq. 7.8. Our goal is to investigate the possibility of building an interferometer such that, after the post-selection, the operation $\hat{U}(t^*)$ from Eq. 7.50 is implemented and we are left with the target state $|w\rangle$.

As an example, we present in Fig. 7.6 an interferometer that could be suitable for the implementation of the walk unitary. The chosen configuration includes four operations applied on the $|\psi_{in}\rangle$ path:

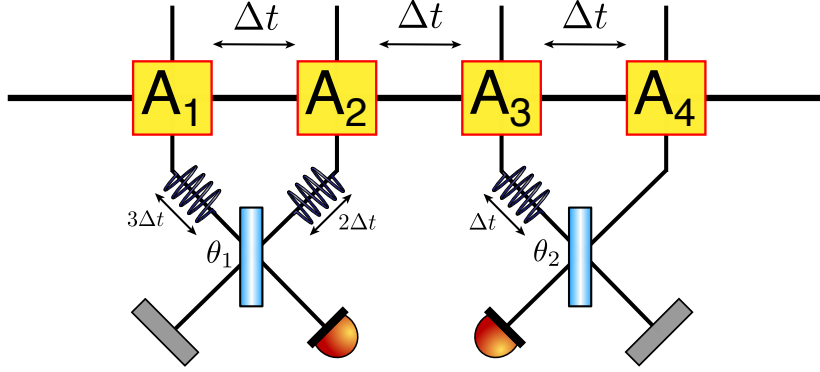


Figure 7.6: Simple attempt of interferometer scheme to implement the quantum search unitary.

- \hat{A}_1 is a photon addition operation on the mode s
- \hat{A}_2 is a photon subtraction operation on the mode s
- \hat{A}_3 is a photon addition operation on the mode w
- \hat{A}_4 is a photon subtraction operation on the mode w

The output arms of the operations \hat{A}_1 and \hat{A}_2 on the interferometer side are mixed together on a beam-splitter, and the same holds for \hat{A}_3 and \hat{A}_4 . Single-photon detectors are placed in arms 1 and 4. Delay lines have been added to the 1, 2 and 3 interferometer path both to enable quantum interference at the beam-splitter level, and for temporal indistinguishability between the two separate blocks.

The effect of the interferometer and the post-selection on the $|1\rangle_1 |0\rangle_2 |0\rangle_3 |1\rangle_4$ states of the 1234 subsystem is to implement the operation:

$$\begin{aligned} \hat{A} = & -\lambda\mu(\cos\theta_1 \cos\theta_2 \hat{a}_s^\dagger \hat{a}_w - \sin\theta_1 \sin\theta_2 \hat{a}_s \hat{a}_w^\dagger) \\ & -\lambda^2 \cos\theta_1 \sin\theta_2 \hat{a}_s^\dagger \hat{a}_w^\dagger + \mu^2 \sin\theta_1 \cos\theta_2 \hat{a}_s \hat{a}_w \end{aligned} \quad (7.58)$$

Comparing the expression obtained for \hat{A} with the expression of $\hat{U}(t^*)$ from Eq. 7.50, i.e. $\hat{U}(t^*) \sim \cosh 2r(\hat{a}_s^\dagger \hat{a}_w + \hat{a}_w^\dagger \hat{a}_s) + \sinh 2r(\hat{a}_s^\dagger \hat{a}_w^\dagger + \hat{a}_w \hat{a}_s)$, we observe that in order to obtain $\hat{A} = \hat{U}(t^*)$, the coefficients in front of the terms $(\hat{a}_s^\dagger \hat{a}_w + \hat{a}_s \hat{a}_w^\dagger)$ and $(\hat{a}_s^\dagger \hat{a}_w^\dagger + \hat{a}_s \hat{a}_w)$ must be equal. This is achieved by setting the beam-splitters parameters to:

$$\begin{cases} \tan\theta_1 = \pm \frac{\lambda}{\mu} \\ \tan\theta_2 = \mp \frac{\mu}{\lambda} \end{cases} \quad (7.59)$$

In this case, \hat{A} can be written as:

$$\hat{A} = f_1(\lambda, \mu)(\hat{a}_s^\dagger \hat{a}_w + \hat{a}_s \hat{a}_w^\dagger) + f_2(\lambda, \mu)(\hat{a}_s^\dagger \hat{a}_w^\dagger + \hat{a}_s \hat{a}_w) \quad (7.60)$$

where

$$\begin{cases} f_1(\lambda, \mu) = -\lambda\theta \cos\left(\arctan\left(\pm\frac{\lambda}{\mu}\right)\right) \cos\left(\arctan\left(\mp\frac{\mu}{\lambda}\right)\right) \\ f_2(\lambda, \mu) = -f_1(\lambda, \mu) \end{cases} \quad (7.61)$$

With this interferometer, we managed to obtain the good combinations of creation and annihilation operators; comparing \hat{A} and $\hat{U}(t^*)$ we indeed find the blocks of operations $(\hat{a}_s^\dagger \hat{a}_w + \hat{a}_w^\dagger \hat{a}_s)$ and $(\hat{a}_s^\dagger \hat{a}_w^\dagger + \hat{a}_w \hat{a}_s)$. However, in this configuration it is impossible to find the required weights $\cosh 2r$ and $\sinh 2r$ for the operators combinations, due to the constraint $f_2 = -f_1$.

7.3.3 Interferometer for quantum search

Many different interferometer configurations have been attempted, resulting for most of them in the impossibility of finding the required linear combination of operators for the quantum walk. Ultimately, we converged to the most general beam-splitter configuration. This configuration has been presented in [Reck 94], to implement the most general unitary achieved with linear optics. Here, the beam-splitter configuration is analogous, but the phase-shifters are not present. The geometry of the interferometer is depicted in Fig. 7.7.

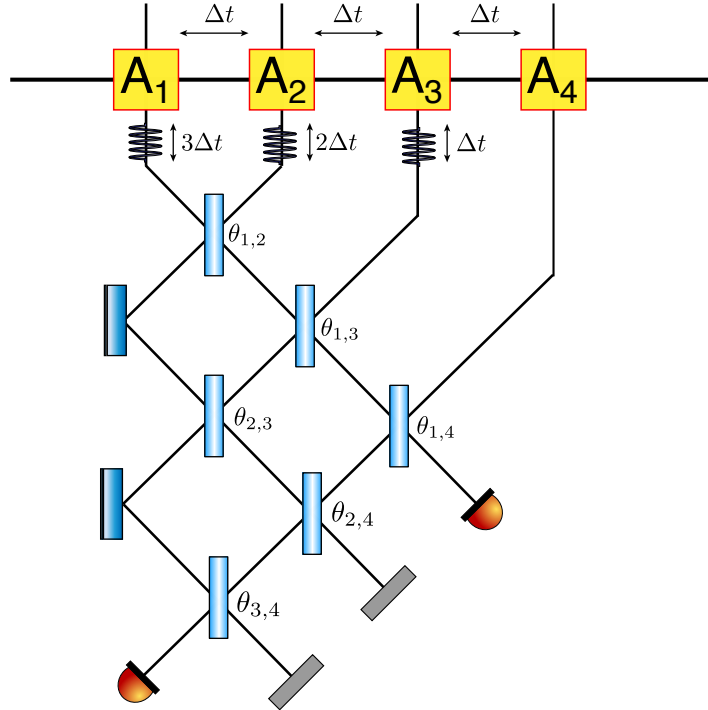


Figure 7.7: Interferometer design that permits the implementation of the quantum search unitary.

operation	parameter	operation	parameter
\hat{A}_1	$a = 2.8743686$	\hat{A}_2	$c = -2.27080046$
	$b = -2.49093484$		$d = -2.59705733$
	$\theta_1 = -\pi/2$		$\theta_2 = -\pi/2$
	$\theta_5 = 0$		$\theta_6 = 0$
\hat{A}_3	$e = 2.95010844$	\hat{A}_4	$g = 4.04377552$
	$f = 3.37396478$		$h = -3.50434573$
	$\theta_3 = \pi/2$		$\theta_4 = \pi/2$
	$\theta_7 = 0$		$\theta_8 = 0$
Interf.	$\theta_{1,2} = 1.3347714$		
	$\theta_{1,3} = 0.64247236$		
	$\theta_{1,4} = 0.13229823$		
	$\theta_{2,3} = 1.22435466$		
	$\theta_{2,4} = 0.65498505$		
	$\theta_{3,4} = 0.78719238$		

Table 7.1: Parameters of the experimental setup for the implementation of a successful quantum search, for squeezing value of the input state $r = 0.08$.

We define the four operations acting on the quantum state as:

$$\begin{aligned}
 \hat{A}_1 &= ae^{i\phi_5} \hat{a}_w^\dagger + be^{i\phi_1} \hat{a}_s^\dagger \\
 \hat{A}_2 &= ce^{i\phi_6} \hat{a}_w + de^{i\phi_2} \hat{a}_s \\
 \hat{A}_3 &= ee^{i\phi_7} \hat{a}_w^\dagger + fe^{i\phi_3} \hat{a}_s^\dagger \\
 \hat{A}_4 &= ge^{i\phi_8} \hat{a}_w^\dagger + he^{i\phi_4} \hat{a}_s^\dagger
 \end{aligned} \tag{7.62}$$

where the parameters $\{a, \dots, h\}$ and $\{\phi_1, \dots, \phi_8\}$ are real numbers. Considering the number of free parameters that we are working with, finding an analytical solution in this case is complicated, and we have to search for a numerical solution to the problem. Most importantly, we emphasize that the parameter values depend on the squeezing r of the input state; different squeezing values correspond to different setup parameters.

From the definition given in Eq. 7.50, the theoretical quantum state of the quantum walk $|\psi_w\rangle = \hat{U}(t^*) |s\rangle$ in our encoding is given by:

$$|\psi_w\rangle = [\cosh 2r(\hat{a}_s^\dagger \hat{a}_w + \hat{a}_w^\dagger \hat{a}_s) + \sinh 2r(\hat{a}_s^\dagger \hat{a}_w^\dagger + \hat{a}_w \hat{a}_s)] |s\rangle \tag{7.63}$$

This state is in general not normalized. We indicate the state implemented by the interferometer and the post-selection on the detector clicks as $|\psi_{exp}\rangle$, to indicate that it is the quantum state built with an experimental setup. In particular, the interferometer

parameter	target value	obtained value
a_k	0	$\sim 10^{-10}$
b_k	0	$\sim 10^{-10}$
c_k	0	$\sim 10^{-9}$
d_k	0	$\sim 10^{-9}$
e_k	0	$\sim 10^{-10}$
f_k	0	$\sim 10^{-10}$
g_k	0	$\sim 10^{-10}$
h_k	0	$\sim 10^{-10}$
l_k	$\cosh(2r) \sim 1.0128273300$	1.0128273303
m_k	$\cosh(2r) \sim 1.0128273300$	1.0128273312
n_k	$\sinh(2r) \sim 0.1606835410$	0.1606835451
o_k	$\sinh(2r) \sim 0.1606835410$	0.1606835428

Table 7.2: Comparison between the target value of the parameters of the quantum state and the values obtained using the setup parameters of Table 7.1 and the scheme of Fig. 7.7, for $r = 0.08$.

of Fig. 7.7, along with the definitions of Eq. 7.62 and the post-selection on the clicks from both detectors, is responsible of mixing two-by-two all the photon subtraction and addition terms. The state at the output has, in general, the following form¹:

$$\begin{aligned}
 |\psi_{exp}\rangle = & \left[(a_k + h_k) \hat{a}_s^\dagger \hat{a}_s + [b_k + g_k] \hat{a}_w^\dagger \hat{a}_w + c_k \hat{a}_s^{2\dagger} + d_k \hat{a}_w^{2\dagger} + e_k \hat{a}_s^2 \right. \\
 & \left. + f_k \hat{a}_w^2 + (h_k + g_k) \mathbb{1} + i l_k \hat{a}_s^\dagger \hat{a}_w + i m_k \hat{a}_w^\dagger \hat{a}_s + i n_k \hat{a}_s^\dagger \hat{a}_w^\dagger + i o_k \hat{a}_s \hat{a}_w \right] |s\rangle
 \end{aligned} \tag{7.64}$$

The 12 parameters $\{a_k, \dots, o_k\}$ that appear in this equation are determined by the weights of the photon addition and subtractions $\{a, \dots, h\}$ and $\{\phi_1, \dots, \phi_8\}$, and by the interferometer angles $\{\theta_{ij}\}$. The g_k and h_k coefficients arise from $\hat{a}_w \hat{a}_w^\dagger$ and $\hat{a}_s \hat{a}_s^\dagger$ respectively, that have been absorbed in other terms in the equation by the use of the commutation relations.

In order for the experimental setup to yield the target state of the walk at the output, we require $|\psi_{exp}\rangle \sim |\psi_w\rangle$. Therefore, the defining parameters $\{a_k, \dots, o_k\}$ of $|\psi_{exp}\rangle$ must read:

$$\begin{aligned}
 a_k = b_k = c_k = d_k = e_k = f_k = g_k = h_k = 0 \\
 l_k = m_k = \cosh(2r) \\
 n_k = o_k = \sinh(2r)
 \end{aligned} \tag{7.65}$$

The protocol is successful if, for a given value r of the initial squeezing, there exists an interferometer such that the output state fulfils Eq. 7.65.

¹We point out that in this equation “ i ” is not a parameter but it stands for the imaginary unit.

By exploring different squeezing values, we observed that it is in general possible to find a setup that guarantees the success of the protocol. In Table 7.2 we listed the results obtained for the interferometer of Fig. 7.7 and the parameters of Table 7.1, for $r = 0.08$, which is consistent with our squeezing value. We denote the state $|\psi_{exp}\rangle$ obtained with these parameters as $|\psi_{exp,w}\rangle$. We proved that the interferometer presented here is successful to implement the quantum search unitary at time t^* . In particular, we obtained $|\psi_{exp,w}\rangle \sim |\psi_w\rangle$.

7.3.4 Fidelity with the target state of the walk

As the state is computed numerically, it is important to calculate the similarity between the target state $|w\rangle$ and the state resulting from interference and post-selection, with parameters determined through the numerical procedure. This step is essential for evaluating the impact of imperfect convergence on the results. In essence, we aim to determine if a numerical value on the order of 10^{-6} can be effectively treated as zero in our context. To assess the similarity between quantum states we use here the so-called *fidelity* measure.

The fidelity of two pure quantum states $|\psi_1\rangle$ and $|\psi_2\rangle$ is defined as:

$$F = |\langle\psi_1|\psi_2\rangle|^2 \quad (7.66)$$

and it measures the degree of overlap between the two states. The use of fidelity to evaluate the similarity of two quantum states is debated in CV, as states with significantly different physical properties can still exhibit a high fidelity [Mandarino 14]. However, it is always true that $F = 1$ indicates identical quantum states. Moreover, in our case we typically compare quantum states that are issued from the same physical process. While we aim for a perfect fidelity of $F = 1$, slight deviations from this value can help us understand how changes in parameters affect the final quantum state. Additionally, assessing the fidelity of the post-selected state is useful to verify that our computational procedure effectively yields the target state.

In this work the fidelity has been calculated analytically. To give an example on how the fidelity is calculated, and to check that the various terms yield the correct result, we show that the quantum state $|\psi_w\rangle$ defined in Eq. 7.63 is equal to $|w\rangle$ defined in Eq. 7.40. We recall that $|\psi_w\rangle$ is in general not normalized. Moreover, here we consider non-normalized states of the form $|w\rangle = \hat{a}_w |MMSV\rangle$ and we factor the normalization constant \mathcal{N} separately. We expect $|\psi_w\rangle = |w\rangle$ and, as a consequence, we expect:

$$F(|\psi_w\rangle, |w\rangle) = \left| \frac{\langle w|\psi_w\rangle}{\sqrt{\langle\psi_w|\psi_w\rangle}\sqrt{\langle w|w\rangle}} \right|^2 = 1 \quad (7.67)$$

The term $\langle\psi_w|\psi_w\rangle$ and $\langle w|\psi_w\rangle$ demand the calculation of 10 and 4 overlap terms respectively, while $\langle w|w\rangle$ has already been calculated in section 7.2.1 and it reads $\langle w|w\rangle = \sinh^2 r$. As an example, the 4 overlap terms that need to be calculated for $\langle w|\psi_w\rangle$ are $\langle w|\hat{a}_s^\dagger\hat{a}_w|s\rangle$,

$\langle w|\hat{a}_w^\dagger\hat{a}_s|s\rangle$, $\langle w|\hat{a}_w^\dagger\hat{a}_s^\dagger|s\rangle$ and $\langle w|\hat{a}_w\hat{a}_s|s\rangle$. The terms for the calculations of the fidelity have been reported in Appendix D.1. The overlap calculations have been carried out and the result is, as expected, $F(|\psi_w\rangle, |w\rangle) = 1$. This result is trivial but it serves to confirm that the analytical calculation of the fidelity is carried out correctly.

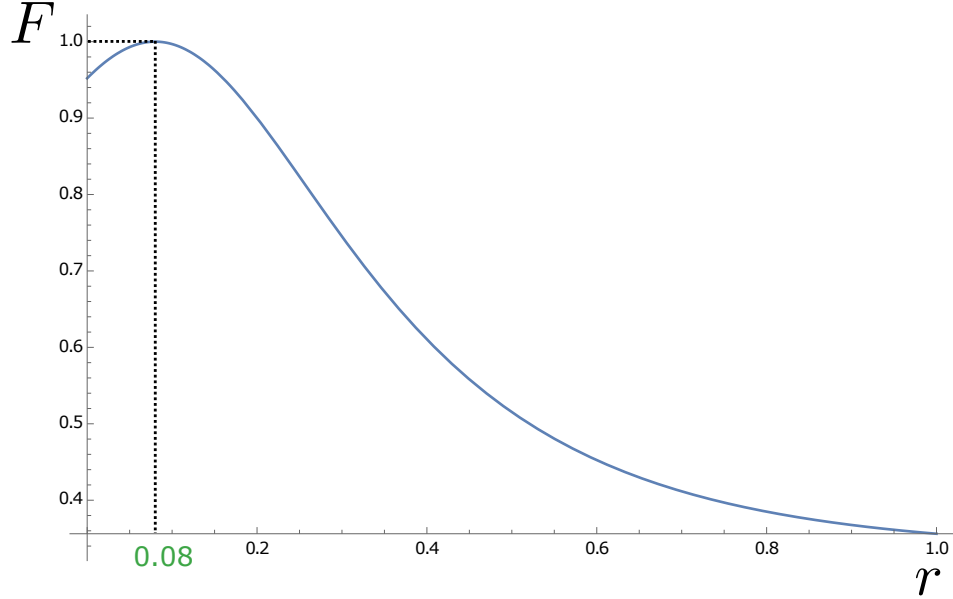


Figure 7.8: Plot of the fidelity between the target state $|w\rangle$ and the output state $|\psi_{exp,w}\rangle$ of the interferometric walk as a function of the squeezing parameter r . The parameters used for the interferometer are reported in Table 7.1 and they have been obtained through numerical simulations for a squeezing value of $r = 0.08$. Here, we show that the fidelity decreases as we deviate from this optimal squeezing value.

To assess how precisely our setup yields the target state of the walk, we will be interested in the fidelity between $|\psi_{exp,w}\rangle$ and $|w\rangle$. This requires the calculation of additional overlap terms, that can be found in Appendix D.1. Carrying out the calculations by using the values of Table 7.2 and for an initial squeezing value of $r = 0.08$, the fidelity reads:

$$F(|\psi_{exp,w}\rangle, |w\rangle) = \left| \frac{\langle w|\psi_{exp,w}\rangle}{\sqrt{\langle\psi_{exp,w}|\psi_{exp,w}\rangle}\sqrt{\langle w|w\rangle}} \right|^2 = 1 \quad (7.68)$$

This value leaves no doubt about the success of the process, indicating that the experimentally realized state $|\psi_{exp,w}\rangle$ is indeed equivalent to the target state $|w\rangle$. The interferometer depicted in Fig. 7.7, using the parameters outlined in Table 7.1, effectively permits the simulation of the quantum walk unitary for quantum search.

We stress that the interferometer parameters required for the quantum walk implementation are specific to a given squeezing value r . Consequently, varying the

squeezing of the input state leads to different parameters for the interferometer. This is illustrated in Fig. 7.8, where we show that, for fixed interferometer parameters, there exists an optimal input squeezing value to achieve unit fidelity in quantum search.

Finally, the effect of the deviations of the parameters of the $|\psi_{exp}\rangle$ state from the target parameters of Table 7.2 can be evaluated, as shown in Fig. 7.9. In general, the higher the squeezing, the more sensitive the output state is to deviations from the ideal parameters.

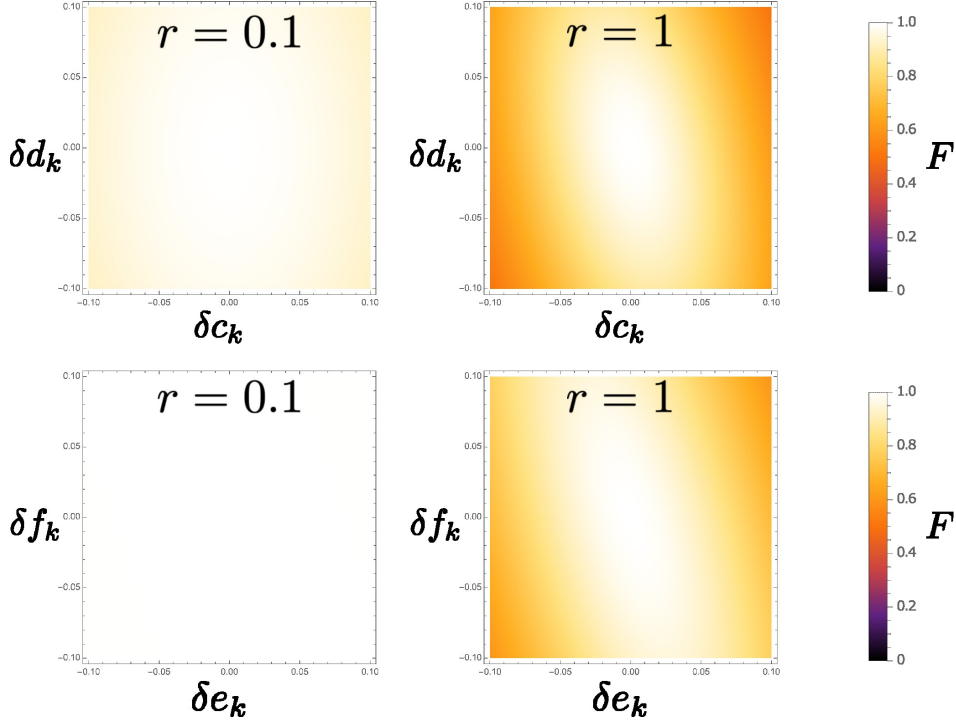


Figure 7.9: Dependence between the fidelity of the output state $|\psi_{exp,w}\rangle$ and the ideal state of the walk on the deviations from the ideal parameters and for different levels of squeezing. Here, only the deviations of the parameters c_k , d_k , e_k and f_k are reported.

7.3.5 Generalities on a realistic experimental implementation

In our experimental configuration, we have the flexibility to operate with both frequency modes and pulsed modes.

Working in the frequency domain necessitates nonlinear processes to achieve both photon addition and photon subtraction. These processes can be tailored to implement either subtraction or addition in a specific superposition of modes by manipulating what we refer to as the *gate beam* of the nonlinear process [Averchenko 14, Averchenko 16, Roeland 22]. The main problem with using frequency modes is that they do not meet the

condition $N \gg 1$, which has been a fundamental assumption in most of this chapter. As a consequence, we cannot apply the results obtained in this work on frequency modes. However, it is not to be excluded that this approach might be feasible with a different design. Moreover, the impact of a small N on the expected result might be negligible. This is a point that can be investigated further, in order to see if it is possible to find a solution even with a finite number of modes.

Time-bin modes, on the other hand, do not suffer from the drawbacks associated with frequency modes. Photon subtraction in this scenario is achieved through low-reflectivity beam-splitters, while photon addition requires a nonlinear process [Parigi 07]. Additionally, time-bin modes meet the condition $N \gg 1$. However, challenges arise in tailoring the superposition as desired. For instance, implementing the input state $|s\rangle$ requires subtracting a photon from a superposition of pulses. While this remains within the framework of linear optics, it does impact the size of the setup and the required components.

One final remark is needed. While squeezing generation is deterministic, the probabilistic nature of the photon addition and subtraction significantly affects the success rate of quantum information processing protocols. In our context, the relationship between the probability of success and various setup parameters is an area that requires further investigation.

Chapter 8

Quantum Synchronization of two coupled oscillators

Contents

8.1	Quantum synchronization	184
8.1.1	Introduction to quantum synchronization	184
8.1.2	Generalities on open quantum systems	185
8.1.3	Coupled dissipative harmonic oscillators	185
8.2	Mapping with experiment	187
8.2.1	Environment as a network of oscillators	188
8.2.2	Interaction between system and environment	189
8.2.3	Simulating the evolution with squeezing and linear optics	190
8.2.4	Local oscillator shaping for basis change	193
8.3	Synchronization in an optical setup	194
8.3.1	Simulation of the dynamics	195
8.3.2	LO shaping for simulation of the dynamics	196
8.3.3	Experimental limitations	199

In this chapter, we drift away from the quantum algorithm field to dive into the realm of quantum simulations. The goal here is to explore a phenomenon known as *quantum synchronization*, that arises in the framework of open quantum systems. We will not treat here the complex problem of the derivation of the master equation, and we redirect the reader to other references that have treated this problem in detail [Breuer 02, Wiseman 10]. Our aim in this chapter is to simulate the Hamiltonian of the system into our optical setup and to observe the emergence of synchronization phenomena. We will proceed by briefly explaining Quantum synchronization from a theoretical point of view and we define the mapping between the theoretical entities and our experimental setup.

8.1 Quantum synchronization

8.1.1 Introduction to quantum synchronization

Synchronization phenomena have been observed in classical dynamical systems since the 17th century in a variety of different interacting systems, from biology to physics and chemistry [Pikovsky 01, Strogatz 18]. When they arise without an external driving force, they are called *spontaneous* or *mutual*. Among the most surprising examples of mutual synchronization that we find in nature, is the synchronous flashing of male fireflies or the synchronous movement of a swarm of birds. Synchronization phenomena have been responsible for the swaying of the Millennium Bridge, due to many pedestrians synchronizing their steps with the vibrations of the bridge, amplifying the oscillations [Strogatz 05]. All these phenomena are often modeled as populations of coupled oscillators that, despite having a distribution of frequencies, have the ability to synchronize to a common frequency and to make a collective behavior emerge.

Synchronization phenomena are now being studied also in the quantum domain [Zhirov 08, Orth 10, Heinrich 11]. In particular, the link between the presence of quantum features, such as entanglement correlations, and the emergence of synchronization is currently being explored [Manzano 13, Jozsa 00, Giorgi 13]. A common factor in the systems that undergo synchronous dynamics is the presence of dissipation into an environment: we are then in the framework of Open Quantum Systems [Breuer 02], where we consider the system of interest embedded in an *environment*, in which the system dissipates part of its energy. Depending on the characteristics of the system and the bath, synchronization can be asymptotic. This usually happens when some of the eigenfrequencies are protected against dissipation.

Here, we focus on two bosonic oscillators dissipating into an environment of bosonic oscillators. Mutual synchronization occurs when the two oscillators, despite having different frequencies, begin to oscillate in unison at a common frequency. This phenomenon is due to dissipation; in particular it has been found that quantum synchronization occurs in the presence of a common bath as a result of a separation between dissipation rates [Giorgi 12]. This condition appears to be general if the bath is infinite, while effects due to the finiteness of the environment hinder synchronization and lead to revivals, limiting synchronization to a transient time [Benedetti 16].

In this work, we want to investigate the mapping between the synchronization effect in the open quantum system framework and a continuous-variable quantum optics experiment, along with the feasibility of simulating quantum synchronization in the experimental platform and the main limitations. We will proceed by first investigating the quantum synchronization effect in the chosen context of harmonic oscillators dissipating into an environment; we will then describe how open quantum system scenarios involving harmonic oscillators are mapped into quantum optics setups. The simulation of the synchronization of a system of two quantum harmonic oscillators embedded in an

n -oscillators bath is carried out numerically and the corresponding experimental parameters are calculated.

8.1.2 Generalities on open quantum systems

An open quantum system is a quantum system S that interacts with other systems, collectively referred to as the *bath* or *environment* E , with which it can exchange energy, information, or particles. These interactions can lead to various effects, such as decoherence and dissipation. In a realistic setting, all quantum systems are open and interact to a certain extent with an environment. However, in some cases these interactions can be neglected, and certain systems can be approximated as being closed, with their evolution that can be described using a unitary operator.

In the context of open quantum systems, we often consider the total system-environment system as a closed system, whose evolution is unitary. If we assume that the total input system $S + E$ is in a separable state, we can introduce the *quantum map* or *quantum operation* \mathcal{E} , expressed as:

$$\hat{\rho}'_S = \mathcal{E}(\hat{\rho}_S) = \text{Tr}_E [\hat{U}(\hat{\rho}_S \otimes \hat{\rho}_E)\hat{U}^\dagger] \quad (8.1)$$

where Tr_E indicates the partial trace on the environment degrees of freedom [Nielsen 10].

While quantum maps are a useful tool to describe the input-output transformations of a quantum system, a continuous-time description of the evolution of the system requires a *master equation* approach. For instance, a large class of completely-positive trace-preserving (CPTP) maps result in a Markovian master equation that can be written in the Lindblad form as [Lindblad 76, Breuer 02]:

$$\frac{d\hat{\rho}_S}{dt} = \mathcal{L}(\rho) = -i [\hat{H}, \hat{\rho}] + \sum_k \gamma_k \left(\hat{L}_k \rho_S \hat{L}_k^\dagger + \{ \hat{L}_k^\dagger \hat{L}_k, \hat{\rho}_S \} \right) \quad (8.2)$$

where we set $\hbar = 1$, the relaxation rates γ_k are positive coefficients, and the \hat{L}_k are called *Lindblad operators*. While it has not been made explicit for notational simplicity, all these quantities are in general time-dependent. In this equation, the first part represents reversible unitary evolution, while the second part introduces irreversibility. Many examples of open quantum systems dynamics can be led, through various approximations, to a Lindblad form [Wiseman 10]. However, it is important to stress that for many processes, like the quantum brownian motion, we cannot in general derive a Markovian master equation, and their evolution must be addressed using different tools, such as the generalized quantum Langevin equations [Breuer 02].

8.1.3 Coupled dissipative harmonic oscillators

In this thesis, we treat the case of two coupled harmonic oscillators immersed in a thermal environment, which is modeled by bosonic oscillators. The Hamiltonian of the system, for

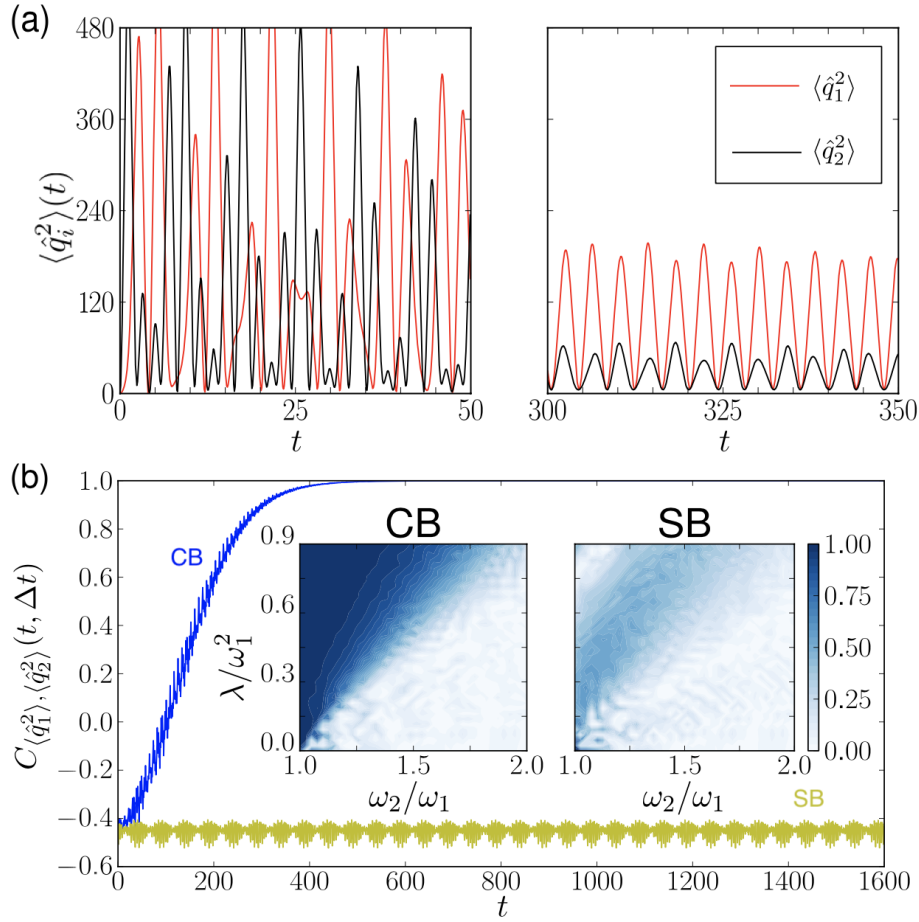


Figure 8.1: (a) Dynamics of second moments $\Delta^2 q_1(t)$ and $\Delta^2 q_2(t)$ of two squeezed vacuum states with squeezing parameters $r_1 = 2$ and $r_2 = 4$ for a CB and (b) synchronization for a CB (blue) and a SB (yellow), from [Giorgi 12]. Here, $\omega_2 = 1.4\omega_1$ and $\lambda = 0.7\omega_1^2$. Time is scaled with ω_1 and the insets in (b) show results for $t = 300$.

$\hbar = 1$ and unit masses, reads:

$$\hat{H}_S = \frac{\hat{p}_1'^2}{2} + \frac{\hat{p}_2'^2}{2} + \frac{\omega_1^2 \hat{q}_1'^2}{2} + \frac{\omega_2^2 \hat{q}_2'^2}{2} + \lambda \hat{q}_1' \hat{q}_2' \quad (8.3)$$

where \hat{q}' and \hat{p}' are the canonical position and momentum operators of the quantum harmonic oscillator and where $|\lambda| < \omega_1 \omega_2$, for an attractive potential. Two possible scenarios have been investigated in previous theoretical works [Giorgi 12], namely the case of a common bath (CB) and of separate baths (SB). In the CB case, the oscillators dissipate into the same environment, while in the SB case the oscillators dissipate into two separate equivalent environments.

Studying the dynamics of the oscillators, we can calculate the equations of motion of the first and second moments, exploring the differences between the CB and the SB case. Here, we mostly focus on the behavior of second moments, which is the quantity of interest in this thesis. In particular, we are interested in observing the emergence of synchronous dynamics between the second moments of the two oscillators. To quantify the synchronization, we use the so-called Pearson coefficient of two quantities $f(t)$ and $g(t)$, defined as:

$$C_{f,g}(t, \Delta t) = \frac{\overline{\delta f \delta g}}{\sqrt{\overline{\delta f^2} \overline{\delta g^2}}} \quad (8.4)$$

where $f = \int_t^{\Delta t+t} dt' f(t')$ and $\delta f = f - \bar{f}$. Completely correlated or anti-correlated evolutions exhibit $|C| \sim 1$.

In Fig. 8.1 from [Giorgi 12], the dynamics of the second moments $\Delta^2 q_1(t)$ and $\Delta^2 q_2(t)$ of two squeezed vacuum states, prescribed by the system Hamiltonian of Eq. 8.3 and the coupling with both a CB and a SB, is shown. In the case of a CB, full synchronization ($C = 1$) is reached after a transient time. This happens for a broad range of parameters and initial conditions, so that the emergence of synchronization in the CB case is a robust feature. In particular, as we may expect, synchronization emerges faster for small detunings, i.e. for $\omega_2/\omega_1 \sim 1$, but in general the detrimental effect of detuning can be compensated by strong λ coupling. The behaviour in the SB case, however, is different. Indeed, even if the detuning is small and the coupling is strong, the two oscillators do not synchronize.

For this reason, in this thesis we consider only the CB case. The aim here is to map the system and environment into our optical setup and to search for the parameters that enable the observation of synchronization. Differently from Ref. [Giorgi 12] and from many of the references on the subject where the environment has an infinite number of oscillators, we will use here a finite number of environment oscillators. Finite-size effects can hinder the emergence of synchronization, and we will investigate here if this holds for our model [Benedetti 16].

8.2 Mapping with experiment

In [Nokkala 18], the authors propose the implementation of the dynamics of a network of coupled harmonic oscillators into an optical setup. A successful simulation of the environment network dynamics following this theoretical framework has been carried out, as reported in [Renault 23]. In this work, we leverage the techniques introduced in Ref. [Nokkala 18] to explore the emergence of synchronization, specifically in the scenario of a common bath.

To begin, we will define the structure of the environment network. Subsequently, we will establish the interaction between the system, consisting of a pair of bosonic oscillators,

and the environment. Finally, we will outline the evolution of these components based on the specified Hamiltonian.

8.2.1 Environment as a network of oscillators

The environment consists of n quantum harmonic oscillators, with bare frequencies ω_i and connected through spring-like couplings v_{ij} , forming a network characterized by a specific adjacency matrix \mathbf{V} . We stress that the couplings between the oscillators and their bare frequencies merely define the dynamics to be simulated and do not correspond to the actual parameters of the experimental setup; for instance, the bare frequencies of the oscillators do not represent the optical frequencies of the quantum states in the experiment.

While the system whose dynamics we are interested in observing is an open quantum system immersed in an environment, the system+environment network is considered here as a closed system. Therefore, the system-environment network is subjected to unitary evolution, and in our case we can calculate precisely its state at a given time. The dynamics of the system itself is then recovered by tracing out the environment degrees of freedom. We mention in advance that simulating the dynamics of the network involves implementing the Bloch-Messiah decomposition, outlined in section 2.1.4. This decomposition allows us to break down the evolution of the oscillators' dynamics (at a specific time) into operations that can be realized in our experimental setup, such as squeezing and linear optics. Furthermore, it enables the exploration of various network configurations, as any quadratic Hamiltonian can be engineered and simulated in the experiment.

The environment Hamiltonian will read:

$$\hat{H}_E = \frac{\hat{\mathbf{p}}'^T \hat{\mathbf{p}}'}{2} + \hat{\mathbf{q}}'^T \mathbf{A} \hat{\mathbf{q}}' \quad (8.5)$$

where $\hat{\mathbf{q}}'$ and $\hat{\mathbf{p}}'$ are the position and momentum operators of the quantum harmonic oscillators and where \mathbf{A} can be expressed as:

$$\mathbf{A} = \frac{\Delta_{\tilde{\omega}}}{2} - \frac{\mathbf{V}}{2} \quad (8.6)$$

Here, \mathbf{V} is the weighted adjacency matrix of the graph (with links weighted by the couplings) and $\Delta_{\tilde{\omega}}$ is a diagonal matrix defined as:

$$\Delta_{\tilde{\omega}} = \begin{pmatrix} \tilde{\omega}_1 & & \\ & \ddots & \\ & & \tilde{\omega}_N \end{pmatrix}, \quad \tilde{\omega}_i^2 = \omega_i^2 + \sum_j v_{ij}^2/2 \quad (8.7)$$

Additionally, we rescale the position and momentum operators by their frequency to

obtain the quadrature operators:

$$\hat{\mathbf{q}} = \hat{\mathbf{q}}' \sqrt{\Delta_\omega} \quad (8.8)$$

$$\hat{\mathbf{p}} = \frac{\hat{\mathbf{p}}'}{\sqrt{\Delta_\omega}} \quad (8.9)$$

where $\Delta_\omega = \text{diag}(\omega_1, \dots, \omega_n)$. In terms of quadrature operators, the Hamiltonian \hat{H}_E reads:

$$\hat{H}_E = \frac{\hat{\mathbf{p}}'^T \Delta_\omega \hat{\mathbf{p}}'}{2} + \hat{\mathbf{q}}'^T \sqrt{\Delta_\omega^{-1}} \mathbf{A} \sqrt{\Delta_\omega^{-1}} \hat{\mathbf{q}}' \quad (8.10)$$

We can equivalently describe this network of harmonic oscillators in terms of non-interacting modes, i.e. in the basis defined by the eigenmodes of the system. This is achieved by diagonalizing the matrix \mathbf{A} to obtain:

$$\mathbf{D} = \mathbf{K}^T \mathbf{A} \mathbf{K}, \quad \mathbf{D} = \text{diag}(\Omega_1^2/2, \Omega_2^2/2, \dots) = (\Delta_\Omega / \sqrt{2})^2 \quad (8.11)$$

where \mathbf{K} is the basis-change matrix that contains the eigenvectors of the system and the Ω_i are the eigenfrequencies. The quadratures of the normal (uncoupled) modes are then defined as:

$$\begin{aligned} \hat{\mathbf{Q}} &= \sqrt{\Delta_\Omega} \mathbf{K}^T \sqrt{\Delta_\omega^{-1}} \hat{\mathbf{q}} \\ \hat{\mathbf{P}} &= \sqrt{\Delta_\Omega^{-1}} \mathbf{K}^T \sqrt{\Delta_\omega} \hat{\mathbf{p}} \end{aligned} \quad (8.12)$$

Writing the Hamiltonian \hat{H}_E in terms of the uncoupled oscillators modes we obtain:

$$\hat{H}_E = \sum_j \frac{\Omega_j}{2} (\hat{P}_j^2 + \hat{Q}_j^2) \quad (8.13)$$

To summarize, the quadratures $\hat{\mathbf{q}}, \hat{\mathbf{p}}$ represent the interacting oscillators network, while $\hat{\mathbf{Q}}, \hat{\mathbf{P}}$ represent the same dynamics, but in the uncoupled modes basis.

8.2.2 Interaction between system and environment

To describe the interaction between the system and the environment, we define the interaction Hamiltonian \hat{H}_I , that contains the necessary information on the couplings between the environment and the system.

The interaction of the i -th oscillator of the system with the environment network is characterized by an interaction term of the form:

$$\hat{H}_{I,i} = -\frac{\hat{q}_{S_i} \mathbf{k}_{S_i}^T \hat{\mathbf{q}}}{\sqrt{\omega_{S_i} \Delta_\omega}} = -\hat{q}_{S_i} \sum_j \frac{k_{S_i,j} \hat{q}_j}{\sqrt{\omega_{S_i} \omega_j}} \quad (8.14)$$

where \hat{q}_{S_i} indicates the quadrature of the i -th oscillator of the system, while with $\hat{\mathbf{q}}, \hat{\mathbf{p}}$ we indicate the environment quadratures in the interacting basis. Here, $k_{S_i,j}$ are the couplings between the i -th oscillator of the system and the j -th environment oscillator in the coupled environment basis. To switch to the uncoupled oscillators basis, we simply have to substitute $\hat{q} \rightarrow \hat{Q}$ and $\hat{p} \rightarrow \hat{P}$, following Eq. 8.12.

We will investigate a minimal coupling scenario, where the system is coupled only to the first oscillator of the environment, i.e. $k_{S_i,j} = 0$ for $j \neq 1$. The term $\hat{H}_{I,i}$ of the interaction Hamiltonian can be expressed as:

$$\hat{H}_{I,i} = -\hat{q}_{S_i} k_{S_i,1} \sum_j \frac{K_{1j} \hat{Q}_j}{\sqrt{\omega_{S_i} \Omega_j}} = -\hat{q}_{S_i} \sum_j \frac{g_{S_i,j} \hat{Q}_j}{\sqrt{\omega_{S_i} \Omega_j}} \quad (8.15)$$

where we introduced the vector $\mathbf{g}_{S_i}^T$ that contains the couplings $g_{S_i,j} = k_{S_i,1} K_{1j}$ between the i -th oscillator of the system and the j -th uncoupled mode of the environment.

While this is valid for any number of system oscillators, in this work we restrict to a system of two oscillators, whose free Hamiltonian has been defined in Eq. 8.3 in terms of position and momentum operators. In Fig. 8.2, the depiction of the couplings between system and environment in the two basis is shown.

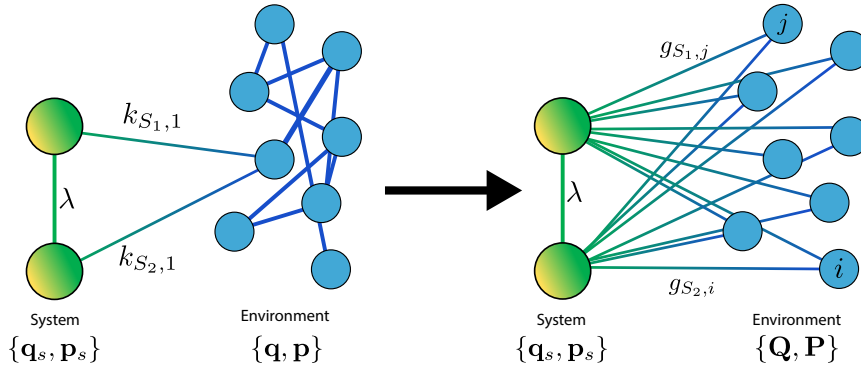


Figure 8.2: Interaction between the system and the environment. Left: the system interacts with the environment (in the coupled picture $\hat{\mathbf{q}}, \hat{\mathbf{p}}$) with couplings $k_{S_1,1}$ and $k_{S_2,1}$ in a minimal coupling scenario. Right: This system-environment network can be equivalently described in the picture where the oscillators of the environment are uncoupled (quadratures $\hat{\mathbf{Q}}, \hat{\mathbf{P}}$), where the interaction among the system oscillators and the uncoupled environment oscillators is described by the vector $\mathbf{g}_{S_i}^T$.

8.2.3 Simulating the evolution with squeezing and linear optics

Our aim is to describe the evolution of the system-environment network prescribed by the Hamiltonian $\hat{H}_{tot} = \hat{H}_S + \hat{H}_E + \hat{H}_I$. This can be calculated analytically and the details are

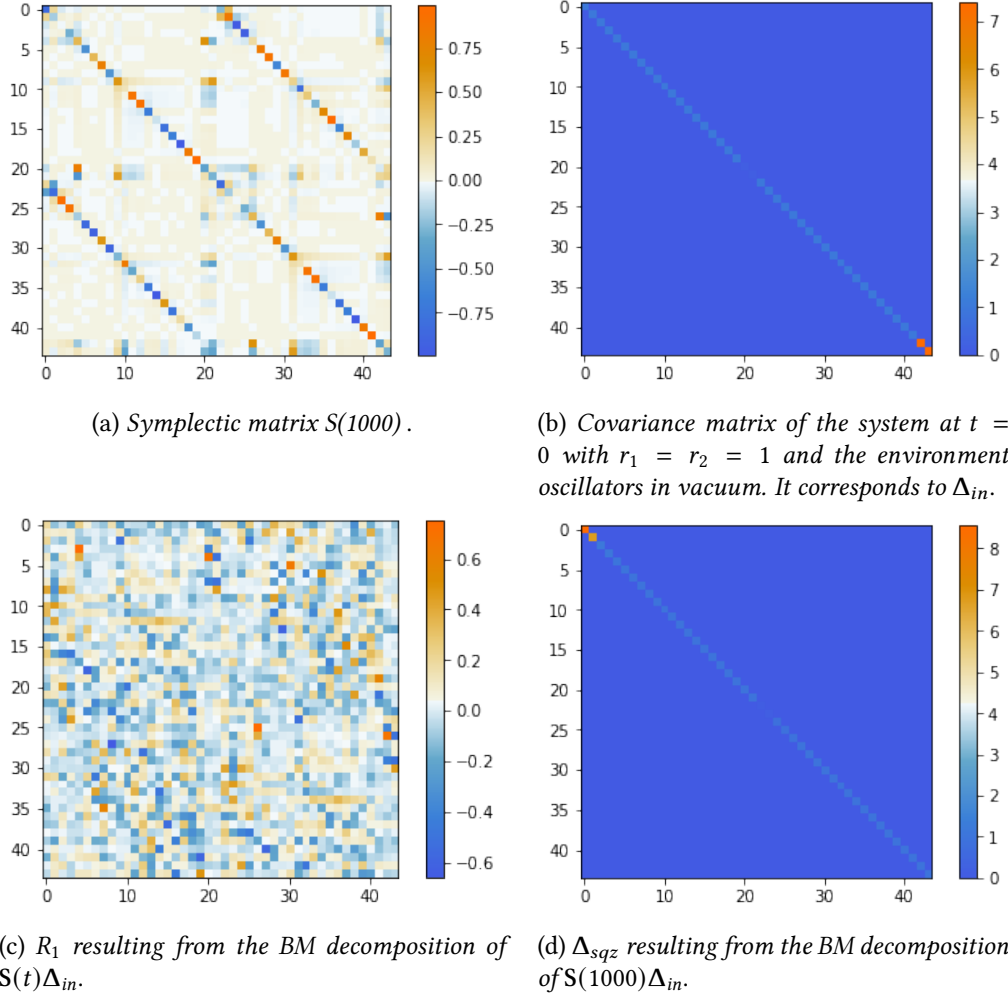


Figure 8.3: Simulated evolution for time $t = 1000$ and $n = 20$. Multiplying the matrix in a) and b) gives us $S_{eff,t}$. The matrix in c) and d) result from the Bloch-Messiah decomposition of $S_{eff,t}$. The system and environment parameters can be found in the following section in Table 8.1.

given in Appendix D.2.

In the $\{\hat{Q}, \hat{q}_S, \hat{P}, \hat{p}_S\}$ basis the quadratures evolve as follows:

$$\begin{pmatrix} \hat{Q}(t) \\ \hat{q}_S(t) \\ \hat{P}(t) \\ \hat{p}_S(t) \end{pmatrix} = S(t) \begin{pmatrix} \hat{Q}(0) \\ \hat{q}_S(0) \\ \hat{P}(0) \\ \hat{p}_S(0) \end{pmatrix} \quad (8.16)$$

where $S(t)$ is given in Appendix D.2. It is easy to verify that the matrix $S(t)$ is symplectic, as we expect. Indeed, the hamiltonian \hat{H}_{tot} is at most quadratic in the creation and annihilation

operators of the network modes. As already seen in section 2.1, we conclude that the unitary evolution prescribed by \hat{H}_{tot} is a Gaussian unitary, and the dynamics of the quadrature operators is described by a symplectic matrix.

A symplectic matrix can be decomposed via Bloch-Messiah reduction, as shown in section 2.1.4. We recall that the Bloch-Messiah decomposition prescribes that:

$$S(t) = S_t = \mathbf{R}'_1 \Delta'_{sqz} \mathbf{R}'_2 \quad (8.17)$$

where \mathbf{R}'_1 and \mathbf{R}'_2 represent linear optics transformations and Δ'_{sqz} represent a squeezing operation. At this point we must stress that in this framework the time t is merely a parameter of our problem: for each time t that we want to access, we will have a different result of the Bloch-Messiah decomposition, corresponding to different experimental parameters that we have to tune (the squeezing values, the mask of the local oscillator,...).

Another point worth mentioning is that $S(t)$ is applied to a set of states, not all of which are vacuum states: in particular, the two oscillators are in squeezed vacuum, while environment oscillators are in vacuum. We initialize the state of our network, as just described, by acting with the matrix Δ_{in} on vacuum. Formally, this means:

$$\begin{pmatrix} \hat{\mathbf{Q}}(0) \\ \hat{\mathbf{q}}_S(0) \\ \hat{\mathbf{P}}(0) \\ \hat{\mathbf{p}}_S(0) \end{pmatrix} = \begin{pmatrix} \hat{\mathbf{q}}_{in} \\ \hat{\mathbf{p}}_{in} \end{pmatrix} = \Delta_{in} \begin{pmatrix} \hat{\mathbf{q}}_{vac} \\ \hat{\mathbf{p}}_{vac} \end{pmatrix} \quad (8.18)$$

where $\{\hat{\mathbf{q}}_{vac}, \hat{\mathbf{p}}_{vac}\}$ are vacuum quadratures and where Δ_{in} is a symplectic transformation that squeezes the system oscillators and leaves the environmental oscillators in vacuum. This will give us $\Delta^2 q_{S_i} = e^{-2r_i}$, $\Delta^2 p_{S_i} = e^{2r_i}$, where the r_i are the squeezing parameters, and $\Delta^2 \mathbf{Q} = \Delta^2 \mathbf{P} = 1$ for all the environmental oscillators¹.

We define:

$$\mathbf{S}_{eff,t} = S_t \Delta_{in} \quad (8.19)$$

as the symplectic matrix acting on the vacuum states of our modes, identified by the quadratures $\{\hat{\mathbf{q}}_{vac}, \hat{\mathbf{p}}_{vac}\}$. Decomposing $\mathbf{S}_{eff,t}$ via the Bloch-Messiah reduction we obtain:

$$\boxed{\mathbf{S}_{eff,t} = \mathbf{R}_{1,t} \Delta_{sqz,t} \mathbf{R}_{2,t} = \mathbf{R}_{1,t} \Delta_{sqz,t}} \quad (8.20)$$

where we can discard $\mathbf{R}_{2,t}$ as it is a linear optics operation acting on vacuum. From now on, we drop the t in the matrices resulting from the decomposition for simplicity of notation but the reader should keep in mind that the matrices \mathbf{R}_1 and Δ_{sqz} are always related to a fixed time parameter t . Some matrix plots of the evolution and its Bloch-Messiah decomposition can be found in Fig. 8.3.

¹We recall that in our convention the vacuum is rescaled to 1.

By exploiting the decomposition presented in Eq. 8.20, we can effectively simulate the Hamiltonian of the harmonic oscillators network at a specific time t . The matrix Δ_{sqz} contains the experimental squeezing values necessary for simulating the network dynamics, according to the parameters of the problem: this includes the initial theoretical squeezing of the two-oscillator system (that does not correspond to the experimental one), as well as the frequencies of the system and the environment. Afterwards, a linear optics operation \mathbf{R}_1 is applied to this resulting set of squeezed modes.

In the experimental platform, we can perform the following symplectic operation on Hermite-Gauss frequency modes:

$$\boxed{S_{exp} = \mathbf{R}_{LO}\Delta_{KTP}} \quad (8.21)$$

Here, Δ_{KTP} is the squeezing generated in the Hermite-Gauss spectral modes through SPDC in the KTP nonlinear crystal, while \mathbf{R}_{LO} is a measurement basis change, equivalent to a linear optics operation on a set of modes. For the simulation of the network evolution at time t , we require $S_{exp} = S_{eff,t}$. This implies that to realize the necessary symplectic transformation for simulating the given dynamics, one should set $\mathbf{R}_{LO} = \mathbf{R}_1$ and $\Delta_{KTP} = \Delta_{sqz}$. While \mathbf{R}_{LO} is easy to implement and to tune (within the limits of the pulse shaper resolution), the same cannot be said for Δ_{KTP} . Indeed, tuning Δ_{KTP} to match Δ_{sqz} would require the shaping of the pump, which is a feasible but experimentally demanding task.

8.2.4 Local oscillator shaping for basis change

In our setup, linear optics operations on frequency modes are easily achieved via measurement basis change. On the quadrature vector, a basis change is described by the general symplectic transformation:

$$\begin{pmatrix} \hat{\mathbf{q}}' \\ \hat{\mathbf{p}}' \end{pmatrix} = \begin{pmatrix} X & -Y \\ Y & X \end{pmatrix} \begin{pmatrix} \hat{\mathbf{q}} \\ \hat{\mathbf{p}} \end{pmatrix} \quad (8.22)$$

as seen in section 2.1.3. This symplectic operation defines new modes described by annihilation operators $\{\hat{b}_m\}$ associated with optical modes $\{\mathbf{g}_m(\mathbf{r}, t)\}$. The creation operators are transformed according to:

$$\hat{b}_i^\dagger = \hat{q}'_i - i\hat{p}'_i = \sum_j (X_{ij}\hat{q}_j - Y_{ij}\hat{p}_j - iY_{ij}\hat{q}_j - iX_{ij}\hat{p}_j) = \sum_j U_{ij}^* \hat{a}_j^\dagger \quad (8.23)$$

where $\mathbf{U} = \mathbf{X} + i\mathbf{Y}$ and \mathbf{X}, \mathbf{Y} are real matrices. Our focus is on the operation defined by:

$$\begin{pmatrix} \hat{\mathbf{q}}_{out} \\ \hat{\mathbf{p}}_{out} \end{pmatrix} = \mathbf{R}_1 \Delta_{sqz} \begin{pmatrix} \hat{\mathbf{q}}_{in} \\ \hat{\mathbf{p}}_{in} \end{pmatrix} = \mathbf{R}_1 \begin{pmatrix} \hat{\mathbf{q}}_{sqz} \\ \hat{\mathbf{p}}_{sqz} \end{pmatrix} \quad (8.24)$$

that describes the output modes that we obtain after applying the linear operation on the squeezed modes. In this context, accessing the quadratures $\hat{\mathbf{q}}_{out,i}$ and $\hat{\mathbf{p}}_{out,i}$, identified by the

creation and annihilation operators \hat{b}_i^\dagger and \hat{b}_i , requires measuring the optical mode $\mathbf{g}_i(\mathbf{r}, t)$, which is sent through the LO.

Comparing Eq. 8.22 and 8.24, we can write:

$$\begin{cases} X_{ij} = R_{1,ij} \\ Y_{ij} = -R_{1,i(j+N)} \end{cases} \quad (8.25)$$

for $1 < i \leq N$. Eq. 8.23 can then be rewritten as:

$$\begin{aligned} \hat{b}_i^\dagger = \sum_{j=1}^N X_{ij} \hat{a}_j^\dagger - i \sum_{j=1}^N Y_{ij} \hat{a}_j^\dagger &= \sum_{j=1}^N R_{1,ij} \hat{a}_j^\dagger + i \sum_{j=1}^N R_{1,i(j+N)} \hat{a}_j^\dagger = \\ &= \sum_{j=1}^N R_{1,ij} \hat{a}_j^\dagger + i \sum_{j=N+1}^{2N} R_{1,ij} \hat{a}_{j-N}^\dagger \end{aligned} \quad (8.26)$$

where in the last sum the index j has been redefined. In this context, the creation and annihilation operators \hat{a}_i^\dagger and \hat{a}_i are associated to the optical modes $\mathbf{f}_i(\mathbf{r}, t)$ and to the squeezed quadratures $(\hat{\mathbf{q}}_{sqz}, \hat{\mathbf{p}}_{sqz})$ of Eq. 8.24. As the optical modes follow the creation operators transformations when a basis change occurs, as seen in section 1.3.2, we finally obtain:

$$\mathbf{g}_i(\mathbf{r}, t) = \sum_{j=1}^N R_{1,ij} \mathbf{f}_j(\mathbf{r}, t) + i \sum_{j=N+1}^{2N} R_{1,ij} \mathbf{f}_{j-N}(\mathbf{r}, t) \quad (8.27)$$

This is a key equation as it defines the mode we have to shape and send with the LO to the homodyne detection in order to address the i -th oscillator, in particular the $\hat{q}_i(t)$ and $\hat{p}_i(t)$ quadratures and their variances. Indeed, if we want S_{exp} to be equal to $S_{eff,t}$, we need to implement with the Local Oscillator the transformation \mathbf{R}_{LO} that matches \mathbf{R}_1 . This transformation should be implemented on the squeezed modes defined by the squeezing transformation Δ_{sqz} . If $\Delta_{sqz} = \Delta_{KTP}$, the squeezed modes are Hermite-Gauss frequency modes.

8.3 Synchronization in an optical setup

Here, we investigate the emergence of synchronization between two harmonic oscillators immersed in an environment with a given shape, using the tools provided in the previous section. The goal of this section is to find suitable parameters that allow for both the emergence of synchronous dynamics and the simulation of said dynamics in our experimental setup, with a finite number of environment oscillators. The main experimental limitations are outlined at the end of the section.

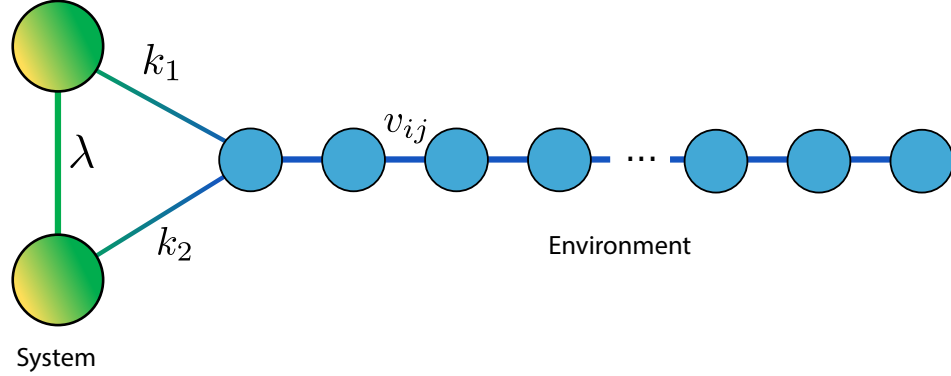


Figure 8.4: Two oscillators coupled with strength λ are connected to a linear environment with strength k_1 and k_2 respectively. The environment oscillators i and j have a coupling v_{ij} .

8.3.1 Simulation of the dynamics

We aim to show the emergence of synchronization between two oscillators coupled between each other with strength λ , that are minimally coupled with a linear environment with couplings k_1 and k_2 , as shown in Fig. 8.4. We begin by defining the parameters of the oscillators network, such as frequencies and coupling strengths. In this section, we will mostly use the parameters of Table 8.1, unless otherwise stated. A sufficient condition for transient synchronization is the presence of a gap between the normal modes damping, as it happens for small detuning, i.e., $|\omega_1 - \omega_2|^2 / \lambda < 1$ [Benedetti 16]. This is true for an infinitely large chain but the finite size of the environment hinders this effect.

We proceed by following the steps described in the previous sections. The goal is to retrieve the matrix $S(t)$, defined in Eq. D.61, as a function of the time parameter t . An example of the symplectic matrix and its Bloch-Messiah decomposition for a linear network can be seen in Fig. 8.3.

The information relative to the variance of the quadratures, the quantity of our interest, is contained in the covariance matrix. According to Eq. 2.25, a symplectic transformation $S(t)$ acts by transforming the covariance matrix as:

$$\mathbf{V}(t) = \mathbf{S}(t)\mathbf{V}(0)\mathbf{S}^T(t) \quad (8.28)$$

where

$$\mathbf{V}(0) = \begin{pmatrix} \mathbb{1}_n & 0 & 0 & 0 & 0 & 0 \\ 0 & e^{-2r_1} & 0 & 0 & 0 & 0 \\ 0 & 0 & e^{-2r_2} & 0 & 0 & 0 \\ 0 & 0 & 0 & \mathbb{1}_n & 0 & 0 \\ 0 & 0 & 0 & 0 & e^{2r_1} & 0 \\ 0 & 0 & 0 & 0 & 0 & e^{2r_2} \end{pmatrix} \quad (8.29)$$

symbol	value	physical meaning
ω_1	0.3	frequency of system oscillator 1
ω_2	$1.4\omega_1$	frequency of system oscillator 2
λ	$0.9\omega_1^2$	coupling between two system oscillators
ω_0	$0.4\omega_1$	frequencies of the environment oscillators
N	300	number of environment oscillators
v_{ij}	$1.1\omega_1^2$	coupling strength of environment oscillators
k_1	$0.3\omega_1^2$	coupling strength between system 1 and the first network node
k_2	$0.3\omega_1^2$	coupling strength between system 2 and the first network node
r_1	2	squeezing of first oscillator
r_2	2	squeezing of second oscillator

Table 8.1: Parameters of the system, the environment and their interaction used for the simulation of the dynamics.

is the covariance matrix of the state at $t = 0$, where the environment oscillators are in vacuum and the system oscillators are vacuum squeezed states, with squeezing parameters r_1 and r_2 respectively.

We calculate $\mathbf{V}(t)$ for various values of the t parameters and we plot the variance values that correspond to the oscillators of the system. Moreover, we calculate the Pearson coefficient, defined in Eq. 8.4, to quantify the synchronization. In Fig. 8.5 we show the emergence of synchronization for a linear network of $n = 300$ oscillators. Note the similarity with Fig. 8.1, from [Giorgi 12].

It is interesting to assess the effect of the number of oscillators and of the squeezing level on synchronization, as they are our main experimental constraints. For the range of parameters tested, for instance the ones reported in Table 8.1, we observed that if we decrease the number of environmental oscillators N the synchronization period gets shorter, as shown in Fig. 8.6. Moreover, we observed that the emergence of synchronization and the length of the synchronization transient period do not depend on the initial squeezing level of the oscillators, as can be seen in Fig. 8.7. While the squeezing level does not pose a significant problem for the experimental implementation, the number of modes N that we can measure can be an important limitation, due to the resolution of the pulse shaper and the finite width of the LO.

8.3.2 LO shaping for simulation of the dynamics

In the previous section, we recovered the transformation $\mathbf{S}(t) = \mathbf{S}_t$, that is to be applied to the initial state of the network, where the oscillators of the system are in squeezed vacuum and the oscillators of the environment are in vacuum. To translate this evolution to the experimental setup, our aim is to reconstruct, for each time t , $S_{eff,t}$ according to Eq. 8.20,

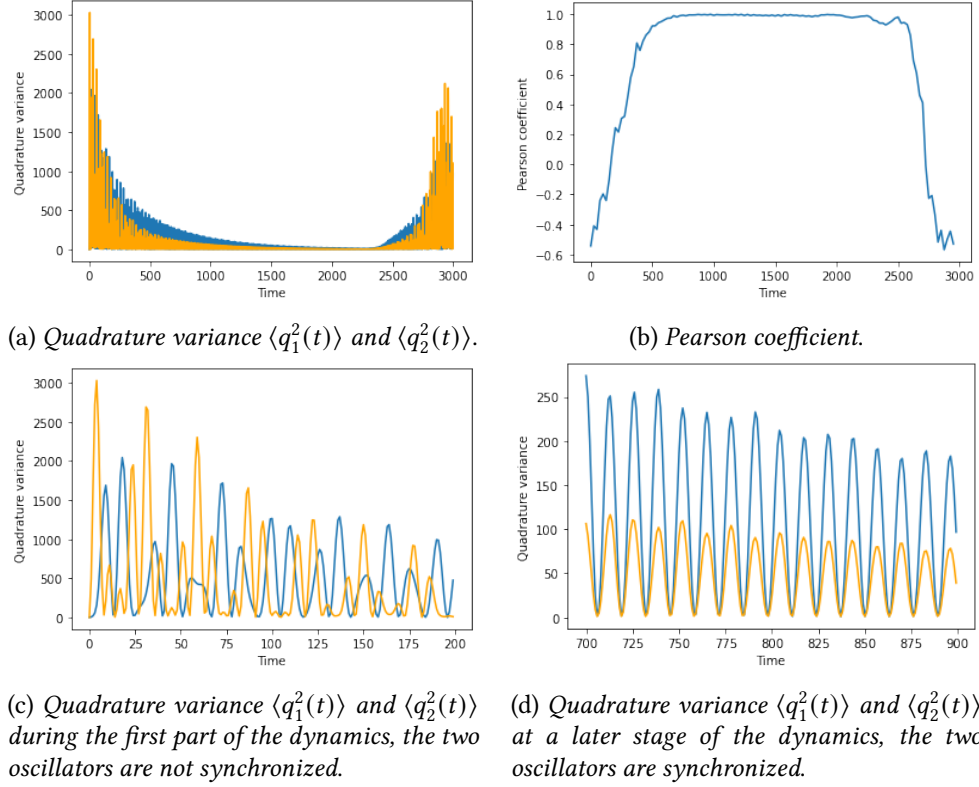


Figure 8.5: Synchronization simulation using the values of Tab. 8.1 (but $r_1 = 2$ and $r_2 = 4$). The decrease of synchronization observed in (b) is due to finite-size effects.

and to tune the experimental parameters so that $S_{exp} = S_{eff,t}$, where S_{exp} has been defined in Eq. 8.21. Here, we focus on the implementation of the linear optics transformation $\mathbf{R}_{LO} = \mathbf{R}_1$ for the specific task of the simulation of the oscillators dynamics, following the details outlined in section 8.2.4.

Experimentally, we produce a set of squeezed states of light in the Hermite-Gauss frequency basis. Hence, the modes $\{\mathbf{f}_j\}$ that appear in Eq. 8.27 coincide with Hermite-Gauss frequency modes, defined as:

$$HG_m(\omega) = e^{-\frac{\omega^2}{2\sigma_\omega^2}} \cdot H_m(\omega/\sigma_\omega) \quad (8.30)$$

Moreover, in our case, there is a $\pi/2$ quadrature shift for consecutive modes, as seen in Section 3.3, and for this reason we need to introduce a factor i in the odd modes (or in the even ones).

The modes $\{\mathbf{g}_j\}$ to be shaped (and measured) are linear combinations of the $\{\mathbf{f}_j\}$ Hermite-Gauss modes, as prescribed by Eq. 8.27, following the definition of \mathbf{R}_1 . We remind

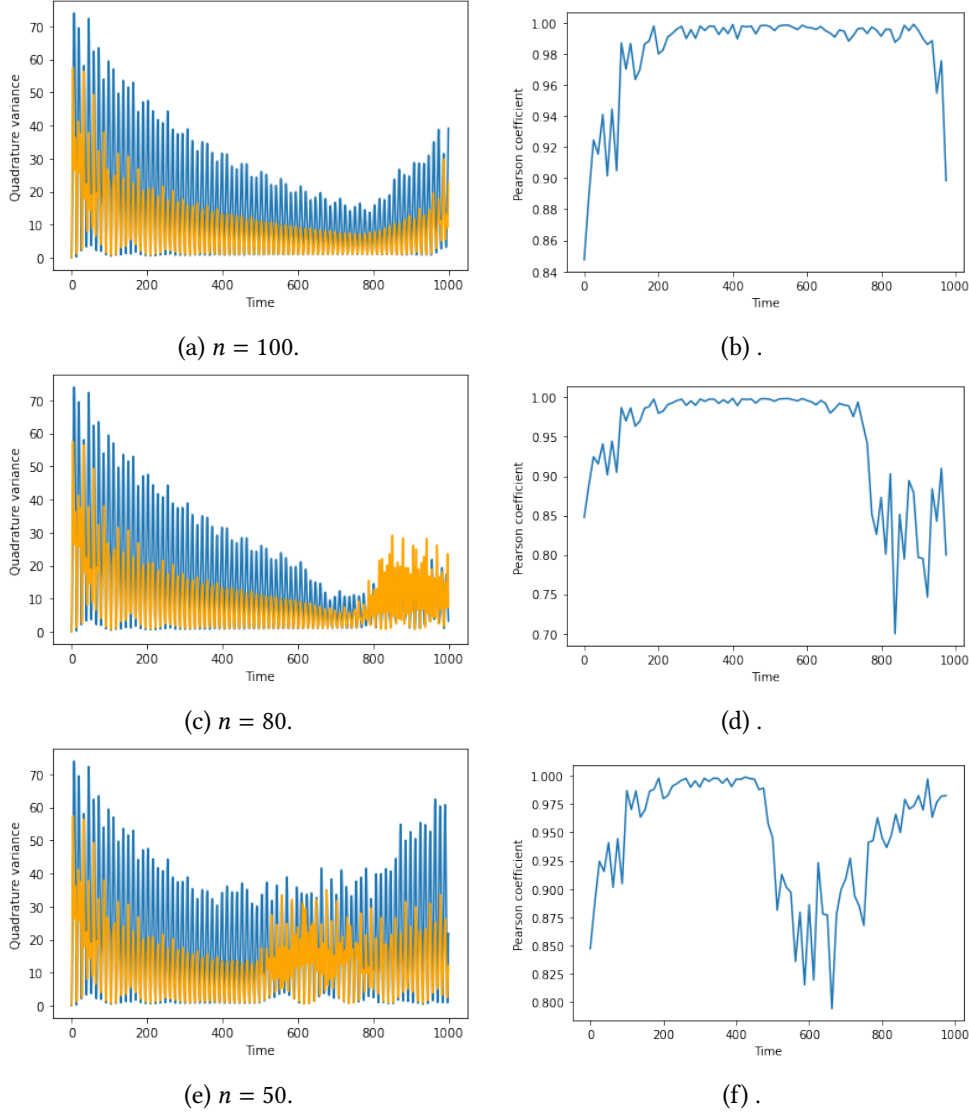


Figure 8.6: Simulations obtained using the values of Table 8.1 (except for $\lambda = 0.7\omega_1^2$ and $r_1 = r_2 = 2$) but changing the number n of environmental oscillators.

that this needs to be repeated for each t . The goal is to take a sufficient number of sampling points, n_{sample} , to reconstruct the synchronization curves of Fig. 8.5. For n_{sample} sampling points, we need to implement $2n_{sample}$ SLM masks, one for each measurement, where the 2 comes from the fact that we address separately each oscillator of the system.

As an example, we can implement the \mathbf{R}_1 linear transformation prescribed for a linear network of $n = 60$ nodes with the values prescribed by Tab. 8.1 by sending the shapes of Fig. 8.8.

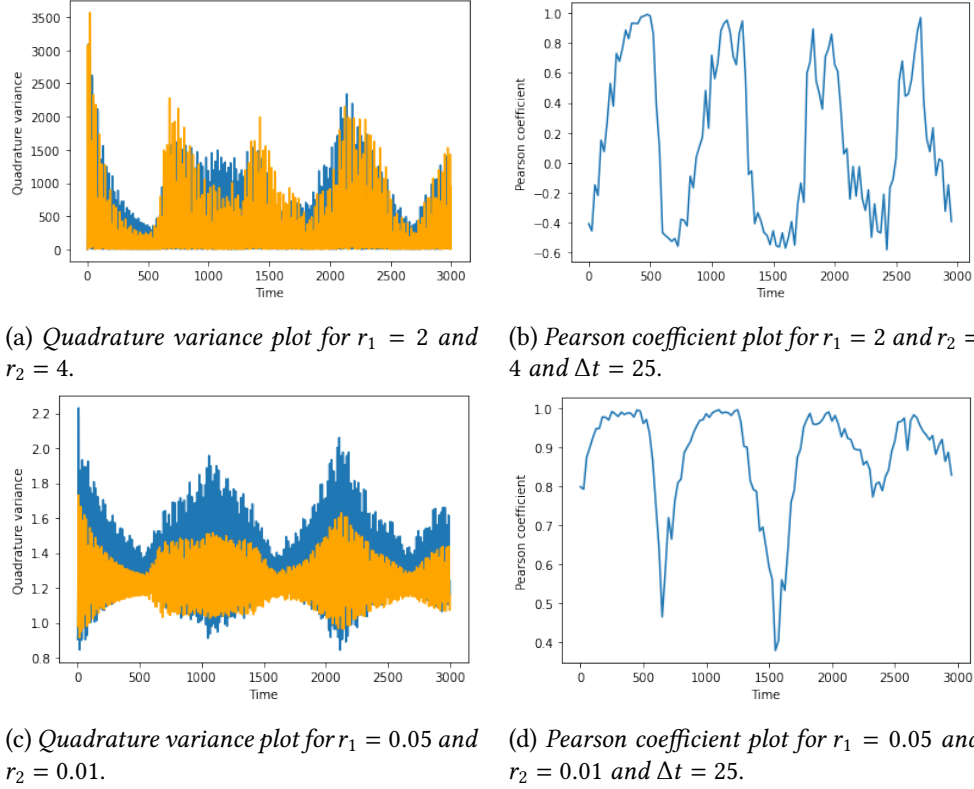
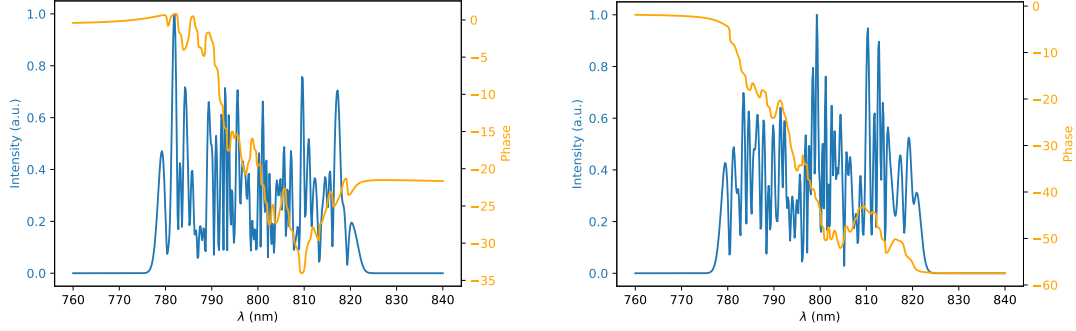


Figure 8.7: Simulations obtained using the values of Table 8.1 but with $n = 60$ environmental oscillators and changing the squeezing values r_1 and r_2 . In the graph a) and c) the blue and orange curves represent $\Delta^2 q_1$ and $\Delta^2 q_2$ respectively. The time “sampling” (timestep) is 1.

8.3.3 Experimental limitations

In this last section, we discuss the challenges and limitations that may arise in the simulation of the synchronous dynamics in our optical setup. The primary limitation stems from the experimental difficulties associated with tuning the level of squeezing of the Hermite-Gauss modes in the optical setup, a necessary step to match the matrix Δ_{KTP} with Δ_{sqz} . While the redistribution of squeezing is technically feasible, it is experimentally demanding, as it requires shaping the pump of the nonlinear process [Michel 21]. This problem has been encountered in [Renault 23], where it was demonstrated that the condition $\Delta_{KTP} \neq \Delta_{sqz}$ merely resulted in a rescaling of the function characterizing the network properties. The next step of this work involves investigating the impact of this condition on the emergence of synchronization, that, as of the writing of this manuscript, is yet to be studied.

A second limitation arises from the shaping capabilities of the pulse shaper and the bandwidth of the local oscillator. In our setup, the LO has a bandwidth of approximately



(a) Intensity and phase of the mode of the field for the first oscillator of the system.

(b) Intensity and phase of the mode of the field for the second oscillator of the system.

Figure 8.8: Local oscillator shapes for accessing the quadratures of the evolved system, following Eq. 8.27 for time parameter $t = 402$ for a network of $n = 60$ nodes starting from Hermite-Gauss modes with $\sigma = 2$ nm.

~ 40 nm, while the ability of the pulse shaper to shape higher order modes is determined by the optical complexity $\eta_{opt} \sim 231$, reported in Eq. 4.29. The examples illustrated in Fig. 8.8 demonstrate that we can simulate a network with $n = 60$ nodes without exceeding the LO bandwidth using HG modes of $\sigma_\omega = 2$ nm. However, the squeezed modes generated in this experiment have a $\sigma_\omega \sim 6$ nm. As the network size increases, the demand for bandwidth in the simulation also grows.

To reduce the width of the generated modes, adjusting the pump of the SPDC process is necessary. As illustrated in Fig. 4.14, the width of the generated light depends on the pump width. For instance, a pump with a spectral width $\Delta\omega = 1$ nm (FWHM) generates squeezed states in HG modes with a spectral width of $\sigma_\omega \sim 3.5$, while still maintaining a reasonable amount of output squeezed modes. Additionally, the bandwidth of the LO can also be expanded with the help of a non-linear fiber [Renault 22]. This enables access to larger networks, even when the Hermite-Gauss squeezed modes have broader profiles.

Conclusion & outlooks

In this work, we have demonstrated the generation of multimode squeezed states multiplexed both in the time and in the frequency domain via spontaneous parametric down-conversion in ppKTP waveguides. While ultrafast pulse shaping permits us to address chosen spectral modes, the fast balanced homodyne detector built in our lab enables us to have access to individual pulses of light. In this experiment we measured, to our knowledge, the largest number of squeezed states in the frequency domain generated via single-pass SPDC.

The main drawback of this work is undeniably the level of squeezing per mode, which is still low. During these years, we have understood the main physical limitations and trade-offs of our physical system. We conclude that the problem with this configuration arises mainly from the high number of spectral modes at these wavelength, which is still considerably high. This does not permit us to increase the length of our crystal to enhance the efficiency of the SPDC process, and we are therefore limited to short ppKTP crystals. Phase-matching engineering is required to decrease the number of modes, and spatial modulation of the poling is currently being investigated.

Nonetheless, the main result of this work is the simultaneous multiplexing of both degrees of freedom, which constitutes an interesting result for future quantum applications. Indeed, the presence of multiple squeezed frequency modes for each pulse opens the way for the implementation of a 3D multiplexed entangled resource at the repetition rate of the laser, where the 2D spectral layers are fully reconfigurable via pulse-shaping of the local oscillator. This way, different 2D spectral structures can be concatenated, via entanglement correlations, in the time domain as fast as the repetition rate of the pulsed laser source (156 MHz). Moreover, spectrally mode-selective non-Gaussian operations, needed for quantum computing protocols, can be implemented on selected nodes of the 3-dimensional structure.

In addition to implementing an entangled multiplexed resource, this thesis explores various applications of multimode squeezed light in quantum information processing. We focused on the fields of quantum algorithms and quantum simulations, and we investigated quantum information processing protocols with the ultimate goal of implementing them in our photonics setup.

We explored quantum walks on a complete graph for quantum search purposes, employing an encoding that maps discrete variables into a photon-subtracted squeezed

field. The proposed setup includes a series of photon subtraction and photon addition operations on specific modes, along with the quantum interference of heralding photons. Here, we demonstrated the successful theoretical implementation of the quantum search unitary operation at the characteristic search time, which rotates the walk from the input state to the desired target state. While the experimental implementation with frequency modes has additional drawbacks that need to be addressed, pulsed modes turn out to be a possible choice for the realization of the walk in the configuration that has been proposed here.

Multimode squeezed light has also been exploited in this work within the open quantum system framework to investigate the emergence of quantum synchronization between two quantum harmonic oscillators. The simulation of the dynamics of a network of quantum oscillators at a given time can be obtained via squeezing operations followed by linear optics, which is implemented via measurement basis change. Although some issues still need to be resolved, the results in this area look promising for a future experimental implementation.

Appendices

Appendix A

Pictures in quantum mechanics

The dynamics of a quantum system can be described mathematically in different ways, that we call *pictures*. Different pictures correspond to different evolutions of the quantum observables and of the quantum states. What needs to stay the same is the expectation value of an observable, as it is the only quantity that has a physical meaning. This is required, as different descriptions must, in any case, yield the same physics. In quantum mechanics, three pictures are widely used: the Schrödinger picture, the Heisenberg picture and the Dirac or interaction picture. Here, we will outline the basic equations and formalism, without giving the proofs.

In the Schrödinger picture, dynamics of the state is governed by the Schrödinger equation:

$$i\hbar \frac{\partial}{\partial t} |\psi(t)\rangle_S = \hat{H} |\psi(t)\rangle_S \quad (\text{A.1})$$

In this picture, the states evolve with time, while the observables do not. We can write:

$$|\psi(t)\rangle_S = \hat{U}(t) |\psi(0)\rangle_S \quad (\text{A.2})$$

$$\hat{O}_S(t) = \hat{O}_S(0) = \hat{O}_S \quad (\text{A.3})$$

where

$$\hat{U} = e^{-\frac{i}{\hbar} \hat{H} t} \quad (\text{A.4})$$

for a time-independent Hamiltonian². This is the picture that is most often used to describe the evolution of a quantum state.

²For a time-dependent Hamiltonian the unitary operator takes the form

$$\hat{U}(t) = e^{-\frac{i}{\hbar} \int_0^t d\tau \hat{H}(\tau)} = \mathbb{1} + \sum_{n=1}^{\infty} \left(\frac{-i}{\hbar}\right)^n \int_0^t ds_n \hat{H}(s_n) \int_0^{s_n} ds_{n-1} \hat{H}(s_{n-1}) \cdots \int_0^{s_2} ds_1 \hat{H}(s_1) \quad (\text{A.5})$$

In the Heisenberg picture the Schrödinger equation becomes:

$$i\hbar \frac{\partial}{\partial t} |\psi(t)\rangle_H = 0 \quad (\text{A.6})$$

The Heisenberg equation of motion, however, is non-trivial, it reads:

$$\frac{d\hat{O}_H(t)}{dt} = \frac{i}{\hbar} [\hat{H}, \hat{O}_H(t)] + \frac{\partial \hat{O}_H(t)}{\partial t} \quad (\text{A.7})$$

In this picture, the observables evolve with time, while the states do not. We can write:

$$|\psi(t)\rangle_H = |\psi(0)\rangle_H \quad (\text{A.8})$$

$$\hat{O}_H(t) = \hat{U}^\dagger(t) \hat{O}_H(0) \hat{U}(t) \quad (\text{A.9})$$

The two pictures are connected by the equations:

$$|\psi(t)\rangle_H = e^{\frac{i}{\hbar} \hat{H} t} |\psi(t)\rangle_S \quad (\text{A.10})$$

$$\hat{O}_S = \hat{O}_H(0) \quad (\text{A.11})$$

Some comments are in order. Here, we postulated a time-independent Hamiltonian for which $\hat{H}_S = \hat{H}_H = \hat{H}$. In general, when the Hamiltonian is time-dependent, this is not true. The Heisenberg Hamiltonian will read $\hat{H}_H = \hat{U}^\dagger \hat{H}_S \hat{U} \neq \hat{H}_S$, where \hat{U} is given by the Dyson expansion. Here, \hat{U} is the “usual” evolution operator.

The interaction or Dirac picture is often presented as a “mix” of the two previous pictures. This is due to the fact that both the states and the operators evolve with time. This picture is often used to describe evolutions generated by a Hamiltonian that can be written as

$$\hat{H}(t) = \hat{H}_0 + \hat{V}(t) \quad (\text{A.12})$$

where the evolution generated by \hat{H}_0 is the “free Hamiltonian” easy to unravel and $\hat{V}(t)$ is an interaction term, which is in general a time-dependent and more complicated perturbation.

The Schrödinger equation in the interaction picture reads:

$$i\hbar \frac{\partial}{\partial t} |\psi(t)\rangle_I = \hat{V}_I(t) |\psi(t)\rangle_I \quad (\text{A.13})$$

We see that the states evolve with the interaction part of the Hamiltonian. However, the Heisenberg equation of motion reads

$$\frac{d\hat{O}_I(t)}{dt} = \frac{i}{\hbar} [\hat{H}_0, \hat{O}_I(t)] + \frac{\partial \hat{O}_I(t)}{\partial t} \quad (\text{A.14})$$

so that the operators evolve with the free Hamiltonian. The evolution of the state and the operators in the Interaction picture are given by:

$$|\psi(t)\rangle_I = \hat{U}_I(t) |\psi(0)\rangle_I \quad (\text{A.15})$$

$$\hat{O}_I(t) = e^{\frac{i}{\hbar}\hat{H}_0 t} \hat{O}_I(0) e^{-\frac{i}{\hbar}\hat{H}_0 t} \quad (\text{A.16})$$

$$(\text{A.17})$$

where

$$\hat{U}_I(t) = \mathcal{T} e^{-\frac{i}{\hbar} \int_0^t d\tau V_I(\tau)} \quad (\text{A.18})$$

The Schrödinger and the Dirac picture are connected by the relations:

$$|\psi(t)\rangle_I = e^{\frac{i}{\hbar}\hat{H}_0 t} |\psi(t)\rangle_S \quad (\text{A.19})$$

$$\hat{O}_I(t) = e^{\frac{i}{\hbar}\hat{H}_0 t} \hat{O}_S e^{-\frac{i}{\hbar}\hat{H}_0 t} \quad (\text{A.20})$$

and in particular

$$\hat{V}_I(t) = e^{\frac{i}{\hbar}\hat{H}_0 t} \hat{V}_S e^{-\frac{i}{\hbar}\hat{H}_0 t} \quad (\text{A.21})$$

Appendix B

More details on ultrafast light

B.1 Laser essentials

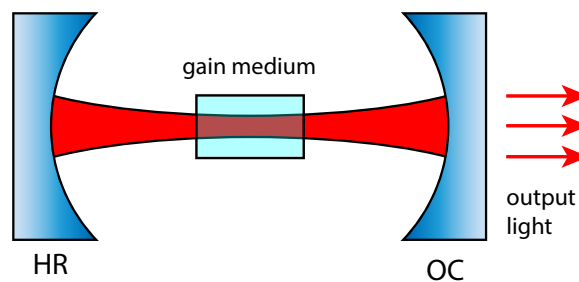


Figure B.1: Scheme of a linear laser cavity. HR = High reflection mirror, OC = output coupler. The cavity is resonant for infrared light. Here, the pump laser, that delivers energy to the active medium, is not depicted.

A basic laser is composed by a set of mirrors that form a cavity (or resonator cavity) and a gain medium, that acts as a coherent amplifier. The cavity can have various shapes, from the simplest linear cavity to more intricate folded configurations. Regardless of the chosen configuration, each laser cavity must contain a slightly transmissive mirror, called Output Coupler (OC). The OC permits to collect a fraction of the light, that is used as the fundamental source to carry out our experiment. A scheme of a linear laser cavity is shown in Fig. B.1. The gain medium, to avoid violating fundamental physics principles, cannot provide amplification by itself. Instead, a pumping mechanism is required, whose role is to deliver energy to the gain medium to excite its atoms. While photons circulate within the cavity, they undergo amplification via stimulated emission: an incoming photon triggers the release of another photon with the same properties from an excited atom, and the power of the incoming radiation is effectively amplified. We have mentioned all the necessary ingredients we need to collect to have a functional laser: a cavity with a specific

configuration, a gain medium carefully selected to achieve the desired pulse duration, and a pumping mechanism that aligns with the gain medium requirements.

Circulating in the cavity, light is amplified by the medium and it suffers also some losses (for example at the OC level). Lasing is possible only when the gain overcomes the losses, resulting in a rapid buildup of the power inside the cavity. However, this results in the de-excitation of the gain medium, as the circulating photons consume the energy stored by the pump in the material, until steady-state is reached.

In order to achieve steady state, the intra-cavity field must be invariant after each round-trip. Specifically, asking for amplitude and phase invariance of the field leads us to the following conditions:

- a gain condition, stating that the gain and losses must be equal at each round-trip (amplitude invariance),
- a phase condition, stating that only certain frequencies (known as *longitudinal modes*) are allowed to resonate in the cavity (phase invariance).

Due to the phase condition, we don't have a continuous spectrum but the frequencies are discretized, following

$$\omega_n = n \frac{2\pi c}{L} = n\omega_r, \quad n \in \mathbb{Z} \quad (\text{B.1})$$

where L is the cavity length and where $\omega_r = \frac{2\pi c}{L}$ is called free-spectral range of the cavity, and it corresponds to the angular frequency of the laser repetition rate.

B.2 Realistic frequency comb

For the longitudinal modes to oscillate, we require the phase $\phi(\omega_n)$ to be invariant after each roundtrip, up to multiples of 2π . However, due to dispersion, there is a dephasing between the different frequencies that oscillate in the cavity, that results, at first order, in a mismatch between the speed of the carrier (phase-velocity, v_ϕ) and the speed of the pulse envelope (group velocity, v_g). The dephasing between two consecutive pulses is

$$\Delta\phi_{CEP} = \left(\frac{1}{v_g} - \frac{1}{v_\phi} \right) \omega_0 L \quad (\text{B.2})$$

and it is called *carrier-envelope phase*. The carrier-envelope offset (CEO) is defined as:

$$\omega_{CEO} = \Delta\phi_{CEP} \frac{\omega_r}{2\pi} \quad (\text{B.3})$$

This leads to a redefinition of the temporal electric field of the pulse train and its Fourier transform:

$$E_{train}^{(+)}(t) = \mathcal{E}_0 \sum_{n=-\infty}^{\infty} \alpha(t - n\tau) e^{-i\omega_0(t-n\tau)} e^{-in\Delta\phi_{CEP}} \quad (\text{B.4})$$

$$E_{train}^{(+)}(\omega) = \omega_r E_{pulse}^{(+)}(\omega) \sum_{n=-\infty}^{\infty} \delta(\omega - n\omega_r - \omega_{CEO}) \quad (\text{B.5})$$

In the spectral domain, the longitudinal modes are redefined to account for this offset:

$$\omega_n = n\omega_r + \omega_{CEO} \quad (\text{B.6})$$

Moreover, due to the added phase between carrier and envelope at each pulse, $E_{train}^{(+)}(t)$ is no longer periodic. A picture of the spectral and temporal description of the frequency comb field can be seen in Fig. 4.5.

B.3 Dispersion of a pulse

Ultrashort pulses consist of multiple spectral components that, when traversing a medium, experience differently the refractive indices. This phenomenon becomes more pronounced when the pulse has a broad spectral profile, emphasizing the crucial role of dispersion compensation in the realm of ultrashort optics.

We rewrite here Eqs. 1.28 and 1.29, that describe the field in the SVE approximation:

$$E^{(+)}(t) = \mathcal{E}_0 \alpha(t) e^{-i\omega_0 t} \quad (\text{B.7})$$

$$E^{(+)}(\omega) = \mathcal{E}_0 \alpha(\Omega) \quad (\text{B.8})$$

where we recall that $\Omega = \omega - \omega_0$. Both complex amplitudes can be rewritten in the exponential form:

$$\alpha(t) = |\alpha(t)| e^{i\phi(t)} \quad (\text{B.9})$$

$$\alpha(\Omega) = |\alpha(\Omega)| e^{i\varphi(\Omega)} \quad (\text{B.10})$$

and we call the functions $\phi(t)$ and $\varphi(\Omega)$ respectively *temporal phase* and *spectral phase*. These two quantities contain information about the dispersion of the pulse.

We expand the spectral phase around the carrier ω_0 , to obtain

$$\varphi(\Omega) \simeq \varphi_0 + \Omega\varphi_1 + \frac{1}{2}\Omega^2\varphi_2 + \mathcal{O}(\Omega^3) \quad (\text{B.11})$$

We will now investigate the effect of the various terms of this expansion, up to the second order [Trebino 00].

The zero-th order term is equal in both the time domain and the spectral domain, i.e. $\varphi_0 = \phi_0$. The field in the temporal domain reads

$$E^{(+)}(t) = \mathcal{E}_0 |\alpha(t)| e^{-i(\omega_0 t - \phi_0)} \quad (\text{B.12})$$

and the effect of the global phase term is a dephasing of the carrier by ϕ_0 .

The first-order term $\Omega\varphi_1$ has the effect of a temporal delay of the pulse. Indeed, the electric field reads:

$$E^{(+)}(t) = \mathcal{E}_0 |\alpha(t - \phi_1)| e^{-i\omega_0 t} \quad (\text{B.13})$$

Note that the zeroth-order and first-order terms do not alter the pulse's shape or carrier frequency. They only introduce an envelope delay and a global phase shift in the carrier, which do not require specific compensation methods.

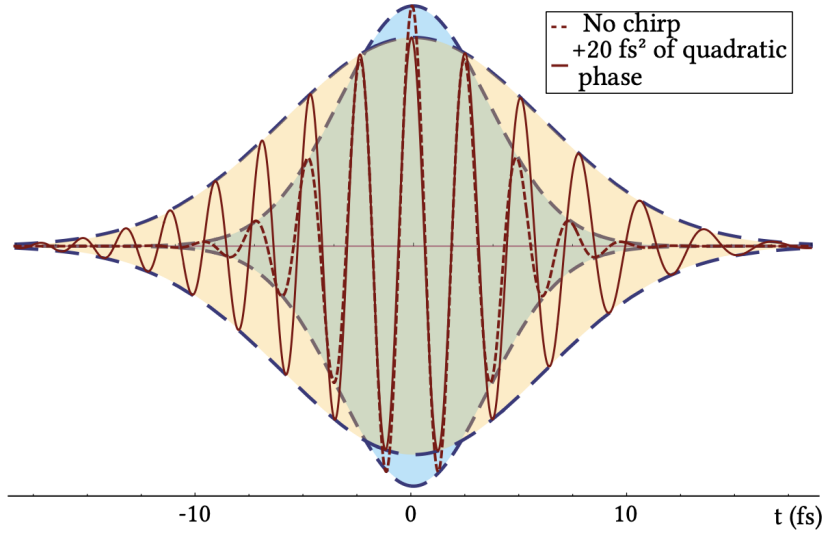


Figure B.2: Comparison between Fourier-transform limited and chirped pulse.
Picture from [Thiel 15]

The effects of the spectral phase become more complex as we go to higher order terms. Quadratic terms of the type $\frac{1}{2}\Omega^2\varphi_2$ not only alter the envelope's shape but also impact the carrier frequency. When such a term is present, we refer to the pulse as *chirped* and, depending on the sign of the chirp coefficient φ_2 , the pulse is said to be *negatively* or *positively chirped*. The degree of chirp is quantified in terms of femtoseconds squared (fs^2). We can examine its influence on a Gaussian pulse characterized by an envelope $\alpha(t) = \alpha u(t)$, where the Fourier transform of $u(t)$ is defined in Eq. 4.8, as:

$$\alpha(t) = \frac{1}{\sqrt{2\pi}} \int_{\mathbb{R}} C_{\omega} \alpha e^{-\frac{\Omega^2}{4\sigma\omega}} e^{\frac{1}{2}\Omega^2\varphi_2} e^{-i\Omega t} \quad (\text{B.14})$$

Completing the square at the exponent¹ leads us to the expression

$$E^{(+)}(t) = \mathcal{E}_0 \alpha C_\zeta e^{-\frac{t^2}{4\zeta^2}} e^{-i\omega_0 t} \quad (\text{B.15})$$

Here, $\zeta = \sigma_t \sqrt{1 - \frac{i\varphi_2}{2\sigma_t^2}}$ is a complex number, that can be split into real and imaginary parts². This separation allows us to examine its effects on both the pulse envelope and carrier. We rewrite the expression

$$\frac{1}{4\zeta^2} = \frac{1}{4\sigma_{t'}^2} + i \frac{\varphi_2}{8\sigma_{t'}^2} \quad (\text{B.16})$$

where

$$\sigma_{t'} = \sigma_t \sqrt{1 + \left(\frac{\varphi_2}{2\sigma_t^2}\right)^2} \quad (\text{B.17})$$

Regardless of the sign of φ_2 , it is important to note that $\sigma_{t'}$ is always greater than σ_t . Eq. B.15 can be rewritten as:

$$E^{(+)}(t) = \mathcal{E}_0 \alpha C_\zeta \exp\left[-\frac{t^2}{4\sigma_{t'}^2}\right] \exp\left[-i\left(\omega_0 + t \frac{\varphi_2}{8\sigma_{t'}^4}\right)t\right] \quad (\text{B.18})$$

The effect of the quadratic phase is two-fold. Firstly, it causes the pulse envelope to widen, extending the temporal duration defined by the standard deviation $\sigma_{t'}$, resulting in pulse broadening. This stands for both positive and negative chirp. Secondly, it introduces linear frequency modulation characterized by the spectral phase $\phi(t) = \frac{\varphi_2}{8\sigma_{t'}^4} t$. Negative chirp implies a decreasing instantaneous frequency over time, while positive chirp indicates an increasing instantaneous frequency. This behavior is shown in Fig. B.2.

Positive quadratic spectral phase is naturally induced by propagation of the pulse in a medium. The amount of chirp introduced by a medium is termed *group velocity dispersion* (GVD), and it reflects the fact that the group velocity is dependent on the frequency of light. As a title of example, a 6 mm fused silica lens introduces 345 fs² of chirp, while 1 m of propagation in air introduces only 21 fs².

Pulses with quadratic spectral phases are not Fourier-transform limited, and in general chirp terms need to be compensated for. The objective is to introduce negative chirp terms to compensate for the positive ones induced by propagation. This compensation can be achieved through various methods, including negatively-chirped mirrors, prism-based pulse compressors, and pulse shapers, which are among the commonly employed devices for chirp compensation.

Higher order terms can also be present, where the instantaneous frequency of the pulse varies non linearly with time, but they will not be treated in this manuscript.

¹The term $e^{-\Omega^2 \zeta^2} e^{-i\Omega t}$ can be rewritten as $e^{-(\Omega\zeta + \frac{it}{2\zeta})^2} e^{-\frac{t^2}{4\zeta^2}}$ where $\zeta^2 = \frac{1}{4\sigma_\omega^2} - \frac{i\varphi_2}{2} = \sigma_t^2 \left(1 - \frac{i\varphi_2}{2\sigma_t^2}\right)$.

²If $\zeta^2 = a - ib$ then $\text{Re}[1/\zeta^2] = a/(a^2 + b^2)$ and $\text{Im}[1/\zeta^2] = b/(a^2 + b^2)$

Appendix C

Signal processing and derivative

Here we explain how the modulation-demodulation-LPF chain has the effect of yielding the derivative of the original signal. The photodiode yields a signal, shown in Fig. 6.8a, of the form:

$$y_{sig} = \sin(\omega_1 t + \epsilon \cos(\omega_2 t)) \quad (C.1)$$

where ω_2 is the optical modulation, while $\omega_1 < \omega_2$ is the characteristic frequency of the parametric amplification oscillations. This signal can be split, via a trigonometric identity, into two components:

$$y_{sig} = \sin(\omega_1 t) \cos(\epsilon \cos(\omega_2 t)) + \cos(\omega_1 t) \sin(\epsilon \cos(\omega_2 t)) \quad (C.2)$$

Let's investigate the terms dependent of ω_2 . As it can be seen in Fig. C.1, the term $\cos(\epsilon \cos(\omega_2 t))$ oscillates at $2\omega_2$ and will be filtered out by the low pass filter. We can then discard this component and concentrating on the remaining one. For small values of ϵ , it reads

$$\sin(\epsilon \cos(\omega_2 t)) \sim \epsilon \cos(\omega_2 t) \quad (C.3)$$

as it can be seen in the plot in Fig. C.1b.

We arrive now at the demodulating stage. The operation of the mixer is a multiplication. At the output of the mixer we get thus

$$y_{out} = y_{sig} \cdot y_{demod} \quad (C.4)$$

We demodulate with the signal $y_{demod} = \cos(\omega_2 t)$, so that, according to what we said earlier, we are left with

$$y_{out} \sim [\sin(\omega_1 t) \cos(\epsilon \cos(\omega_2 t)) + \cos(\omega_1 t) \epsilon \cos(\omega_2 t)] \cdot \cos(\omega_2 t) \quad (C.5)$$

We already said that we can discard the first term as it is doomed to be filtered out. However, the second term yields

$$\epsilon \cos(\omega_1 t) \cos^2(\omega_2 t) = \epsilon \cos(\omega_1 t) \left(\frac{1 - \cos(2\omega_2 t)}{2} \right) \quad (C.6)$$

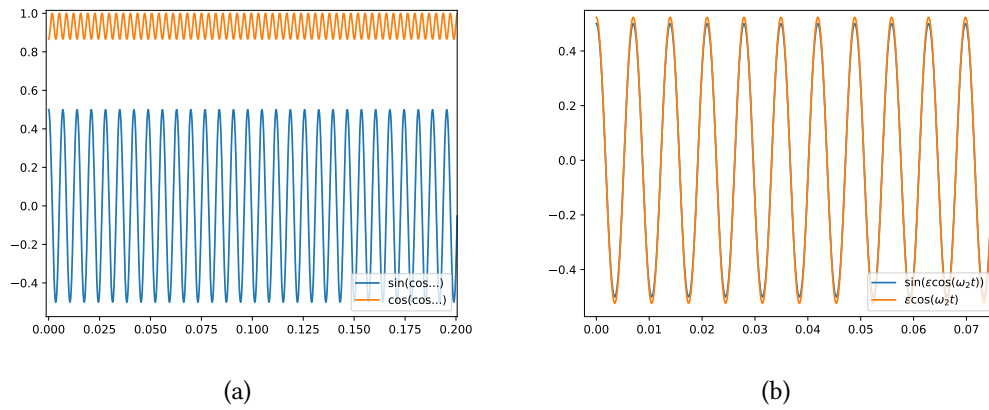


Figure C.1: a) Characteristic of the plot: $\omega_1 = 10$ Hz, $\omega_2 = 900$ Hz, $\epsilon = \pi/6$, b) $\epsilon = \pi/6$

where also the term dependent on $2\omega_2$ will be filtered out by the low pass filter. We now apply the low-pass filter to be left with

$$y_{err}(t) = \frac{\epsilon}{2} \cos(\omega_1 t) \tag{C.7}$$

In Fig. C.2 the plots of the various signals are shown, and we can see how we recover the derivative of the original un-modulated parametric amplification signal via the modulation, demodulation and low pass filtering technique.

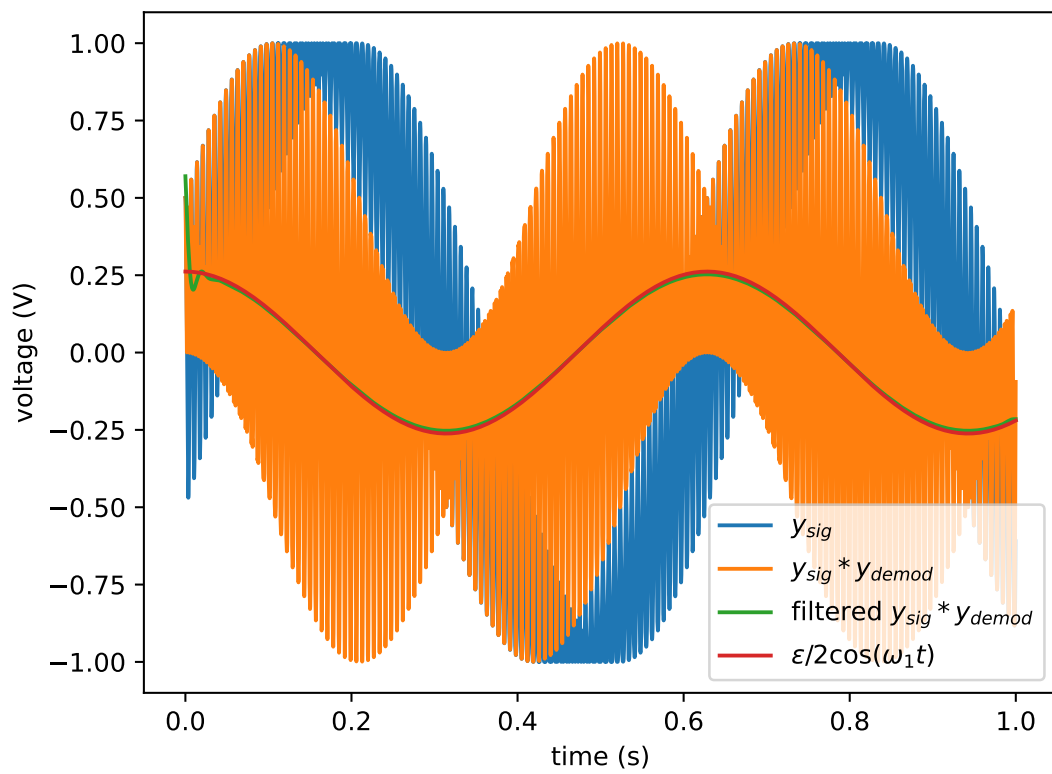


Figure C.2: Signals at various stages in the AC lock technique.

Appendix D

Details on calculations

D.1 Calculations on fidelity with target state

We provide here all the terms used for the calculation of the fidelity. The results are analytical, and the only condition required is $N \gg 1$.

The equation of the state after the post-selection process is, from Eq. 7.64:

$$|\psi_{exp}\rangle = \left[(a_k + h_k) \hat{a}_s^\dagger \hat{a}_s + [b_k + g_k] \hat{a}_w^\dagger \hat{a}_w + c_k \hat{a}_s^{2\dagger} + d_k \hat{a}_w^{2\dagger} + e_k \hat{a}_s^2 + f_k \hat{a}_w^2 + (h_k + g_k) \mathbb{1} + i l_k \hat{a}_s^\dagger \hat{a}_w + i m_k \hat{a}_w^\dagger \hat{a}_s + i n_k \hat{a}_s^\dagger \hat{a}_w^\dagger + i o_k \hat{a}_s \hat{a}_w \right] |s\rangle \quad (D.1)$$

The normalization reads:

$$\begin{aligned} \langle \psi_{exp} | \psi_{exp} \rangle = & l_k^2 B_1 + m_k^2 B_2 + n_k^2 B_3 + o_k^2 B_4 + 2l_k n_k B_5 + 2l_k o_k B_6 + 2m_k n_k B_7 \\ & + 2m_k o_k B_8 + 2l_k m_k B_9 + 2n_k o_k B_{10} + 2(a_k + h_k)(h_k + g_k) A_1 \\ & + 2c_k(h_k + g_k) A_2 + 2(b_k + g_k)(h_k + g_k) A_3 + 2d_k(h_k + g_k) A_4 \\ & + 2e_k(h_k + g_k) A_5 + 2f_k(h_k + g_k) A_6 + (h_k + g_k)^2 A_7 + C_1(a_k + h_k)^2 \\ & + 2(a_k + h_k)(b_k + g_k) C_2 + 2(a_k + h_k)c_k C_3 + 2(a_k + h_k)d_k C_4 \\ & + 2(a_k + h_k)e_k C_5 + 2(a_k + h_k)f_k C_6 + (b_k + g_k)^2 C_7 + 2(b_k + g_k)c_k C_8 \\ & + 2(b_k + g_k)d_k C_9 + 2(b_k + g_k)e_k C_{10} + 2(b_k + g_k)f_k C_{11} + c_k^2 C_{12} \\ & + 2c_k d_k C_{13} + 2c_k e_k C_{14} + 2c_k f_k C_{15} + d_k^2 C_{16} + 2d_k e_k C_{17} + 2d_k f_k C_{18} \\ & + e_k^2 C_{19} + 2e_k f_k C_{20} + f_k^2 C_{21} \end{aligned} \quad (D.2)$$

The coefficients of this equations have been determined by the analytic calculation of the overlap of the various terms. They are given by:

$$\begin{aligned}
 A_1 &= 2k_1^2 + k_2^2 & (D.3) & & C_3 &= 6k_1k_2k_3 + 6k_1^2k_2 + 3k_2^3 & (D.22) \\
 A_2 &= 3k_1k_2 & (D.4) & & C_4 &= 2k_1^2k_2 + k_2^3 & (D.23) \\
 A_5 &= 3k_1k_2 & (D.5) & & C_5 &= 12k_1^2k_2 + 3k_2^3 & (D.24) \\
 A_3 &= k_1^2 & (D.6) & & C_6 &= 2k_1^2k_2 + k_2^3 & (D.25) \\
 A_4 &= k_1k_2 & (D.7) & & C_7 &= k_1k_4 & (D.26) \\
 A_6 &= k_1k_2 & (D.8) & & C_8 &= 3k_1^2k_2 & (D.27) \\
 A_7 &= k_1 & (D.9) & & C_9 &= k_1k_8 & (D.28) \\
 B_1 &= k_1^3 + k_1^2k_3 + k_1k_2^2 & (D.10) & & C_{10} &= 3k_1^2k_2 & (D.29) \\
 B_2 &= k_2^2k_3 + 2k_1^2k_3 & (D.11) & & C_{11} &= k_1k_5 & (D.30) \\
 B_3 &= k_1^2k_3 + k_1k_2^2 + k_2^2k_3 & (D.12) & & C_{12} &= 4k_1^2k_3 + 2k_1k_3^2 + 4k_2^2k_3 + 5k_1k_2^2 & (D.31) \\
 B_4 &= k_1k_2^2 + 2k_1^3 & (D.13) & & C_{13} &= 3k_1k_2^2 & (D.32) \\
 B_5 &= k_1^2k_2 + k_1k_2k_3 + k_2^3 & (D.14) & & C_{14} &= 15k_1k_2^2 & (D.33) \\
 B_6 &= 3k_1^2k_2 & (D.15) & & C_{15} &= 3k_1k_2^2 & (D.34) \\
 B_7 &= 3k_1k_2k_3 & (D.16) & & C_{16} &= k_1k_9 & (D.35) \\
 B_8 &= k_2^3 + 2k_1^2k_2 & (D.17) & & C_{17} &= 3k_1k_2^2 & (D.36) \\
 B_9 &= 3k_1k_2^2 & (D.18) & & C_{18} &= k_1k_7 & (D.37) \\
 B_{10} &= 3k_1k_2^2 & (D.19) & & C_{19} &= 9k_1k_2^2 + 6k_1^3 & (D.38) \\
 C_1 &= k_2^2k_3 + 2k_1^2k_3 + 8k_1k_2^2 + 4k_1^3 & (D.20) & & C_{20} &= 3k_1k_2^2 & (D.39) \\
 C_2 &= 2k_1^3 + k_1k_2^2 & (D.21) & & C_{21} &= k_1k_6 & (D.40)
 \end{aligned}$$

where the k parameters are dependent on the squeezing level of the input state and they are given by:

$$k_1 = \sinh^2 r \quad (D.41)$$

$$k_2 = -\sinh^2 r \cosh r \quad (D.42)$$

$$k_3 = \cosh^2 r \quad (D.43)$$

$$k_4 = \cosh^2 r \sinh^2 r (2 + \tanh^2 r) \quad (D.44)$$

$$k_5 = -3 \cosh r \sinh^3 r \quad (D.45)$$

$$k_6 = \sinh^2 r / 2 (3 \cosh(2r) - 1) \quad (D.46)$$

$$k_7 = 3 \cosh^2 r \sinh^2 r \quad (D.47)$$

$$k_8 = -\cosh^3 r \sinh r (2 + \tanh^2 r) \quad (D.48)$$

$$k_9 = \cosh^2 r / 2 * (3 * \cosh(2r) + 1) \quad (D.49)$$

The overlap between the $|\psi_{exp}\rangle$ state and the target state reads:

$$\langle w|\psi_{exp}\rangle = -i(l_k k_1^2 + m_k k_2^2 + n_k k_1 k_2 + o_k k_1 k_2) \quad (D.50)$$

while the overlap with the superposition state $|s\rangle$ is:

$$\langle s|\psi_{exp}\rangle = (a_k + h_k)A_1 + c_k A_2 + (b_k + g_k)A_3 + d_k A_4 + e_k A_5 + f_k * A_6 + (h_k + g_k)A_7 \quad (D.51)$$

From these equations it is possible to calculate the fidelity between the state $|\psi_{exp}\rangle$ and every superposition of $|s\rangle$ and $|w\rangle$.

D.2 Evolution of the system-environment network for synchronization

Our aim is to describe the evolution of the system-environment network prescribed by the Hamiltonian $\hat{H}_{tot} = \hat{H}_S + \hat{H}_E + \hat{H}_I$. To achieve this, we start by diagonalizing \hat{H}_{tot} . We will designate with \mathbf{B} the matrix that contains the information about the total system couplings and frequencies, analogous to the \mathbf{A} environment matrix of Eq. 8.10.

The matrix \mathbf{B} is related to its diagonal form by:

$$\mathbf{B} = \mathbf{O}(\Delta_f/\sqrt{2})^2 \mathbf{O}^T \quad (D.52)$$

and \hat{H}_{tot} can be expressed as:

$$\hat{H}_{tot} = \sum_i \frac{f_i}{2} (\hat{Q}_i^2 + \hat{P}_i^2) \quad (D.53)$$

Here, $\{\hat{Q}, \hat{P}\}$ are the quadratures in the uncoupled basis of the system-environment network, while f_i are the eigenfrequencies. In Fig. D.1 the depiction of the couplings between system and environment in the two bases $\{\hat{Q}, \hat{q}_S, \hat{P}, \hat{p}_S\}$ and $\{\hat{Q}, \hat{Q}_S, \hat{P}, \hat{P}_S\}$ is shown. Analogously to Eq. 8.12, the quadrature transformation reads:

$$\hat{\mathcal{X}} = \sqrt{\Delta_f^{-1}} \mathbf{O}^T \sqrt{\Delta_\Omega} \hat{\mathcal{X}} \quad (D.54)$$

$$\hat{\mathcal{X}}_S = \sqrt{\Delta_f} \mathbf{O}^T \sqrt{\Delta_{\omega_S}^{-1}} \hat{\mathcal{X}}_S \quad (D.55)$$

where $\hat{\mathcal{X}} = \{\hat{Q}, \hat{P}\}$ and the subscript S indicates the system. Working in the $\{\hat{Q}, \hat{P}\}$ basis is convenient because we can easily calculate the quadrature evolution. Once this is done, we can switch back to the previous basis.

The quadrature operator at time t is defined as:

$$\hat{\mathcal{X}}(t) = e^{i\hat{H}_{tot}t} \hat{\mathcal{X}}(0) e^{-i\hat{H}_{tot}t} \quad (D.56)$$

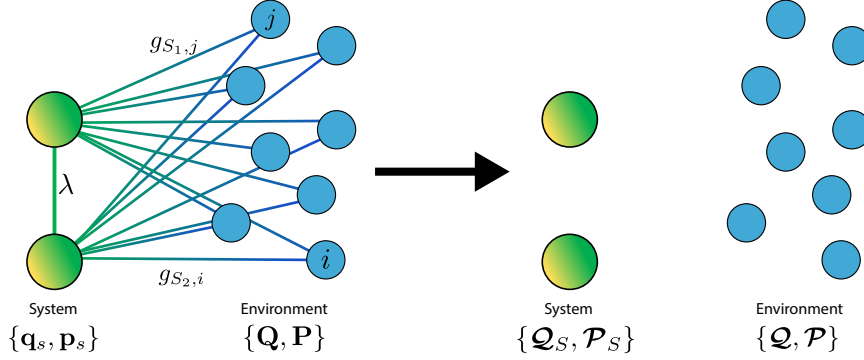


Figure D.1: Network depicted in two different bases. On the left the network is described by the $\{\hat{Q}, \hat{q}_s, \hat{P}, \hat{p}_s\}$ quadratures, while after the diagonalization the oscillators of the system+environment network are all uncoupled and described by the quadratures $\{\hat{Q}, \hat{Q}_S, \hat{P}, \hat{P}_S\}$

To calculate this expression, we use the formula:

$$e^{i\hat{A}\hat{B}}e^{-i\hat{A}} = \hat{B} + \sum_n \frac{i^n}{n!} [\hat{A}, [\hat{A}, \dots [\hat{A}, \hat{B}]] \dots] \quad (\text{D.57})$$

where we will replace $\hat{A} = \hat{H}_{tot}t$ and $\hat{B} = \hat{\chi}_i(0)$. Carrying out the calculations we obtain

$$\begin{aligned} \hat{Q}_i(t) &= \hat{Q}_i(0) \cos(f_it) + \hat{P}_i(0) \sin(f_it) \\ \hat{P}_i(t) &= -\hat{Q}_i(0) \sin(f_it) + \hat{P}_i(0) \cos(f_it) \end{aligned} \quad (\text{D.58})$$

that we can rewrite more compactly as:

$$\begin{pmatrix} \hat{Q}(t) \\ \hat{P}(t) \end{pmatrix} = \begin{pmatrix} D_{\cos,t}^f & D_{\sin,t}^f \\ -D_{\sin,t}^f & D_{\cos,t}^f \end{pmatrix} \begin{pmatrix} \hat{Q}(0) \\ \hat{P}(0) \end{pmatrix} \quad (\text{D.59})$$

where $D_{\cos,t}^f$ and $D_{\sin,t}^f$ are diagonal matrices with entries $\cos(f_it)$ and $\sin(f_it)$ respectively. Recalling Eq. D.55, we can write:

$$\begin{pmatrix} \hat{Q}(t) \\ \hat{q}_s(t) \\ \hat{P}(t) \\ \hat{p}_s(t) \end{pmatrix} = \begin{pmatrix} C_1^{-1} & 0 \\ 0 & C_2^{-1} \end{pmatrix} \begin{pmatrix} \hat{Q}(t) \\ \hat{Q}_S(t) \\ \hat{P}(t) \\ \hat{P}_S(t) \end{pmatrix} \quad (\text{D.60})$$

where $C_1 = \sqrt{\Delta_f} \mathbf{O}^T \sqrt{\Delta_{\Omega/\omega_s}^{-1}}$ and $C_2 = \sqrt{\Delta_f^{-1}} \mathbf{O}^T \sqrt{\Delta_{\Omega/\omega_s}}$. It follows that the evolution of

Eq. D.59 in the $\{\hat{\mathbf{Q}}, \hat{\mathbf{q}}_S, \hat{\mathbf{P}}, \hat{\mathbf{p}}_S\}$ basis can be written as:

$$\begin{pmatrix} \hat{\mathbf{Q}}(t) \\ \hat{\mathbf{q}}_S(t) \\ \hat{\mathbf{P}}(t) \\ \hat{\mathbf{p}}_S(t) \end{pmatrix} = \begin{pmatrix} C_1^{-1} D_{\cos,t}^f C_1 & C_1^{-1} D_{\sin,t}^f C_2 \\ -C_2^{-1} D_{\sin,t}^f C_1 & C_2^{-1} D_{\cos,t}^f C_2 \end{pmatrix} \begin{pmatrix} \hat{\mathbf{Q}}(0) \\ \hat{\mathbf{q}}_S(0) \\ \hat{\mathbf{P}}(0) \\ \hat{\mathbf{p}}_S(0) \end{pmatrix} = \mathbf{S}(t) \begin{pmatrix} \hat{\mathbf{Q}}(0) \\ \hat{\mathbf{q}}_S(0) \\ \hat{\mathbf{P}}(0) \\ \hat{\mathbf{p}}_S(0) \end{pmatrix} \quad (\text{D.61})$$

References

- [Aaboud 17] M. Aaboud *et al.* *Evidence for light-by-light scattering in heavy-ion collisions with the ATLAS detector at the LHC*. *Nature Physics*, vol. 13, no. 9, pages 852–858, 2017. [Online URL](#). (Cited on page 59.)
- [Aasi 13] J. Aasi *et al.* *Enhanced sensitivity of the LIGO gravitational wave detector by using squeezed states of light*. *Nature Photonics*, vol. 7, no. 8, pages 613–619, 2013. [Online URL](#). (Cited on page 83.)
- [Adesso 14] Gerardo Adesso, Sammy Ragy & Antony R. Lee. *Continuous Variable Quantum Information: Gaussian States and Beyond*. *Open Systems & Information Dynamics*, vol. 21, no. 01n02, page 1440001, 2014. [Online URL](#). (Cited on pages 3 and 38.)
- [Agrawal 20] G.P. Agrawal. *Applications of nonlinear fiber optics*. Elsevier Science, 2020. (Cited on page 88.)
- [Ansquer 22] Matthieu Ansquer. *Modal approach to the dynamics of optical frequency combs and applications*. Theses, Sorbonne Université, February 2022. (Cited on pages 52 and 111.)
- [Arute 19] Frank Arute *et al.* *Quantum supremacy using a programmable superconducting processor*. *Nature*, vol. 574, no. 7779, pages 505–510, 2019. [Online URL](#). (Cited on page 2.)
- [Arzani 19a] Francesco Arzani, Alessandro Ferraro & Valentina Parigi. *High-dimensional quantum encoding via photon-subtracted squeezed states*. *Phys. Rev. A*, vol. 99, page 022342, Feb 2019. [Online URL](#). (Cited on pages 168 and 169.)
- [Arzani 19b] Francesco Arzani, Giulia Ferrini, Frédéric Grosshans & Damian Markham. *Random coding for sharing bosonic quantum secrets*. *Phys. Rev. A*, vol. 100, page 022303, Aug 2019. [Online URL](#). (Cited on page 3.)

- [Asavanant 19] Warit Asavanant, Yu Shiozawa, Shota Yokoyama, Baramée Charoensombutamon, Hiroki Emura, Rafael N. Alexander, Shuntaro Takeda, Jun ichi Yoshikawa, Nicolas C. Menicucci, Hidehiro Yonezawa & Akira Furusawa. *Generation of time-domain-multiplexed two-dimensional cluster state*. Science, vol. 366, no. 6463, pages 373–376, 2019. [Online URL](#). (Cited on pages 3, 84, and 141.)
- [Aspect 82] Alain Aspect, Jean Dalibard & Gérard Roger. *Experimental Test of Bell’s Inequalities Using Time-Varying Analyzers*. Phys. Rev. Lett., vol. 49, pages 1804–1807, Dec 1982. [Online URL](#). (Cited on page 2.)
- [Aström 95] Karl Johan Aström & Tore Hägglund. *Pid controllers: Theory, design, and tuning*. ISA - The Instrumentation, Systems and Automation Society, 1995. (Cited on page 147.)
- [Aström 08] Karl Johan Aström & Richard M. Murray. *Feedback systems: An introduction for scientists and engineers*. Princeton University Press, USA, 2008. (Cited on page 147.)
- [Averchenko 14] Valentin A. Averchenko, Valérian Thiel & Nicolas Treps. *Nonlinear photon subtraction from a multimode quantum field*. Phys. Rev. A, vol. 89, page 063808, Jun 2014. [Online URL](#). (Cited on pages 169 and 180.)
- [Averchenko 16] V Averchenko, C Jacquard, V Thiel, C Fabre & N Treps. *Multimode theory of single-photon subtraction*. New Journal of Physics, vol. 18, no. 8, page 083042, aug 2016. [Online URL](#). (Cited on pages 169 and 180.)
- [Bach 16] Florian Bach, Mark Mero, Valdas Pasiskevicius, Andrius Zukauskas & Valentin Petrov. *High Repetition Rate, Femtosecond and Picosecond Laser Induced Damage Thresholds of Rb:KTiOPO₄ at 1.03 μ m*. In Lasers Congress 2016 (ASSL, LSC, LAC), page JTu2A.31. Optica Publishing Group, 2016. (Cited on page 105.)
- [Bachor 19] H.A. Bachor & T.C. Ralph. *A guide to experiments in quantum optics*. Wiley, 2019. (Cited on pages 14, 44, 46, 48, 49, and 56.)
- [Barbosa 13] F. A. S. Barbosa, A. S. Coelho, K. N. Cassemiro, P. Nussenzveig, C. Fabre, M. Martinelli & A. S. Villar. *Beyond Spectral Homodyne Detection: Complete Quantum Measurement of Spectral Modes of Light*. Phys. Rev. Lett., vol. 111, page 200402, Nov 2013. [Online URL](#). (Cited on pages 48, 56, and 57.)

- [Barbosa 20] F. A. S. Barbosa, A. S. Coelho, K. N. Cassemiro, M. Martinelli, P. Nussenzweig & A. S. Villar. *Assumption-free measurement of the quantum state of light: Exploring the sidebands of intense fields*. Phys. Rev. A, vol. 102, page 063705, Dec 2020. [Online URL](#). (Cited on pages 47 and 48.)
- [Bell 64] J. S. Bell. *On the Einstein Podolsky Rosen paradox*. Physics Physique Fizika, vol. 1, pages 195–200, Nov 1964. [Online URL](#). (Cited on page 2.)
- [Benedetti 16] Claudia Benedetti, Fernando Galve, Antonio Mandarino, Matteo G. A. Paris & Roberta Zambrini. *Minimal model for spontaneous quantum synchronization*. Phys. Rev. A, vol. 94, page 052118, Nov 2016. [Online URL](#). (Cited on pages 184, 187, and 195.)
- [Bennett 97] Charles H. Bennett, Ethan Bernstein, Gilles Brassard & Umesh Vazirani. *Strengths and Weaknesses of Quantum Computing*. SIAM Journal on Computing, vol. 26, no. 5, pages 1510–1523, 1997. [Online URL](#). (Cited on page 162.)
- [Bernstein 93] Ethan Bernstein & Umesh Vazirani. *Quantum Complexity Theory*. In Proceedings of the Twenty-Fifth Annual ACM Symposium on Theory of Computing, STOC '93, pages 11–20, New York, NY, USA, 1993. Association for Computing Machinery. (Cited on page 2.)
- [Bierlein 87] John D. Bierlein, August Ferretti, Lothar H. Brixner & William Y. Hsu. *Fabrication and characterization of optical waveguides in KTiOPO4*. Applied Physics Letters, vol. 50, no. 18, pages 1216–1218, 05 1987. [Online URL](#). (Cited on page 96.)
- [Bloembergen 74] N. Bloembergen. *Laser-induced electric breakdown in solids*. IEEE Journal of Quantum Electronics, vol. 10, no. 2, pages 375–386, (Cited on page 105.)
- [Bourassa 21] J. Eli Bourassa, Rafael N. Alexander, Michael Vasmer, Ashlesha Patil, Ilan Tzitrin, Takaya Matsuura, Daiqin Su, Ben Q. Baragiola, Saikat Guha, Guillaume Dauphinais, Krishna K. Sabapathy, Nicolas C. Menicucci & Ish Dhand. *Blueprint for a Scalable Photonic Fault-Tolerant Quantum Computer*. Quantum, vol. 5, page 392, February 2021. [Online URL](#). (Cited on pages 3 and 83.)
- [Boyd 08] R.W. Boyd & D. Prato. *Nonlinear optics*. Elsevier Science, 2008. (Cited on pages 60, 61, 63, and 64.)

- [Braunstein 98] Samuel L. Braunstein & H. J. Kimble. *Teleportation of Continuous Quantum Variables*. Phys. Rev. Lett., vol. 80, pages 869–872, Jan 1998. [Online URL](#). (Cited on page 37.)
- [Braunstein 00] Samuel L. Braunstein & H. J. Kimble. *Dense coding for continuous variables*. Phys. Rev. A, vol. 61, page 042302, Mar 2000. [Online URL](#). (Cited on page 37.)
- [Braunstein 05a] Samuel L. Braunstein. *Squeezing as an irreducible resource*. Phys. Rev. A, vol. 71, page 055801, May 2005. [Online URL](#). (Cited on page 42.)
- [Braunstein 05b] Samuel L. Braunstein & Peter van Loock. *Quantum information with continuous variables*. Rev. Mod. Phys., vol. 77, pages 513–577, Jun 2005. [Online URL](#). (Cited on pages 3, 22, and 38.)
- [Brecht 14] Benjamin Brecht. *Engineering ultrafast quantum frequency conversion*. PhD thesis, Paderborn University, 2014. (Cited on pages 98 and 100.)
- [Breuer 02] H.P. Breuer & F. Petruccione. *The theory of open quantum systems*. Oxford University Press, 2002. (Cited on pages 39, 183, 184, and 185.)
- [Bruss 19] D. Bruss & G. Leuchs. *Quantum information: From foundations to quantum technology applications*. Wiley, 2019. (Cited on page 2.)
- [Cai 17] Y. Cai, J. Roslund, G. Ferrini, F. Arzani, X. Xu, C. Fabre & N. Treps. *Multimode entanglement in reconfigurable graph states using optical frequency combs*. Nature Communications, vol. 8, no. 1, page 15645, 2017. [Online URL](#). (Cited on pages 3, 84, and 142.)
- [Chabaud 21] Ulysse Chabaud, Pierre-Emmanuel Emeriau & Frédéric Grosshans. *Witnessing Wigner Negativity*. Quantum, vol. 5, page 471, June 2021. [Online URL](#). (Cited on page 25.)
- [Chen 14] Moran Chen, Nicolas C. Menicucci & Olivier Pfister. *Experimental Realization of Multipartite Entanglement of 60 Modes of a Quantum Optical Frequency Comb*. Phys. Rev. Lett., vol. 112, page 120505, Mar 2014. [Online URL](#). (Cited on pages 3 and 84.)
- [Childs 04a] Andrew M. Childs & Jeffrey Goldstone. *Spatial search by quantum walk*. Phys. Rev. A, vol. 70, page 022314, Aug 2004. [Online URL](#). (Cited on pages 3, 160, 162, 163, and 165.)

- [Childs 04b] Andrew MacGregor Childs. *Quantum information processing in continuous time*. PhD thesis, Massachusetts Institute of Technology, 2004. (Cited on page 163.)
- [Cirac 97] J. I. Cirac, P. Zoller, H. J. Kimble & H. Mabuchi. *Quantum State Transfer and Entanglement Distribution among Distant Nodes in a Quantum Network*. Phys. Rev. Lett., vol. 78, pages 3221–3224, Apr 1997. [Online URL](#). (Cited on page 3.)
- [Daiss 21] Severin Daiss, Stefan Langenfeld, Stephan Welte, Emanuele Distante, Philip Thomas, Lukas Hartung, Olivier Morin & Gerhard Rempe. *A quantum-logic gate between distant quantum-network modules*. Science, vol. 371, no. 6529, pages 614–617, 2021. [Online URL](#). (Cited on page 3.)
- [Deutsch 85] David Deutsch & Roger Penrose. *Quantum theory, the Church–Turing principle and the universal quantum computer*. Proceedings of the Royal Society of London. A. Mathematical and Physical Sciences, vol. 400, no. 1818, pages 97–117, 1985. [Online URL](#). (Cited on page 2.)
- [Dmitriev 14] V.G. Dmitriev, G.G. Gurzadyan & D.N. Nikogosyan. Handbook of nonlinear optical crystals. Springer Series in Optical Sciences. Springer Berlin Heidelberg, 2014. (Cited on page 61.)
- [Dosseva 16] Annamaria Dosseva, Łukasz Cincio & Agata M. Brańczyk. *Shaping the joint spectrum of down-converted photons through optimized custom poling*. Phys. Rev. A, vol. 93, page 013801, Jan 2016. [Online URL](#). (Cited on page 126.)
- [Dowling 03] Jonathan P. Dowling & Gerard J. Milburn. *Quantum technology: the second quantum revolution*. Philosophical Transactions of the Royal Society of London. Series A: Mathematical, Physical and Engineering Sciences, vol. 361, no. 1809, pages 1655–1674, 2003. [Online URL](#). (Cited on page 2.)
- [Duan 00] Lu-Ming Duan, G. Giedke, J. I. Cirac & P. Zoller. *Inseparability Criterion for Continuous Variable Systems*. Phys. Rev. Lett., vol. 84, pages 2722–2725, Mar 2000. [Online URL](#). (Cited on page 56.)
- [Dubreuil] Nicolas Dubreuil. *Nonlinear Optics - introduction Lecture Notes*. Institut d’Optique WebPage. (Cited on pages 61 and 62.)

- [Eckstein 11] Andreas Eckstein, Benjamin Brecht & Christine Silberhorn. *A quantum pulse gate based on spectrally engineered sum frequency generation*. Opt. Express, vol. 19, no. 15, pages 13770–13778, Jul 2011. [Online URL](#). (Cited on page 142.)
- [Einstein 35] A. Einstein, B. Podolsky & N. Rosen. *Can Quantum-Mechanical Description of Physical Reality Be Considered Complete?* Phys. Rev., vol. 47, pages 777–780, May 1935. [Online URL](#). (Cited on page 2.)
- [Ell 01] R. Ell, U. Morgner, F. X. Kärtner, J. G. Fujimoto, E. P. Ippen, V. Scheuer, G. Angelow, T. Tschudi, M. J. Lederer, A. Boiko & B. Luther-Davies. *Generation of 5-fs pulses and octave-spanning spectra directly from a Ti:sapphire laser*. Opt. Lett., vol. 26, no. 6, pages 373–375, Mar 2001. [Online URL](#). (Cited on page 88.)
- [Fabre 20] C. Fabre & N. Treps. *Modes and states in quantum optics*. Rev. Mod. Phys., vol. 92, page 035005, Sep 2020. [Online URL](#). (Cited on pages 10, 19, and 43.)
- [Fallahkhair 08] Arman B. Fallahkhair, Kai S. Li & Thomas E. Murphy. *Vector Finite Difference Modesolver for Anisotropic Dielectric Waveguides*. Journal of Lightwave Technology, vol. 26, no. 11, pages 1423–1431, (Cited on page 96.)
- [Farhi 96] Edward Farhi & Sam Gutmann. *An Analog Analogue of a Digital Quantum Computation*, 1996. (Cited on page 164.)
- [Fejer 92] M.M. Fejer, G.A. Magel, D.H. Jundt & R.L. Byer. *Quasi-phase-matched second harmonic generation: tuning and tolerances*. IEEE Journal of Quantum Electronics, vol. 28, no. 11, pages 2631–2654, (Cited on page 69.)
- [Ferraro 05] Alessandro Ferraro, Stefano Olivares & Matteo G. A. Paris. *Gaussian states in continuous variable quantum information*, 2005. (Cited on pages 37, 38, and 42.)
- [Feynman 82] Richard P. Feynman. *Simulating physics with computers*. International Journal of Theoretical Physics, vol. 21, no. 6, pages 467–488, 1982. [Online URL](#). (Cited on page 2.)
- [Fizeau 49] H. Fizeau. *Sur une expérience relative à la vitesse de propagation de la lumière*. Comptes Rendus de l'Academie de Sciences, vol. 29, no. 90, (Cited on page 2.)

- [Fortier 19] Tara Fortier & Esther Baumann. *20 years of developments in optical frequency comb technology and applications*. Communications Physics, vol. 2, no. 1, page 153, 2019. [Online URL](#). (Cited on page 91.)
- [Foucault 53] L. Foucault. Sur les vitesses relatives de la lumière dans l’air et dans l’eau. Bachelier, 1853. (Cited on page 2.)
- [Fresnel 19] A.J. Fresnel. Mémoire sur la diffraction de la lumière. De l’Imprimerie de Feugueray, rue du Cloître Saint-Benoit, no. 4, 1819. (Cited on page 2.)
- [Gardiner 04] C. Gardiner & P. Zoller. Quantum noise: A handbook of markovian and non-markovian quantum stochastic methods with applications to quantum optics. Springer Series in Synergetics. Springer, 2004. (Cited on page 52.)
- [Gerke 15] S. Gerke, J. Sperling, W. Vogel, Y. Cai, J. Roslund, N. Treps & C. Fabre. *Full Multipartite Entanglement of Frequency-Comb Gaussian States*. Phys. Rev. Lett., vol. 114, page 050501, Feb 2015. [Online URL](#). (Cited on page 137.)
- [Gerry 05] C. Gerry & P.L. Knight. Introductory quantum optics. Cambridge University Press, 2005. (Cited on page 10.)
- [Gessner 18] Manuel Gessner, Luca Pezzè & Augusto Smerzi. *Sensitivity Bounds for Multiparameter Quantum Metrology*. Phys. Rev. Lett., vol. 121, page 130503, Sep 2018. [Online URL](#). (Cited on page 3.)
- [Giorgi 12] Gian Luca Giorgi, Fernando Galve, Gonzalo Manzano, Pere Colet & Roberta Zambrini. *Quantum correlations and mutual synchronization*. Phys. Rev. A, vol. 85, page 052101, May 2012. [Online URL](#). (Cited on pages 184, 186, 187, and 196.)
- [Giorgi 13] G. L. Giorgi, F. Plastina, G. Francica & R. Zambrini. *Spontaneous synchronization and quantum correlation dynamics of open spin systems*. Phys. Rev. A, vol. 88, page 042115, Oct 2013. [Online URL](#). (Cited on page 184.)
- [Gottesman 99] Daniel Gottesman & Isaac L. Chuang. *Demonstrating the viability of universal quantum computation using teleportation and single-qubit operations*. Nature, vol. 402, no. 6760, pages 390–393, 1999. [Online URL](#). (Cited on page 3.)

- [Gottesman 01] Daniel Gottesman, Alexei Kitaev & John Preskill. *Encoding a qubit in an oscillator*. Phys. Rev. A, vol. 64, page 012310, Jun 2001. [Online URL](#). (Cited on page 168.)
- [Griffiths 14] D.J. Griffiths. Introduction to electrodynamics. Pearson Education, 2014. (Cited on page 8.)
- [Grover 96] Lov K. Grover. *A Fast Quantum Mechanical Algorithm for Database Search*. In Proceedings of the Twenty-Eighth Annual ACM Symposium on Theory of Computing, STOC '96, pages 212–219, New York, NY, USA, 1996. Association for Computing Machinery. (Cited on pages 2, 159, and 162.)
- [Grynberg 10] Gilbert Grynberg, Alain Aspect, Claude Fabre & Claude Cohen-Tannoudji. Introduction to quantum optics: From the semi-classical approach to quantized light. Cambridge University Press, 2010. (Cited on pages 10, 14, 15, 16, 19, 27, and 62.)
- [Gu 09] Mile Gu, Christian Weedbrook, Nicolas C. Menicucci, Timothy C. Ralph & Peter van Loock. *Quantum computing with continuous-variable clusters*. Phys. Rev. A, vol. 79, page 062318, Jun 2009. [Online URL](#). (Cited on page 3.)
- [Heinrich 11] Georg Heinrich, Max Ludwig, Jiang Qian, Björn Kubala & Florian Marquardt. *Collective Dynamics in Optomechanical Arrays*. Phys. Rev. Lett., vol. 107, page 043603, Jul 2011. [Online URL](#). (Cited on page 184.)
- [Hildenbrand 08] Anne Hildenbrand. *Etude de l'endommagement laser dans les cristaux non linéaires en régime nanoseconde*. PhD thesis, 2008. 2008AIX30055. (Cited on page 105.)
- [Horoshko 19] D. B. Horoshko, L. La Volpe, F. Arzani, N. Treps, C. Fabre & M. I. Kolobov. *Bloch-Messiah reduction for twin beams of light*. Phys. Rev. A, vol. 100, page 013837, Jul 2019. [Online URL](#). (Cited on page 77.)
- [Huntington 05] E. H. Huntington, G. N. Milford, C. Robilliard, T. C. Ralph, O. Glöckl, U. L. Andersen, S. Lorenz & G. Leuchs. *Demonstration of the spatial separation of the entangled quantum sidebands of an optical field*. Phys. Rev. A, vol. 71, page 041802, Apr 2005. [Online URL](#). (Cited on pages 46 and 47.)

- [Huygens 90] Christiaan Huygens. *Traité de la lumière: Où sont expliquées les causes de ce qui luy arrive dans la reflexion & dans la refraction*. Leiden: Pieter van der Aa, 1690. (Cited on page 1.)
- [Inoue 23] A. Inoue, T. Kashiwazaki, T. Yamashima, N. Takanashi, T. Kazama, K. Enbutsu, K. Watanabe, T. Umeki, M. Endo & A. Furusawa. *Toward a multi-core ultra-fast optical quantum processor: 43-GHz bandwidth real-time amplitude measurement of 5-dB squeezed light using modularized optical parametric amplifier with 5G technology*. *Applied Physics Letters*, vol. 122, no. 10, page 104001, 03 2023. [Online URL](#). (Cited on page 84.)
- [Jackson 12] J.D. Jackson. *Classical electrodynamics*. Wiley, 2012. (Cited on page 8.)
- [Jacquard 17] Clément Jacquard. *A single-photon subtractor for spectrally multimode quantum states*. PhD thesis, Sorbonne Université, 2017. 2017PA066155. (Cited on pages 113 and 172.)
- [Jozsa 00] Richard Jozsa, Daniel S. Abrams, Jonathan P. Dowling & Colin P. Williams. *Quantum Clock Synchronization Based on Shared Prior Entanglement*. *Phys. Rev. Lett.*, vol. 85, pages 2010–2013, Aug 2000. [Online URL](#). (Cited on page 184.)
- [Kato 02] Kiyoshi Kato & Eiko Takaoka. *Sellmeier and thermo-optic dispersion formulas for KTP*. *Appl. Opt.*, vol. 41, no. 24, pages 5040–5044, Aug 2002. [Online URL](#). (Cited on pages 106 and 109.)
- [Kim 08] M. S. Kim, H. Jeong, A. Zavatta, V. Parigi & M. Bellini. *Scheme for Proving the Bosonic Commutation Relation Using Single-Photon Interference*. *Phys. Rev. Lett.*, vol. 101, page 260401, Dec 2008. [Online URL](#). (Cited on page 172.)
- [Kimble 08] H. J. Kimble. *The quantum internet*. *Nature*, vol. 453, no. 7198, pages 1023–1030, 2008. [Online URL](#). (Cited on page 3.)
- [Kouadou 21] Tiphaine Kouadou. *Single-Pass Generation and Detection of Ultrafast Multimode Squeezed Light*. Theses, Sorbonne Université, March 2021. (Cited on pages 54, 84, 117, and 126.)
- [Kouadou 23] Tiphaine Kouadou, F. Sansavini, M. Ansquer, J. Henaff, N. Treps & V. Parigi. *Spectrally shaped and pulse-by-pulse multiplexed multimode squeezed states of light*. *APL Photonics*, vol. 8, no. 8, page 086113, 08 2023. [Online URL](#). (Cited on pages 3, 4, 84, 100, and 119.)

- [Kumar 12] R. Kumar, E. Barrios, A. MacRae, E. Cairns, E.H. Huntington & A.I. Lvovsky. *Versatile wideband balanced detector for quantum optical homodyne tomography*. Optics Communications, vol. 285, no. 24, pages 5259–5267, 2012. [Online URL](#). (Cited on page 127.)
- [Larsen 19] Mikkel V. Larsen, Xueshi Guo, Casper R. Breum, Jonas S. Neergaard-Nielsen & Ulrik L. Andersen. *Deterministic generation of a two-dimensional cluster state*. Science, vol. 366, no. 6463, pages 369–372, 2019. [Online URL](#). (Cited on pages 3, 84, and 141.)
- [LaVolpe 19] Luca LaVolpe. *Single-Pass Squeezing and Spatio-temporal Modes*. Theses, Sorbonne Université, March 2019. (Cited on pages 105, 110, and 117.)
- [LaVolpe 20] Luca LaVolpe, Syamsundar De, Tiphaine Kouadou, Dmitri Horoshko, Mikhail I. Kolobov, Claude Fabre, Valentina Parigi & Nicolas Treps. *Multimode single-pass spatio-temporal squeezing*. Opt. Express, vol. 28, no. 8, pages 12385–12394, Apr 2020. [Online URL](#). (Cited on page 84.)
- [Lenzini 18] Francesco Lenzini, Jiri Janousek, Oliver Thearle, Matteo Villa, Ben Haylock, Sachin Kasture, Liang Cui, Hoang-Phuong Phan, Dzung Viet Dao, Hidehiro Yonezawa, Ping Koy Lam, Elanor H. Huntington & Mirko Lobino. *Integrated photonic platform for quantum information with continuous variables*. Science Advances, vol. 4, no. 12, page eaat9331, 2018. [Online URL](#). (Cited on page 84.)
- [Leonhardt 97] U. Leonhardt. *Measuring the quantum state of light*. Cambridge Studies in Modern Optics. Cambridge University Press, 1997. (Cited on page 25.)
- [Levin 17] D.A. Levin & Y. Peres. *Markov chains and mixing times*. MBK. American Mathematical Society, 2017. (Cited on page 160.)
- [Lindblad 76] G. Lindblad. *On the generators of quantum dynamical semigroups*. Communications in Mathematical Physics, vol. 48, no. 2, pages 119–130, 1976. [Online URL](#). (Cited on page 185.)
- [Loudon 00] R. Loudon. *The quantum theory of light*. OUP Oxford, 2000. (Cited on pages 10, 15, 50, and 71.)
- [Lvovsky 16] A. I. Lvovsky. *Squeezed light*, 2016. (Cited on pages 30, 126, 127, and 171.)

- [Magnus 54] Wilhelm Magnus. *On the exponential solution of differential equations for a linear operator*. Communications on Pure and Applied Mathematics, vol. 7, no. 4, pages 649–673, 1954. [Online URL](#). (Cited on pages 72 and 74.)
- [Mandarino 14] Antonio Mandarino, Matteo Bina, Stefano Olivares & Matteo G. A. Paris. *About the use of fidelity in continuous variable systems*. International Journal of Quantum Information, vol. 12, no. 02, page 1461015, 2014. [Online URL](#). (Cited on page 178.)
- [Manzano 13] Gonzalo Manzano, Fernando Galve, Gian Luca Giorgi, Emilio Hernández-García & Roberta Zambrini. *Synchronization, quantum correlations and entanglement in oscillator networks*. Scientific Reports, vol. 3, no. 1, page 1439, 2013. [Online URL](#). (Cited on page 184.)
- [Mari 12] A. Mari & J. Eisert. *Positive Wigner Functions Render Classical Simulation of Quantum Computation Efficient*. Phys. Rev. Lett., vol. 109, page 230503, Dec 2012. [Online URL](#). (Cited on pages 25 and 37.)
- [Martinelli 23] Marcelo Martinelli. *From spectral matrix to sideband structure: exploring stereo multimodes*. J. Opt. Soc. Am. B, vol. 40, no. 5, pages 1277–1291, May 2023. [Online URL](#). (Cited on page 47.)
- [Matthews 12] Jonathan C. F. Matthews & Mark G. Thompson. *An entangled walk of photons*. Nature, vol. 484, no. 7392, pages 47–48, 2012. [Online URL](#). (Cited on pages 3 and 161.)
- [Maxwell 96] J.C. Maxwell & T.F. Torrance. *A dynamical theory of the electromagnetic field*. Torrance collection. Wipf and Stock, 1996. (Cited on pages 2 and 8.)
- [Medeiros de Araujo 12] Renné Medeiros de Araujo. *Génération et manipulation de peignes de fréquences quantiques multimodes*. Theses, Université Pierre et Marie Curie - Paris VI, November 2012. (Cited on pages 62, 71, and 132.)
- [Menicucci 06] Nicolas C. Menicucci, Peter van Loock, Mile Gu, Christian Weedbrook, Timothy C. Ralph & Michael A. Nielsen. *Universal Quantum Computation with Continuous-Variable Cluster States*. Phys. Rev. Lett., vol. 97, page 110501, Sep 2006. [Online URL](#). (Cited on page 3.)

- [Michel 21] Thibault Michel. *Optimization of the pump spectral shape in a parametric down conversion process to generate multimode entangled states*. PhD thesis, Sorbonne Université, The Australian National University, 2021. (Cited on pages 71, 116, 131, 132, and 199.)
- [Mondain 19] F. Mondain, T. Lunghi, A. Zavatta, E. Gouzien, F. Doustre, M. De Micheli, S. Tanzilli & V. D’Auria. *Chip-based squeezing at a telecom wavelength*. *Photon. Res.*, vol. 7, no. 7, pages A36–A39, Jul 2019. [Online URL](#). (Cited on page 84.)
- [Monmayrant 10] Antoine Monmayrant, Sébastien Weber & Béatrice Chatel. *A newcomer’s guide to ultrashort pulse shaping and characterization*. *Journal of Physics B: Atomic, Molecular and Optical Physics*, vol. 43, no. 10, page 103001, may 2010. [Online URL](#). (Cited on pages 111 and 112.)
- [Mosley 07] P Mosley & Peter Mosley. *Generation of heralded single photons in pure quantum states*. PhD thesis, University of Oxford, 2007. (Cited on page 79.)
- [Murphy 01] Thomas E. Murphy. *Design, fabrication and measurement of integrated Bragg grating optical filters*. PhD thesis, Massachusetts Institute of Technology, 2001. (Cited on pages 95 and 96.)
- [Newton 04] Isaac Newton. *Opticks: or, A Treatise of the Reflexions, Refractions, Inflexions and Colours of Light*, 1704. (Cited on page 1.)
- [Nielsen 10] M.A. Nielsen & I.L. Chuang. *Quantum computation and quantum information: 10th anniversary edition*. Cambridge University Press, 2010. (Cited on pages 2, 22, 39, and 185.)
- [Nielsen 23] Jens A. H. Nielsen, Jonas S. Neergaard-Nielsen, Tobias Gehring & Ulrik L. Andersen. *Deterministic Quantum Phase Estimation beyond N00N States*. *Phys. Rev. Lett.*, vol. 130, page 123603, Mar 2023. [Online URL](#). (Cited on page 83.)
- [Nokkala 18] J Nokkala, F Arzani, F Galve, R Zambrini, S Maniscalco, J Piilo, N Treps & V Parigi. *Reconfigurable optical implementation of quantum complex networks*. *New Journal of Physics*, vol. 20, no. 5, page 053024, may 2018. [Online URL](#). (Cited on pages 3 and 187.)
- [Nokkala 21] Johannes Nokkala, Rodrigo Martínez-Peña, Gian Luca Giorgi, Valentina Parigi, Miguel C. Soriano & Roberta Zambrini. *Gaussian states of continuous-variable quantum systems provide universal*

-
- and versatile reservoir computing*. Communications Physics, vol. 4, no. 1, page 53, 2021. [Online URL](#). (Cited on page 3.)
- [Novo 15] Leonardo Novo, Shantanav Chakraborty, Masoud Mohseni, Hartmut Neven & Yasser Omar. *Systematic Dimensionality Reduction for Quantum Walks: Optimal Spatial Search and Transport on Non-Regular Graphs*. Scientific Reports, vol. 5, no. 1, page 13304, 2015. [Online URL](#). (Cited on page 165.)
- [O’Brien 07] Jeremy L. O’Brien. *Optical Quantum Computing*. Science, vol. 318, no. 5856, pages 1567–1570, 2007. [Online URL](#). (Cited on page 3.)
- [O’Brien 09] Jeremy L. O’Brien, Akira Furusawa & Jelena Vucković. *Photonic quantum technologies*. Nature Photonics, vol. 3, no. 12, pages 687–695, 2009. [Online URL](#). (Cited on page 3.)
- [Ogata 10] K. Ogata. *Modern control engineering*. Instrumentation and controls series. Prentice Hall, 2010. (Cited on page 148.)
- [Okamoto 06] K. Okamoto. *Fundamentals of optical waveguides*. Electronics & Electrical. Elsevier Science, 2006. (Cited on page 94.)
- [Orth 10] Peter P. Orth, David Roosen, Walter Hofstetter & Karyn Le Hur. *Dynamics, synchronization, and quantum phase transitions of two dissipative spins*. Phys. Rev. B, vol. 82, page 144423, Oct 2010. [Online URL](#). (Cited on page 184.)
- [Ou 07] Zhe-Yu Jeff Ou. *Multi-photon quantum interference*. Springer New York, NY, 2007. (Cited on page 79.)
- [Pack 04] Michael V. Pack, Darrell J. Armstrong & Arlee V. Smith. *Measurement of the $\chi(2)$ tensors of $KTiOPO_4$, $KTiOAsO_4$, $RbTiOPO_4$, and $RbTiOAsO_4$ crystals*. Appl. Opt., vol. 43, no. 16, pages 3319–3323, Jun 2004. [Online URL](#). (Cited on page 64.)
- [Padberg 20] Laura Padberg, Matteo Santandrea, Michael Rüsing, Julian Brockmeier, Peter Mackwitz, Gerhard Berth, Artur Zrenner, Christof Eigner & Christine Silberhorn. *Characterisation of width-dependent diffusion dynamics in rubidium-exchanged KTP waveguides*. Opt. Express, vol. 28, no. 17, pages 24353–24362, Aug 2020. [Online URL](#). (Cited on page 97.)
- [Parigi 07] Valentina Parigi, Alessandro Zavatta, Myungshik Kim & Marco Bellini. *Probing Quantum Commutation Rules by Addition and*

- Subtraction of Single Photons to/from a Light Field*. *Science*, vol. 317, no. 5846, pages 1890–1893, 2007. [Online URL](#). (Cited on pages 172 and 181.)
- [Patera 08] Giuseppe Patera. *Quantum properties of ultra-short pulses generated by SPOPOs: multi-mode squeezing and entanglement*. Theses, Université Pierre et Marie Curie - Paris VI, November 2008. (Cited on page 73.)
- [Pikovsky 01] A. Pikovsky, M. Rosenblum & J. Kurths. *Synchronization: A universal concept in nonlinear sciences*. Cambridge Nonlinear Science Series. Cambridge University Press, 2001. (Cited on page 184.)
- [Pinel 12] Olivier Pinel, Julien Fade, Daniel Braun, Pu Jian, Nicolas Treps & Claude Fabre. *Ultimate sensitivity of precision measurements with intense Gaussian quantum light: A multimodal approach*. *Phys. Rev. A*, vol. 85, page 010101, Jan 2012. [Online URL](#). (Cited on page 3.)
- [Pirandola 16] Stefano Pirandola & Samuel L. Braunstein. *Physics: Unite to build a quantum Internet*. *Nature*, vol. 532, no. 7598, pages 169–171, 2016. [Online URL](#). (Cited on page 3.)
- [Preskill 99] John Preskill. *Plug-in quantum software*. *Nature*, vol. 402, no. 6760, pages 357–358, 1999. [Online URL](#). (Cited on page 3.)
- [Preskill 18] John Preskill. *Quantum Computing in the NISQ era and beyond*. *Quantum*, vol. 2, page 79, August 2018. [Online URL](#). (Cited on page 3.)
- [Ra 20] Young-Sik Ra, Adrien Dufour, Mattia Walschaers, Clément Jacquard, Thibault Michel, Claude Fabre & Nicolas Treps. *Non-Gaussian quantum states of a multimode light field*. *Nature Physics*, vol. 16, no. 2, pages 144–147, 2020. [Online URL](#). (Cited on page 3.)
- [Ramos-Israde 21] Elier Ramos-Israde, Karina Garay-Palmett & Roger S. Cudney. *Randomly aperiodically poled LiNbO3 crystal design by Monte Carlo–Metropolis with simulated annealing optimization for ultrabroadband photon pair generation*. *Appl. Opt.*, vol. 60, no. 34, pages 10587–10593, Dec 2021. [Online URL](#). (Cited on page 126.)

- [Raussendorf 01] Robert Raussendorf & Hans J. Briegel. *A One-Way Quantum Computer*. Phys. Rev. Lett., vol. 86, pages 5188–5191, May 2001. [Online URL](#). (Cited on page 3.)
- [Reck 94] Michael Reck, Anton Zeilinger, Herbert J. Bernstein & Philip Bertani. *Experimental realization of any discrete unitary operator*. Phys. Rev. Lett., vol. 73, pages 58–61, Jul 1994. [Online URL](#). (Cited on page 175.)
- [Renault 22] Paul Renault. *Non Markovian behavior and spectral density measurement in optical quantum networks*. Theses, Sorbonne Université, April 2022. (Cited on page 200.)
- [Renault 23] P. Renault, J. Nokkala, G. Roeland, N.Y. Joly, R. Zambrini, S. Maniscalco, J. Piilo, N. Treps & V. Parigi. *Experimental Optical Simulator of Reconfigurable and Complex Quantum Environment*. PRX Quantum, vol. 4, page 040310, Oct 2023. [Online URL](#). (Cited on pages 3, 187, and 199.)
- [Révész 13] P. Révész. *Random walk in random and non-random environments*. World Scientific, 2013. (Cited on page 160.)
- [Robertson 29] H. P. Robertson. *The Uncertainty Principle*. Phys. Rev., vol. 34, pages 163–164, Jul 1929. [Online URL](#). (Cited on page 18.)
- [Roeland 22] Ganaël Roeland, Srinivasan Kaali, Victor Roman Rodriguez, Nicolas Treps & Valentina Parigi. *Mode-selective single-photon addition to a multimode quantum field*. New Journal of Physics, vol. 24, no. 4, page 043031, apr 2022. [Online URL](#). (Cited on page 180.)
- [Roelofs 94] M. G. Roelofs, A. Suna, W. Bindloss & J. D. Bierlein. *Characterization of optical waveguides in KTiOPO4 by second harmonic spectroscopy*. Journal of Applied Physics, vol. 76, no. 9, pages 4999–5006, 11 1994. [Online URL](#). (Cited on page 96.)
- [Roman-Rodriguez 21] V Roman-Rodriguez, B Brecht, Srinivasan K, C Silberhorn, N Treps, E Diamanti & V Parigi. *Continuous variable multimode quantum states via symmetric group velocity matching*. New Journal of Physics, vol. 23, no. 4, page 043012, apr 2021. [Online URL](#). (Cited on pages 66 and 100.)
- [Roslund 14] Jonathan Roslund, RennéMedeiros de Araújo, Shifeng Jiang, Claude Fabre & Nicolas Treps. *Wavelength-multiplexed quantum*

- networks with ultrafast frequency combs*. Nature Photonics, vol. 8, no. 2, pages 109–112, 2014. [Online URL](#). (Cited on page 3.)
- [Scully 72] Marlan O. Scully & Murray Sargent. *The concept of the photon*. Physics Today, vol. 25, no. 3, pages 38–47, 03 1972. [Online URL](#). (Cited on page 15.)
- [Shor 94] P.W. Shor. *Algorithms for quantum computation: discrete logarithms and factoring*. In Proceedings 35th Annual Symposium on Foundations of Computer Science, pages 124–134, 1994. (Cited on page 2.)
- [Siegman 86] A.E. Siegman. *Lasers*. G - Reference, Information and Interdisciplinary Subjects Series. University Science Books, 1986. (Cited on page 11.)
- [Simon 00] R. Simon. *Peres-Horodecki Separability Criterion for Continuous Variable Systems*. Phys. Rev. Lett., vol. 84, pages 2726–2729, Mar 2000. [Online URL](#). (Cited on page 137.)
- [Snyder 83] A.W. Snyder & J. Love. *Optical waveguide theory*. Science paperbacks. Springer US, 1983. (Cited on pages 94 and 95.)
- [Strogatz 05] Steven H. Strogatz, Daniel M. Abrams, Allan McRobie, Bruno Eckhardt & Edward Ott. *Crowd synchrony on the Millennium Bridge*. Nature, vol. 438, no. 7064, pages 43–44, 2005. [Online URL](#). (Cited on page 184.)
- [Strogatz 18] S.H. Strogatz. *Nonlinear dynamics and chaos: With applications to physics, biology, chemistry, and engineering*. CRC Press, 2018. (Cited on page 184.)
- [Tan 20] Kok Chuan Tan, Seongjeon Choi & Hyunseok Jeong. *Negativity of Quasiprobability Distributions as a Measure of Nonclassicality*. Phys. Rev. Lett., vol. 124, page 110404, Mar 2020. [Online URL](#). (Cited on page 25.)
- [Thiel 15] Valérian Thiel. *Modal analysis of an ultrafast frequency comb : from classical to quantum spectral correlations*. Theses, Université Pierre et Marie Curie - Paris VI, October 2015. (Cited on pages 91, 92, 111, 123, and 212.)
- [Tho 23] *Driver PID Settings*. https://www.thorlabs.com/newgrouppage9.cfm?objectgroup_id=9013, 2023. Accessed: 10-10-2023. (Cited on page 148.)

- [Trebino 00] R. Trebino. Frequency-resolved optical gating: The measurement of ultrashort laser pulses: The measurement of ultrashort laser pulses. Springer US, 2000. (Cited on pages 111 and 211.)
- [Treps 05] N. Treps, V. Delaubert, A. Maître, J. M. Courty & C. Fabre. *Quantum noise in multipixel image processing*. Phys. Rev. A, vol. 71, page 013820, Jan 2005. [Online URL](#). (Cited on page 21.)
- [Vahlbruch 16] Henning Vahlbruch, Moritz Mehmet, Karsten Danzmann & Roman Schnabel. *Detection of 15 dB Squeezed States of Light and their Application for the Absolute Calibration of Photoelectric Quantum Efficiency*. Phys. Rev. Lett., vol. 117, page 110801, Sep 2016. [Online URL](#). (Cited on page 84.)
- [Vaughan 05] Joshua C. Vaughan, Thomas Hornung, T. Feuerer & Keith A. Nelson. *Diffraction-based femtosecond pulse shaping with a two-dimensional spatial light modulator*. Opt. Lett., vol. 30, no. 3, pages 323–325, Feb 2005. [Online URL](#). (Cited on page 112.)
- [Wang 15] D.N. Wang, Y. Wang & C.R. Liao. Femtosecond laser micromachining on optical fiber, pages 359–381. Woodhead Publishing, 12 2015. (Cited on page 105.)
- [Weedbrook 12] Christian Weedbrook, Stefano Pirandola, Raúl García-Patrón, Nicolas J. Cerf, Timothy C. Ralph, Jeffrey H. Shapiro & Seth Lloyd. *Gaussian quantum information*. Rev. Mod. Phys., vol. 84, pages 621–669, May 2012. [Online URL](#). (Cited on pages 3, 37, 38, and 42.)
- [Weiner 88] A. M. Weiner, J. P. Heritage & E. M. Kirschner. *High-resolution femtosecond pulse shaping*. J. Opt. Soc. Am. B, vol. 5, no. 8, pages 1563–1572, Aug 1988. [Online URL](#). (Cited on page 112.)
- [Weiner 11] A.M. Weiner. Ultrafast optics. Wiley Series in Pure and Applied Optics. Wiley, 2011. (Cited on pages 60, 61, 62, 66, 70, 86, 88, and 111.)
- [Weiss 94] G.H. Weiss. Aspects and applications of the random walk. International Congress Series. North-Holland, 1994. (Cited on page 160.)
- [Wigner 32] E. Wigner. *On the Quantum Correction For Thermodynamic Equilibrium*. Phys. Rev., vol. 40, pages 749–759, Jun 1932. [Online URL](#). (Cited on page 25.)

- [Williamson 36] John Williamson. *On the Algebraic Problem Concerning the Normal Forms of Linear Dynamical Systems*. American Journal of Mathematics, vol. 58, no. 1, pages 141–163, 1936. [Online URL](#) (consulté le 2023-10-24). (Cited on page 42.)
- [Wiseman 10] H.M. Wiseman & G.J. Milburn. Quantum measurement and control. Cambridge University Press, 2010. (Cited on pages 183 and 185.)
- [Wong 16] Thomas G. Wong, Luís Tarrataca & Nikolay Nahimov. *Laplacian versus adjacency matrix in quantum walk search*. Quantum Information Processing, vol. 15, no. 10, pages 4029–4048, 2016. [Online URL](#). (Cited on pages 160 and 162.)
- [Yang 21] Zijiao Yang, Mandana Jahanbozorgi, Dongin Jeong, Shuman Sun, Olivier Pfister, Hansuek Lee & Xu Yi. *A squeezed quantum microcomb on a chip*. Nature Communications, vol. 12, no. 1, page 4781, 2021. [Online URL](#). (Cited on page 84.)
- [Yariv 89] A. Yariv. Quantum electronics. Wiley, 1989. (Cited on page 11.)
- [Yefet 13] Shai Yefet. *Control and Manipulation of the Kerr-lens Mode-locking Dynamics in Lasers*. PhD thesis, Bar Ilan University, May 2013. (Cited on page 88.)
- [Yokoyama 13] Shota Yokoyama, Ryuji Ukai, Seiji C. Armstrong, Chanond Sornphiphatphong, Toshiyuki Kaji, Shigenari Suzuki, Jun-ichi Yoshikawa, Hidehiro Yonezawa, Nicolas C. Menicucci & Akira Furusawa. *Ultra-large-scale continuous-variable cluster states multiplexed in the time domain*. Nature Photonics, vol. 7, no. 12, pages 982–986, 2013. [Online URL](#). (Cited on pages 3, 84, 141, and 142.)
- [Yoshida 06] Hidetsugu Yoshida, Hisanori Fujita, Masahiro Nakatsuka, Masashi Yoshimura, Takatomo Sasaki, Tomosumi Kamimura & Kunio Yoshida. *Dependences of Laser-Induced Bulk Damage Threshold and Crack Patterns in Several Nonlinear Crystals on Irradiation Direction*. Japanese Journal of Applied Physics, vol. 45, no. 2R, page 766, feb 2006. [Online URL](#). (Cited on page 105.)
- [Yuen 83] Horace P. Yuen & Vincent W. S. Chan. *Noise in homodyne and heterodyne detection*. Opt. Lett., vol. 8, no. 3, pages 177–179, Mar 1983. [Online URL](#). (Cited on page 52.)

-
- [Zhang 03] Jing Zhang. *Einstein-Podolsky-Rosen sideband entanglement in broadband squeezed light*. Phys. Rev. A, vol. 67, page 054302, May 2003. [Online URL](#). (Cited on pages 47, 49, and 57.)
- [Zhang 21] Zheshen Zhang & Quntao Zhuang. *Distributed quantum sensing*. Quantum Science and Technology, vol. 6, no. 4, page 043001, jul 2021. [Online URL](#). (Cited on page 3.)
- [Zhirov 08] O. V. Zhirov & D. L. Shepelyansky. *Synchronization and Bistability of a Qubit Coupled to a Driven Dissipative Oscillator*. Phys. Rev. Lett., vol. 100, page 014101, Jan 2008. [Online URL](#). (Cited on page 184.)
- [Zhong 20] Han-Sen Zhong, Hui Wang, Yu-Hao Deng, Ming-Cheng Chen, Li-Chao Peng, Yi-Han Luo, Jian Qin, Dian Wu, Xing Ding, Yi Hu, Peng Hu, Xiao-Yan Yang, Wei-Jun Zhang, Hao Li, Yuxuan Li, Xiao Jiang, Lin Gan, Guangwen Yang, Lixing You, Zhen Wang, Li Li, Nai-Le Liu, Chao-Yang Lu & Jian-Wei Pan. *Quantum computational advantage using photons*. Science, vol. 370, no. 6523, pages 1460–1463, 2020. [Online URL](#). (Cited on page 2.)
- [Zippilli 15] Stefano Zippilli, Giovanni Di Giuseppe & David Vitali. *Entanglement and squeezing of continuous-wave stationary light*. New Journal of Physics, vol. 17, no. 4, page 043025, apr 2015. [Online URL](#). (Cited on pages 56 and 57.)